Universität Augsburg
Mathematisch-Naturwissenschaftlich-
Technische Fakultät

Compressibility and Capacitance of Quantum Systems

Dissertation

zur Erlangung des akademischen Grades
Dr. rer. nat.

eingereicht an der
Mathematisch-Naturwissenschaftlich-Technischen Fakultät
der Universität Augsburg

von

Kevin Patrick Steffen

Augsburg, Juli 2017

Tag der mündlichen Prüfung:	04. September 2017
Erstgutachter:	Prof. Dr. Thilo Kopp
Zweitgutachter:	Prof. Dr. Gert-Ludwig Ingold

Contents

1. Prologue

The technical progress of electronic devices is accompanied by or even based upon the miniaturization of electrical circuits. As characteristic lengths reach the nanoscale regime, quantum mechanical effects play an increasing role and may impede technical advances. For example, in metal-oxide semiconductor field-effect transistors (MOSFETs) larger gate capacitances reduce the power dissipation as they render smaller gate voltages possible. The capacitance can be increased by either reducing the plate distance d or by increasing the dielectric constant ϵ of the insulator between the gates. But d possesses a lower boundary below which the gate currents induced by quantum mechanical tunnel processes exceed reasonable values. Even for arbitrarily large ϵ, a finite screening length inside the gate electrodes limits the effective gate distance and hence the capacitance [1].

On the other hand, quantum mechanical phenomena may also open up new possibilities for the realization of electronic devices with enhanced or unique properties. A class of materials that is promising in this respect are heterostructures with transition-metal oxides [2], for which already today interfaces and surfaces can be fabricated with properties sufficient for functionality [3]. The paradigm example of a representative of oxide heterostructures is $LaAlO_3/SrTiO_3$ (LAO/STO), as the two-dimensional electron system at the interface between the two bulk insulators $LaAlO_3$ and $SrTiO_3$ features electronic correlations. These give rise to a plethora of physical phenomena, as, e.g., superconductivity [4], magnetism [5] and even the coexistence of superconductivity and magnetism [6, 7]. A seizable spin-orbit coupling is also present at the LAO/STO interface [8]. As the electron density n at the interface can be varied by at least one order of magnitude by application of a backgate voltage, the LAO/STO system offers an excellent aptitude for the utilization in electronic devices.

Measurements of the capacitance of a LAO/STO heterostructure by Lu Li *et al.* revealed an increase of more than 40% above the geometric capacitance at low electron densities [9]. The observed enhancement is much larger than in any other system so far. It can be traced back to the negative compressibility $\kappa < 0$ of the dilute electronic subsystem in one electrode [10, 11, 12]: In a homogeneous electron system at low densities the negative contribution of the exchange and correlation term to the compressibility dominates over the positive kinetic contribution.

These findings and previous theoretical work [10, 11, 12] point to a new way to enhance the capacitance: As the modification of the material between the electrodes, i.e., the search for high dielectrics[1], has reached its limits, the turn towards the electrode material promises substantial progress.

This theoretical work examines how the properties of two-dimensional quantum mechanical electronic systems on the electrodes affect the capacitance and electronic stability of a two-plate capacitor. We investigate different models for the electronic systems and identify conditions under which the capacitance is enhanced beyond the geometric value.

The layout we analyze consists of two static two-dimensional electron systems with Helmholtz free energy F_i, $i = 1, 2$, at a fixed distance d that are coupled to each other. The total electron

[1] The denotation is actually "high-κ", where κ refers to the real part of the dielectric constant ϵ. In this work, however, κ is exclusively the compressibility.

density is $n_\mathrm{t} = n_1 + n_2$, where n_i is the electron density in subsystem i. Then the Helmholtz free energy of the total system is given by (for details see Section 2.2):

$$F_\mathrm{t}(n_1, n_\mathrm{t}) = F_1(n_1) + F_2(n_\mathrm{t} - n_1) + F_\mathrm{es}(n_1, n_\mathrm{t}) - eV_\mathrm{ext} n_1 A$$

Here $V_\mathrm{ext} = V_\mathrm{s}$, where V_s is the voltage from an external voltage source, e is the elementary charge and A is the area of one electrode. F_es is the energy of the direct Coulomb interactions between all charges. The differential capacitance is given by the differential change of charge on one electrode divided by the differential voltage that induced the change in charge. As n_1 has to minimize F_t, one can extract V_s from the first derivative of the equation above. Thus the inverse differential capacitance C_diff^{-1} of this layout is proportional to the second derivative of F_t with respect to the electron density on one layer:

$$\frac{1}{C_\mathrm{diff}} = \frac{\partial V_s}{eA\partial n_1} = \frac{1}{e^2A^2}\left(\frac{\partial^2 F_1}{\partial n_1^2} + \frac{\partial^2 F_2}{\partial n_1^2} + \frac{\partial^2 F_\mathrm{es}}{\partial n_1^2}\right) = \frac{1}{e^2A^2}\left(\frac{\partial^2 F_1}{\partial n_1^2} + \frac{\partial^2 F_2}{\partial n_2^2}\right) + \frac{1}{C_\mathrm{geo}} \tag{1.1}$$

This relation, read from left to right, demonstrates that the differential capacitance is a series connection of the geometric capacitance, as derived from the electrostatic term F_es, with two capacitances that originate from the quantum mechanical energies of the electronic systems. For effective distances d/ϵ in the nanometer regime, these two "quantum capacitances" can be of the same order of magnitude as the inverse geometrical capacitance, $C_\mathrm{geo}^{-1} = 4\pi d/\epsilon A$. If the sum of the "quantum capacitances" is negative, then the differential capacitance exceeds the geometric value, $C_\mathrm{diff} > C_\mathrm{geo}$.

The second partial derivatives appearing in the capacitance are closely connected to the inverse compressibility κ^{-1}. The sign of the compressibility determines the stability of a system; for $\kappa < 0$ the system is instable (see Section 2.1). For constant temperature and volume of the system, κ^{-1} is given by

$$\frac{1}{\kappa} = n_\mathrm{t}^2 \frac{\mathrm{d}\mu}{\mathrm{d}n_\mathrm{t}} = n_\mathrm{t}^2 \frac{\mathrm{d}^2 F_\mathrm{t}/A}{\mathrm{d}n_\mathrm{t}^2}, \tag{1.2}$$

where μ is the chemical potential. The total derivatives are taken with respect to the thermodynamic variable of the system, which is the total electron density n_t. The electron densities on the plates, n_1 and n_2, are functions of n_t and adjust in such a way that F_t is minimized.

If the electronic systems of the electrodes were isolated, then the second partial derivatives appearing in Eq. (1.1) could be replaced by total derivatives and the quantum capacitances would be proportional to the respective compressibilities. Then, the condition for $C_\mathrm{diff} > C_\mathrm{geo}$ corresponds to a negative compressibility in the isolated electron systems. This highlights the road map for capacitance enhancement beyond the geometrical value: Identify electronic systems that possess negative compressibility *if they are considered as isolated* and then incorporate them into the electrodes of a capacitor. Despite the instable electronic subsystems, the total combined system may possess a positive compressibility as *(i)* the electrostatic energy yields a positive contribution and *(ii)* the compressibility has to be evaluated according to Eq. (1.2). The latter yields, due to the total derivatives with respect to n_t, a different result than the single partial derivatives with respect to n_i, which occur in the negative compressibilities of the *isolated* subsystems.

The relation between capacitance and compressibility is discussed in Section 2.3 in more detail. We introduce a rather general distribution of positive background charge, which can be varied by parameters to account for different physical situations as, e.g., the layout of a polar heterostructure or a standard two-plate capacitor. Within this model we analyze the impact of the different configurations of positive background charge on the stability of the system. Chapter 2

is concluded by a short overview of some physical systems that displayed enhanced capacitance or negative compressibility experimentally and a short list of other theoretical approaches.

The remaining chapters are dedicated to different mechanism that are able to enhance the capacitance. According to Eq. (1.2), the compressibility is negative if an increase of the total charge n_t reduces the chemical potential. Hence we look for systems in which the band structure depends on the density.

At low electron densities the contribution of the exchange and correlation energy to the compressibility dominates over the kinetic term and thus induces $\kappa < 0$. This is well established both in theory (e.g., in Monte Carlo simulations [13, 14]) and experiment [10, 11]. The Hartree-Fock evaluation of the free electron gas is discussed in Chapter 3 to examine the role of the exchange contribution to the compressibility. We provide an overview of results for the correlation terms derived by Monte Carlo studies and their second derivative. The main work of Chapter 3 is the introduction of finite temperature into the Hartree-Fock theory on the level of first order perturbation theory. This alters the low density behavior quite drastically: At $T = 0$, the second derivative of the exchange term with respect to the density, and thus the inverse compressibility of the system, diverges to $-\infty$. At $T > 0$ this divergence of the exchange term vanishes and the inverse compressibility diverges to $+\infty$ for $n \to 0$ due to the entropic contribution.

Chapter 4 deals with the impact of spin-orbit coupling (SOC) at the LAO/STO interface on capacitance and compressibility. The strength of the SOC α increases with the magnitude of the symmetry breaking electrical field at the interface. We introduce a density dependence of this parameter by coupling to a second electron system: A transfer of charges from the second system to the interface leaves an electrically uncompensated positive background charges behind, which in turn create a symmetry breaking field at the interface that increases α. The SOC introduces a splitting of priorly spin-degenerate bands. The resulting band structure depends strongly on α: An increase of α shifts the minimum of the lower band to lower values. Thus the density dependence of α may cause the decrease of the chemical potential of the interface system with increased electron density. We start our analysis with the two-band Rashba model [15, 16, 17] and then turn our focus to a six-band model that accounts for the Ti t_{2g} orbitals that the electrons at the LAO/STO interface reside in [18].

The interplay between Rashba SOC and exchange interaction are explored in Chapter 5. We employ the Hartree-Fock approximation and then perform a diagonalization of the two-band model both analytically and numerically. The latter method, which—in contrast to the analytical approach—does not impose a symmetry a priori onto the solution, yields an intriguing groundstate at low densities which is characterized by a finite center of wave vectors in the Brillouin zone.

The starting point of Chapter 6 is the extended Hubbard model with nearest and next-nearest neighbor hopping. An attractive nearest-neighbor interaction V may render the compressibility negative for electron densities away from half filling, i.e., away from the correlation peak, which originates from the on-site repulsion U. We compare results from Hartree and Hartree-Fock calculations with data that was obtained with the Kotliar-Ruckenstein [19] slave-boson technique. The capacitance and compressibility are determined for different configurations of the positive background charge.

2. Introduction to Capacitance and Compressibility

2.1. Compressibility of a Thermodynamic System

The Helmholtz free energy $F(T, \mathcal{V}, N)$ of a general thermodynamic system is a function of the temperature T, the volume $\mathcal{V}$ and the number of particles N. It is connected to the internal energy E via a Legendre transformation:

$$F(T, \mathcal{V}, N) = E(S(T, \mathcal{V}, N), \mathcal{V}, N) - S(T, \mathcal{V}, N)T \tag{2.1}$$

The total differential of the Helmholtz free energy is given by

$$\mathrm{d}F(T, \mathcal{V}, N) = -S\mathrm{d}T - p\mathrm{d}\mathcal{V} + \mu\mathrm{d}N, \tag{2.2}$$

so that pressure p and chemical potential μ are:

$$p = -\left(\frac{\partial F}{\partial \mathcal{V}}\right)_{T,N}, \qquad \mu = \left(\frac{\partial F}{\partial N}\right)_{T,\mathcal{V}} \tag{2.3}$$

The isothermal compressibility κ is the change of volume with pressure at constant temperature and constant particle number:

$$\frac{1}{\kappa} = -\mathcal{V}\left(\frac{\partial p}{\partial \mathcal{V}}\right)_{T,N} = \mathcal{V}\left(\frac{\partial^2 F}{\partial \mathcal{V}^2}\right)_{T,N} \tag{2.4}$$

The inverse compressibility is also called the bulk modulus. With the introduction of the particle density $n = N/\mathcal{V}$ as number of particles per volume,

$$\left(\frac{\partial}{\partial n}\right)_{T,N} = \left(\frac{\partial \mathcal{V}}{\partial n}\right)_{T,N}\left(\frac{\partial}{\partial \mathcal{V}}\right)_{T,N} = -\frac{N}{n^2}\left(\frac{\partial}{\partial \mathcal{V}}\right)_{T,N} \tag{2.5}$$

is valid. This relation can be used to transform the inverse compressibility in Eq. (2.4) to

$$\frac{1}{\kappa} = n^2\left(\frac{\partial^2 F/\mathcal{V}}{\partial n^2}\right)_{T,N} \tag{2.6}$$

The equation above also holds true if instead of the particle number N the volume $\mathcal{V}$ is kept constant when taking the partial derivative (c.f. App. A.1). The chemical potential can also be expressed by the derivative with respect to particle density:

$$\mu = \left(\frac{\partial F/\mathcal{V}}{\partial n}\right)_{T,\mathcal{V}} \tag{2.7}$$

For the rest of this work it is assumed that all derivatives are taken at constant temperature T and constant volume $\mathcal{V}$, so that the indices can be omitted. This restriction represents the experimental situation where the setup is cooled to constant temperature and stable against structural deformation.

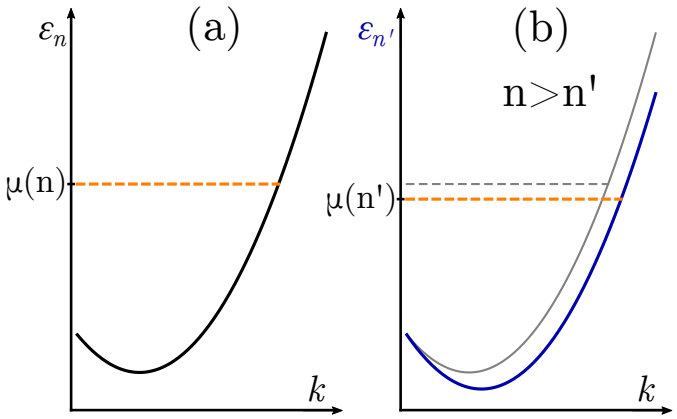

Figure 2.1.: Energy bands ε_n for a given density n as function of wavevector k. (a) Chemical potential μ for given density (orange dashed line). (b) An increase to density $n' > n$ lowers the energy band $\varepsilon_{n'}$ (blue) compared to ε_n (grey). The chemical potential of the higher density is lower than $\mu(n)$ (grey dashed). In this case, the electric compressibility is negative.

The stability of a system is determined by the sign of its compressibility. This can easily be seen with definition Eq. (2.4): At constant particle number the pressure p should decrease with increasing volume $\mathcal{V}$ of the system; otherwise the system would expand even without applied pressure. Therefore a stable system requires the compressibility to be positive, or equivalently that

$$\frac{\partial^2 F/\mathcal{V}}{\partial n^2} > 0 \qquad \Leftrightarrow \qquad \frac{\partial \mu}{\partial n} > 0 \tag{2.8}$$

The meaning of the chemical potential μ depends on the system which is considered [20]: For a chemical reaction it characterizes the rate of change, for a concentration gradient the tendency to diffuse and for a system with constant entropy (and volume) the change in energy when one particle is added to the system. The last instance is of biggest relevance in solid-state physics, where electrons play the central role: If a system of electrons has free energy F and particle density n, then the chemical potential μ obtained by Eq. (2.7) is the energy of the highest filled energy level (at zero temperature).[1] The electron system is instable if an increase of electron density lowers the chemical potential, i.e., $\partial\mu/\partial n < 0$. This is only feasible for energy levels that depend on the electron density and are shifted down with increasing n. (Fig. 2.1)

If the calculation of the compressibility shows it to be negative, there are three possibilities that have to be considered:

First, $\kappa < 0$ could be an indicator that another phase, for which the system is stable, exists. It might be necessary to extend the model which produced the negative compressibility to capture this phase.

Second, the system with negative compressibility could be coupled to another system, which stabilizes the total system. For example, many properties in solid-state theory are understood by taking only the valence band electrons into account. But these electrons are coupled to a lattice of positive ions, which constitute the positively charged background, by Coulomb interaction. A possible instability in the valence electron system could be compensated by the positive compressibility of the background.

Third, the system could phase separate, i.e., two spatially separated phases with positive respective compressibilities exist. A well-known textbook example is the coexistence of the liquid and gaseous phase for a certain range of volume and pressure. The spatial separation of phases is often accompanied by a spatially non-uniform particle density. For charged particles, like electrons in a solid, this induces an electrostatic energy cost, which has to be incorporated into the free energy.

[1] The chemical potential for a given number N of electrons may be identified at temperature T through $\mu(T) = F(T, N+1) - F(T, N)$.

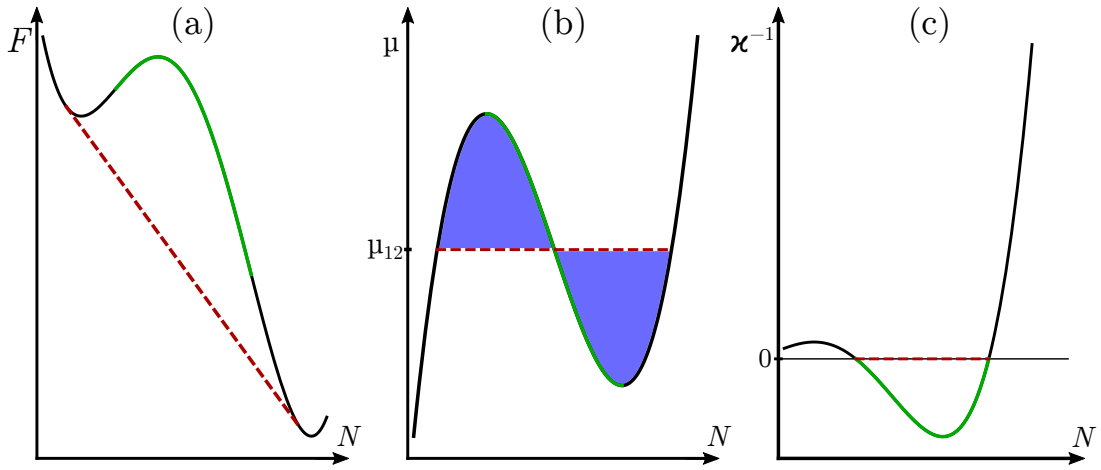

Figure 2.2.: Schematic plot of (a) the Helmholtz free energy F, (b) the corresponding chemical potential μ and (c) the inverse compressibility κ^{-1} (solid lines). In the range of the green solid line the compressibility is negative. In the Maxwell construction μ_{12} encloses two areas of equal size ((b), blue). The red dashed lines are the reconstructed curves for F, μ and κ^{-1}.

All of the three alternatives above have to be carefully examined and compared; the ground-state of the system has the lowest free energy.

The case of phase separation at the liquid-gas transition has been extensively analyzed by means of the van der Waals equation of state for a gas [21]. For a certain range of parameters the liquid and gaseous phase coexist. In this range the temperature, pressure and chemical potential of both phases have to be identical for the system being in equilibrium. The Maxwell construction can be used to determine the chemical potential of such a phase separated system. Therefore an isothermal curve in the pressure over volume diagram is plotted and one has to identify the constant pressure which intersects three times with the isothermal and encloses two areas of equal size with it. In the next paragraphs this concept is extended to analyze the behavior of the Helmholtz free energy and chemical potential in the case of phase separation.

We investigate a system where the compressibility is negative for an interval of particle numbers. The compressibility left and right of this interval is positive, so that the system can phase separate. Both phases shall be in thermal equilibrium, i.e., the temperature T is constant and can therefore be omitted. If one starts at low particle number, far left of the interval of negative compressibility, all particles of the system are in phase ph_1. As the number of particles is increased beyond a certain particle number N_1, a new phase ph_2 will emerge. Up to the particle number N_2 phase ph_1 and ph_2 coexist spatially separated. Above N_2 all particles are in phase ph_2. So, for a given Helmholtz free energy, between which values N_1 and N_2 do the phases ph_1 and ph_2 coexist and what is the chemical potential for the phase separated state? Figure 2.2 shows a schematic plot of a Helmholtz free energy F and the corresponding chemical potential μ and the inverse compressibility κ^{-1} as function of the particle number N before phase separation (solid lines). After phase separation takes place, both phases are at the same pressure and chemical potential for $N_1 \leq N \leq N_2$:

$$\mu(N_1) = \mu(N) \equiv \mu_{12} \quad \overset{\text{Eq. (2.3)}}{\Longleftrightarrow} \quad \left[\left(\frac{\partial F}{\partial N}\right)_{\mathcal{V}}\right]\Bigg|_{N=N_1} = \left(\frac{\partial F}{\partial N}\right)_{\mathcal{V}}, \qquad N_1 \leq N \leq N_2 \tag{2.9}$$

According to Eq. (2.3) the chemical potential is the first derivative of the Helmholtz free energy F with respect to the particle number. Hence, since the chemical potential is constant in the phase separated state for $N_1 \leq N \leq N_2$, F is linear in N for this particle number range:

$$F(\mathcal{V}, N) = F(\mathcal{V}, N_1) + \left[\left(\frac{\partial F}{\partial N}\right)_{\mathcal{V}}\right]\Bigg|_{N=N_1} (N - N_1), \qquad N_1 \leq N \leq N_2 \tag{2.10}$$

Eq. (2.10) combined with Eq. (2.9), yields the Legendre transform of F,

$$[F(\mathcal{V}, N) - N\mu(N)]|_{N=N_1} = F(\mathcal{V}, N) - N\mu(N), \qquad N_1 \leq N \leq N_2 \tag{2.11}$$

$$\Omega(\mathcal{V}, \mu(N_1)) = \Omega(\mathcal{V}, \mu(N)), \qquad N_1 \leq N \leq N_2, \tag{2.12}$$

which is the grand potential. It follows from $\partial\Omega/\partial\mathcal{V} = -p$ that the pressure p is equal for all $N_1 \leq N \leq N_2$. At $N = N_2$, Eq. (2.10) becomes

$$F(\mathcal{V}, N_2) - F(\mathcal{V}, N_1) = \left[\left(\frac{\partial F}{\partial N}\right)_{\mathcal{V}}\right]\Bigg|_{N=N_1} (N_2 - N_1) \tag{2.13}$$

$$\int_{N_1}^{N_2} \mathrm{d}N \frac{\partial F}{\partial N} = \int_{N_1}^{N_2} \mathrm{d}N \left[\left(\frac{\partial F}{\partial N}\right)_{\mathcal{V}}\right]\Bigg|_{N=N_1}$$

$$\int_{N_1}^{N_2} \mathrm{d}N\mu = \int_{N_1}^{N_2} \mathrm{d}N\mu_{12} \tag{2.14}$$

The last relation gives a graphical construction rule for μ_{12} if $\mu(N)$ is known: The two areas enclosed between μ_{12} and $\mu(N)$ have to be of equal size (c.f. Fig. 2.2b). This is analogous to the Maxwell construction. We would like to note that in the Maxwell construction usually the pressure p_{12} of equilibrium, which also ensures the condition of equal chemical potential, is determined. Here we determined the chemical potential μ_{12}, which guarantees the equality of pressure in the phase separated state.

Alternatively to the graphical construction the two equations (2.9) and (2.10) can be taken at $N = N_2$ and solved for N_1 and N_2.

The particle range of phase coexistence is larger than (and includes) the particle range of negative compressibility. Since for the latter the chemical potential decreases with increasing particle number, the condition of equal chemical potential cannot be fulfilled at the limits of the $\kappa < 0$ range. This leads to phase separation in a range of particle number where the compressibility is positive.

The Helmholtz free energy of the phase separated state is always smaller than that of the system before separation (c.f. Fig. 2.2a) for particles without electrical charge. But if the particles are charged, e.g., like electrons in a solid body, a charge distribution, which deviates from the neutralizing background charge distribution, introduces an additional electrostatic energy cost.

Note that in the phase separated state the chemical potential is independent of the particle number, which introduces difficulties for computational methods which rely on scanning through all values of chemical potential for the determination of the occupation number of energy bands. A small change in chemical potential around μ_{12} generates a jump in particle number from around N_1 to around N_2. This characterizes a first order phase transition. If one is interested in $F(n)$ for the instable phase, which could be stabilized by coupling to other degrees of freedom, other methods, which do not rely on the chemical potential, have to be used.

2.2. Coupled Electron Systems

The classical capacitance of two parallel metallic plates with distance d and area A can be easily calculated with Gauss's theorem and is a function of the geometric dimensions $C_{\mathrm{geo}} = A/4\pi d$.

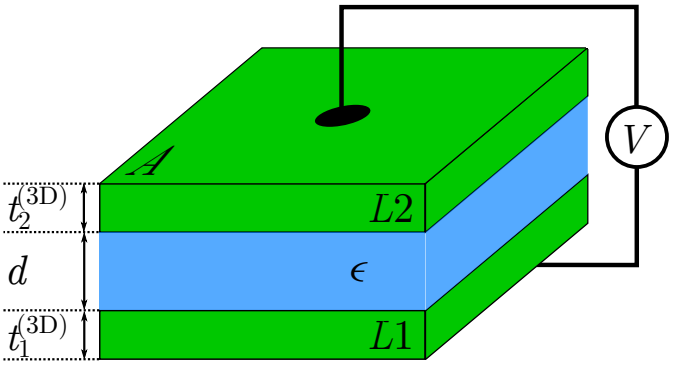

Figure 2.3.: The top electrode $L1$ with thickness $t_1^{(3D)}$ and area A is connected by a voltage source/voltmeter V with the bottom electrode $L2$ with thickness $t_2^{(3D)}$. The distance between the electrodes is d and the enclosed isolator has the dielectric constant ϵ.

But how is the capacitance affected by the properties of the metallic electron system on the electrodes when quantum mechanical effects play a role? To answer this question we investigate the following model: Two parallel electrodes with area A and distance d are connected by a voltage source, which applies the voltage V_s between the electrodes (Fig. 2.3). The space between the electrodes is filled with an insulating layer with dielectric constant ϵ. The thickness of a three-dimensional electrode i is given by $t_i^{(3D)}$.

We model each electrode as electron system with a background charge that neutralizes the negative charge of the electrons. We first calculate the grand canonical energy for each electron system seperately without coupling to each other, i.e., we treat the two systems as independent. After that a Legendre transformation is performed to obtain the Helmholtz free energies of the isolated electron systems.[2] $F_1(n_1)$ denotes the Helmholtz free energy of the lower layer (L1) and $F_2(n_2)$ the Helmholtz free energy of the upper layer (L2). The electron number density $n_i = N_i/\mathcal{V}$ is the number of electrons on the respective layer divided by the volume of the electrode. We consider two- and three-dimensional electron systems in this work; the latter are of thickness $t^{(3D)}$:

$$\mathcal{V} = \begin{cases} A, & 2D \\ A * t^{(3D)}, & 3D \end{cases} \tag{2.15}$$

The next step is to connect the two electron systems by a voltage source. The total electron number density in the system after this is $n_\mathrm{t} = n_1 + n_2$, which is equal in size to the total background charge carrier density, so that the total system is electrically neutral. The Helmholtz free energy of the total system is

$$F_\mathrm{tot}(n_1, n_\mathrm{t}) = F_1(n_1) + F_2(n_\mathrm{t} - n_1) + F_\mathrm{es}(n_1, n_\mathrm{t}) - eV_\mathrm{ext} n_1 \mathcal{V} \tag{2.16}$$

Here we used $n_2 = n_\mathrm{t} - n_1$. e is the charge of an electron. The third term, F_es, is the electrostatic energy. It includes the static Coulomb interaction (classical term) of the background charge with itself and the electrons and the direct Coulomb interaction of the electrons. It depends on the spatial distribution of the positive background charge and is analyzed later in more detail. The last term consists of potential differences between the two layers: the external voltage from the voltage source V_s and a possible offset in chemical potentials between the two electrodes μ_offset:

$$V_\mathrm{ext} = V_\mathrm{s} + \mu_\mathrm{offset} \tag{2.17}$$

The Helmholtz free energies $F_i(n_i)$ of layer i can be decomposed into their contributions [12]:

$$F_i = F_{\mathrm{kin},i} + F_{\mathrm{ex},i} + F_{\mathrm{c},i} + F_{\mathrm{ext},i} \tag{2.18}$$

[2] As a requirement for this approach the grand canonical energy has to be convex. If it is not, e.g., because ranges of it display negative compressibility and a Maxwell construction was used to obtain a stable system, the Helmholtz free energy is calculated directly by predefining the electron density instead of the chemical potential.

The first three terms are of pure electronic origin: The kinetic energy F_{kin}, the exchange energy F_{ex} and the correlation energy F_{c} of the electrons of the respective layer. The electron-electron interaction is split into three parts: The direct $\mathbf{q} = 0$ interaction, called Hartree term in the Hartree-Fock approximation, and the static direct Coulomb interaction energy with the background charge are included in the electrostatic energy F_{es}. The exchange contribution is a consequence of the indistinguishability of electrons; it corresponds to the Fock energy. The difference between the exact groundstate energy and the Hartree-Fock energy is called correlation energy. The distinction between F_{ex} and F_{c} is useful in the free electron gas, where F_{ex} is easily calculated, but may be unnecessary in more complex models. The term F_{ext} arises from the interaction between the electrons and external potentials. It includes, e.g., surface potentials and potential wells (like confining potentials in semiconductor heterojunctions). All interactions with "non charge-carrier degrees of freedom" (ncc), like for example phonons, are represented by this term.

We assume that the distance between the electrodes is so small that quantum mechanical energies are of the same order as the electrostatic energy, but not so small that the wave functions of the electrons on different electrodes overlap substantially. Thus we do not include phenomena like tunneling or spontaneous interlayer coherence (SILC) [22]. The latter is a groundstate with interlayer-coherence; its impact on the capacitance of a two-layer capacitor was analyzed in an earlier work [23]. The inclusion of such interlayer phenomena would add a term $F_{12}(n_1, n_{\mathrm{t}} - n_1)$ to the Helmholtz free energy Eq. (2.16).

The thermodynamic variables of the combined system are the temperature T, the volume $\mathcal{V}$ and the total electron number density n_{t}. The number density is a suitable replacement for the electron number as $\mathcal{V}$ is kept fixed through this work. The electron number density n_1 is not a thermodynamic variable. It is determined by the condition that it minimizes the free energy of the total system:

$$\frac{\partial F_{\mathrm{tot}}}{\partial n_1} = 0 \qquad \text{and} \qquad \frac{\partial^2 F_{\mathrm{tot}}}{\partial n_1^2} > 0 \tag{2.19}$$

The first relation equals the condition that the electrochemical potentials of both electrodes are the same.

If two metals are connected in such a way that electrons are allowed to flow freely between them, they are on the same electrochemical potential. Typically two metals differ in their work function W, which is the minimum energy required to move an electron from inside the bulk just outside of the surface. It is the sum of the highest occupied energy ε_{F} and a term W_s, which is the work that has to be spent to move the electron through the dipole layer on the surface. The difference in work functions leads to a charge transfer between the connected, former electrically neutral metals. The transfer of charges generates an electric field, which induces a potential difference between the two metals that shifts the bulk energy levels. The potential difference, which is based on charge transfer, is called the electrical voltage V_e.[3] The system is in equilibrium when the potential difference generated is equal to the difference in work functions of the two metals.

The insertion of Eq. (2.16) into the left-hand side of Eq. (2.19) yields

$$\begin{aligned}\frac{\partial F_{\mathrm{tot}}}{\partial n_1} &= \frac{\partial}{\partial n_1}\left[F_1(n_1) - eV_{\mathrm{ext}} n_1 \mathcal{V}\right] - \frac{\partial}{\partial n_2}\left[F_2(n_2)\right] - \frac{\partial}{\partial n_1} F_{\mathrm{es}}(n_1, n_{\mathrm{t}} - n_1, n_{\mathrm{t}}) \\ &\stackrel{!}{=} 0\end{aligned} \tag{2.20}$$

[3] In contrast, a difference in electrochemical potentials is the voltage as measured by standard voltmeters. Note that Ashcroft and Mermin [24] swapped the chemical potential and electrochemical potentials (as discussed in Reference [25]).

The last term F_{es} reduces to the electrostatic energy of the electric field between the two layers; its derivative yields the electrical voltage V_e. The derivatives of both square brackets produce the work functions of the respective electrodes: The work against the dipole layer W_s is included in the derivate of the energy $F_{\mathrm{ext},i}$ within F_i, and the derivative of the rest of F_i yields the chemical potential. Hence, the difference in work functions equals the (electrical) potential difference induced by the transferred charge, which implies the equality of electrochemical potentials on both electrodes (for $V_{\mathrm{s}} = 0$).

For three-dimensional electrodes the bulk chemical potential μ remains unaltered for realistically large charge transfers. The transferred charge resides on the surface of the electrodes and alters there the local charge distribution. However, in two-dimensional systems μ is perceptibly affected by the transfer of charge.

For a general configuration, the capacitance between two electrodes is defined as [26]

$$C = \frac{Q}{V_{\mathrm{s}}}, \tag{2.21}$$

where Q is the charge induced by the (electrochemical) potential difference between the electrodes V_{s}. The differential capacitance

$$C_{\mathrm{diff}} = \frac{\mathrm{d}Q}{\mathrm{d}V_{\mathrm{s}}}, \tag{2.22}$$

is the ratio between an infinitesimal small change in charge $\mathrm{d}Q$ and the corresponding infinitesimal potential difference $\mathrm{d}V_{\mathrm{s}}$. The classic textbook example in electrostatics consists of two infinite parallel metallic plates at distance d. The space between the plates is filled by an isolator with dielectric constant ϵ. According to Gauss's law, the electric field generated by the charge per area $\pm Q/A$ at one infinitely expanded plate is $\pm\frac{2\pi}{\epsilon}Q/A$. The voltage between the two conductors is obtained by integrating the (spatially constant) electric field over the distance: $V_{\mathrm{s}} = \frac{4\pi}{\epsilon}dQ/A$. The capacitance of this configuration,

$$C_{\mathrm{geom}} = \frac{Q}{V_{\mathrm{s}}} = \frac{A}{4\pi d/\epsilon} \tag{2.23}$$

depends only on the spatial dimensions of area A and the effective dielectric thickness d/ϵ; thus it is called the geometric capacitance.
Below, several schemes to go beyond the geometric capacitance are briefly discussed:

- Lindhard function to include screening (Büttiker) [27]
  The derivation above is only correct under the premise that the charge Q of a classical system resides on the two-dimensional surface of the electrodes. If we investigate two-dimensional electron systems this is true by definition; but for a realistic three-dimensional electrode screening becomes important. Mead concluded by the analysis of a tunnel current through a thin dielectric [28] between two electrodes, that the electric field penetrates into the electrodes. This increases the effective distance between the plates of the capacitor beyond the geometric value. To calculate the distribution of charge under the influence of an external field one has to take electron-electron interactions into account. Büttiker derived a general expression for the capacitance [27], whereby he used the Lindhard function to incorporate screening. For two three-dimensional electrodes he found the effective distance of the capacitance,

$$\frac{A}{C} = 4\pi(d + \lambda_1 + \lambda_2) = 4\pi d + \frac{1}{e^2\mathcal{N}_1^{(3D)}\lambda_1} + \frac{1}{e^2\mathcal{N}_2^{(3D)}\lambda_2}, \tag{2.24}$$

to be enhanced by the Thomas-Fermi screening length λ_i in layer i. This length can be expressed by the density of states (DOS) $\mathcal{N}_i^{(3D)}$ of the bulk material. For two-dimensional electrodes one has to remove the λ_i in the right-hand side of the above relation and replace $\mathcal{N}_i^{(3D)}$ by $\mathcal{N}_i^{(2D)}$.

The quantum mechanical contributions, which are encoded in the DOS $\mathcal{N}$ in the r.h.s. of Eq. (2.24), become relevant for the capacitance if they are of the same order as the classical electrostatic contribution $4\pi d$, i.e., for small plate distances.

- Charge distribution profile (Ku and Ullman) [29]
  The discrepancy between measured and geometric capacitance for small effective dielectric thicknesses can be explained on the basis of the spatial charge distribution induced by finite screening: Ku and Ullman pointed out [29] that the applied voltage V_s differs from the voltage difference $V_1 - V_2$ of the surface of the electrodes. This is because the variation of the charge density inside the electrodes in the range of screening induces a space dependent potential. If the contact potentials of the electrodes are equal, the charge Q transferred due to the applied voltage V_s generates the constant electric field $\mathbf{E}$ between the electrodes and the voltage difference $V_1 - V_2 = V_e$:

$$V_e = V_1 - V_2 = \int_{-d/2}^{d/2} \mathrm{d}x|\mathbf{E}| = |\mathbf{E}|d = 4\pi\frac{Q/A}{\epsilon} \tag{2.25}$$

  With Q from Eq. (2.25) one finds directly:

$$\frac{A}{C} = \frac{V_\mathrm{s}}{Q/A} = 4\pi\frac{d}{\epsilon}\left(1 + \frac{V_\mathrm{s} - (V_1 - V_2)}{V_1 - V_2}\right), \tag{2.26}$$

  The second term in the parentheses of the inverse capacitance is the correction due to the finite screening length (c.f. Eq. (2.24)). For electrodes with unequal contact potential, a voltmeter, which does not allow charge to flow, measures the difference in the electrochemical potential. When the electrodes are connected, charge will flow between the layers and the arising electrostatic field generates a shift of the (bulk) chemical potential by V_e, so that both electrodes are on the same electrochemical potential.

- Center of charge approach (Lang and Kohn) [30]
  For the derivation of Ku and Ullman the surfaces of the electrodes have to be unambiguously definable. This challenge is skirted by the approach of Lang and Kohn [30]: They applied density-functional theory to calculate the electron distribution on three-dimensional electrodes with a homogeneous positive background self-consistently. The resulting spatial electron distribution $\rho(x)$ defines a center of charge x_i for both electrodes:

$$x_1 = \frac{\int_{-\infty}^{0} \mathrm{d}x x\rho(x)}{\int_{-\infty}^{0} \mathrm{d}x\rho(x)}, \qquad x_2 = \frac{\int_{0}^{\infty} \mathrm{d}x x\rho(x)}{\int_{0}^{\infty} \mathrm{d}x\rho(x)} \tag{2.27}$$

  The denominator of both x_i equals the charge on both electrodes; its absolute value is equal for both layers. The electrical potential difference $V_e(\infty) - V_e(-\infty) \equiv V_e^\infty$ is connected to $\rho(x)$ via the Poisson equation:

$$4\pi\int_{-\infty}^{\infty} \mathrm{d}x x\rho(x) = -\int_{-\infty}^{\infty} \mathrm{d}x x\frac{\partial^2}{\partial x^2}V(x) = \int_{-\infty}^{\infty} \mathrm{d}x\frac{\partial V(x)}{\partial x} = V_e^\infty \tag{2.28}$$

  The combination of Eq. (2.27) and (2.28) yields

$$C = \frac{Q}{V_e^\infty} = \frac{A}{4\pi(x_1 - x_2)} \tag{2.29}$$

for the capacitance, where the distance between the centers of charge plays the role of the effective plate distance, a quantity which depends on the charge Q on the electrodes.

The numerical results of Lang and Kohn showed the center of charge being outside of the positive background, i.e., the effective plate distance was smaller than the geometric distance. This has to be contrasted to the increased effective plate distance for finite screening [29, 31]. The center of charge approach uses the classical Poisson equation to derive a potential difference from the given distribution of charge in Eq. (2.28). This captures only the electrostatic part, which originates from a possible dipole layer, of the work functions and neglects the contributions from the chemical potentials. On the other hand, the capacitance derived in Eq. (2.26) by the charge distribution profile approach of Ku and Ullman depends on the applied voltage V_s, which includes the full difference in work functions between the electrodes. Only if the chemical potentials of both electrodes are equal, both approaches yield the same result for the capacitance. Then the surfaces of the electrodes in the finite screening approach have to be defined accordingly (App. A.2).

- Decomposition into a sum of inverse capacitances
  In this work we do not include self-consistent corrections arising from the inhomogeneous distribution of electrons in three-dimensional electrodes. Instead we calculate the Helmholtz free energy for a spatially homogeneous bulk system, including quantum mechanical interactions. We assume that the additional charge on the electrodes is distributed spatially constant in the region from the surface of the electrode up to the screening length λ [12]. The volume of our system considered is then $\mathcal{V}_i = A\lambda_i$. The simplification over the fully self-consistent evaluation makes this an effective model that can help to analyze the qualitative effects of the quantum mechanical contributions on capacitance and compressibility.

  The capacitance of a two-electrode layout as described at the beginning of this section can also be derived from its Helmholtz free energy Eq. (2.16) [32]: n_1 has to minimize the total free energy (c.f. Eq. (2.19)),

$$\frac{\partial F_\mathrm{tot}}{\partial n_1} = \frac{\partial F_1}{\partial n_1} + \frac{\partial F_2}{\partial n_1} + \frac{\partial F_\mathrm{es}}{\partial n_1} - eV_\mathrm{ext}\mathcal{V} \stackrel{!}{=} 0 \tag{2.30}$$

  When the contact potentials of the electrodes are unequal, electrons will be transferred between the layers and the electrodes are charged even without the application of voltage V_s. With $V_\mathrm{ext} = V_\mathrm{s} + \mu_\mathrm{offset}$, the equation above can be resolved for V_s, which is then a function of electron number density n_1 on the lower layer. The inverse of the differential capacitance defined in Eq. (2.22),

$$C_\mathrm{diff}^{-1} = \frac{\partial V_\mathrm{s}}{e\mathcal{V}\partial n_1} \stackrel{(2.30)}{=} \frac{1}{e^2\mathcal{V}^2}\left(\frac{\partial^2 F_1}{\partial n_1^2} + \frac{\partial^2 F_2}{\partial n_1^2} + \frac{\partial^2 F_\mathrm{es}}{\partial n_1^2}\right) = \frac{1}{e^2\mathcal{V}^2}\frac{\partial^2 F_\mathrm{tot}}{\partial n_1^2} \tag{2.31}$$

  is the change of voltage between the electrodes with charge on one of the electrodes. The differential capacitance is only a well-defined quantity if n_1, which has to minimize the total free energy, is not at one boundary of its definition range. $n_1 = 0$ or $n_1 = n_\mathrm{t}$ imply the possibility that both electrodes are not at the same electrochemical potential. For example, imagine the situation that the offset in chemical potentials between the two layers is so large that even after the transfer of the total charge to the layer with lower potential, which is realistically feasible for two-dimensional systems, a discontinuity in the electrochemical potential persists. The application of a (infinitesimal) voltage, which is smaller than the discontinuity, by an external voltage source would not transfer any charges between the electrodes, so that the capacitance is zero.

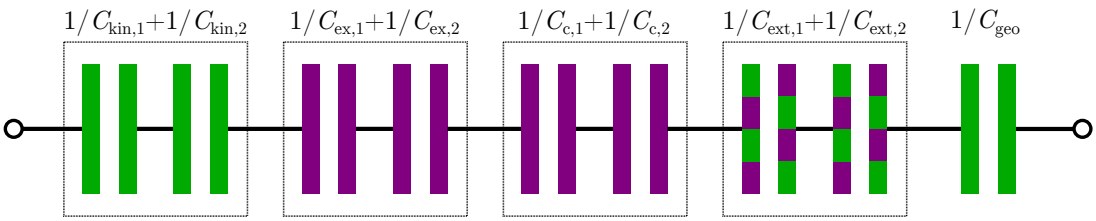

Figure 2.4.: The total capacitance Eq. (2.33) can be represented as a series connection of quantum capacitances with the geometric capacitance C_{geo}. The color indicates the sign: green contributions are positive, purple negative and the sign of $C_{\mathrm{ext,i}}$ depends on the model. Adapted from Ref. [12].

The relation above was derived by Kopp and Mannhart in an alternative way [12]: The Helmholtz free energy is expanded in the charge of the lower electrode up to second order. If this expansion is around the charge which minimizes the free energy, $e\mathcal{V}n_1$, the first derivative vanishes. The coefficient of the second order term is identified with the inverse capacitance. This is in analogy to the Coulomb energy stored in a classical capacitor,

$$F_{\mathrm{Coul}} = \frac{Q^2}{2C_{\mathrm{geom}}}. \tag{2.32}$$

The inverse capacitance is proportional to the second derivate of the free energy with respect to the charge on one layer. The insertion of the free energy terms (2.18) into Eq. (2.31),

$$\begin{aligned}\frac{1}{C_{\mathrm{diff}}} &= \sum_i \frac{\partial^2 F_{\mathrm{kin},i}}{\partial n_i^2} + \sum_i \frac{\partial^2 F_{\mathrm{ex},i}}{\partial n_i^2} + \sum_i \frac{\partial^2 F_{\mathrm{c},i}}{\partial n_i^2} + \sum_i \frac{\partial^2 F_{\mathrm{ext},i}}{\partial n_i^2} + \frac{\partial^2 F_{\mathrm{es}}}{\partial n_1^2} \\ &\equiv \sum_i \frac{1}{C_{\mathrm{kin},i}} + \sum_i \frac{1}{C_{\mathrm{ex},i}} + \sum_i \frac{1}{C_{\mathrm{c},i}} + \sum_i \frac{1}{C_{\mathrm{ext},i}} + \frac{1}{C_{\mathrm{geom}}}\end{aligned} \tag{2.33}$$

shows that the inverse differential capacitance of the system splits up in purely quantum mechanical contributions and the inverse geometric capacitance. The latter arises from F_{es}, which consists of the long-ranged Coulomb interactions.

The differential capacitance of the system can be expressed as a series connection of "kinetic capacitance" C_{kin}, "exchange capacitance" C_{ex}, "correlation capacitance" C_{c} and capacitance from electron-ncc interactions C_{ext} with the geometric capacitance C_{geom} (c.f. Fig. 2.4, [12]). The individual quantum mechanical capacitances can be positive or negative:

The kinetic capacitance is always positive. The exchange energy originates from the $\mathbf{q} \neq 0$ electron-electron interaction in first order perturbation theory.[4] Due to the anticommutation relation, the sign of F_{ex} is always negative, which is passed on to C_{ex}. The correlation energy F_{c} is the difference between the exact electron-electron interaction energy without Hartree contribution and the exchange energy. As shown in the next chapter, the correlation capacitance is negative for a free electron gas with uniform and rigid background. C_{ext} depends strongly on the microscopic model, so that it can be both positive and negative [12].

The inverse capacitance can exceed the geometric value if the sum of the other terms in Eq. (2.33) is negative. The sign of the sum of quantum mechanical contributions from one layer i to Eq. (2.33) equals the sign of the compressibility of this layer (without direct

[4] The direct ($\mathbf{q} = 0$) interaction is included in the Hartree term.

Coulomb interactions) if this layer is considered as isolated. Normally $\partial^2 F_i/\partial n_i^2 < 0$ would induce an instability for an isolated system, but here layer i is only a part of a larger system. The compressibility—and with it the stability—of the total system is determined by the second derivate of the Helmholtz free energy with respect to the total charge n_t.

2.3. Compressibility and its Dependence on the Distribution of the Positive Background Charge

The central idea of this work is to find systems, which display negative compressibility $\partial^2 F_i/\partial n_i^2 < 0$ if considered as isolated, and combine them with another system, so that $\sum_i \partial^2 F_i/\partial n_i^2 < 0$. This arrangement then has a capacitance that is larger than the classical geometric capacitance. The total system may be stabilized by other contributions, most prominently the term arising from the Coulomb energy. We will show below that the capacitance of the system can be kept constant whilst the stability can be tuned by altering the distribution of the positive background charge for two-dimensional layers. This section is based on Ref. [32] for the most part.

The compressibility of the total system is given by Eq. (2.6), where the partial derivate implies that the temperature T and the particle number N (or the volume $\mathcal{V}$) are kept fixed. Here it may be replaced by the total derivate with respect to the total number density of electrons n_t in the system, which is the only thermodynamic variable as T and $\mathcal{V}$ are fixed:

$$\frac{1}{\kappa} = n_\mathrm{t}^2 \frac{\mathrm{d}^2 F_\mathrm{tot}/\mathcal{V}}{\mathrm{d}n_\mathrm{t}^2} \tag{2.34}$$

The electron number density n_1 on electrode 1 has to minimize $F_\mathrm{t} \equiv F_\mathrm{tot}$ by Eq. (2.19). Thus, n_1 is a function of n_t and the applied voltage V_s:

$$n_1 = n_1(n_\mathrm{t}, V_\mathrm{s})$$

If Eq. (2.19) is satisfied by n_1, this stays true for a differential change of the total charge density n_t:

$$\frac{\mathrm{d}}{\mathrm{d}n_\mathrm{t}} \frac{\partial F_\mathrm{t}}{\partial n_1} = 0 \qquad \Longleftrightarrow \qquad \frac{\partial^2 F_\mathrm{t}}{\partial n_1 \partial n_\mathrm{t}} + \frac{\partial^2 F_\mathrm{t}}{\partial n_1^2} \frac{\partial n_1}{\partial n_\mathrm{t}} = 0 \tag{2.35}$$

The Helmholtz free energy F_t depends indirectly over n_1 on n_t and also directly on n_t. Hence the compressibility can be written by partial derivatives [32]:

$$\frac{1}{\kappa} \frac{\mathcal{V}}{n_\mathrm{t}^2} = \frac{\mathrm{d}^2 F_\mathrm{t}(n_1(n_\mathrm{t}), n_\mathrm{t})}{\mathrm{d}n_\mathrm{t}^2} = \frac{\partial^2 F_\mathrm{t}}{\partial n_\mathrm{t}^2} + 2\frac{\partial^2 F_\mathrm{t}}{\partial n_1 \partial n_\mathrm{t}} \frac{\partial n_1}{\partial n_\mathrm{t}} + \frac{\partial^2 F_\mathrm{t}}{\partial n_1^2} \left(\frac{\partial n_1}{\partial n_\mathrm{t}}\right)^2 \tag{2.36}$$

$$\overset{(2.35)}{=} \frac{\partial^2 F_\mathrm{t}}{\partial n_\mathrm{t}^2} - \frac{\partial^2 F_\mathrm{t}}{\partial n_1^2} \left(\frac{\partial n_1}{\partial n_\mathrm{t}}\right)^2 \tag{2.37}$$

$$\overset{(2.35)}{=} \left(\frac{\partial^2 F_\mathrm{t}}{\partial n_1^2}\right)^{-1} \left[\frac{\partial^2 F_\mathrm{t}}{\partial n_1^2} \frac{\partial^2 F_\mathrm{t}}{\partial n_\mathrm{t}^2} - \left(\frac{\partial^2 F_\mathrm{t}}{\partial n_1 \partial n_\mathrm{t}}\right)^2\right] \tag{2.38}$$

The term with the factor $\partial_{n_1} F_\mathrm{t}$ in Eq. (2.36) vanishes due to Eq. (2.19). With Eq. (2.35) the inverse compressibility in lines (2.37) and (2.38) can be expressed either without mixed partial derivative or without $\partial_{n_\mathrm{t}} n_1$, respectively.

In the Helmholtz free energy Eq. (2.16) of the system, all terms but the electrostatic term depend either on n_1 or on $n_\mathrm{t} - n_1$:[5]

$$F_\mathrm{t}(n_1, n_\mathrm{t}) = F_1(n_1) + F_2(n_\mathrm{t} - n_1) + F_\mathrm{es}(n_1, n_\mathrm{t}) - eV_\mathrm{ext} n_1 \mathcal{V}$$

This functional dependence allows to rewrite the second derivatives [32]:

$$\frac{\partial^2 F_\mathrm{t}}{\partial n_1 \partial n_\mathrm{t}} = -F_2'' + \frac{\partial^2 F_\mathrm{es}}{\partial n_1 \partial n_\mathrm{t}} \overset{(2.35)}{=} -\frac{\partial^2 F_\mathrm{t}}{\partial n_1^2}\frac{\partial n_1}{\partial n_\mathrm{t}} \tag{2.39}$$

$$\frac{\partial^2 F_\mathrm{t}}{\partial n_\mathrm{t}^2} = F_2'' + \frac{\partial^2 F_\mathrm{es}}{\partial n_\mathrm{t}^2} \overset{(2.39)}{=} \frac{\partial^2 F_\mathrm{t}}{\partial n_1^2}\frac{\partial n_1}{\partial n_\mathrm{t}} + \frac{\partial^2 F_\mathrm{es}}{\partial n_1 \partial n_\mathrm{t}} + \frac{\partial^2 F_\mathrm{es}}{\partial n_\mathrm{t}^2} \tag{2.40}$$

F_i'' is the second derivative of F_i with respect to its argument. The last line inserted into Eq. (2.37) yields

$$\frac{1}{\kappa}\frac{\mathcal{V}}{n_\mathrm{t}^2} = \frac{\partial^2 F_\mathrm{t}}{\partial n_1^2}\frac{\partial n_1}{\partial n_\mathrm{t}}\left(1 - \frac{\partial n_1}{\partial n_\mathrm{t}}\right) + \left(\frac{\partial^2}{\partial n_\mathrm{t}^2} + \frac{\partial^2}{\partial n_1 \partial n_\mathrm{t}}\right) F_\mathrm{es} \tag{2.41}$$

$$= \frac{e^2 \mathcal{V}^2}{C_\mathrm{diff}}\frac{\partial n_1}{\partial n_\mathrm{t}}\left(1 - \frac{\partial n_1}{\partial n_\mathrm{t}}\right) + \mathcal{D}F_\mathrm{es} \tag{2.42}$$

for the inverse compressibility. Here we used the definition (2.31) of the differential capacitance and introduced the differential operator $\mathcal{D} \equiv (\partial_{n_\mathrm{t}}^2 + \partial_{n_1}\partial_{n_\mathrm{t}})$. The result relates the compressibility with capacitance, charge transfer function $\partial_{n_\mathrm{t}} n_1$ and $\mathcal{D}F_\mathrm{es}$. The latter is zero for $F_\mathrm{es} = F_\mathrm{es}(n_1, n_\mathrm{t} - n_1)$, that is, $\mathcal{D}F_\mathrm{es} = 0$ for a typical two-electrode capacitance. In this case Eq. (2.42) produces a simple criterion for positive compressibility by evaluation of $\partial_{n_\mathrm{t}} n_1$

$$\mathcal{D}F_\mathrm{es} = 0 \qquad \Rightarrow \quad \kappa > 0 \quad \Longleftrightarrow \quad 0 < \frac{\partial n_1}{\partial n_\mathrm{t}} < 1 \tag{2.43}$$

The charge transfer function $\partial_{n_\mathrm{t}} n_1$ exposes how the electron density on the lower electrode is modified with a change of the total electron density. In an instable system with $\mathcal{D}F_\mathrm{es} = 0$, the introduction of additional electrons into the system would either decrease the number of electrons on the lower layer ($\partial_{n_\mathrm{t}} n_1 < 0$) or transfer more electrons than were added onto the lower layer ($\partial_{n_\mathrm{t}} n_1 > 1$).[6] This means that the introduction of electrons into the system will trigger a charge transfer between the electrodes that is larger than the amount of inserted charge.

The electrostatic energy $F_\mathrm{es}(n_1, n_\mathrm{t})$ arises from the direct Coulomb interaction between all charges in the system, including the positive background charge. A mathematically simple model with yet a wide range of applicability is introduced to analyze the impact of the distribution of the positive background charge on compressibility and capacitance [32]: The electrons reside in two two-dimensional electrodes separated by the distance d. The fraction γn_t of the positive background charge density is located at αd from the lower electrode; and the rest of positive charge $(1-\gamma)n_\mathrm{t}$ at βd, where $0 \leq \alpha \leq \beta \leq 1$. The positive charge is distributed spatially uniform in the two-dimensional layers. The space between all four planes of charge is filled by an isolator with dielectric constant ϵ (c.f. Fig. 2.5a).

This model captures a multitude of physical layouts: For $\alpha = 0$ and $\beta = 1$ the layers of positive background charge coincide with the electrodes. This is the common case realized in a physical setup where two electrodes are separated by an insulating, uniform dielectric. The parameter γ

[5] Interlayer correlations, like tunneling or interlayer coherence, could also possess a functional dependence beyond n_1 and $n_\mathrm{t} - n_1$. One could define $F'_\mathrm{es}(n_1, n_\mathrm{t}) = F_\mathrm{es}(n_1, n_\mathrm{t}) + F_\mathrm{interlayer}(n_1, n_\mathrm{t})$ to retain the form of Eq. (2.16), if interlayer terms were included.

[6] Both statements are equivalent in a sense that one statement guarantees that the other statement is true for the other electrode.

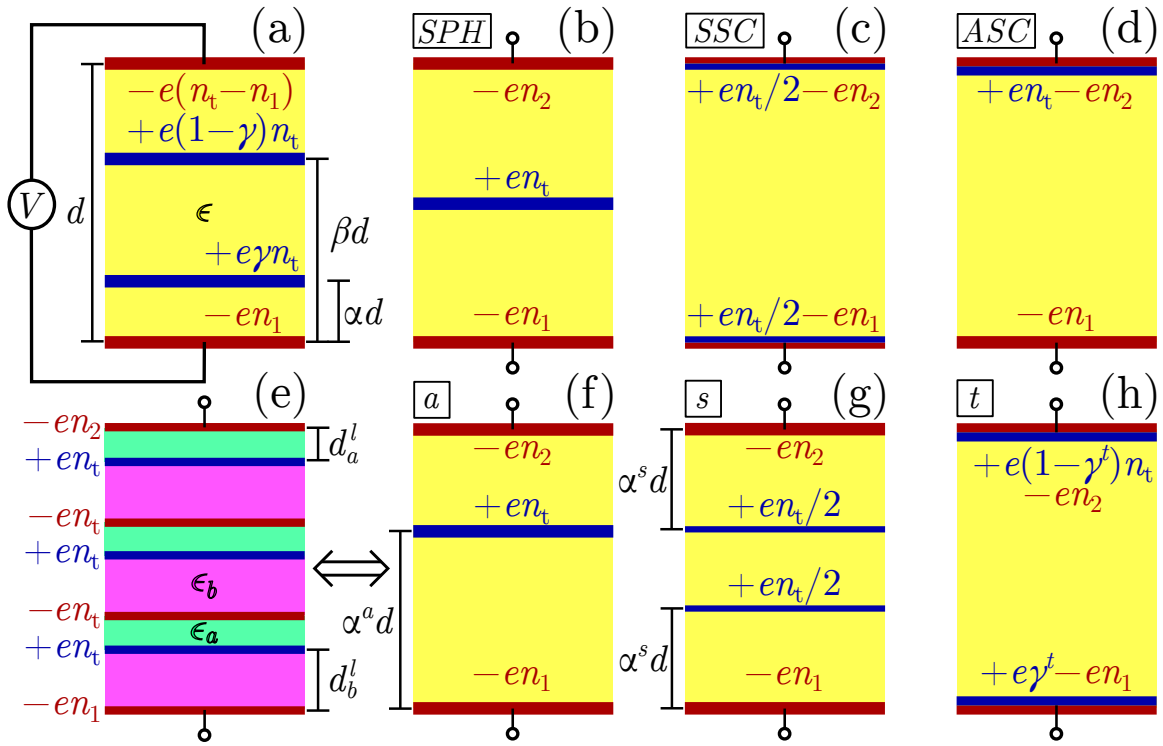

Figure 2.5.: (a) General electrostatic layout, characterized by the locations αd and βd as well as the charge densities $n_t\gamma$ and $n_t(1-\gamma)$ at these positions of the positive background charge. (b)–(d) Special instances of (a), with all three parameters α, β and γ fixed. (e) Polar heterostructure with charge density $\pm en_t$ on the polar layers. For the right choice of parameters as detailed in Eq. (2.44) the electrostatic energy is equal to layout (f). (f)–(h) Instances of (a) that can be described by one parameter. For details on (b)–(d) and (f)–(h) see main text.

identifies the fraction of the total positive charge on the lower electrode. It allows to account for specific densities of mobile electrons, which are equal to the densities of the neutralizing positive background ions, of different electrode materials. For $\gamma = 0$ all positive charge resides on the lower layer, so that the upper electrode consists of empty bands in a charge-neutral layer. In another instance of the model, namely for $\alpha = \beta$, the positive charge is also located completely in one layer. The position of the plane of positve charge is parameterized by α. This setup corresponds to a polar heterostructure (c.f. Fig. 2.5e and [33, 32]), which possesses the same electrostatic energy. The position of the positively charged (effective) layer depends on the properties of the polar material, the single layers of which are characterized by specific atomic thicknesses d_a^l and d_b^l with effective dielectric constants ϵ_a and ϵ_b, respectively: For l layers of each kind of polar layer, the total effective thickness is

$$d/\epsilon = l\left(\frac{d_a^l}{\epsilon_a} + \frac{d_b^l}{\epsilon_b}\right) \quad \text{and} \quad \alpha = l\frac{d_b^l}{d}\frac{\epsilon}{\epsilon_b}. \tag{2.44}$$

One could also deposit a thin insulating film and a contacted terminating electrode on top of the polar heterostructure to modify α experimentally.

We introduce three configurations that represent special cases of the physical setups above [32]:

- the *symmetric polar heterostructure* (SPH) with $\alpha = \beta = \frac{1}{2}$, where the positive charge is in the layer in the middle between the electrodes (Fig. 2.5b);
- the *symmetric standard capacitor* (SSC) with $\alpha = 0$, $\beta = 1$ and $\gamma = \frac{1}{2}$, where half of the positive charge is on each electrode (Fig. 2.5c);

- the *asymmetric standard capacitor* (ASC) with $\alpha = 0$, $\beta = 1$ and $\gamma = 0$, where the positive charge is on the upper electrode (Fig. 2.5d).

Also three more general setups, which depend on one parameter each, are defined:

- the asymmetric case a with $\beta^a = \alpha^a$, where the positive charge is concentrated in one layer (Fig. 2.5f);
- the symmetric distribution s with $\beta^s = 1 - \alpha^s$, $\gamma^s = \frac{1}{2}$, where half of the positive charge is located at the same distance $\alpha^s d$ from each electrode (Fig. 2.5g);
- the standard configuration t with $\alpha^t = 0$, $\beta^t = 1$, $0 \leq \gamma^t \leq 1$, where the positive charge is in the layer of the electrodes (Fig. 2.5h).

The latter three configurations reproduce the special cases for certain values of the characterizing parameter. For example, the symmetric and standard configuration reduce to the SSC for $\alpha^s = 0$ and for $\gamma^t = \frac{1}{2}$, respectively.

The electrostatic energy of the general model can be easily calculated over the energy of the electric fields:

$$F_{\text{es}}^g = 2D\left[\alpha n_1^2 + (\beta - \alpha)(\gamma n_{\text{t}} - n_1)^2 + (1 - \beta)(n_{\text{t}} - n_1)^2\right], \tag{2.45}$$

with $D = \pi e^2 A d/\epsilon$. The second derivative of F_{es} recovers the geometric capacitance,

$$\frac{\partial^2 F_{\text{es}}^g}{\partial n_1^2} = 4D = \frac{4\pi e^2 A d}{\epsilon} \overset{(2.23)}{=} \frac{e^2 A^2}{C_{\text{geo}}}, \tag{2.46}$$

which depends solely on the effective distance between the electrodes. Hence the differential capacitance C_{diff} is independent of the arrangement of the positive background charge. The compressibility, on the other hand, is a function of the distribution of positive background charge, as both $\partial_{n_{\text{t}}} n_1$ and $\mathcal{D}F_{\text{es}}^g$ appear directly in Eq. (2.42). This allows to tune the stability of the system while leaving its capacitance unchanged. The term with the differential operator,

$$\mathcal{D}F_{\text{es}}^g = 4D(\beta - \alpha)\gamma(\gamma - 1), \tag{2.47}$$

vanishes if $\alpha = \beta$, $\gamma = 0$ or $\gamma = 1$. For these parameters all positive charge is located in one layer and the electrostatic energy is a function of n_1 and $n_{\text{t}} - n_1$. Due to the restriction $\alpha < \beta$, $\mathcal{D}F_{\text{es}}^g$ is negative otherwise. The compressibility Eq. (2.42) for the general electrostatic layout is

$$\frac{1}{\kappa}\frac{A}{n_{\text{t}}^2} = \frac{e^2 A^2}{C_{\text{diff}}}\frac{\partial n_1}{\partial n_{\text{t}}}\left(1 - \frac{\partial n_1}{\partial n_{\text{t}}}\right) - \frac{e^2 A^2}{C_{\text{geo}}}(\beta - \alpha)\gamma(1 - \gamma) \tag{2.48}$$

The system is stable for $\kappa > 0$:

$$\kappa > 0 \qquad \Longleftrightarrow \qquad \frac{C_{\text{diff}}}{C_{\text{geo}}}(\beta - \alpha)\gamma(1 - \gamma) < \frac{\partial n_1}{\partial n_{\text{t}}}\left(1 - \frac{\partial n_1}{\partial n_{\text{t}}}\right) \tag{2.49}$$

This inequality yields an upper bound for the enhancement of the differential capacitance over the geometric capacitance: The right-hand side of the inequality above is positive for $0 < \partial_{n_{\text{t}}} n_1 < 1$ and smaller than $\frac{1}{4}$. For $\mathcal{D}F_{\text{es}} = 0$, i.e., when all positive charge is in one layer, the left-hand side of the inequality is zero. This means there is no limitation to capacitance enhancement from the stability criterion for the asymmetric case a, the SPH and the ASC. For the standard configuration t the inequality reduces to

$$\frac{C_{\text{diff}}^t}{C_{\text{geo}}} < \frac{1}{4\gamma^t(1 - \gamma^t)} \tag{2.50}$$

i	$\partial_{n_1}\partial_{n_t}F^i_{es}$	$\partial^2_{n_t}F^i_{es}$	$\mathcal{D}F^i_{es}$	A^i
a	$-4D(1-\alpha^a)$	$4D(1-\alpha^a)$	0	$4\left[(4D\alpha^a+F_1'')(1-\alpha^a)+F_2''\alpha^a\right]$
s	$-2D$	$D(1+2\alpha^s)$	$D(2\alpha^s-1)$	$F_1''+F_2''+2(F_1''+F_2''+4D)\alpha^s$
t	$-4D\gamma^t$	$4D(\gamma^t)^2$	$4D\gamma^t(\gamma^t-1)$	$4[(F_1''+F_2'')(\gamma^t)^2+F_2''(1-2\gamma^t)]$

Table 2.1.: Derivatives of the electrostatic energy and constant A_i of Eq. (2.54) for the asymmetric a, symmetric s and standard t configuration of the positive background charge.

Again, for $\gamma = 0$ or $\gamma = 1$, there is no limitation for capacitance enhancement. For $\gamma = \frac{1}{2}$, i.e., when there is an equal amount of positive background charge on each electrode, the system becomes instable if $C^{t,\gamma=1/2}_{\text{diff}} > C_{\text{geo}}$. Consequently, the SSC configuration allows no capacitance enhancement. A more asymmetric positive charge distribution between the plates allows a larger C^t_{diff}. The symmetric distribution s,

$$\frac{C^s_{\text{diff}}}{C_{\text{geo}}} < \frac{1}{1-2\alpha^s}, \tag{2.51}$$

permits $C^s_{\text{diff}} > C_{\text{geo}}$ for $\alpha^s \neq 0$. As $\partial_{n_1}F^s_{\text{es}} = 4D(n_1 - n_t/2)$ is independent of α^s, so is $n^s_1(n_t, V_s)$, which is determined by the minimization of the free energy Eq. (2.30). This induces that also $\partial_{n_t}n_1$ is independent of α_s, so that the inverse compressibilities differ only by

$$\frac{n_t^2}{A}\mathcal{D}F^s_{\text{es}} = -\frac{n_t^2}{A}D(1-2\alpha^s), \tag{2.52}$$

according to Eq. (2.42) for different values of α^s. The inverse compressibility is smaller for smaller distance between the layer of positive charge and the electrodes. The symmetric layout s turns into the SPH layout for $\alpha^s = \frac{1}{2}$ and into the SSC layout for $\alpha^s = 0$. Thus the inverse compressibility of the SPH is exactly $n^2_{n_t}D/A$ larger than that of the SSC, i.e., the SPH is more stable than the SSC.

Eq. (2.38) expresses the compressibility without charge transfer function $\partial_{n_t}n_1$; the insertion of the form Eq. (2.16) yields:

$$\frac{1}{\kappa}\frac{A}{n_t^2} = \frac{1}{F_1''+F_2''+4D}\left[(F_1''+F_2''+4D)\left(F_2''+\frac{\partial^2 F_{\text{es}}}{\partial n_t^2}\right)-\left(-F_2''+\frac{\partial^2 F_{\text{es}}}{\partial_{n_1}\partial_{n_t}}\right)^2\right] \tag{2.53}$$

$$= \frac{F_1''F_2''+DA^i}{F_1''+F_2''+4D} \tag{2.54}$$

A^i denotes the special setups of the general electrostatic energy F^g_{es} of Eq. (2.45): $i = \{a, s, t\}$. The values for $i = a, s, t$ are given in Table 2.1; they reduce to

$$A^{\text{SPH}} = 2(F_1''+F_2''+2D), \qquad A^{\text{SSC}} = F_1''+F_2'', \qquad A^{\text{ASC}} = 4F_2'', \tag{2.55}$$

for the parameterless, special cases. The denominator of Eq. (2.54) is proportional to the differential capacitance, which has to be positive due to the minimization criterion Eq. (2.19). This denominator is also the prefactor of α^s in A^s in the symmetric layout s. This means that the stability of the system increases with α^s and has its maximum at $\alpha^s = \frac{1}{2}$, which corresponds to the SPH. As lined out above, the SSC allows no capacitance enhancement without destabilizing the total system.

For an enhancement of the differential capacitance beyond the geometric value, one needs $F_1'' + F_2'' < 0$, but also $\kappa > 0$. The former induces that A^t of the standard layout has the form of a parabola in γ^t, the maximum of which is at $\gamma^t_m = F_2''/(F_1''+F_2'')$ with a value of

$A^t = 4F_1''F_2''/(F_1'' + F_2'')$. It is $0 < \gamma_m^t < 1$ only true for $F_1'' < 0 \,\&\, F_2'' < 0$, i.e., if this condition is fulfilled, then the system is most stable for γ_m^t. It is $\gamma_m^t < 0$ for $F_2'' > 0$; the system is then most stable for $\gamma^t = 0$ and $A^t = 4F_2''$. On the other hand, $\gamma_m^t > 1$ is true for $F_1'' > 0$ and then the system is most stable for $\gamma^t = 1$ and it is $A^t = 4F_1''$. Summing these inequalities up for capacitance enhancement in the standard layout t, where the layers of positive charge coincide with the electrodes and γ^t characterizes the fraction of charge on the lower electrode: If the second derivative of the free energy of one of the electrodes is positive, then the stability of the system increases with the fraction of the positive charge in this layer.

In the asymmetric layout a, where the positive charge is concentrated in one layer, which is located $\alpha^a d$ from the lower electrode, A^a depends quadratically on α^a. The function has its maximum value of $4D+(F_1''-F_2'')^2/4D+2(F_1''+F_2'')$ at $\alpha_m^a = (4D-F_1''+F_2'')/8D$. If $\alpha_m^a \notin [0,1]$, then the system is most stable for $A^i(\alpha = 0/1)$:

$$F_1'' > 4D + F_2'' \qquad \Rightarrow \alpha_m^a < 0, \qquad A^i(\alpha = 0) = 4F_1'' \tag{2.56}$$

$$F_2'' > 4D + F_1'' \qquad \Rightarrow \alpha_m^a > 1, \qquad A^i(\alpha = 1) = 4F_2''. \tag{2.57}$$

If the second derivative of the free energy of one of the electrodes is more than $4D$ larger than that of the other electrode, the inverse compressibility is larger (the system is more stable) if the layer of positive charge is located nearer to this electrode.

The antecedent analysis illustrates the importance of the distribution of the positive background charge: The model chosen for the electrostatic layout allows to tune the compressibility of the system without impact on the differential capacitance. The latter is increased by negative second derivatives of F_1 and F_2, which in turn tend to destabilize the total system. This effect can be countered by an appropriate choice of the electrostatic layout: For example, contrary to the SSC, which allows no capacitance enhancement, the SPH is much more stable. If $F_i'' > 0$ for electrode i, it is best for the stability of the system to place the majority of the positive charge near this electrode.

In Section 4.3.2 we investigate the effect of the symmetric and asymmetric layouts on the inverse compressibility for different values of α^s and α^a, respectively. There the lower electrode comprises a two-dimensional electron system with spin-orbit coupling, while a two-dimensional free electrons gas resides at the upper electrode (see Fig. 4.11).

Two identical electron systems, which are characterized by the extended Hubbard model with attractive nearest-neighbor interaction V, are coupled in Section 6.4.2. The inverse compressibility of the combined system is compared for the SPH, SSC and ASC configuration of the positive background charge for different values of V (see Fig. 6.4).

2.4. Experimental Findings of Negative Capacitance and Compressibility of Subsystems

In this section we provide a short overview of some of the physical systems in which enhanced capacitance or negative compressibility have been observed experimentally:

- Oxide heterostructures: $LaAlO_3/SrTiO_3$
  A two-dimensional electron gas may form at the interface between the bulk insulators $LaAlO_3$ (LAO) and $SrTiO_3$ (STO) [34]. This is the case if the electrically neutral $(TiO_2)^0$ (001) oriented surface of $SrTiO_3$ is in contact with the layer $(LaO)^+$ [34] and the thickness of LAO amounts to at least four unit cells [35]. As the LAO consists of alternating positive $(LaO)^+$ and negative $(AlO_2)^-$ layers, this layout (see Fig. 2.5e for a schematic plot of a polar heterostructure) stimulated a theory for the emergence of the interface electronic system called the polar catastrophe hypothesis [34]. The electrons occupy Ti $3d$ t_{2g} states

of the interface TiO_2 layer [18] and their distribution in z direction can be characterized as two-dimensional [36, 37]. The electron density at the LAO/STO interface is typically in the range of several $10^{13}\,\mathrm{cm}^{-2} \approx 3 \times 10^{-4}\,a_\mathrm{B}^{-2}$ and can be tuned by the application of a backgate bias by at least one order of magnitude. The electron system at the interface features electronic correlations, which entails a wide range of physical phenomena, ranging from superconductivity [4] over magnetism [5] to the coexistence of superconductivity and magnetism [6, 7]. Additionally, seizable spin-orbit coupling was measured at the LAO/STO interface due to the presence of a symmetry-breaking electrical field [8].

The capacitance of LAO/STO heterostructures was determined by Lu Li *et al.* for several samples [9]. They used top gates on LAO of varying thickness of 10–12 unit cells and applied back gate voltages to tune the electron density n at the interface. For low n an enhancement of the capacitance of more than 40% at $T = 4.2\,K$ and of about 10% at room temperature over the high-density value—that was identified with the geometrical capacitance—was observed, which are values that are unmatched in magnitude by other systems, like, e.g., semiconductors. This was traced back to a negative contribution of electronic correlations to the capacitance by electric-field penetration measurements. The increase of the capacitance for densities near depletion of the interface was found by later measurements at room temperature as well [38].

In a setup with top gate the minimum number of LAO layers is limited by the appearance of tunneling between the top gate and interface. This can be circumvented by the use of Kelvin probe microscopy, which determines the difference in contact potentials between the interface and microscope tip and thus the difference in chemical potentials. Tinkl *et al.* deployed Kelvin probe microscopy on a 4 unit cells thick layer of LAO on top of STO for different interface densities, which were tuned by application of a back gate bias. Their results for the interface electron system showed that the derivative of the chemical potential, which is proportional to the inverse compressibility, is negative at small n.

Although the occurrence of negative compressibility could be qualitatively related to electronic exchange and correlation effects, a good quantitative agreement of the experimental results of the LAO/STO interface with a theoretical model is not known to date. In this regard, and because the LAO/STO system can be considered as a representative for a multitude of perovskite oxide heterostructures, we use in this work mostly parameters that correspond to the LAO/STO system.

- Ferroelectrics

  The class of ferroelectrics is of interest regarding high capacitance for two reasons: On the one hand, they feature typically quite large dielectric constants ϵ. For example ϵ of lead zirconate titanate $Pb(Zr_xTi_{1-x})O_3$ (PZT) is in the range of several 1000 [39]. On the other hand, it was proposed that a capacitor with a ferroelectric as insulator between the metallic plates may display a negative second derivative of its free energy with respect to the density on the plates [40]. The energy over electric polarization curve of a ferroelectric exhibits two minima with a maximum between them for zero applied field. The system adopts one of the states with minimal energy, where the second derivative is positive and consequently its capacitance. This induces a finite electric polarization, which in turn generates an electric field at the metal electrodes and a transfer of charge Q between the electrodes—even without external voltage. The ferroelectric capacitor is now connected in series with a second, standard capacitor, which has its minimum in energy at $Q = 0$, i.e., at the charge where the maximum of the ferroelectric capacitor lies. Under the assumption that the energy of the standard capacitor is large enough in comparison with the ferroelectric capacitor, the combined system will have its minimum at $Q = 0$, so that the inverse

differential capacitance is obtained by the second derivate of the total energy with respect to Q at this point. As the ferroelectric capacitor is at a local maximum for $Q = 0$, its contribution is negative, which corresponds to a negative capacitance as pointed out by the authors of Ref. [40]. The total capacitance of this layout is hence larger than the value of the standard capacitor. For the stability one has to consider the coupled system of both capacitors, so that although the ferroelectric capacitor alone would be instable [41], the total system features a positive compressibility. The enhancement of the capacitance by this mechanism was shortly after the proposal confirmed experimentally for ferroelectric capacitors comprising PZT [42, 43] and $Ba_{0.8}Sr_{0.2}TiO_3$ [44].

The described mechanism by ferroelectrics and this work are based on the same concept for capacitance enhancement, i.e., the coupling of an instable system with a stabilizing system, but they use a different realization. The ferroelectrics modify the material between the electrodes, while the approach of this work is to tune the electrode material. Both strategies are in principal combinable for a maximum of capacitance enhancement under the condition that the minimum of the total energy lies at a density for which the ferroelectric contribution is maximal.

- Semiconductors
  Another class of materials for which negative compressibility has been experimentally observed are two-dimensional semiconductor electron systems in presence of a strong perpendicular magnetic field. Those systems feature low carrier densities of $n \approx 10^{-5}\, a_\mathrm{B}^{-2}$ for Si [45] and $n \approx 5 \times 10^{-6}\, a_\mathrm{B}^{-2}$ for GaAs/AlGaAs heterostructures [10] so that electron-electron interactions become more important. The perpendicular magnetic field induces the quantization of electronic states into Landau levels, which suppresses the kinetic energy and thus enhances the relevance of the electron-electron interactions. Kravchenko *et al.* identified the compressibility of the quantum contributions in Si-MOSFETs for different magnetic fields by measurement of the deviation of the capacitance to its zero field value [45]. They found a negative compressibility for high fields, which they traced back to the exchange interaction. Eisenstein, Pfeiffer and West developed the so-called penetration field method, which measures the inverse compressibility without the Coulomb terms directly [10]. They applied this method to GaAs/AlGaAs heterostructures and found a negative κ^{-1} of the quantum contributions at low densities for zero and finite magnetic field [10, 11]. This result was also confirmed within the scope of later measurements [46].

- Graphene
  In conventional graphene both the kinetic and the exchange energy per particle feature the same density dependence $n^{1/2}$, so that a negative compressibility is not anticipated [47]. In case of a strong perpendicular magnetic field the quenching of the kinetic energy enables the possibility that the exchange interaction induces $\kappa^{-1} < 0$. This was demonstrated experimentally by Yu *et al.* by observing capacitances with values larger than the geometric capacitance in presence of a strong magnetic field [47].

- Mechanical systems
  As a mechanical quantity, the compressibility expresses the resistance of a system to volume change. A mechanical system with negative compressibility would expand at the application of pressure and thus be instable. The inverse compressibility translates to the stiffness for a given mechanical body. Analogous to quantum mechanical systems, a system with negative stiffness can be stabilized by combination with a system of positive stiffness. Then the total system is stable and features a stiffness that is larger than the largest stiffness of the constituents. This was demonstrated by experiments combining the

ferroelastic materials VO_2 [48] or $BaTiO_3$ [49], which undergo a temperature controlled phase transition with an attendant volume change, with a tin matrix.

2.5. Further Theoretical Approaches to Capacitance Analysis

This section mentions shortly other methods for the analysis of the capacitance of multicomponent electron systems:

- Hale and Freericks evaluated the capacitance of a multilayered nanostructure with strong electronic correlations [50]. They coupled two semi-infinite metallic leads to a dielectric barrier region described by the Falicov-Kimball model [51] at half filling. Then the problem was solved by inhomogeneous dynamical mean field theory using the so-called quantum zipper algorithm [52]. The resulting lateral distribution of electronic charge was related to the capacitance. Through variation in the large parameter space (i.a., chemical potential, thickness of the correlated dielectric, temperature) they discovered that the most substantial enhancement of the capacitance was generated by an increase in interaction strength in the correlated dielectric barrier.

- Skinner and Shklovskii argued that at very low electron densities in one electrode the electrons therein form a Wigner crystal-like state [53]. They proposed to treat this state purely classical as a system of localized electrons, which induce image charges in the second electrode. The image charge and its generating electron are separated by the distance between the electrodes and constitute dipoles. If the electron density is so low that the interparticle spacing is much larger than the electrode distance, the electron-electron interaction can be replaced by the dipole-dipole interaction. As the latter is much weaker than the former, this induces an enhancement of the capacitance over the classical electrostatic value.

- Berktold and Mannhart developed a new measurement method and a corresponding model that allows the experimental determination of the capacitance even in presence of strong leakage currents and does not depend on the measurement at several frequencies [54].

- Although the paper of Liebsch [55] does not deal with capacitance, an interesting concept appeared in this work. Liebsch studied Sr doped $LaAlO_3$ close to a Mott transition in a multiband model within dynamical mean field theory. He discovered that near this phase transition a small change in density could cause a large interorbital charge transfer with negative compressibility for one subband. This situation is analogous to a capacitor, whereby a subband corresponds to an electrode, which can possess negative compressibility [12].

3. Exchange and Correlation Contributions at Finite Temperature

3.1. Hartree-Fock Approximation

For the remaining chapters we assume the positive background charge to be uniformly distributed. In this model, also known as "Jellium model", the positive charge carrier density equals the electron number density n. The link to "real world systems", where the many-body electrons of interest often coexist in presence of ionic lattices, is made by effective parameters. In this model the material properties of the considered metals and interfaces are encoded in the effective band mass of the conduction electrons $m^* = m/m_e$ and effective dielectric constant ϵ_{eff}. The latter incorporates the effective screening by all charges except the conduction electrons: It consists of the polarizability of the underlying lattice, i.e., the static response of the core electrons to electric fields and potentially ionic displacements.

The goal of Hartree-Fock theory is to find an approximation to the Hamiltonian $\hat{\mathcal{H}}$ exact to lowest order in the interaction. In second quantization this effective Hamiltonian $\hat{\mathcal{H}}^{HF}$ can be written as sum of products of only two creation and destruction operators and is therefore easy to diagonalize [24, 56]. It is of the form[1]

$$\hat{\mathcal{H}}^{HF} = \sum_{\alpha,\beta} \left(T_{\alpha,\beta} + V^{\text{ext}}_{\alpha,\beta} \right) \hat{a}^\dagger_\alpha \hat{a}_\beta + \sum_{\alpha,\beta} V^{HF}_{\alpha,\beta} \hat{a}^\dagger_\alpha \hat{a}_\beta. \tag{3.1}$$

The objective is to find the effective potential $V^{HF}_{\alpha,\beta}$, which is usually non-local. This is achieved by the condition that $\langle \psi^{HF} | \hat{\mathcal{H}} | \psi^{HF} \rangle$ has to be extremal, whereas $|\psi^{HF}\rangle$ denotes the groundstate of $\hat{\mathcal{H}}^{HF}$. This ensures that the first variation is zero; the second variation determines if the solution is a minimum or saddle point. The groundstate wave function of $\hat{\mathcal{H}}^{HF}$ is a single Slater determinant of orthonormal one-electron wave functions.

Another method to derive $\hat{\mathcal{H}}^{HF}$ uses Wick's theorem, which allows to extract the "one-body part" of the two-body interaction [56]. The "one-body part" constitutes the last term of Eq. (3.1) and the true two-body portion $\hat{\mathcal{H}}^{(2)}_{e-e}$ plays only a role in second and higher variation: $\langle \psi^{HF} | \hat{\mathcal{H}}^{(2)}_{e-e} | \psi^{HF} \rangle = 0$ since a state with two electron-hole pairs is orthogonal to $|\psi^{HF}\rangle$ and $\langle \delta\psi^{HF} | \hat{\mathcal{H}}^{(2)}_{e-e} | \psi^{HF} \rangle = 0$ since at most one electron hole-pair is excited by the variation. If the derived $\hat{\mathcal{H}}^{HF}$ is stationary in $|\psi^{HF}\rangle$, i.e., its first variation vanishes, then also $\hat{\mathcal{H}}$ is stationary in $|\psi^{HF}\rangle$, which is defined self-consistently as groundstate, closing the loop [56].

Wick's theorem [57] allows to express a product of creation and destruction operators as sum of normal ordered products. Normal order is denoted by $::$ and with respect to a vacuum state, for which the expectation value of normal ordered operators vanishes. The contraction is the difference between two operators and its normal order,

$$\overbrace{\hat{a}^\dagger_\alpha \hat{a}_\beta} = \hat{a}^\dagger_\alpha \hat{a}_\beta - :\hat{a}^\dagger_\alpha \hat{a}_\beta: = \langle \hat{a}^\dagger_\alpha \hat{a}_\beta \rangle, \tag{3.2}$$

[1] For non number-conserving problems one could add terms of the form $\hat{a}_\alpha \hat{a}_\beta$ and $\hat{a}^\dagger_\alpha \hat{a}^\dagger_\beta$ to the last term of Eq. (3.1).

which is either 0 (: $\hat{a}_\alpha^\dagger \hat{a}_\beta := \hat{a}_\alpha^\dagger \hat{a}_\beta$) or 1 (: $\hat{a}_\alpha^\dagger \hat{a}_\beta := -\hat{a}_\beta \hat{a}_\alpha^\dagger$) due to the anticommutation relation. Thus it can be written as expectation value in an arbitrary normalized state. For two creation and destruction operators each, Wick's theorem reduces to:

$$\begin{aligned}\hat{a}_\alpha^\dagger \hat{a}_\beta^\dagger \hat{a}_\gamma \hat{a}_\delta =: \hat{a}_\alpha^\dagger \hat{a}_\beta^\dagger \hat{a}_\gamma \hat{a}_\delta : &+ \langle \hat{a}_\alpha^\dagger \hat{a}_\delta \rangle \langle \hat{a}_\beta^\dagger \hat{a}_\gamma \rangle - \langle \hat{a}_\alpha^\dagger \hat{a}_\gamma \rangle \langle \hat{a}_\beta^\dagger \hat{a}_\delta \rangle \\ &+ \langle \hat{a}_\alpha^\dagger \hat{a}_\delta \rangle : \hat{a}_\beta^\dagger \hat{a}_\gamma : + \langle \hat{a}_\beta^\dagger \hat{a}_\gamma \rangle : \hat{a}_\alpha^\dagger \hat{a}_\delta : - \langle \hat{a}_\alpha^\dagger \hat{a}_\gamma \rangle : \hat{a}_\beta^\dagger \hat{a}_\delta : - \langle \hat{a}_\beta^\dagger \hat{a}_\delta \rangle : \hat{a}_\alpha^\dagger \hat{a}_\gamma :\end{aligned} \tag{3.3}$$

The expectation value $\langle .. \rangle$ is taken in the groundstate $|\psi^{HF}\rangle$, which defines the so-called Fermi-vacuum. In the Fermi vacuum $\hat{a}_\beta$ is either a destruction operator (if the state β is unoccupied in the Fermi sea of the groundstate) or a creation operator. In the latter case a hole is created in the Fermi sea. In Hartree-Fock theory the first term $: \hat{a}_\alpha^\dagger \hat{a}_\beta^\dagger \hat{a}_\gamma \hat{a}_\delta :$ in Eq. (3.3), which corresponds to the two-particle interaction part, is neglected, so that the product of four operators reduces to an effective one-particle expression. This omits quantum fluctuations from the Hamiltonian. If one replaces the normal ordered products by Eq. (3.2), one arrives at the Hartree-Fock approximation (HFA):

$$\begin{aligned}\hat{a}_\alpha^\dagger \hat{a}_\beta^\dagger \hat{a}_\gamma \hat{a}_\delta \overset{\text{HFA}}{=} &\langle \hat{a}_\alpha^\dagger \hat{a}_\delta \rangle \hat{a}_\beta^\dagger \hat{a}_\gamma + \langle \hat{a}_\beta^\dagger \hat{a}_\gamma \rangle \hat{a}_\alpha^\dagger \hat{a}_\delta - \langle \hat{a}_\alpha^\dagger \hat{a}_\delta \rangle \langle \hat{a}_\beta^\dagger \hat{a}_\gamma \rangle \\ &- \left(\langle \hat{a}_\alpha^\dagger \hat{a}_\gamma \rangle \hat{a}_\beta^\dagger \hat{a}_\delta + \langle \hat{a}_\beta^\dagger \hat{a}_\delta \rangle \hat{a}_\alpha^\dagger \hat{a}_\gamma - \langle \hat{a}_\alpha^\dagger \hat{a}_\gamma \rangle \langle \hat{a}_\beta^\dagger \hat{a}_\delta \rangle \right)\end{aligned} \tag{3.4}$$

A general many-body Hamiltonian in second quantization is of the form

$$\hat{\mathcal{H}} = \sum_{\alpha,\beta} \left(T_{\alpha,\beta} + V_{\alpha,\beta}^{\text{ext}} \right) \hat{a}_\alpha^\dagger \hat{a}_\beta + \frac{1}{2} \sum_{\alpha,\beta,\gamma,\delta} v_{\alpha\beta\gamma\delta} \hat{a}_\alpha^\dagger \hat{a}_\beta^\dagger \hat{a}_\gamma \hat{a}_\delta, \tag{3.5}$$

where the second term contains the many-body interactions. $T_{\alpha,\beta}$ and $V_{\alpha,\beta}^{\text{ext}}$ are the matrix elements of the kinetic operator and external potential, respectively:

$$A_{\alpha,\beta} \equiv \langle i, \beta | \hat{A}_i | i, \alpha \rangle = \sum_{\sigma_1,\sigma_2} \int \mathrm{d}\mathbf{r}_i \phi_\beta^*(\mathbf{r}_i, \sigma_1) [\hat{A}_i]_{\sigma_1,\sigma_2} \phi_\alpha(\mathbf{r}_i, \sigma_2) \tag{3.6}$$

Here $\phi_\alpha(\mathbf{r}_i, \sigma)$ is the wave function of the i-th electron with spin σ in the one-particle state α. $V_{\alpha,\beta}^{\text{ext}}$ includes all external fields and the potential from the positive ions. The matrix element of the two-particle part is

$$\begin{aligned}v_{\alpha\beta\gamma\delta} &\equiv \left(\langle i, \alpha | \langle j, \beta | \right) \hat{V}_{ij} \left(| j, \gamma \rangle | i, \delta \rangle \right) \\ &= \sum_{\sigma_1,\sigma_2,\sigma_3,\sigma_4} \int \mathrm{d}\mathbf{r}_i \int \mathrm{d}\mathbf{r}_j \phi_\alpha^*(\mathbf{r}_i, \sigma_1) \phi_\beta^*(\mathbf{r}_j, \sigma_2) \left[\hat{V}_{ij} \right]_{\sigma_2,\sigma_3,\sigma_1,\sigma_4} \phi_\gamma(\mathbf{r}_j, \sigma_3) \phi_\delta(\mathbf{r}_i, \sigma_4)\end{aligned} \tag{3.7}$$

Combining Eq. (3.3) with Eq. (3.5), we arrive at the Hartree-Fock Hamiltonian:

$$\begin{aligned}\hat{\mathcal{H}}^{HF} = \sum_{\alpha,\beta} \left(T_{\alpha,\beta} + V_{\alpha,\beta}^{\text{ext}} \right) \hat{a}_\alpha^\dagger \hat{a}_\beta + \frac{1}{2} \sum_{\alpha,\beta,\gamma,\delta} v_{\alpha\beta\gamma\delta} \Big[&\langle \hat{a}_\alpha^\dagger \hat{a}_\delta \rangle \hat{a}_\beta^\dagger \hat{a}_\gamma + \langle \hat{a}_\beta^\dagger \hat{a}_\gamma \rangle \hat{a}_\alpha^\dagger \hat{a}_\delta - \langle \hat{a}_\alpha^\dagger \hat{a}_\delta \rangle \langle \hat{a}_\beta^\dagger \hat{a}_\gamma \rangle \\ &- \left(\langle \hat{a}_\alpha^\dagger \hat{a}_\gamma \rangle \hat{a}_\beta^\dagger \hat{a}_\delta + \langle \hat{a}_\beta^\dagger \hat{a}_\delta \rangle \hat{a}_\alpha^\dagger \hat{a}_\gamma - \langle \hat{a}_\alpha^\dagger \hat{a}_\gamma \rangle \langle \hat{a}_\beta^\dagger \hat{a}_\delta \rangle \right) \Big]\end{aligned} \tag{3.8}$$

The first three terms together in the sum over $v_{\alpha\beta\gamma\delta}$ are called the Hartree term, while the following three summands constitute the Fock term. The negative sign of the Fock term is a consequence of the anticommutation relations between fermions and thus of the Pauli principle.

In the jellium model the potential from the positive background charge is spatially constant. Hence plane waves are a solution to the Hartree-Fock Hamiltonian, since they induce a spatially uniform electron density. For plane waves the Hartree term cancels the contribution from the underlying positive background to the external potential $V^{\text{ext}}_{\alpha,\beta}$: Due to the long range order of the Coulomb interaction, the energy from the electrostatic interaction diverges with size of the system. There are three different contributions to the electrostatic energy: the electron-background interaction, which is included in $V^{\text{ext}}_{\alpha,\beta}$, the direct electron-electron interaction in the Hartree term and the background-background interaction. The sign of the latter two is opposite to the first contribution. While each term diverges with the system size, the sum of them is zero for an electrically neutral system. If the Hartree-Fock system is coupled to another layer or the positive background charge is shifted against the layer of electrons, then an additional electrostatic term arises in the Helmholtz free energy as described in the previous chapter. This energy F_{es} is then treated formally separately from the single layer energies. We can thus ignore the Hartree term and $V^{\text{ext}}_{\alpha,\beta}$—under the additional assumption of absence of external fields—in the following considerations.

Plane waves are characterized by their wave vectors $\mathbf{k}$, so that the well known [23, 56, 58] matrix elements $T_{\alpha,\beta}$ and $v_{\alpha,\beta,\gamma,\delta}$ become:

$$v_{\mathbf{k_1}\sigma_1,\mathbf{k_2}\sigma_2,\mathbf{k_3}\sigma_3,\mathbf{k_4}\sigma_4} = \frac{e^2}{\mathcal{V}\epsilon_{\text{eff}}}\delta_{\sigma_1,\sigma_4}\delta_{\sigma_2,\sigma_3}\delta_{\mathbf{k}_1+\mathbf{k}_2,\mathbf{k}_3+\mathbf{k}_4}v^d(\mathbf{k}_4-\mathbf{k}_1); \quad v^d(\mathbf{q}) = \begin{cases} \dfrac{2\pi}{|\mathbf{q}|}, & 2D \\ \dfrac{4\pi}{|\mathbf{q}|^2}, & 3D \end{cases} \tag{3.9}$$

$$T_{\mathbf{k_1}\sigma_1,\mathbf{k_2}\sigma_2} = \frac{\hbar^2\mathbf{k}_1^2}{2m^*}\delta_{\sigma_1,\sigma_2}\delta_{\mathbf{k}_1,\mathbf{k}_2} \tag{3.10}$$

Here $\delta_{\alpha,\beta} \in \{0,1\}$ is the Kronecker delta and d in the superscript the dimension. The next step is to combine these matrix elements with the Hartree-Fock Hamiltonian Eq. (3.8), convert the sums over wave-vectors into integrals and exploit the Kronecker deltas. The Hartree-Fock Hamiltonian without the Hartree contribution turns into the Fock Hamiltonian:

$$\begin{aligned}\hat{\mathcal{H}}^F = &\frac{\mathcal{V}}{(2\pi)^d}\sum_\sigma \int \mathrm{d}k^d \frac{\hbar^2k^2}{2m^*}\hat{a}^\dagger_{\mathbf{k}\sigma}\hat{a}_{\mathbf{k}\sigma} \\ &- \frac{1}{2}\frac{e^2\mathcal{V}}{(2\pi)^{2d}\epsilon_{\text{eff}}}\sum_\sigma\int \mathrm{d}k^d \int \mathrm{d}q^d v^d(q)\left[2\langle\hat{a}^\dagger_{\mathbf{k}+\mathbf{q}\sigma}\hat{a}_{\mathbf{k}+\mathbf{q}\sigma}\rangle\hat{a}^\dagger_{\mathbf{k}\sigma}\hat{a}_{\mathbf{k}\sigma} - \langle\hat{a}^\dagger_{\mathbf{k}+\mathbf{q}\sigma}\hat{a}_{\mathbf{k}+\mathbf{q}\sigma}\rangle\langle\hat{a}^\dagger_{\mathbf{k}\sigma}\hat{a}_{\mathbf{k}\sigma}\rangle\right]\end{aligned} \tag{3.11}$$

The electrons in the Fock term interact only with the effective potential of electrons with the same spin, contrary to the Hartree term, where the interaction takes place with both spin directions. This is reflected in the pair correlation function $g_{\sigma_1\sigma_2}(\mathbf{r}_1,\mathbf{r}_2)$, which is the probability that an electron with spin σ_2 is located at $\mathbf{r}_2$ when another electron with spin σ_1 can be found at $\mathbf{r}_2$:

$$g_{\sigma_1\sigma_2}(\mathbf{r}_1,\mathbf{r}_2) = \frac{\langle\hat{\Psi}^\dagger_{\sigma_1}(\mathbf{r}_1)\hat{\Psi}^\dagger_{\sigma_2}(\mathbf{r}_2)\hat{\Psi}_{\sigma_2}(\mathbf{r}_2)\hat{\Psi}_{\sigma_1}(\mathbf{r}_1)\rangle}{n_{\sigma_1}(\mathbf{r}_1)n_{\sigma_2}(\mathbf{r}_2)}, \qquad \hat{\Psi}^\dagger_\sigma(\mathbf{r}) = \frac{1}{\sqrt{\mathcal{V}}}\sum_{\mathbf{k}}\exp(i\mathbf{k}\mathbf{r})\hat{a}_{\mathbf{k}\sigma} \tag{3.12}$$

The expectation value in the nominator is taken in the groundstate and $\hat{\Psi}^\dagger_\sigma(\mathbf{r})$ is the field operator that destroys an electron with spin σ at position $\mathbf{r}$. In the uniform electron gas the

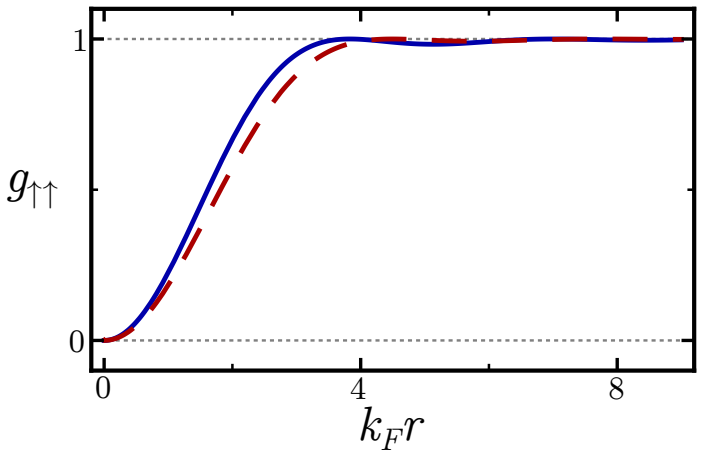

Figure 3.1.: Pair correlation function $g_{\uparrow\uparrow}(k_F r)$ for a uniform electron gas in two (blue) and three (red, dashed) dimensions. For small distances electrons of the same spin repell each other.

pair correlation function depends on the distance between $\mathbf{r}_1$ and $\mathbf{r}_2$, $g_{\sigma_1\sigma_2}(|\mathbf{r}_1 - \mathbf{r}_2)|$. Analytical expressions can be derived in two [56, 59] and three [60] dimensions:

$$g_{\sigma\sigma}(r) = \begin{cases} 1 - \left| 2\dfrac{J_1(k_{F,\sigma} r)}{k_{F,\sigma} r} \right|^2 & , 2D \\ 1 - \left| 3\dfrac{\sin(k_{F,\sigma} r) - k_{F,\sigma} r \cos(k_{F,\sigma} r)}{(k_{F,\sigma} r)^3} \right|^2 & , 3D \end{cases} \tag{3.13}$$

$k_{F,\sigma}$ is the Fermi wave vector for spin σ and $J_1(x)$ the Bessel function of the first kind. $g_{\sigma,\sigma}$ vanishes at $r = 0$ (Fig. 3.1): The probability to find two electrons of the same spin at the same point in space is zero, which is a consequence of the Pauli principle. On the other hand, the pair correlation function between electrons of different spins is spatially constant $g_{\uparrow\downarrow} = g_{\downarrow\uparrow} = 1$. The positions of electrons with different spins are not correlated by the Pauli principle, as they differ already in the quantum number spin. The probability to find another electron of equal spin at large distance is 1, is like in the uncorrelated case and a consequence of the uniformity of the electron gas. But in the vicinity of an electron with spin up (down), the probability is low that another spin up (down) electron is present; this creates a region of absence of electrons with the same spin around the electron, the so-called "exchange hole". The total charge missing in this hole is equal to the charge of the electron at the center of the exchange hole. For this electron the density of electrons in closest proximity is smaller than the uniform positive background charge density, which is then no longer electrostatically compensated. This leads to an interaction of the electron with the uncompensated positive background charge of the exchange hole, which induces the negative sign of the exchange energy.

In the groundstate all states with wave vectors smaller than the Fermi wave vector $k_{F,\sigma}$ are occupied, i.e., the groundstate is a Fermi circle in 2D and a Fermi sphere in 3D in k-space. The electron density n_σ is obtained by summing over all occupied states:

$$n_\sigma = \frac{1}{\mathcal{V}} \sum_{\mathbf{k}} \langle \hat{a}^\dagger_{\mathbf{k}\sigma} \hat{a}_{\mathbf{k}\sigma} \rangle = \begin{cases} \dfrac{k_{F,\sigma}^2}{4\pi}, & 2D \\ \dfrac{k_{F,\sigma}^3}{6\pi^2}, & 3D \end{cases} \tag{3.14}$$

The evaluation of the expectation value of the Fock Hamiltonian Eq. (3.11) yields the Helmholtz free energy of the system; the density dependence is obtained by replacing $k_{F,\sigma}$ by the relation

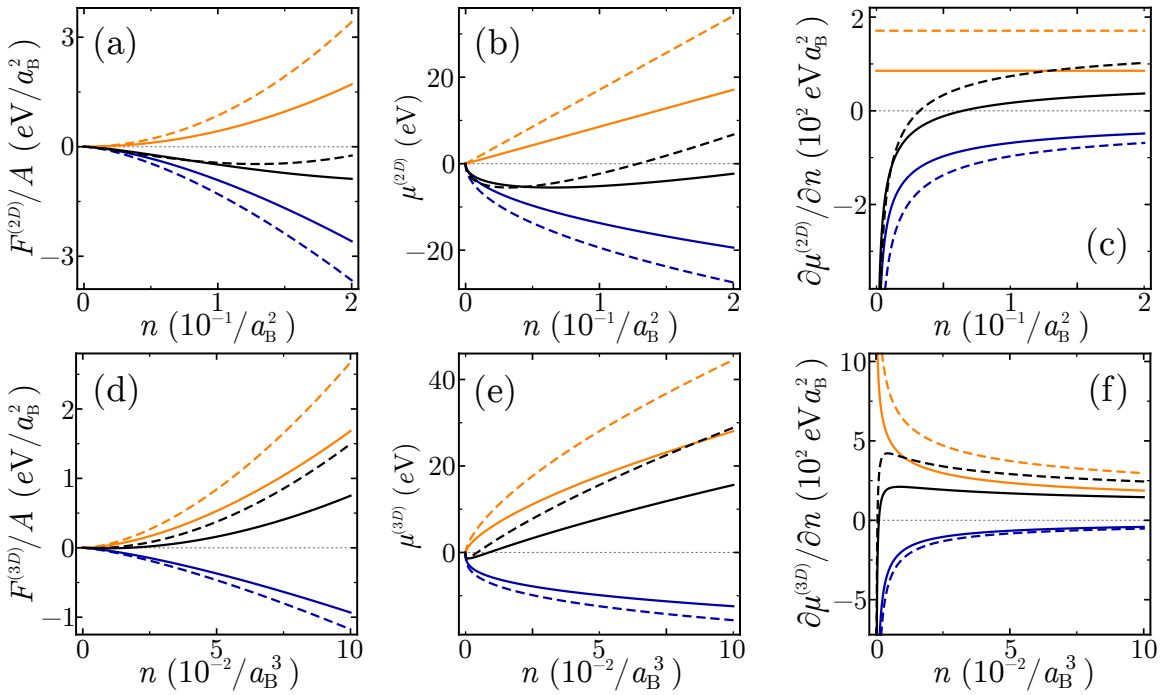

Figure 3.2.: Total free energy (black), kinetic energy (orange) and exchange energy (blue) per area of a two (a) and three (d) dimensional electron system according to Eq. (3.16) and Eq. (3.17) for $\epsilon_{\text{eff}} = 1 = m^*$. Solid lines correspond to $\xi = 0$ and dashed lines to $\xi = 1$. (b-c) and (e-f) represent the first and second derivatives with respect to the density of the free energies. The unit of the densities correspond to $1/a\text{B}^2 = 3.57 \times 10^{16}\,\text{cm}^{-2}$ and $1/a\text{B}^3 = 6.75 \times 10^{24}\,\text{cm}^{-2}$.

above. The polarization ξ is the relative difference between electron density with spin up and spin down,

$$\xi = \frac{n_\uparrow - n_\downarrow}{n_\uparrow + n_\downarrow}; \qquad \text{with } n = n_\uparrow + n_\downarrow, \tag{3.15}$$

the free energy in two and three dimensions was calculated in [56, 23]:

$$F^{(2D)}(n) = \frac{\pi\hbar^2}{2m^*} A(1+\xi^2)n^2 - \frac{4}{3}\frac{e^2 A}{\sqrt{2\pi}\epsilon_{\text{eff}}}\left[(1+\xi)^{3/2} + (1-\xi)^{3/2}\right] n^{3/2} \tag{3.16}$$

$$F^{(3D)}(n) = \frac{\hbar^2}{2m^*}\frac{3(3\pi^2)^{2/3}}{10}\mathcal{V}\left[(1+\xi)^{5/3} + (1-\xi)^{5/3}\right] n^{5/3} - \frac{3}{8}\frac{e^2}{\epsilon_{\text{eff}}}\mathcal{V}\left(\frac{3}{\pi}\right)^{1/3}\left[(1+\xi)^{4/3} + (1-\xi)^{4/3}\right] n^{4/3} \tag{3.17}$$

For the uniform electron gas the Hartree-Fock theory provides the same groundstate energy as first order perturbation theory. Figures 3.2a and 3.2d plot the kinetic, exchange and total free energy per area for two and three dimensions. A finite polarization ξ increases the kinetic energy while the exchange energy is reduced. For large densities the kinetic energy dominates

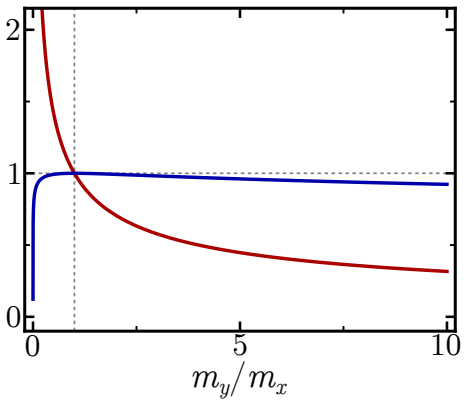

Figure 3.3.: The kinetic energy is modified by a factor of $1/\sqrt{\mathcal{Y}}$ (red) and the exchange energy by a factor of $\frac{2}{\pi}(\mathcal{Y}^{1/4}K[1-\mathcal{Y}])$ (blue) for an anisotropy of $\mathcal{Y} \equiv m_y/m_x$ between the band masses.

the exchange contribution. The second derivative of the exchange energy is negative, which is a consequence of the negative sign of the exchange energy:

$$\frac{\partial^2 F^{(2D)}}{\partial n^2} = \frac{\pi\hbar^2}{2m^*}2A(1+\xi^2) - \frac{e^2 A}{\sqrt{2\pi}\epsilon_{\text{eff}}}\left[(1+\xi)^{3/2}+(1-\xi)^{3/2}\right]n^{-1/2} \tag{3.18}$$

$$\begin{aligned}\frac{\partial^2 F^{(3D)}}{\partial n^2} = {} & \frac{\hbar^2}{2m^*}\frac{2(3\pi^2)^{2/3}}{3}\mathcal{V}\left[(1+\xi)^{5/3}+(1-\xi)^{5/3}\right]n^{-1/3} \\ & - \frac{1}{6}\frac{e^2}{\epsilon_{\text{eff}}}\mathcal{V}\left(\frac{3}{\pi}\right)^{1/3}\left[(1+\xi)^{4/3}+(1-\xi)^{4/3}\right]n^{-2/3}\end{aligned} \tag{3.19}$$

For two as well as for three dimensions and $n \to 0$ the second derivative of the exchange energy diverges to $-\infty$. The second derivative of the kinetic energy is positive and either constant (2D) or diverges to $+\infty$ for $n \to 0$ (3D), but weaker than the second derivative of the exchange energy does. Consequently the second derivative of the free energy diverges to $-\infty$ for very small densities, as can be seen in Fig. 3.2c and 3.2f. Hence the uniform electron gas displays negative compressibility for small n: This is a feature which is able to increase the capacitance beyond the geometrical value of a confined electron system.

So one is interested to enlarge the weight of the exchange energy compared to the kinetic energy to either increase the absolute value of the negative inverse compressibility or to shift the density at which the compressibility becomes negative to larger values. In systems with large effective mass m^* the kinetic energy is diminished and in systems with small effective dielectric constant ϵ_{eff} the exchange energy more negative. In two-dimensional systems for which the effective mass depends on the direction, the occupied states do not form a Fermi circle but an ellipse in k-space, which affects also the exchange energy. For an electron mass of m_i in i-direction, the Helmholtz free energy was derived in App. A.3:

$$F^{(2D)} = \frac{\pi\hbar^2}{2m_e^{-1}}A\frac{1+\xi^2}{\sqrt{m_x m_y}}n^2 - \frac{8}{3\pi}\frac{e^2 A}{\sqrt{2\pi}\epsilon_{\text{eff}}}\left(\frac{m_y}{m_x}\right)^{1/4}K\left[1-\frac{m_y}{m_x}\right]\left[(1+\xi)^{3/2}+(1-\xi)^{3/2}\right]n^{3/2} \tag{3.20}$$

Here $K[k]$ is the complete elliptic integral of the first kind; it is zero at $k=-\infty$ and increases monotonically to $+\infty$ at $k=1$. For $k=0$, i.e., when the mass is isotropic $m_x = m_y$, $K[k=0] = \pi/2$ and the equation above reduces to Eq. (3.16). With an "anisotropy ratio" $\mathcal{Y} \equiv m_y/m_x$, the kinetic energy is modified by a factor $1/\sqrt{\mathcal{Y}}$—if $m^* = m_x/m_e$ is the isotropic mass—and the exchange energy by $\frac{2}{\pi}(\mathcal{Y}^{1/4}K[1-\mathcal{Y}])$. Both factors are plotted in Fig. 3.3: At $\mathcal{Y}=1$ both factors are 1. The kinetic energy decreases monotonically with increasing $\mathcal{Y}$. The factor of the exchange energy, on the other hand, increases steeply from 0 at $\mathcal{Y}=0$ to its maximum value of 1 at $\mathcal{Y}=1$ and then decreases monotonically. For $\mathcal{Y}>1$ the factor of the exchange energy is

larger than that of the kinetic energy. Consequently, if the mass in one direction is held constant and the mass of the other direction increased, the weight of the exchange energy is enlarged.

A widely used variable, that replaces the electron density, is the dimensionless interparticle spacing r_s, which is the radius of the volume per electron expressed in Bohr radii $a_\mathrm{B} = \frac{\hbar^2}{m_e e^2}$, and is also called Wigner-Seitz radius. m_e is the electron mass and $\hbar$ the reduced Planck constant or Dirac constant. r_s is connected to the the electron number density:

$$r_s^{(2D)} = \left(\frac{1}{\pi n a_\mathrm{B}^2}\right)^{1/2} \qquad r_s^{(3D)} = \left(\frac{3}{4\pi n a_\mathrm{B}^3}\right)^{1/3} \tag{3.21}$$

The energy per particle $\varepsilon(r_s)$ is then [56, 60] for the unpolarized ($\xi = 0$) state:

$$\varepsilon^F(r_s) = \frac{e^2}{2a_\mathrm{B}} \begin{cases} \dfrac{1}{r_s^2} - \dfrac{8\sqrt{2}}{3\pi\epsilon_\mathrm{eff} r_s} & \simeq \dfrac{1}{r_s^2} - \dfrac{1.200}{r_s} \quad , 2D \\ \dfrac{3}{5}\left(\dfrac{9\pi}{4}\right)^{2/3} \dfrac{1}{r_s^2} - \dfrac{3}{2\pi\epsilon_\mathrm{eff} r_s}\left(\dfrac{9\pi}{4}\right)^{1/3} & \simeq \dfrac{2.21}{r_s^2} - \dfrac{0.916}{r_s} \quad , 3D \end{cases} \tag{3.22}$$

The Rydberg energy $e^2/2a_\mathrm{B} = \hbar^2/2m_e a_\mathrm{B}^2 \simeq 13.6\,e\mathrm{V} \equiv 1\mathrm{Ry}$ was placed in front of the parenthesis. The representation above illustrates that the kinetic energy and the exchange energy are of comparable order, since r_s/a_B ranges typically from 2 to 6 in metals. For large r_s, which corresponds to small density, the importance of the exchange term rises, so that for very small densities the exchange even dominates the kinetic term.

3.2. Groundstate of the Free Electron Gas

As found in the previous section, the free electron gas within HFA can be characterized by its spin polarization ξ. While the kinetic energy increases with polarization, the exchange energy—due to its negative sign—decreases with ξ. On the other hand, for very low densities the absolute value of the exchange energy is much larger than the kinetic energy. This implies that at low densities the state with the lowest energy, i.e., the groundstate, will be polarized with $\xi = 1$. So the question arises at wich density does the so-called Bloch transition [61], i.e., the transition between a fully polarized/ferromagnetic state and a fully unpolarized state, take place? The answer within HFA is given by Eq. (3.16) and Eq. (3.17):

$$r_{s,BT}^{(2D)} \simeq 2.01\frac{m^*}{\epsilon_\mathrm{eff}}, \qquad r_{s,BT}^{(3D)} \simeq 5.45\frac{m^*}{\epsilon_\mathrm{eff}} \tag{3.23}$$

Unfortunately, these predictions of HFA are far from reality: More accurate calculations (see next section) based on Monte Carlo studies, predict for two dimensions the Bloch transition to be at $r_{s,BT} \simeq 26$ [62]. In three dimensions the transition is either continuous over the range $20 \pm 5 \leq r_s \leq 40 \pm 5$, with $\xi = 1$ beyond $r_{s,BT} = 40$ [63] or of second order to a partially polarized phase at $r_s = 50 \pm 2$ with $\xi = 1$ at $r_{s,BT} = 100$ [64] [12]. While the prediction of the transition density is qualitatively incorrect, Hartree-Fock theory accomplishes to capture the existence of the Bloch transition.

The plane waves-solution of the HFA wave function faces another problem *within* its own theory: Another solution to the Hartree-Fock equations in three dimensions was found by Overhauser [65, 66], the so-called charge density waves (CDW) and spin density waves (SDW). These are spatially inhomogeneous solutions and their spin dependent electron density can typically be parameterized as [56]:

$$n_\uparrow(\mathbf{r}) = \frac{n}{2} + A\cos\left(\mathbf{Q}\mathbf{r} + \frac{\phi}{2}\right) \qquad n_\downarrow(\mathbf{r}) = \frac{n}{2} + A\cos\left(\mathbf{Q}\mathbf{r} - \frac{\phi}{2}\right) \tag{3.24}$$

A pure CDW is at hand for $\phi = 0$, whereas the spin density is spatially uniform, and a pure SDW for $\phi = \pi$, whereas the charge density is spatially uniform. In the SDW the spins are locally parallel, which reduces the exchange energy. The kinetic energy cost is small compared to the gain in exchange energy since the most pertubed states are mixed with states of almost equal kinetic energy [66]. Later Overhauser [67] and Fedders and Martin [68] prooved that the paramagnetic solution of the HFA has always a higher energy than the SDW solution at zero temperature. The Hartree-Fock solution of the uniform electron gas represents merely a saddle point in energy at zero temperature. However, there exists a critical temperature above which the paramagnetic phase is lower in energy than the SDW solution [67, 68].

Eq. (3.22) indicates that for very low densities the kinetic energy, which is proportional to $1/r_s^2$, can be neglected in comparison to the Coulomb energy, which goes as $1/r_s$. Wigner proposed in 1934 [69] that a "crystal" of electrons is formed at very high r_s. In this lattice the potential energy of the electrons dominates and the one-electron wave functions in HFA are δ-functions centered at the positions of a Bravais lattice. Wigner called this an "inverted alkali metal" [70], because the positive charge is uniformly distributed and the electrons are localized. For an approximate calculation of the energy of the Wigner lattice one assumes it to be formed of electrically neutral unit cells with a dipole moment, the interaction of which decreases rapidly with distance. In three dimensions the body-centered cubic and in two dimensions the hexagonal lattice structure has the lowest energy. The Monte Carlo results mentioned above found that the transition from the ferromagnetic phase to the Wigner crystal occurs at very low density. Early results for the two-dimensional electron gas from Tanatar and Ceperley [14] suggested that there is a direct phase transition from a paramagnetic phase to the Wigner crystal at $r_s = 37 \pm 5$, while at $r_s = 40$ the energy of paramagnetic, ferromagnetic and Wigner phase were approximately equal. More recently, Attaccalite *et al.* [62] identified the phase transition from ferromagnetic to Wigner phase to be at $r_s \sim 35$. In three dimensions Ortiz *et al.* [63] suggested that the electrons crystallize at $r_s = 65 \pm 10$ into the Wigner lattice from the polarized phase, while Zong *et al.* proposed $r_s = 100 \pm 20$ as the interparticle spacing of this phase transition.

All these data above suggest that the uniform solution of the HFA is inadequate to describe the free electron gas correctly. Nevertheless, the employment of plane waves can be justified as technique to catch first insights on the properties of the electron system. While the HFA fails to predict the correct density of the phase transition between unpolarized and polarized phase, it is yet a tool to qualitatively describe these phases. Furthermore, above a certain temperature the energy of the uniform electron gas is lower than that of the CDW/SDW states. And finally, we assume in this work that the electron density is above the transition point to the Wigner crystal. As we will see in the next section, the difference between HFA and the exact groundstate energy is often negligible for the density range we are interested in.

3.3. Correlation Energy and Second Derivatives with Respect to Density

The correlation energy is the difference between the exact groundstate energy and the Hartree-Fock energy; i.e., it includes the electron-electron interactions that go beyond the interaction with an effective mean field, which are labeled as quantum fluctuations. The exact groundstate energy of the free electron gas is calculated by quantum Monte Carlo simulations. There are several quantum Monte Carlo (MC) methods, like, e.g., the variational MC, diffusion MC and path integral MC [56]. The first two require an initial guess of a trial wave function, the symmetry of which determines the symmetry of the solution received by both methods.

The correlation energies have been evaluated for three-dimensional [13] and two-dimensional [14, 71] electron gases with homogeneous background charge (jellium model) by the variational Monte

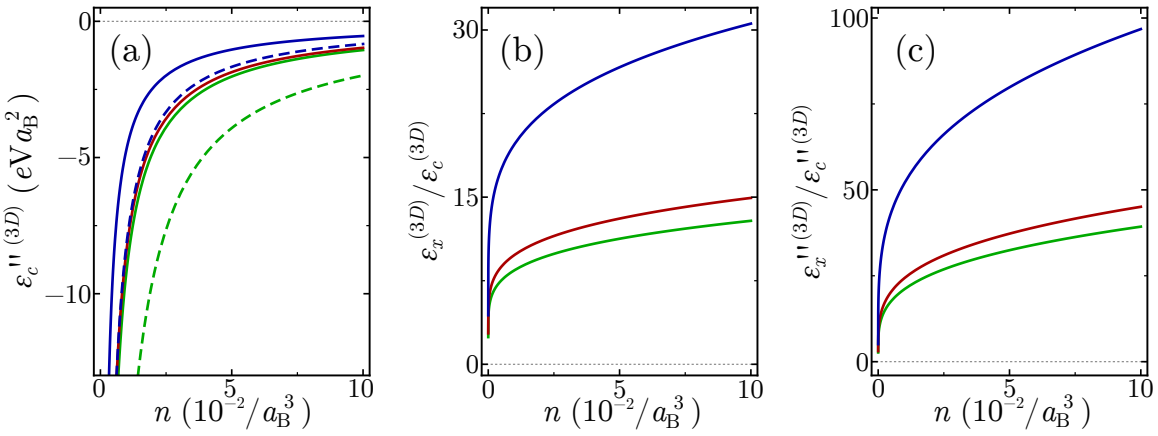

Figure 3.4.: Here $\varepsilon_i''^{(3D)} \equiv \partial^2(\varepsilon_i^{(3D)}n)/\partial n^2$ is the second derivative of the exchange ($i = x$) or correlation ($i = c$) energy per area with respect to the density n. (a) Second derivative of the correlation energy per particle as given in Eq. (3.25) for $\xi = 0$ (green), $\xi = 0.5$ (red) and $\xi = 1$ (blue). The solid lines refer to the fit from Perdew and Wang [73] and the dashed curves to the older fit of Ceperley [13]. (b) Ratio between exchange energy and correlation energy per particle. (c) Ratio between inverse exchange capacitance and inverse correlation capacitance.

Carlo method. The energies depend on the spin polarization ξ. An interpolation formula for the correlation energy per electron for general ξ, which is based on numerical data from Monte Carlo calculations that is either for the unpolarized state ($\xi = 0$) or fully polarized state ($\xi = 1$), was suggested by Vosko, Wilk and Nusair [72] in the three-dimensional case:

$$\varepsilon_c^{(3D)}(r_s,\xi) = \varepsilon_c^{(3D)}(r_s,0) + \alpha_c^{(3D)}(r_s)\frac{f(\xi}{f''(\xi)}(1-\xi^4) + \left[\varepsilon_c^{(3D)}(r_s,1) - \varepsilon_c^{(3D)}(r_s,0)\right] f(\xi)\xi^4 \quad (3.25)$$

They based their proposal on the study of the ξ-dependence of the correlation energy in Random Phase Approximation (RPA). The interpolation function $f(\xi)$ is defined as

$$f(\xi) = \frac{(1+\xi)^{4/3} + (1-\xi)^{4/3} - 2}{2^{4/3} - 2}. \quad (3.26)$$

The dimensionless interparticle spacing r_s was introduced in Eq. (3.21). The functions $\varepsilon_c^{(3D)}(r_s,0)$, $\varepsilon_c^{(3D)}(r_s,1)$ and $-\alpha_c^{(3D)}(r_s)$ can be expressed by a general form $G(r_s,\mathbf{p})$ that depends on several parameters $\mathbf{p}$. These parameters have to reproduce the exactly known high-density expansion and the low-density expansion for the correlation energy and fit $\varepsilon_c(r_s,\xi)$ to the Monte Carlo data. Perdew and Wang [73] proposed an analytical form for $G(r_s,\mathbf{p})$ that improved on earlier suggestions [72, 74]:

$$G(r_s,A,\alpha_1,\beta_1,\beta_2,\beta_3,\beta_4,p) = -2A(1+\alpha_1 r_s)\ln\left[1 + \frac{1}{2A(\beta_1 r_s^{1/2} + \beta_2 r_s + \beta_3 r_s^{3/2} + \beta_4 r_s^{p+1})}\right] \quad (3.27)$$

The result of the fit of the parameters to the Green's-function Monte Carlo data of Ceperley and Alder [75] is displayed in Table I of reference [73]. We used these parameters in combination with Eq. (3.25) to calculate the inverse correlation capacitance $e^2\mathcal{V}/C_c = \partial^2(F_c/\mathcal{V})/\partial n^2$. Note that the correlation energy per volume of the system $F_c/\mathcal{V}$ is obtained by multiplication of Eq. (3.25) with the electron number density. We compared these results with the older fit for

the energy of Ceperley (Eq. (30) in reference [13])[2] in Fig. 3.4a. The correlation capacitance is negative in the three-dimensional case for all densities and polarizations. The capacitance from the exchange energy per particle [56]

$$\varepsilon_x^{(3D)} = -\frac{3}{2\pi}\left(\frac{9\pi}{4}\right)^{1/3}\frac{(1+\xi)^{4/3}+(1-\xi)^{4/3}}{2r_s}, \tag{3.28}$$

is also negative (c.f. Fig. 3.2f). A comparison between inverse correlation capacitance and exchange capacitance (Fig. 3.4c) shows that the absolute value of the inverse exchange contribution is larger than the absolute value of the correlation contribution. At the interparticle spacing $r_s = 6$, which is the lower bound for the density of typical metals, the ratio between the inverse capacitances is $\simeq 12$ for $\xi = 0$ and $\simeq 30$ for $\xi = 1$. This ratio increases stronger than linearly with density to $\simeq 30$ and $\simeq 75$, respectively, at $r_s = 1.8$. The minimum value of the ratio can be obtained from the low density limit of the correlation energy [73]

$$\varepsilon_c^{(3D)}(r_s,\xi) \overset{r_s\to\infty}{\longrightarrow} -\frac{d_0(\xi)}{r_s}+\frac{d_1(\xi)}{r_s^{3/2}} \quad \Rightarrow \quad \frac{C_\mathrm{c}}{C_\mathrm{x}} = \frac{3}{4\pi}\left(\frac{9\pi}{4}\right)^{1/3}\frac{(1+\xi)^{4/3}+(1-\xi)^{4/3}}{|d_0(\xi)|}$$

as $\simeq 2.11$ and $\simeq 3.51$ for the unpolarized and the polarized state, where the values for $d_0(\xi)$ were taken from Table I of reference [73]. This provides evidence that the contribution to the capacitance from the correlation term can approximatively be neglected compared to the exchange contribution, especially at densities of normal metals. Note that including the correlation contribution would enhance the capacitance above the exchange contribution.

Attaccalite *et al.* performed diffusion Monte Carlo simulations for a two-dimensional electron gas at several polarizations [62]. They introduced the functional form

$$\begin{aligned}\varepsilon_c^{(2D)}(r_s,\xi) = \left(e^{-\beta r_s}-1\right)\left(\varepsilon_x^{(2D)}(r_s,\xi)-(1+\frac{3}{8}\xi^2+\frac{3}{128}\xi^4)\varepsilon_x^{(2D)}(r_s,0)\right)\\ +\alpha_0^{(2D)}(r_s)+\alpha_1^{(2D)}(r_s)\xi^2+\alpha_2^{(2D)}\xi^4\end{aligned} \tag{3.29}$$

for the correlation energy per electron. $\varepsilon_x^{(2D)}(r_s,\xi)$ is the exchange term

$$\varepsilon_x^{(2D)}(r_s,\xi) = -\frac{2\sqrt{2}}{3\pi r_s}\left[(1+\xi)^{3/2}+(1-\xi)^{3/2}\right]. \tag{3.30}$$

The $\alpha_i^{(2D)}$ $(i=1,2,3)$ are a generalization of the Perdew and Wang [73] form:

$$\alpha_i^{(2D)}(r_s,\xi) = A_i + \left(B_i r_s + C_i r_s^2 + D_i r_s^3\right)\ln\left[1+\frac{1}{E_i r_s + F_i r_s^{3/2} + G_i r_s^2 + H_i r_s^3}\right] \tag{3.31}$$

The fitted parameters are given in Table I of reference [62]. We employed these results to calculate the inverse correlation capacitance (Fig. 3.5a) per area for three polarizations $\xi = 0$, $\xi = 0.5$ and $\xi = 1$. This plot includes also $\partial^2(\varepsilon_c^{(2D)}n)/\partial n^2 = e^2A/C_\mathrm{c}$ obtained from the correlation energy approximation of Tanatar and Ceperley (reference [14], Eq. (14)) for the polarized and unpolarized state (dashed lines). The correlation capacitance is negative in all cases for the two-dimensional electron gas. The ratio between the inverse exchange capacitance (Fig. 3.2c) and inverse correlation capacitance is increasing with density (Fig. 3.5c). For $n =$

[2] The correlation energy is obtained by subtracting the kinetic contribution h_0/r_s^2 and the exchange contribution h_1/r_s from Eq. (30). Note that in Table IV one has to read $\alpha_4 h_0$ as α_4/h_0, as was pointed out by Kopp ([12], reference 50)

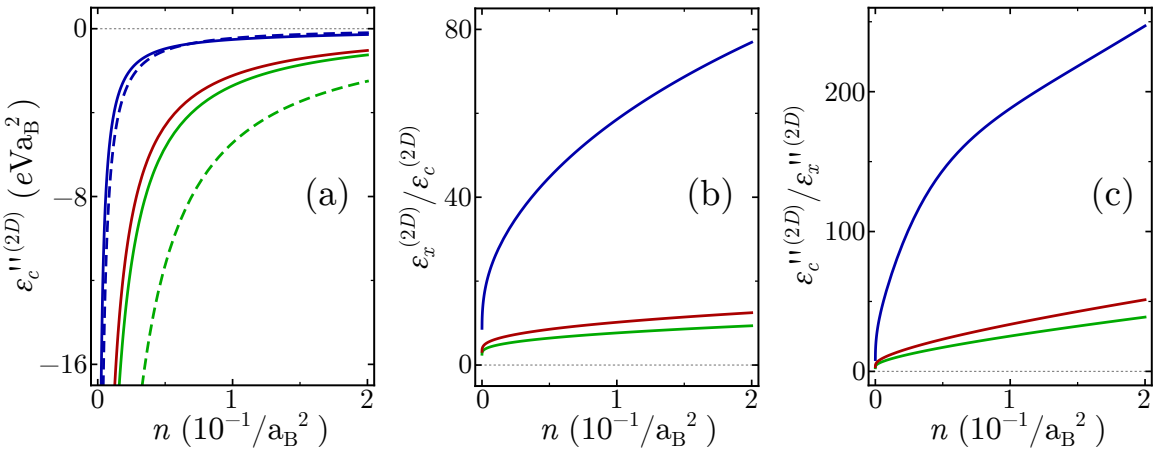

Figure 3.5.: Here $\varepsilon_i''^{(2D)} \equiv \partial^2(\varepsilon_i^{(2D)}n)/\partial n^2$ is the second derivative of the exchange ($i = x$) or correlation ($i = c$) energy per area with respect to the density n and proportional to the inverse capacitance. (a) Second derivative of the correlation energy per particle as given in Eq. (3.29) for $\xi = 0$ (green), $\xi = 0.5$ (red) and $\xi = 1$ (blue). The solid lines refer to the fit from Attaccalite [62] and the dashed curves to the older fit of Tanatar and Ceperley [14]. (b) Ratio between exchange energy and correlation energy per particle. (c) Ratio between inverse exchange capacitance and inverse correlation capacitance.

$0.01/a_\mathrm{B}^2 \approx 3.6 * 10^{14}\mathrm{cm}^{-2}$ this ratio is $\simeq 8.5$ for the unpolarized and $\simeq 63$ for the polarized state. In the high-r_s limit from Ceperley [13], we get as miminum value of the ratio between inverse exchange and correlation capacitance

$$\varepsilon_c^{(2D)}(r_s,\xi) \overset{r_s\to\infty}{\longrightarrow} -\frac{f_0}{r_s} + \frac{f_1}{r_s^{3/2}} \quad \Rightarrow \quad \frac{C_\mathrm{c}}{C_\mathrm{x}} = \frac{4\sqrt{2}}{3\pi}\frac{(1+\xi)^{3/2}+(1-\xi)^{3/2}}{|f_0|},$$

which is $\simeq 0.54$ for $f_0 = -2.2122$ from [13] in the unpolarized case. Hence, the correlation capacitance can be neglected at larger densities.

3.4. Uniform Electron Gas and its Compressibility at Finite Temperature

This section addresses the effect of finite temperature on the energy and its derivatives of a uniform free electron gas. For finite temperature the grand potential Ω is evaluated by several approximate methods and hence a useful quantity. It is connected to the Helmholtz free energy F and the internal energy E by Legendre transformation:

$$\Omega(T,\mathcal{V},\mu) = F(T,\mathcal{V},N) - \mu N = E(S,\mathcal{V},N) - ST - \mu N \tag{3.32}$$

Ω is a function of the temperature T, the volume $\mathcal{V}$ and the chemical potential μ, so that

$$\mathrm{d}\Omega(T,\mathcal{V},\mu) = -S\mathrm{d}T - p\mathrm{d}V - N\mathrm{d}\mu \qquad \Rightarrow \left(\frac{\partial\Omega}{\partial T}\right)_{\mathcal{V},\mu} = -S, \qquad \left(\frac{\partial\Omega}{\partial\mu}\right)_{T,\mathcal{V}} = -N \tag{3.33}$$

the entropy S and the particle number N can be derived from Ω. One can infer the grand potential from the relation

$$\exp\left(-\beta\Omega\right) = \mathrm{Tr}\left[-\beta\hat{K}\right] \tag{3.34}$$

Here $1/\beta = k_\mathrm{B}T$, where $k_\mathrm{B} \simeq 8.617 \times 10^{-5} e\mathrm{V/K}$ is the Boltzmann constant, and Tr[.] is the trace [60]. $\hat{K}$ is defined over the Hamiltonian $\hat{\mathcal{H}}$ by

$$\hat{K} = \hat{K}_0 + \hat{V} = \hat{\mathcal{H}} - \mu\hat{N}, \qquad \text{with} \quad \hat{\mathcal{H}} = \hat{\mathcal{H}}_0 + \hat{V} \quad \text{and} \quad \hat{K}_0 = \hat{\mathcal{H}}_0 - \mu\hat{N}, \tag{3.35}$$

where one assumes that $\hat{\mathcal{H}}_0$ is exactly solvable and $\hat{V}$ a perturbation of the Hamiltonian. The grand potential Ω_0 is the grand potential with vanishing $\hat{V} = 0$. For example, an exactly solvable Hamiltonian could be of the form

$$\hat{K}_0 = \sum_{\mathbf{k},\sigma} \varepsilon_\sigma^K(\mathbf{k}) \hat{a}^\dagger_{\mathbf{k}\sigma} \hat{a}_{\mathbf{k}\sigma} \tag{3.36}$$

with $\varepsilon_\sigma^K(\mathbf{k}) = \varepsilon_\sigma(\mathbf{k}) - \mu$, where $\varepsilon_\sigma(\mathbf{k})$ are the eigenvalues of $\hat{\mathcal{H}}_0$. If the eigenstates of $\hat{\mathcal{H}}_0$ are used to perform the trace in Eq. (3.34), then the matrix elements of $\hat{K}_0$ are diagonal and

$$\exp\left(-\beta\Omega_0\right) = \Pi_{\mathbf{k},\sigma} \left(1 + \exp\left(-\beta\varepsilon_\sigma^K(\mathbf{k})\right)\right) \tag{3.37}$$

$$\iff \qquad \beta\Omega_0 = -\sum_{\mathbf{k},\sigma} \ln\left[1 + \exp\left(-\beta\varepsilon_\sigma^K(\mathbf{k})\right)\right] \tag{3.38}$$

From this the electron density n can be evaluated by using Eq. (3.33):

$$n = \frac{1}{\mathcal{V}} \sum_{\mathbf{k},\sigma} \langle \hat{a}^\dagger_{\mathbf{k}\sigma} \hat{a}_{\mathbf{k}\sigma} \rangle \overset{(3.33)}{=} -\frac{1}{\mathcal{V}} \left(\frac{\partial\Omega_0}{\partial\mu}\right)_{T,\mathcal{V}} = \frac{1}{\mathcal{V}} \sum_{\mathbf{k},\sigma} \frac{1}{1 + \exp\left(\beta(\varepsilon_\sigma(\mathbf{k}) - \mu)\right)} \tag{3.39}$$

This defines the Fermi function $f_\sigma(\mathbf{k})$

$$n_{\mathbf{k}\sigma} \equiv \langle \hat{a}^\dagger_{\mathbf{k}\sigma} \hat{a}_{\mathbf{k}\sigma} \rangle = \frac{1}{1 + \exp\left(\beta(\varepsilon_\sigma(\mathbf{k}) - \mu)\right)} \equiv f_\sigma(\mathbf{k}), \tag{3.40}$$

which converts into the Heaviside step function at zero temperature. The combination of Eq. (3.33) and Eq. (3.38) yields—after some further manipulation (c.f. App. A.4)—the entropy S:

$$S_0 \overset{(3.33)}{=} -\left(\frac{\partial\Omega_0}{\partial T}\right)_{\mathcal{V},\mu} = -k_\mathrm{B} \sum_{\mathbf{k},\sigma} \left(n_{\mathbf{k}\sigma} \ln\left[n_{\mathbf{k}\sigma}\right] + \left(1 - n_{\mathbf{k}\sigma}\right) \ln\left[1 - n_{\mathbf{k}\sigma}\right]\right) \tag{3.41}$$

The Helmholtz free energy of the exactly solvable system is given by the Legendre transform, so that Eq. (3.38) becomes (c.f. App. A.4)

$$F_0 = \Omega_0 + \mu N = \sum_{\mathbf{k},\sigma} \varepsilon_\sigma^K(\mathbf{k}) n_{\mathbf{k}\sigma} - TS_0 + \mu N = \sum_{\mathbf{k},\sigma} \varepsilon_\sigma(\mathbf{k}) n_{\mathbf{k}\sigma} - TS_0 \tag{3.42}$$

While at zero temperature the entropy S_0 vanishes, this quantity becomes relevant for finite temperature.

We calculated the free energy of a uniform gas of non-interacting electrons in App. A.4. The energy is spin independent and given by the kinetic energy of free electrons:

$$\varepsilon_\sigma(\mathbf{k}) = \varepsilon(\mathbf{k}) = \frac{\hbar^2 k^2}{2m^*} \equiv ak^2 \tag{3.43}$$

The groundstate energy of the unpolarized electron gas is then

$$\begin{aligned} F_0 = E_\mathrm{kin} - TS_0 &= \frac{A}{2\pi a\beta^2} \left[\frac{\pi^2}{6} - \frac{1}{2}\mu^2\beta^2 + \mathrm{Li}_2\left[-e^{-\mu\beta}\right]\right] \\ &\quad + \frac{A}{2\pi a\beta^2} \left\{\frac{1}{2}\ln^2\left[1 + e^{-\mu\beta}\right] - \frac{1}{2}\ln^2\left[1 + e^{\mu\beta}\right] + \mathrm{Li}_2\left[-e^{-\mu\beta}\right] - \mathrm{Li}_2\left[-e^{\mu\beta}\right] - \frac{\pi^2}{6}\right\} \\ &= \frac{A}{2\pi a\beta^2} \left[\frac{1}{2}\left(\ln^2\left[1 - e^{-\zeta}\right] - \zeta^2 - \ln^2\left[e^\zeta - 1\right]\right) + 2\mathrm{Li}_2\left[\frac{1}{e^\zeta - 1}\right] - \mathrm{Li}_2\left[1 - e^\zeta\right]\right] \end{aligned} \tag{3.44}$$

Here $\mathrm{Li}_n[x]$ is the polylogarithm function (or in case of the subscript 2 the dilogarithm). It increases monotonically from $x = -\infty$ to 0 at $x = 0$ and is defined up to $x = 1$, where $\mathrm{Li}_2[1] = \pi^2/6$. In the last line $\zeta = 2\pi an\beta$ was introduced: As for $T = 0$ the Fermi wave vector is given by $k_\mathrm{F} = \sqrt{2\pi n}$, the quantity $\zeta = E_\mathrm{F}/k_\mathrm{B}T$ is the ratio between Fermi energy and thermal energy, or—with the former energy defining a temperature $E_\mathrm{F} = k_\mathrm{B}T_\mathrm{F}$—the ratio between Fermi temperature and temperature: $\zeta = T_\mathrm{F}/T$. The chemical potential is connected to ζ by

$$\beta\mu = \ln\left[\exp\left(2\pi na\beta\right) - 1\right] \equiv \ln\left[e^\zeta - 1\right] \tag{3.45}$$

We assumed that the exchange interaction is a perturbation of the free electrons, so that the kinetic energy Eq. (3.43) remains unaltered by exchange. This is the lowest level of Hartree-Fock approximation, where only the single "oyster" diagram is considered [76] for the Fock term. This approximation does not fulfill self-consistency relations, which are necessary to guarantee conservation laws [77]. In general one has to proceed with caution when a zero-temperature formalism is expanded to finite temperature: For example, in the Brueckner-Goldstone formula [78], which corresponds to the standard perturbation theory approach, one could replace the Heaviside step functions by Fermi functions at finite temperature. Unfortunately, an expansion beyond the original domain of definition of this theory would ignore the contributions of so-called "anomalous diagrams" [79], which should appear already in second order of perturbation theory. It was shown by Luttinger and Ward [80] that these "anomalous diagrams" vanish in case of an isotropic perturbation. If the electron-electron interaction is anisotropic, then their inclusion in a self-consistent manner alters the shape of the Fermi surface, while perturbation theory assumes a spherical Fermi surface originating most often from the kinetic energy.

For our level of approximation we are on the safe side, as we do not go beyond first order perturbation theory and the effective exchange potential is isotropic. The same approach as used here was applied by Gupta and Rajagopal [81] for the calculation of the exchange contribution of a three-dimensional electron gas. According to the minimum principle of Feynman [82], the free energy F of the system is $F \leq F_0 + \langle\hat{V}\rangle_0$, where the expectation value $\langle.\rangle_0$ is taken in the eigenstates of the unperturbed Hamiltonian $\hat{\mathcal{H}}_0$, so that our approximation provides an upper bound for F.

A more accurate calculation of the groundstate free energy could be performed under the framework of the *linked cluster method* [60, 83]: The l-th order of the self-energy $\Sigma_l(p)$ is obtained by summing over all linked l-th order diagrams, thereby omitting all unlinked diagrams. With $\mathcal{G}^{(0)}(p)$ being the unperturbed Green's function, the l-th order contribution to Ω is given by [76]:

$$\Omega_l = \frac{1}{\beta}\sum_{\mathbf{p},ip_n}\frac{1}{l}\mathcal{G}^{(0)}(p)\Sigma_l(p) \tag{3.46}$$

In self-consistent Hartree-Fock approximation all one-bubble diagrams as depicted in Fig. 4 of Ref. [76] are included and the self-energy $\Sigma_l(p)$ appears in the Fermi function.

In our approximation, the exchange energy can be split into a product (c.f. App. A.4 for more details): the first factor is the exchange energy at zero temperature F_x^0 and the second factor includes all temperature dependence as function of ζ:

$$F_\mathrm{x} = F_\mathrm{x}^0 I_\mathrm{x}(\zeta) = F_\mathrm{x}^0\frac{3}{8\zeta^{3/2}}\mathcal{I}(\zeta) \tag{3.47}$$

$$F_\mathrm{x}^0 = -\frac{8}{3}\frac{e^2 A}{\sqrt{2\pi}\epsilon_\mathrm{eff}}n^{3/2} \tag{3.48}$$

$$\mathcal{I}(\zeta) = \int_0^{2\pi}\mathrm{d}\theta\int_0^\infty\mathrm{d}q\int_0^\infty\mathrm{d}k k\frac{e^\zeta - 1}{e^\zeta - 1 + e^{k^2}}\frac{e^\zeta - 1}{e^\zeta - 1 + e^{k^2+2kq\cos\theta+q^2}} \tag{3.49}$$

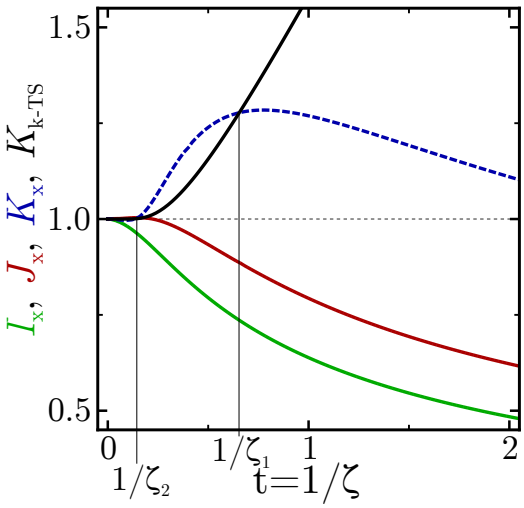

Figure 3.6.: The ratio between finite and zero-temperature values of the exchange energy is I_x (green), the ratio between its first derivatives with respect to density n is J_x (red) and the ratio of its second derivative is K_x (blue). The second derivative of the kinetic energy is modified by $K_{\mathrm{k-TS}}$ in comparison to the $T = 0$ value (black). Between $1/\zeta_2 \approx 0.14$ and $1/\zeta \approx 2.8$ the second derivative of the exchange energy at finite temperature is larger than the zero temperature value.

The integral $\mathcal{I}$ has to be evaluated numerically. As we are interested in the inverse compressibility, the second derivatives with respect to the density are determined:

$$\frac{\partial^2 E_\mathrm{kin}}{\partial n^2} = 2\pi a A \frac{e^\zeta\left(e^\zeta - 1 - \zeta\right)}{\left(e^\zeta - 1\right)^2} \equiv \frac{\mathrm{d}^2 E^0_\mathrm{kin}}{\mathrm{d}n^2} K_\mathrm{kin}(\zeta) \tag{3.50}$$

$$-T\frac{\partial^2 S}{\partial n^2} = 2\pi a A \frac{\zeta e^\zeta}{\left(1 - e^\zeta\right)^2} \tag{3.51}$$

$$\Rightarrow \frac{\mathrm{d}^2 F_0}{\mathrm{d}n^2} = 2\pi a A \frac{e^\zeta}{e^\zeta - 1} \equiv \frac{\mathrm{d}^2 E^0_\mathrm{kin}}{\mathrm{d}n^2} K_{\mathrm{k-TS}}(\zeta) \tag{3.52}$$

$$\frac{\mathrm{d}^2 F_\mathrm{x}}{\mathrm{d}n^2} = \frac{\mathrm{d}^2 F^0_\mathrm{x}}{\mathrm{d}n^2} \frac{\zeta^{1/2}}{2} \frac{\mathrm{d}^2 \mathcal{I}}{\mathrm{d}\zeta^2} \equiv \frac{\mathrm{d}^2 F^0_\mathrm{x}}{\mathrm{d}n^2} K_\mathrm{x}(\zeta) \tag{3.53}$$

Here

$$\frac{\mathrm{d}^2 E^0_\mathrm{kin}}{\mathrm{d}n^2} = 2\pi a A \qquad \text{and} \qquad \frac{\mathrm{d}^2 F^0_\mathrm{x}}{\mathrm{d}n^2} = -2\frac{e^2 A}{\sqrt{2\pi}\epsilon_\mathrm{eff}} n^{-1/2} \tag{3.54}$$

are the second derivatives of the $T = 0$ energies and the functions $K_{\mathrm{k-TS}}(\zeta)$ and $K_\mathrm{x}(\zeta)$ encode the temperature dependence of the second derivatives. A first insight into the behavior of the contributions can be gained by taking the limits $\zeta \to 0$ and $\zeta \to \infty$. The former corresponds to $T \to \infty$ at constant density or $n \to 0$ at constant temperature and the latter to $T \to 0$ at constant density or $n \to \infty$ at constant temperature.

$$\lim_{\zeta\to 0} \frac{\partial^2 E_\mathrm{kin}}{\partial n^2} = \pi a A \qquad\qquad \lim_{\zeta\to \infty} \frac{\partial^2 E_\mathrm{kin}}{\partial n^2} = 2\pi a A \tag{3.55}$$

$$\lim_{\zeta\to 0} \frac{\partial^2 (-TS)}{\partial n^2} = A \lim_{n\beta\to 0} \frac{1}{n\beta} = \infty \qquad\qquad \lim_{\zeta\to \infty} \frac{\partial^2 (-TS)}{\partial n^2} = 0 \tag{3.56}$$

$$\lim_{\zeta\to 0} \frac{\mathrm{d}^2 F_\mathrm{x}}{\mathrm{d}n^2} = \lim_{\zeta\to 0} \frac{\mathrm{d}^2 F^0_\mathrm{x}}{\mathrm{d}n^2} \frac{(2\pi)^{3/2}}{8} \zeta^{1/2} = -\frac{e^2 A}{\epsilon_\mathrm{eff}} \frac{\pi}{2} \sqrt{2\pi a\beta} \qquad\qquad \lim_{\zeta\to \infty} \frac{\mathrm{d}^2 F_\mathrm{x}}{\mathrm{d}n^2} = 0 \tag{3.57}$$

Assume the temperature to be fixed; then $\zeta \to \infty$ corresponds to $n \to \infty$. As the contributions to the inverse compressibility from the entropy and exchange vanish in this limit, only the kinetic contribution is relevant: its value is equal to the $T = 0$ kinetic compressibility. For $n \to 0$ or $\zeta \to 0$ on the other hand, the kinetic contribution is reduced to half of its $T = 0$ value, while the entropic contribution is positive and diverges as $1/n$. The exchange contributes a finite

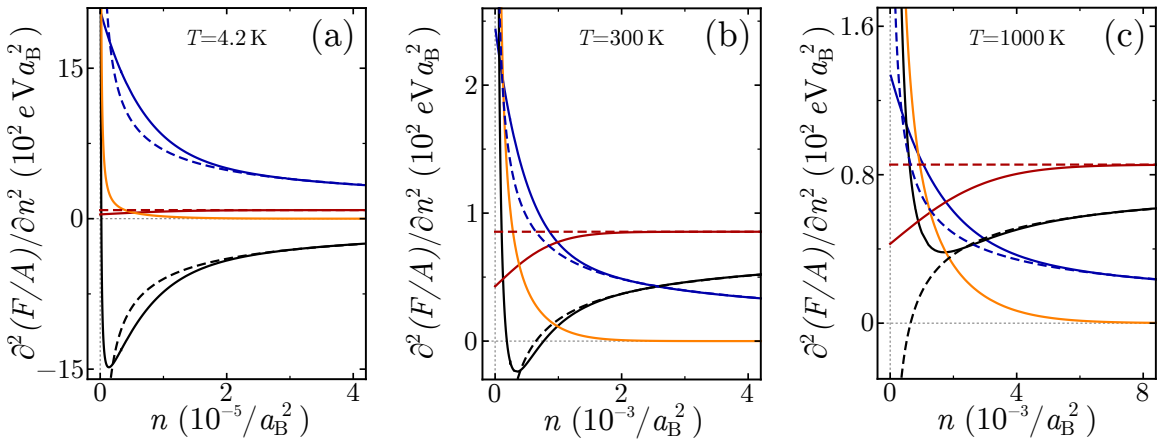

Figure 3.7.: Second derivatives of the kinetic/internal energy (red), the entropic energy (orange), the absolute value of the exchange energy (blue) and the total Helmholtz free energy (black) at $T = 4.2\,\mathrm{K}$ (a), $T = 300\,\mathrm{K}$ (b) and $T = 1000\,\mathrm{K}$ (c) for $m^* = 1$ and $\epsilon_\mathrm{eff} = 10$. The dashed lines depict the corresponding values for $T = 0\,\mathrm{K}$.

negative value, which is proportional to $1/\sqrt{T}$, which recovers the divergence of $T = 0$. As the second derivatives of the kinetic, entropic and exchange energy are numerically found to be each monotonic, the compressibility is always positive for n small enough at finite temperature, which contrasts the $T = 0$ divergence to negative values due to the dominance of the exchange contribution.

In general, for finite temperatures we obtain

$$\kappa^{-1} = \frac{n^2}{A}\left(\frac{\mathrm{d}^2 E^0_\mathrm{kin}}{\mathrm{d}n^2} K_{\mathrm{k-TS}}(\zeta) + \frac{\mathrm{d}^2 E^0_\mathrm{x}}{\mathrm{d}n^2} K_\mathrm{x}(\zeta)\right) \tag{3.58}$$

for the inverse compressibility. Figure 3.6 shows $K_{\mathrm{k-TS}}$ and $K_\mathrm{x}(\zeta)$ plotted over $t \equiv 1/\zeta$. For ζ between $\zeta_2 \approx 1/0.65$ and $\zeta_1 \approx 1/0.14$, $K_\mathrm{x}(\zeta)$ is larger than $K_{\mathrm{k-TS}}(\zeta)$. That means, for a given temperature T and mass m^*, ζ_1 and ζ_2 determine an interval of density $\mathcal{J}_{T,m^*}$ in which the negative exchange contribution is more enhanced than the positive contributions from kinetic and entropic energy. One can denote the density, at which for $T = 0$ the inverse compressibility is zero, i.e., at which the kinetic and exchange contribution cancel each other, as n_c^0. If n_c^0 is an element of $\mathcal{J}_{T,m^*}$ for fixed mass m^*, the compressibility is already negative above n_c^0 for finite temperature. In case of n_c^0 lying far enough left of $\mathcal{J}_{T,m^*}$, i.e., for T large enough, the compressibility is positive for every density.

The functions $K_{\mathrm{k-TS}}(\zeta)$ and $K_\mathrm{x}(\zeta)$ approach 1 for large ζ and differ less than 1% from this value for $\zeta > 6$. Hence, with $\zeta = 2\pi n a/k_\mathrm{B}T$, we can reason that for $\frac{\pi}{3m^*} n a_\mathrm{B}^2 > k_\mathrm{B}T/E_\mathrm{Rydberg}$ the finite temperature values of the second derivative can be approximated by the zero temperature values for most purposes.

The second derivatives of the free energies are given in Fig. 3.7(a-c) for $T = 4.2\,\mathrm{K}$, $T = 300\,\mathrm{K}$ and $T = 1000\,\mathrm{K}$, respectively: An interval of density for which the exchange contribution (blue curves) at finite temperature (solid lines) is more negative than its corresponding $T = 0$ value (dashed curves) always exists. In contrast to $T = 0$, the exchange contribution is finite at $n \to 0$ for $T > 0$. As demonstrated above, the internal energy contribution (red) drops to half of its $T = 0$ value for $n \to 0$, while the contribution from the entropy diverges to a positive value in this limit. The simple monotonic behavior of the second derivative of the total free energy (black) at $T = 0$—namely an increase from $-\infty$ to the kinetic contribution $2\pi a A$ with n going from 0 to ∞—is thus replaced by a more complicated dependence on n at $T > 0$. For $n \to 0$ the second derivative of free energy is always positive due to the entropic contribution, while for

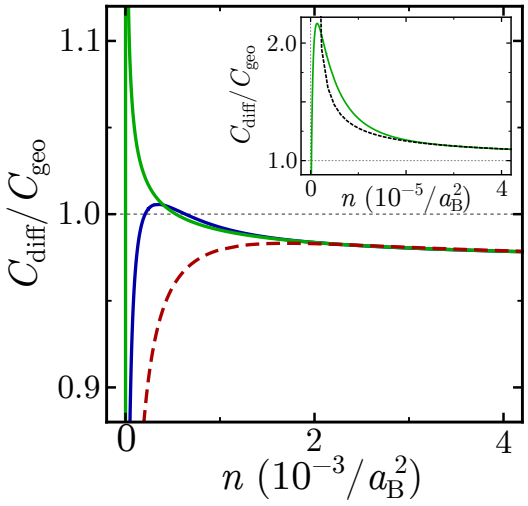

Figure 3.8.: Differential capacitance C_{diff} for two two-dimensional electron systems normalized to the geometric capacitance $C_{\mathrm{geo}} = A\epsilon/4\pi d$ for $T = 4.2\,\mathrm{K}$ (green), $T = 300\,\mathrm{K}$ (blue) and $T = 1000\,\mathrm{K}$ (red, dashed) and $d/\epsilon = 4a_{\mathrm{B}}$. The $T = 4.2\,\mathrm{K}$ value differs from the $T = 0$ value (black, dashed) only for very small densities (inset). n denotes the density on the lower electrode, where the electrons have effective mass $m^* = 1$ and the intralayer Coulomb interaction is modified by $\epsilon_{\mathrm{eff}} = 10$. We assume that the density on the upper electrode, where the electrons are characterized by $m^* = 10$, is so large that the exchange contribution to the free energy of this subsystem can be neglected and the second derivative of the subsystem-free energy is approximately given by the $T = 0$ value.

very large densities the kinetic contribution $2\pi aA$ dominates. The behavior in between these limits depends strongly on the temperature: For low temperatures there exists a minimum of the second derivative with a negative value. An increase in temperature shifts this minimum to higher densities and increases its value, up to the point where it is place above the abscissa, i.e., the compressibility of the system is then positive for every density.

The temperature dependence of the Helmholtz free energy is reflected directly in the capacitance of a two-layer arrangement made up of two-dimensional electron gases as introduced in the previous chapter. The inverse differential capacitance of such a setup, given by Eq. (2.33), is the sum of the second derivatives of the free energies of the subsystems and the inverse geometric capacitance. As the second derivative of the free energy differs from the $T = 0$ value appreciably only for small densities and we assume that the total density in the system is sufficiently large, finite temperature effects are relevant for one electrode at most. The meaning of "(sufficiently) small/large" densities depends on the temperature; as pointed out above, for $\zeta > 6$ the second derivatives of the free energy for zero and finite temperature differ less than 1%. The corresponding density at $T = 4.2\,\mathrm{K}$ and $m^* = 1$ would be $n \approx 2.5 \times 10^{-5}/a_{\mathrm{B}}^2 \approx 9.1 \times 10^{11}/\mathrm{cm}^2$. This density can also be identified in the inset of Fig. 3.8. There the differential capacitance C_{diff} normalized to the geometric capacitance C_{geo} is displayed as function of the density at $T = 0$, $T = 4.2\,\mathrm{K}$, $T = 300\,\mathrm{K}$ and $T = 1000\,\mathrm{K}$. For large densities C_{diff} is smaller than the geometric capacitance, as the exchange contribution is negligible against the positive kinetic contribution. For $n \to 0$ the diverging entropic contribution overcompensates the negative exchange contribution, so that the differential capacitance drops to zero for all finite temperatures, as against the $T = 0$ case, where the unimpeded negative exchange contribution drives $C_{\mathrm{diff}} \to \infty$ (c.f. inset of Fig. 3.8). For $T = 1000\,\mathrm{K}$ the second derivative of the free energy is positive (c.f. Fig. 3.7c), and $C_{\mathrm{diff}} < C_{\mathrm{geo}}$ for all densities. For smaller temperatures the entropic contribution is only relevant over a narrow density range and the exchange contribution can drive the compressibility of the subsystem negative. If the second derivative of the free energy of one subsystem is more negative than the second derivative of the other subsystem is positive, the differential capacitance can exceed the geometric value (c.f. $T = 300\,\mathrm{K}$ and $T = 4.2\,\mathrm{K}$ in Fig. 3.8).

While the approximation made to obtain the temperature dependence corresponds only to first order perturbation theory, we draw two qualitatively valid results for the second derivative of the free energy with respect to the density: Firstly, the corrections to $T = 0$ are only relevant below a certain electron density for a given temperature. For example, at $T = 4.2\,\mathrm{K}$ and $m^* = 1$ this critical density is of the order of the density in semiconductor heterostructures, but below the

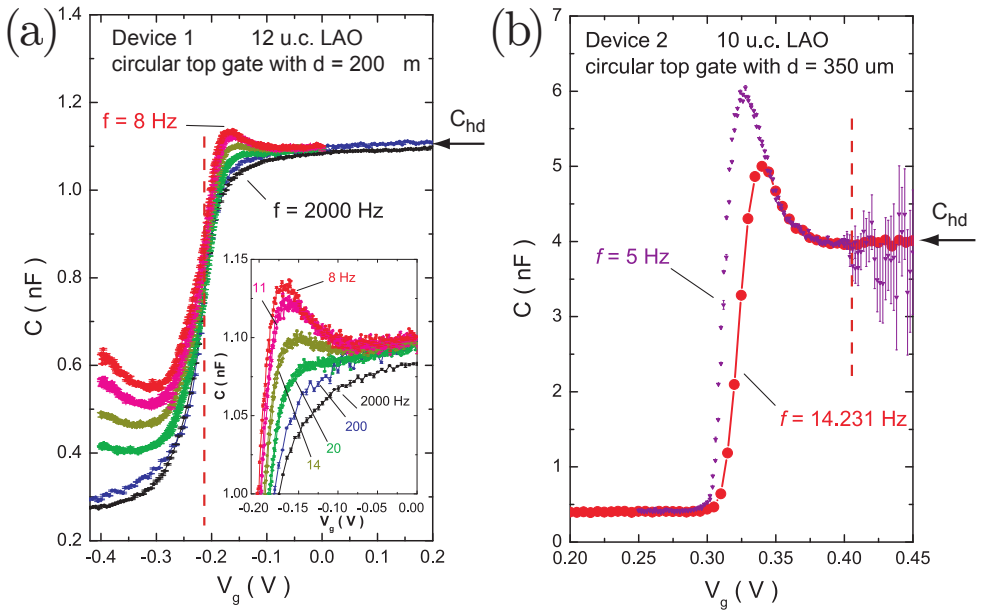

Figure 3.9.: Capacitance as function of backgate voltage V_g as measured in Ref. [9] for the LAO/STO interface and a top gate for different thicknesses of the LAO layer. The density on the interface increases with V_g. In the high density limit, when quantum corrections are negligible, the capacitance is given by the geometric value $C_{\mathrm{geo}} = C_{\mathrm{hd}}$. Below a certain gate voltage the interface system becomes depleted and the capacitance drops to zero. Adapted from Ref. [9].

characteristic n of $LaAlO_3/SrTiO_3$ interfaces. And secondly, we found that the $n \to 0$ behavior is completely opposite to the zero temperature behavior: Due to the entropic contribution the second derivative diverges to $+\infty$ instead to the exchange induced $-\infty$ of $T = 0$. We would like to point out the latter is in better accordance with the low density limits of the experiments of Lu Li *et al.* [9] (see Fig. 3.9): They found that the capacitance drops down to zero and the second derivative of the interface free energy, obtained by penetration field measurements, is positive for small densities.

4. Density Dependent Spin-Orbit Coupling

This chapter is for the most part based on Reference [33].

4.1. Spin-Orbit Coupling

An electron with momentum $\mathbf{p}$ that moves perpendicular to an electric field $\mathbf{E}$ experiences a magnetic field $\mathbf{B} \propto \mathbf{E} \times \mathbf{p}/m_e$ in its rest frame. This momentum-dependent magnetic field couples to the spin of the electron via the Zeeman effect and introduces a spin-orbit coupling (SOC). In case of a free atom, for example, the electric field is generated by the atomic nucleus and the SOC gives rise to the Pauli term [84]

$$\hat{\mathcal{H}}_{PSO} = \frac{\mu_\mathrm{B}}{\hbar m_e c}(\mathbf{E} \times \mathbf{p})\mathbf{S}, \tag{4.1}$$

which represents the non-relativistic approximation to the Dirac equation. Here μ_B is the Bohr magneton and $\mathbf{S} = \hbar/2\boldsymbol{\sigma}$ the spin, with $\boldsymbol{\sigma} = (\sigma_x, \sigma_y, \sigma_z)$ being the Pauli spin matrices. For the free atom the spin degeneracy is lifted by the Pauli SOC [85].

In a crystal, on the other hand, spin degeneracy arises from the combination of inversion symmetry in both space and time [84, 85]: Kramers theorem [86], which is a consequence of time inversion symmetry, states that the energy of a state is degenerate with the energy of the state with opposite spin and wave vector, $E_+(\mathbf{k}) = E_-(-\mathbf{k})$. For a spatial inversion-symmetric system, $E(\mathbf{k}) = E(-\mathbf{k})$, Kramers theorem induces spin degeneracy for each wave vector $\mathbf{k}$ [1], which is lifted for inversion asymmetric (IA) fields.

The symmetry of the electric field in a crystal can be broken by bulk inversion asymmetry (BIA), by structure inversion asymmetry (SIA) or by the low symmetry of atoms at an interface [84]. BIA occurs in crystals that lack a center of inversion, like, for example, the zinc-blende structure, as pointed out by Dresselhaus [87]. The zinc-blende structure is, e.g., realized in III-V semiconductor compounds like InSb, GaAs and CdTe. The Dresselhaus spin-orbit splitting occurs for bands with symmetry Γ_6 and is cubic in the wave vector [88]. Rashba [15] and Rashba and Sheka [16, 17] showed in 1959 for the wurtzite structure, which features IA, that the (now known as Rashba-) spin splitting is linear in the wave vector k and isotropic near the Γ-point. [88] Examples for the wurtzite structure are III-V and II-VI semiconductors like GaN, CdS, and ZnO.

In quasi two-dimensional electron systems, which form, e.g., in semiconductor heterojunctions as AlAs-$Al_xGa_{1-x}As$, at interfaces of oxide heterostructures or at metallic surfaces, SIA occurs if the confining potential is asymmetric. Motivated by experimental observations of k-linear spin splitting in semiconductor heterojunctions [89], Vas'ko [90] and Bychkov and Rashba [91, 92] introduced a SOC interaction term to the Hamiltonian of the free electron gas of the form

$$\mathcal{H}_\mathrm{R} = \alpha_\mathrm{R}(\boldsymbol{\sigma} \times \mathbf{k})z. \tag{4.2}$$

[1] Kramers theorem is also valid for free atoms, where the electronic states with total angular momentum $\pm J$ are degenerate. As $J = L + S$, where L is the angular momentum and S the spin quantum number, states with the same $L > 0$ but different spin S are not degenerate.

The Rashba parameter α_R defines the strength of the Rashba interaction, the origin of which is the symmetry breaking electric field in **z**-direction, perpendicular to the plane of the two-dimensional electron gas. This model is analyzed in detail in the next section.

The Rashba parameter α_R is proportional to external applied fields [84]. The proportionality factor depends on properties of the valence and conduction bands and is complicated to evaluate. Thus—and because Eq. (4.2) is not exact as the plane-wave approximation fails in the vicinity of the nuclei [89]—α_R is often treated as a phenomenological parameter, which has to be extracted from experiments. The naive approach of directly identifying α_R by comparison of Eq. (4.1) and Eq. (4.2) fails for two closely related reasons: Firstly, the experimentally measured spin splitting induced by external electric fields is several orders of magnitude larger than expected from this simple estimation [84, 93]. Secondly, the theorem of Ehrenfest [94], which states that on average no force is acting on a nondegenerate bound state, induces that the expectation value of the electric fields acting in z-direction is exactly or nearly zero. The latter argument, proposed by Darr, Kotthaus and Ando [95], entailed an extensive discussion [96], which was resolved by Lassnig [97]: He demonstrated that the Rashba SOC (RSOC) for the conduction electrons arises from the electric field which acts on the valence band [84], the expectation value of which is non-zero for the conduction electrons. This is because the potential discontinuities at the confining interfaces are different for the conduction and valence band. Thus spin splitting in two-dimensional electron systems arises due to the combination of atomic SOC and the coupling of a symmetry breaking electric field (SBEF) in the valence band.

4.2. Density Dependent Rashba Spin-Orbit Coupling

The Hamiltonian of a two-dimensional free electron gas confined in the x-y-plane with RSOC due to a SBEF in z-direction, as given in Eq. (4.2), is

$$\hat{\mathcal{H}} = \frac{\hat{p}_x^2+\hat{p}_y^2}{2m_0}\sigma_0 + \frac{\alpha_\mathrm{R}}{-i\hbar}\left(\hat{p}_y\sigma_x - \hat{p}_x\sigma_y\right) = \begin{pmatrix} \dfrac{\hat{p}_x^2+\hat{p}_y^2}{2m_0} & \dfrac{\alpha_\mathrm{R}}{-i\hbar}(\hat{p}_y + i\hat{p}_x) \\ \dfrac{\alpha_\mathrm{R}}{-i\hbar}(\hat{p}_y - i\hat{p}_x) & \dfrac{\hat{p}_x^2+\hat{p}_y^2}{2m_0} \end{pmatrix}, \tag{4.3}$$

where m_0 is the effective mass of an electron. This Hamiltonian can be diagonalized analytically, which is a reason for the popularity of this model. The resulting dispersion and a set of new eigenfunctions are then given by (e.g., [98])

$$\varepsilon_\pm(\mathbf{k}) = \frac{\hbar^2k^2}{2m_0} \pm \alpha_\mathrm{R}k = \frac{k^2}{2\pi N_0} \pm \alpha_\mathrm{R}k = \frac{1}{2\pi N_0}\left(k \pm \pi N_0\alpha_\mathrm{R}\right)^2 - \frac{\pi N_0}{2}\alpha_\mathrm{R}^2 \tag{4.4}$$

$$\psi_+(\mathbf{r}) = e^{i\mathbf{kr}}\left(|\uparrow\rangle + ie^{i\Theta_\mathbf{k}}|\downarrow\rangle\right), \qquad \psi_-(\mathbf{r}) = e^{i\mathbf{kr}}\left(ie^{-i\Theta_\mathbf{k}}|\uparrow\rangle + |\downarrow\rangle\right),$$

$\Theta_\mathbf{k}$ is the angle of $\mathbf{k}$ with respect to the x-axis, $|\uparrow\rangle$, $|\downarrow\rangle$ correspond to spin-up and spin-down with respect to the z direction and $N_0 = m_0/\pi\hbar^2$ is the density of states in the absence of RSOC.

The Dresselhaus spin splitting under strain in z-direction has the same dispersion in leading order of k as described by Eq. (4.4), when α_R is replaced by a constant α_D, but different eigenfunctions [84, 89]. These determine the orientation of the spin for a given wave vector, which is depicted for RSOC in Fig. 4.1b and 4.1c by arrows. For the same wave vector $\mathbf{k}$, the spins of the lower and upper band point in opposite directions. If one moves on a circle around $k = 0$ in clockwise orientation in the lower band, the orientation of the spins also turns clockwise for RSOC.

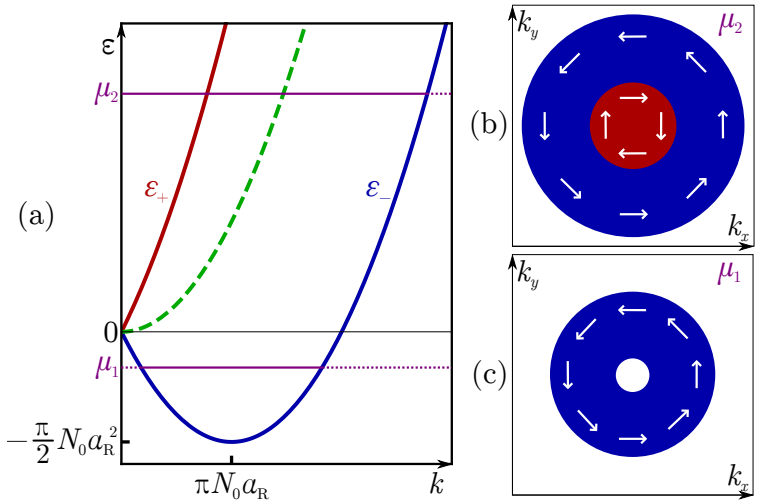

Figure 4.1.: (a) Dispersion of a two-dimensional electron system with RSOC (red and blue) and for the case $\alpha_R = 0$ (green, dashed). For $\mu_2 > 0$ two bands are (for $\mu_1 < 0$ one band is) populated. The corresponding occupation in k-space is illustrated in (b) and (c), respectively. The white arrows indicate the spin components of the states in the x-y plane of real space. Adapted from Ref. [33].

For $\alpha_R = 0$ the dispersion Eq. (4.4) reduces to the kinetic energy of free electrons, which is doubly degenerate for spin up and down. For finite α_R this degeneracy is lifted (c.f. Fig. 4.1a) by RSOC; the difference in energy between the lower and upper band is linear in the wave vector: $\varepsilon_+(k) - \varepsilon_-(k) = 2\alpha_R k$. Fig. 4.1b and 4.1c display the occupation in k-space for $\mu < 0$ and $\mu > 0$. In the former case only the lower band is occupied and the Fermi surface has the form of an annulus. As can be read directly from Eq. (4.4), the lower band has a circular minimum at $|\mathbf{k}| = \pi N_0 \alpha_R$ with a value of $\varepsilon_{\min} = -\pi N_0 \alpha_R^2/2$. The radius of the circle of minima increases with α_R, while the value of $\varepsilon_{\min}$ decreases quadratically with α_R. Since the Rashba parameter α_R is proportional to the SBEF, an increase of the electric field lowers the chemical potential.

This behavior of the dispersion enables a setup, where negative compressibility is possible: The two-dimensional electron system $S1$ with RSOC is coupled to a second electron system $S2$, so that the total system is charge neutral, i.e., the negative charge of the electrons is neutralized by an equal amount of (immovable) positive background charge. If electrons are transferred from $S2$ to the system with RSOC, then the now uncompensated positive background charge creates an additional symmetry breaking electric field in $S1$, which in turn increases α_R.[2] Then two effects compete regarding the chemical potential μ: the transferred electrons increase μ, while the increase of α_R has the opposite impact. If the latter mechanism dominates the first mechanism, $S1$ would feature negative compressibility *if $S1$ is considered as isolated.* But $S1$ is not isolated, as it has to be coupled to $S2$ to allow for electron transfer for the increase of the SBEF and α_R. In this case, as established in chapter 2.3, one has to consider the *total* system for the determination of the compressibility and hence stability of the system.

The mechanism of uncompensated positive charge increasing the SBEF and hence α_R, so that μ of $S1$ decreases with electron density, was suggested by Caprara, Grilli *et al.* [99, 100]. They proposed that negative compressibility and thus phase separation could be found at the $LaAlO_3/SrTiO_3$ interface because of this effect. But they did not include the system that generated the SBEF into their considerations, i.e., they considered the electron system with the RSOC as isolated. We would like to remark that in this case the SBEF is an external variable. When calculating the compressibility by taking the second derivative of the Helmholtz free energy with respect to the electron density of the system, all external variables are kept fixed. This implies that α_R has to be taken as density independent for the derivation of the stability of the system.

[2] Neither the spatial distribution of the positive charge outside of $S1$ nor of the electrons of $S2$ are affecting this argument. The only assumptions are (*i*) that there are positive and negative charges outside of $S1$ and that (*ii*) these are homogeneously distributed perpendicular to the z-direction at one side of the half space created by the two-dimensional $S1$.

Only through the coupling to a second system of electrons, the SBEF and thus α_{R} can be made to depend on the internal variable density and affect the sign of the compressibility. Thus the examination of the total system is essential for the exploitation of the mechanism described above. Due to the coupling the Helmholtz free energy of the total system is composed of the terms

$$F_{\mathrm{tot}}(n_1, n_{\mathrm{t}}) = F_1(n_1) + F_2(n_{\mathrm{t}} - n_1) + F_{\mathrm{es}}(n_1, n_{\mathrm{t}}) - eV_{\mathrm{ext}} n_1 \mathcal{V}. \tag{4.5}$$

Here the total electron density $n_{\mathrm{t}} = n_1 + n_2$ is the sum of the electron densities n_i of subsystem si, $i = 1, 2$, where the index $i = 1$ refers to the system with RSOC. F_i is the Helmholtz free energy of si, F_{es} the electrostatic energy, and the last term includes the potential differences between the two subsystems: the external voltage from the voltage source V_{s} and a possible offset in chemical potentials.

The last three terms of Eq. (4.5) depend on the physical system to be analyzed. Here we want to concentrate on polar heterostructures, of which the $LaAlO_3/SrTiO_3$ (LAO/STO) heterostructure is a prominent example. The electrons at the LAO/STO interface are exposed to a confining SBEF and the arising RSOC is in focus of experiment [8, 101, 102] and theory [93, 103].

The electrostatic energy can be treated in the framework of the general electrostatic layout introduced in Chapter 2.3 by Eq. (2.45). The physical situation of a polar heterostructure is depicted in Fig. 2.5e and the electrostatically equivalent layout in Fig. 2.5f (*asymmetric case*). The electronic system $s1$ at the interface constitutes the lower electrode of the setup which is connected with the topmost polar layer (AlO_2 in case of LAO/STO) by a voltage source. The topmost layer and a top gate form together the second electrode and thus $s2$. Between the two electrodes polar layers with fixed charge carrier density $\pm n_{\mathrm{t}}$ alternate at distances d_b from the bottom and d_a from the top (Fig. 2.5e). The total system is charge neutral and for $n_1 = 0$, i.e., before electronic reconstruction, no electric field is generated by the charges at the interface. As the electrodes become connected, electronic reconstruction takes place and electrons from $s2$ transfer to the interface; in LAO/STO they occupy the Ti_{3d} states [34, 35]. The electrons, which relocated to $s1$, leave uncompensated positive background charge behind that creates a SBEF at the interface. Only charge outside of $s1$ induces a SBEF, as the charge within the two-dimensional plane of $s1$ creates an electric field that is symmetric in z-direction. While in LAO the distances between the polar layers d_a^l and d_b^l are approximately of the same size, the exact relation connecting the dielectric constants ϵ_a and ϵ_b between the polar layers is unknown. To reduce the number of parameters, we assume for the most part that $d_a^l/\epsilon_a = d_b^l/\epsilon_b$, i.e., $\alpha = \beta = 1/2$ in the definition of the general electrostatic layout. Then Eq. (2.45) reduces to the energy of the symmetric polar heterostructure (SPH):

$$F_{\mathrm{es}}(n_1, n_{\mathrm{t}}) = D\left[n_1^2 + (n_{\mathrm{t}} - n_1)^2\right] \tag{4.6}$$

Here $D = \pi e^2 A d/\epsilon$, where d is the distance between the two electrodes, ϵ a layer-independent dielectric constant between $s1$ and $s2$ and A the area of the system in the x-y-plane. The effects of different electrostatic layouts are investigated in Subsection 4.3.2.

This section focuses on two-dimensional electron systems $s2$ at the top electrode; a closer examination of three-dimensional electrodes is given in Subsection 4.2.3. In experiments the topmost LaO_2 layer of the LAO/STO heterostructure is usually gated by a $YBa_2Cu_3O_7$ (YBCO) or Au electrode. These introduce three-dimensional electron systems for $s2$, but most of the difference of the capacitance to a two-dimensional electron system can be traced back to a finite screening length that increases the effective plate distance (c.f. Eq. (2.24)). Here we focus the considerations to a non-interacting free electron gas with Helmholtz free energy:

$$F_2(n_{\mathrm{t}} - n_1) = \frac{A}{2N_2}(n_{\mathrm{t}} - n_1)^2 \tag{4.7}$$

The density of states $N_2 = m_2/\pi\hbar^2$ is a parameter that controls the importance of the surface system for the total system, as for very large effective electron masses m_2 the term F_2 becomes small.

The density n_1 on the interface depends on the voltage V_s appearing in the last term $-eV_\mathrm{ext}n_1\mathcal{V}$ of Eq. (4.5). But neither the capacitance nor the compressibility of the system depend directly on this term, as its second partial derivatives with respect to n_1 and n_t vanish and the capacitance Eq. (2.31) and inverse compressibility Eq. (2.38) are proportional to these derivatives.

The dispersion Eq. (4.4) describing subsystem $s1$ leads to a free energy (c.f. App. A.5)

$$F_1^{\lessgtr}(n_1) = A \cdot \begin{cases} \dfrac{n_1^3}{6\pi N_1^3 \alpha_\mathrm{R}^2} - \dfrac{\pi}{2} N_1 \alpha_\mathrm{R}^2 n_1 & ,\mu_1 < 0 \\ \dfrac{n_1^2}{2N_1} - \pi N_1 \alpha_\mathrm{R}^2 n_1 + \dfrac{\pi^2}{6} N_1^3 \alpha_\mathrm{R}^4 & ,\mu_1 > 0 \end{cases} \tag{4.8}$$

The chemical potential of the isolated subsystem $s1$, denoted by μ_1, discriminates how many bands are occupied: According to dispersion Eq. (4.4), all states of the upper band are empty for $\mu_1 < 0$, while for $\mu_1 \geq 0$ electrons occupy both bands. At $\mu_1 = 0$ the density in the lower subband equals $n_1^0 = \pi N_1^2 \alpha_\mathrm{R}^2$.

As pointed out at the end of the previous section, the Rashba parameter α_R is proportional to the SBEF [84]. Two contributions constitute the SBEF at $s1$: An internal field $E_\mathrm{int} = E_0$, which exists at the interface even in the absence of external charges, like the fields that arise, e.g., from confining potentials or from dipolar distortions of neighboring layers, and an external field E_ext, which is generated by external charges outside of the interface. The latter can therefore, as the uncompensated positive background charges create E_ext, be expanded in the density n_1: $E_\mathrm{ext}(n_1) = E_1 \cdot n_1 + O(n_1^2)$.[3] The expansion of the Rashba parameter, for which $\alpha_\mathrm{R} \propto E_\mathrm{int} + E_\mathrm{ext}(n_1)$ holds, in the density n_1 at the interface yields

$$\alpha_\mathrm{R}(n_1) = \alpha_0 + \alpha_1 n_1 + O(n_1^2). \tag{4.9}$$

4.2.1. Comparison of Parameters to Experiment

This approximate relation can be used to fit the parameters α_0 and α_1 to experimental results. Caviglia *et al.* [8] performed magnetotransport measurements on the electron system at the LAO/STO interface, tuning the electron density by a gate. The diffusion constant obtained through experiment is related to α_R and the spin relaxation time τ_{so}, which characterizes the spin relaxation processes induced by the D'yakonov-Perel' mechanism and Elliot-Yafet mechanism [104]. After identifying the dominant mechanism, Caviglia *et al.* deduced a plot relating α_R to the gate voltage (Fig. 3c in Ref. [8]). For gate voltages that induce densities where the superconducting dome is present, they found $\alpha_\mathrm{R}^\mathrm{exp} \approx (1, \ldots, 5) \times 10^{-12}\, e\mathrm{Vm}$. In this range α_R increases approximately linearly with the gate voltage. An estimation of the density difference between the top and foot of the superconducting dome can be extracted from Ref. [105]: $\Delta n \approx 0.015 e^-/\mathrm{uc} = 9.9 \times 10^{12}/\mathrm{cm}^2$. This corresponds to

$$\alpha_1 \approx \frac{4 \cdot 10^{-12}\, e\mathrm{Vm}}{9.9 \cdot 10^{12}\, \mathrm{cm}^{-2}} \approx 4.0 \cdot 10^{-23}\, e\mathrm{V} \cdot \mathrm{cm}^3 \approx 270\, e\mathrm{V} a_\mathrm{B}^3 \tag{4.10}$$

The Rashba parameter α_R was found to be nearly constant for smaller electron densities, where the interface becomes depleted, with a value of $\alpha_0 \approx 10^{-10}\, e\mathrm{Vcm} \approx 1.9 \times 10^{-2}\, e\mathrm{V} a_\mathrm{B}$. As the densities of the measurement are rough estimates, the obtained values for α_0 and α_1 possess

[3] We assumed that no positive charge resides in the plane of $s1$. If this is not the case, a negative coefficient $E_{0,\mathrm{ext}}$ has to be added to the expansion.

a large uncertainty. Although these parameters may be smaller than evaluated, the deviation should be less than an order of magnitude.

"uc" above denotes the STO unit cell with a side length of $a \approx 3.901\,\text{Å} \approx 7.372\,a_\text{B}$ [106] (or $a \approx 3.87\,\text{Å}$ according to Ref. [107]). This induces a charge density of $n \approx 0.01840\,a_\text{B}^{-2} \approx 6.677 \times 10^{14}\,\text{cm}^{-2}$ for one electron per unit cell. A more refined model than employed in this section, uses the six d_{xy}, d_{xz} and d_{yz} bands to describe the electrons at the LAO/STO interface and is examined in the next section in more detail. Angle-resolved photoemission spectroscopy (ARPES) determined a light mass $m_l = 0.7\,m_e$ and a heavy mass $m_h = 15\,m_e$ for the electrons in these six bands [108]. The diagonalization of the six-band model shows that the electrons in the lowest band exhibit an effective mass of $m_1 = 0.7\,m_e$ in the vicinity of the band minimum [102], so that we use this value in this section for the effective two-band model.

For the estimation of the range of effective plate distances one has to take into account that the LAO/STO interface becomes only conducting with at least four layers of LAO [35] deposited on STO. LAO has a (pseudo-) cubic lattice parameter of $a \approx 3.791\,\text{Å} \approx 7.164\,a_\text{B}$ [106]. The dielectric constant of bulk LAO is in the range of $\epsilon_\text{LAO} \approx 24 - 25$ [109] from $T = 0K$ to room temperature (or $\epsilon_\text{LAO} \approx 24 - 25$ [110] for thin films). This implies that the magnitude of the minimal effective thickness $d/\varepsilon_\text{LAO} \approx 4 \times 7.164/25\,a_\text{B} \approx 1.15\,a_\text{B}$ between the two electrodes can become of the order of one Bohr radius.

4.2.2. Compressibility and Capacitance

In the beginning of this section we neglect the term arising from the external potential V_ext in Eq. (4.5) and use the expansion of α_R, as given in Eq. (4.9), up to linear order in the density n_1.

For densities n_1 larger than $n_1^0 = \pi N_1^2 \alpha_\text{R}^2$ both bands in the lower electrode are occupied, i.e., n_1^0 indicates the density the lower band can hold before electrons are allocated to states in the upper band. For $\alpha_\text{R} = \alpha_0 + \alpha_1 n_1$ this capacity increases quadratically with n_1, so that for very large n_1 only the lower band is populated. This is illustrated by Fig. 4.1a, as the radius of the circle of minima increases with α_R. Solving n_1^0 for n_1 gives two solutions,

$$n_\pm = \frac{1}{2\pi(N_1\alpha_1)^2}\left(1 - 2\pi N_1^2\alpha_0\alpha_1 \pm \sqrt{1 - 4\pi N_1^2\alpha_0\alpha_1}\right). \tag{4.11}$$

For $n_- \leq n_1 \leq n_+$ both bands are occupied, while else the upper band stays empty. Only if $1 > 4\pi N_1^2\alpha_0\alpha_1$ both solutions $n_\pm$ exist and only then the upper band can be populated at all. For the parameters extracted from experiment in the previous subsection, it is $4\pi N_1^2\alpha_0\alpha_1 \approx 0.017$, i.e., the two-band solution exists. If $\alpha_0 = 0$, then $n_- = 0$ and two bands are occupied for n_1 up to $n_1 \leq 1/\pi(N_1\alpha_1)^2 \equiv 1/\eta$ and for larger interface densities only one band is populated.

The Helmholtz free energy of the total system is the sum of the terms of Eq. (4.6), Eq. (4.7) and Eq. (4.8). This energy depends on the density n_1 and the total density n_t. As only the latter is a thermodynamic variable, the former adjusts in such a way that it minimizes the total Helmholtz free energy (c.f. Eq. (2.19)): $\partial_{n_1} F_\text{tot} = 0$. If the local minimum obtained by this relation lies outside of the interval of definition of $n_1 \in [0, n_\text{t}]$ or no minimizing solution exists, one of the boundary values $n_1 = 0$ or $n_1 = n_\text{t}$ minimizes F_tot. The resulting interface density is a function of the total density, $n_1 = n_1(n_\text{t})$. The problem can be solved analytically, but as the solution is quite complex (as, i.a., a distinction of cases regarding $n_1 \lessgtr n_\pm$ and $n_1 \in (0, n_\text{t})$ is necessary) and not illustrative, a numerical treatment is applied for the most part. On the other hand, for $\alpha_0 = 0$ the problem was solved analytically.

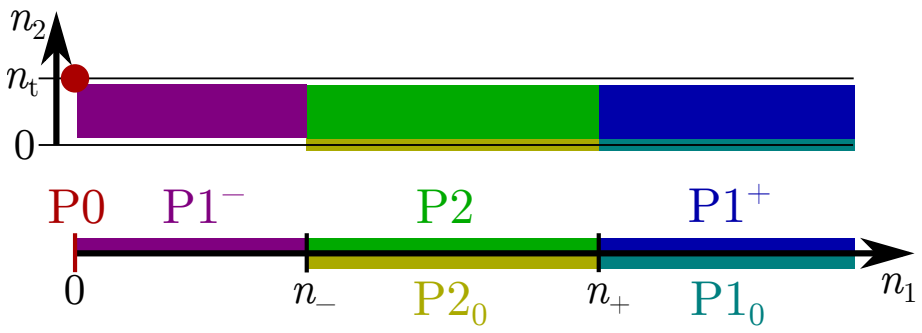

Figure 4.2.: Scheme of the phases: The number following the "P" denotes the number of occupied bands in the lower electrode $s1$ and a subindex 0 indicates that no electrons reside in the upper electrode $s2$. The possible densities in the surface electrode $s2$ are depicted in the upper part, while the lower part displays the possible densities in the interface system. The red dot in the upper part corresponds to P0, where all electrons reside in $s2$.

After identifying $n_1(n_t)$, the Helmholtz free energy depends directly and indirectly on the thermodynamic variable n_t and the inverse compressibility is given by the second total derivative (c.f. Eq. (2.34)):

$$\frac{1}{\kappa} = n_t^2 \frac{\mathrm{d}^2 F_{\mathrm{tot}}/A}{\mathrm{d}n_t^2} \tag{4.12}$$

The inverse differential capacitance, as derived in Eq. (2.31), is defined as second derivative of the free energy with respect to the density of one electrode

$$C_{\mathrm{diff}}^{-1} = \frac{1}{e^2 A^2} \frac{\partial^2 F_{\mathrm{tot}}}{\partial n_1^2} = \frac{1}{e^2 A^2} \left(\frac{\partial^2 F_1^{\lessgtr}}{\partial n_1^2} + \frac{A}{N_2} + 4D \right). \tag{4.13}$$

A premise for this relation is that n_1 takes no boundary value, as then the differential capacitance is not well defined or zero (see remark after Eq. (2.31) in Chapter 2.2). The contribution of the interface system can be easily calculated by taking the second derivative of $F_1^{\lessgtr}(n_1)$, which is given in Eq. (4.8). For $\alpha_0 = 0$ the result is of a particularly simple form,

$$\frac{\partial^2 F_1^{\lessgtr}}{\partial n_1^2} = \frac{A}{N_0} \cdot \begin{cases} -3\eta n_1 & , \mu < 0 \Leftrightarrow n_1 > \frac{1}{\eta} \\ 1 - 6\eta n_1 + 2\eta^2 n_1^2 & , \mu > 0 \Leftrightarrow n_1 < \frac{1}{\eta} \end{cases} \tag{4.14}$$

Here $\eta = \pi(N_1\alpha_1)^2$ defines the inverse of the density at which the transition between one ($\mu < 0$) and two occupied bands ($\mu > 0$) takes place. Note that the second derivative with respect to n_1 would be proportional to the compressibility, if one would (wrongly) consider the interface as isolated. The contribution to the differential capacitance for one occupied band is always negative: As the density n_1, which is proportional to the strength of the RSOC $\alpha_R = \alpha_1 n_1$, increases, the minimum of the lower band shifts to smaller values, so that the chemical potential drops. For two occupied bands ($\mu > 0$) the contribution from $F_1^{>}$ to C_{diff} is positive for $n_1 < (3 - \sqrt{7})/2\eta \approx 0.177/\eta$ and negative for larger n_1.

Six different solutions were found for the groundstate by searching for the minimizing interface density n_1: They are denoted in the format $\mathrm{P}i_j^{\pm}$ and are characterized by the number of occupied bands in the RSOC system (number $i = 0, 1, 2$), the occupation of the upper electrode (subindex $j = 0$ for empty $s2$) and the position of the minimizing n_1 relative to $n_\pm$ (c.f. Fig. 4.2 for a schematic plot):

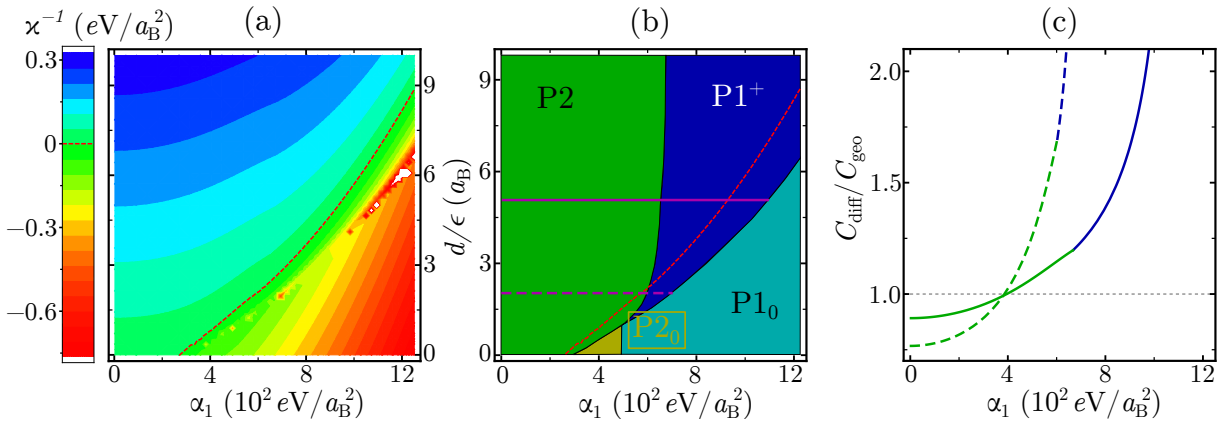

Figure 4.3.: Inverse compressibility (a) and phases (b) for $m_1 = 0.7m_e$, $m_2 = m_e$, $n_t = 1e^-/\text{uc} = 6.7 \times 10^{14}\,\text{cm}^{-2}$, $V_{ext} = 0$ and $\alpha_0 = 0$ as function of the effective plate distance d/ϵ and α_1, as defined in Eq. (4.9). The red dashed line indicates $\kappa^{-1} = 0$. The phases in (b) are P2 (green), P1$^+$ (blue), P1$_0$ (cyan) and P2$_0$ (yellow). The two purple lines in (b) correspond to the two values $d/\epsilon = 2\,a_B$ (dashed) and $d/\epsilon = 5\,a_B$ (continuous). The differential capacitance normalized to the geometric capacitance is plotted in (c) for the two purple lines. The colors in (c) correspond to the color of the phases in (b). Adapted from Ref. [33].

- $n_1 = 0$ (P0): All electrons reside in the surface system and the compressibility is independent of the interface:

$$\kappa_{P0}^{-1} = n_t^2 \left(\frac{1}{N_2} + \frac{2D}{A} \right) \tag{4.15}$$

- $0 < n_1 < n_-$ (P1$^-$): The existence of this phase requires $\alpha_0 \neq 0$, as else $n_- = 0$. The upper band of the interface electron system is empty and states at the surface electrode are occupied. The compressibility depends on the solution $n_1(n_t)$ found by minimizing the total energy:

$$\begin{aligned} \kappa_{P1^-}^{-1} = n_t^2 \frac{d^2}{dn_t^2} \Bigg[& \frac{n_1(n_t)^3}{6\pi N_1^3(\alpha_0 + \alpha_1 n_1(n_t))^2} - \frac{\pi}{2} N_1(\alpha_0 + \alpha_1 n_1(n_t))^2 n_1(n_t) \\ & + \frac{(n_t - n_1(n_t))^2}{2N_2} + \frac{D}{A}\left(n_1(n_t)^2 + (n_t - n_1(n_t))^2\right) \Bigg] \end{aligned} \tag{4.16}$$

The differential capacitance is

$$C_{\text{diff},P1^-}^{-1} = \frac{1}{e^2 A^2} \left[\frac{\alpha_0^2 n_1}{\pi N_1^3(\alpha_0 + \alpha_1 n_1(n_t))^4} - 2\pi\alpha_0\alpha_1 - 3\pi\alpha_1^2 n_1 + \frac{1}{N_2} + \frac{4D}{A} \right] \tag{4.17}$$

- $n_- < n_1 < \min(n_t, n_+)$ (P2): Here both bands of $s1$ are occupied and the inverse compressibility and differential capacitance are (dropping the formal dependence of n_1 on n_t in the notation):

$$\begin{aligned} \kappa_{P2}^{-1} = n_t^2 \frac{d^2}{dn_t^2} \Bigg[& \frac{n_1^2}{2N_1} - \pi N_1(\alpha_0 + \alpha_1 n_1)^2 n_1 + \frac{\pi^2}{6} N_1^3(\alpha_0 + \alpha_1 n_1)^4 \\ & + \frac{(n_t - n_1)^2}{2N_2} + \frac{D}{A}\left(n_1^2 + (n_t - n_1)^2\right) \Bigg] \end{aligned} \tag{4.18}$$

$$C_{\text{diff},P2}^{-1} = \frac{1}{e^2 A^2} \left[\frac{1}{N_1} - 2\pi N_1\alpha_1(2\alpha_0 + 3\alpha_1 n_1) + 2\pi^2 N_1^3\alpha_1^2(\alpha_0 + \alpha_1 n_1)^2 + \frac{1}{N_2} + \frac{4D}{A} \right]$$

- $n_1 = n_\mathrm{t} < n_+$ ($\mathrm{P2}_0$): The surface electrode is empty and both bands of the interface are occupied. The inverse compressibility simplifies for $n_1 = n_\mathrm{t}$ to

$$\kappa^{-1}_{\mathrm{P2}_0} = \frac{n_\mathrm{t}^2}{N_1}\left[1 - 2\pi N_1^2\alpha_1(2\alpha_0 + 3\alpha_1 n_\mathrm{t}) + 2\pi^2 N_1^4\alpha_1^2(\alpha_0 + \alpha_1 n_\mathrm{t})^2 + \frac{2DN_1}{A}\right]. \tag{4.19}$$

- $n_+ < n_1 < n_\mathrm{t}$ ($\mathrm{P1}^+$): As in $\mathrm{P1}^-$, the electrons in $s1$ populate only the lower band; accordingly the compressibility is given by Eq. (4.16) and the capacitance by Eq. (4.17).

- $n_+ < n_1 = n_\mathrm{t}$ ($\mathrm{P1}_0$): All electrons reside in the lower electrode and there only the lower band is occupied. The insertion of $n = n_\mathrm{t}$ implies

$$\kappa^{-1}_{\mathrm{P1}_0} = \frac{n_\mathrm{t}^2}{N_1}\left[\frac{\alpha_0^2 n_\mathrm{t}}{\pi N_1^2(\alpha_0 + \alpha_1 n_\mathrm{t})^4} - \pi N_1^2\alpha_1(2\alpha_0 + 3\alpha_1 n_\mathrm{t}) + \frac{2DN_1}{A}\right]. \tag{4.20}$$

The phase boundary between $\mathrm{P1}^+$ and $\mathrm{P1}_0$ for $\alpha_0 = 0$ can be expressed analytically by equalizing the respective free energies of the phases and solving for D,

$$\frac{D}{A} = \frac{(3\pi N_1^2\alpha_1^2 n_\mathrm{t})^2 - 1}{12\pi N_1^3\alpha_1^2 n_\mathrm{t}}. \tag{4.21}$$

App. A.5 demonstrates analytically that—using this relation—the compressibility of $\mathrm{P1}_0$ as given in Eq. (4.20), is always negative and the compressibility of $\mathrm{P2}_0$ of Eq. (4.18) is negative at the phase border to $\mathrm{P1}_0$. For these two phases all electrons reside in the lower electrode, which corresponds to a "phase separation between the layers". If the total system is not stabilized by non-electronic effects, phase separation in the interface electron system will occur, i.e., the described phases are instable. The phase boundary between $\mathrm{P1}_0$ and $\mathrm{P2}_0$ follows directly from $n_\mathrm{t} \lessgtr n_+ = 1/\pi(N_1\alpha_1)^2$ and is independent of d/ϵ: For large total densities $n_\mathrm{t} > n_+$ the radius of the circle of minima of the dispersion in the lower electrode is so large that the lower band houses all electrons.

The strength of the RSOC α_1 and the effective plate distance d/ϵ control the stability of the system (c.f. Fig. 4.3a) and its phase (c.f. Fig. 4.3b). Here $\alpha_0 = 0$ and the parameters of LAO/STO as described in the previous subsection were used in the plot. An increase of α_1 moves the occupation of the lower electrode from two bands to one band at higher α_1, as the capacity of the lower band increases with α_1. It depends on the effective plate distance d/ϵ if electrons populate the upper electrode: For large d/ϵ the electrostatic energy dominates and impedes the occupation of just one electrode. In Fig. 4.3a negative compressibility was found for sufficiently large α_1 and sufficiently small d/ϵ; the boundary of the $\kappa < 0$ region is indicated by the red dashed line. All phases except P0 exhibit negative compressibility in certain parameter regimes. Phase P2 was found to be unstable only for very small d/ϵ (less than $\approx 0.2\,a_\mathrm{B}$) and large $\alpha_1 \gtrsim 300\,e\mathrm{V}/a_\mathrm{B}^2$.

While—or because—α_1 drives the system unstable, it also increases the capacitance of the system (Fig. 4.3c). For α_1 large enough the differential capacitance exceeds the geometric capacitance $C_\mathrm{geo} = A\epsilon/4\pi d$, but for too large values of α_1, the compressibility becomes negative. At small α_1, the differential capacitance is smaller than the geometric capacitance as the DOS of the surface system and contributions from the interface are positive. In relation to C^{-1}_geo these effects become more important for small d/ϵ, which is why the dashed $d/\epsilon = 2\,a_\mathrm{B}$ curve has a smaller value than the solid $d/\epsilon = 5\,a_\mathrm{B}$ curve for small α_1. For large α_1 the sign of the contribution from the system with RSOC is negative and the same reason, i.e., that quantum effects are more important at small effective plate distances, causes the $d/\epsilon = 2\,a_\mathrm{B}$ relative capacitance to overtake the $d/\epsilon = 5\,a_\mathrm{B}$ relative capacitance.

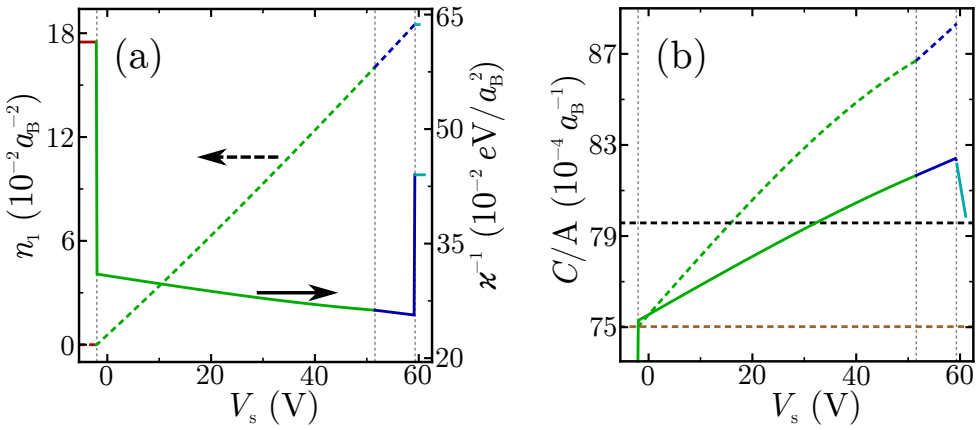

Figure 4.4.: The parameters $m_1 = 0.7\,m_e$, $m_2 = m_e$, $d/\epsilon = 10\,a_B$, $n_t = 1e^-/\text{uc}$, $\alpha_0 = 0$ and $\alpha_1 = 540\,eVa_B^3$ were used. (a) Density on the interface electron system as function of external voltage V_s (left scale, dashed curve). An offset in chemical potentials between the two electrodes induces the density $n_1 = 2 \times 10^{13}\,\text{cm}^{-2} = 5.6 \times 10^{-4}\,a_B^{-2}$ at $V_s = 0$. The inverse compressibility, found as analytical solution (right scale, solid curve), has discontinuities between different phases, which are indicated by the color code introduced in Fig. 4.2 and the dashed horizontal lines. With increase of V_s the system switches from P0 (left) over P2 and $P1^+$ to $P1_0$ (right). (b) Geometric capacitance per area (black, dashed), capacitance per area for a system without RSOC (brown, dashed), capacitance per area $e\Delta n_1/\Delta V_s$ (solid) and differential capacitance per area (dashed). Adapted from Ref. [33].

The density n_1 on the interface is controlled by, i.a., the fourth term of the Helmholtz free energy, Eq. (4.5), which depends on the external voltage V_{ext}. The "built-in" offset in chemical potentials between the electrodes determines the density n_1 in absence of a voltage V_s from a voltage source. A negative gate voltage can deplete the interface system (Fig. 4.4a) and induce phase P0, while a positive voltage increases n_1 up to n_t (dashed curve in the figure). Passing through increasing voltages V_s, the system undergoes phase transitions from P0 over P2 (note that $P1^-$ does not exist for the used value of $\alpha_0 = 0$) and $P1^+$ to $P1_0$. The latter two phases appear only for $n_t > 1/\pi(N_1\alpha_1)^2$, as only then the RSOC is strong enough to render the capacity of the lower band large enough to hold all electrons of the system. The compressibility of the system (solid curve in Fig. 4.4a) is positive for all occurring phases and exhibits two discontinuities at the transitions P0 $\rightarrow$ P2 and $P1^+ \rightarrow P1_0$. In phase P0 the compressibility κ_{P0} is independent of the parameters of the interface system, which is empty in this phase (c.f. Eq. (4.15)). On the other hand, in phase $P1_0$ all electrons reside on the interface, so that the compressibility does not depend on the surface system. Additionally, the electrostatic energy F_{es} induces a jump in the inverse compressibility: Its contribution is the same for $n_1 = 0$ and $n_1 = n_t$ and proportional to the total second derivative of F_{es} with respect to n_t,

$$\frac{d^2F_{es}(n_1 = 0)}{dn_t^2} = \frac{d^2F_{es}(n_1 = n_t)}{dn_t^2} = 2D \tag{4.22}$$

For a finite $0 < n_1 < n_t$ one has to take the dependence of $n_1(n_t)$ into account:

$$\frac{d^2F_{es}(n_1)}{dn_t^2} = \frac{\partial^2F_{es}}{\partial n_t^2} + 2\frac{\partial^2F_{es}}{\partial n_1 \partial n_t}\frac{\partial n_1}{\partial n_t} + \frac{\partial^2F_{es}}{\partial n_1^2}\left(\frac{\partial n_1}{\partial n_t}\right)^2 = D\left[1 + \left(1 - 2\frac{\partial n_1}{\partial n_t}\right)^2\right] \tag{4.23}$$

For $\partial n_1/\partial n_t \rightarrow 0$ or $\partial n_1/\partial n_t \rightarrow 1$ at $n_1 \rightarrow 0$ or $n_1 \rightarrow n_t$, respectively, the contribution from the electrostatic energy to the inverse compressibility would be continuous. But, according to

Eq. (2.35), which is valid if n_1 minimizes the total free energy, i.e., also in the case of $n_1 \to 0$ and $n_1 \to n_\mathrm{t}$, the derivative of n_1 with respect to n_t is given by

$$\frac{\partial n_1}{\partial n_t} = -\frac{\partial^2 F_\mathrm{t}}{\partial n_1 \partial n_\mathrm{t}} \Big/ \frac{\partial^2 F_\mathrm{t}}{\partial n_1^2}, \tag{4.24}$$

which is clearly not 0 or 1 at $n_1 \to 0$ and $n_1 \to n_\mathrm{t}$ in general, due to the electrostatic energy (and $F_1(n_1)$): While the contribution $F_2(n_\mathrm{t} - n_1)$ alone would lead to $\partial n_1/\partial n_\mathrm{t} = 1$, it is

$$\frac{\partial^2 F_\mathrm{es}}{\partial n_1^2} = 4D \neq -\frac{\partial^2 F_\mathrm{es}}{\partial n_1 \partial n_\mathrm{t}} = 2D. \tag{4.25}$$

This proves, irrespective of special cases where the contribution of $F_1(n_1)$ is zero or $-2D$, that at $n_1 \to 0$ and $n_1 \to n_\mathrm{t}$ the electrostatic contribution induces a jump in the compressibility.

The capacitance depends strongly on the density on the interface, which is tuned by the gate voltage (see Fig. 4.4b). The contribution from the interface electron system to the differential capacitance is given in Eq. (4.14): The second derivative is negative for $n_1 \gtrsim 0.177/\pi(N_1\alpha_1)^2 = 0.177/\eta$ and hence increases the capacitance. An increase of n_1 has a similar effect as increasing α_1 (see Fig. 4.3c), as both enhance the strength of the RSOC. For $n_1 \to 0$ the differential capacitance is equal to a system without RSOC ($\alpha_1 = 0$, brown dashed curve in Fig. 4.4b), $C_{\alpha=0} = 1/4D + A/e^2N_1 + A/e^2N_2$) and C_diff is smaller than the geometric capacitance, as the quantum contributions from both electrodes are positive. With increasing n_1, the contribution from the RSOC system becomes negative and then even overcompensates the contribution from $s2$. Beyond this point, $C_\mathrm{diff} > C_\mathrm{geo}$ is valid. The differential capacitance increases more steeply than the "finite capacitance" $C = e\Delta n_1/\Delta V_\mathrm{s}$, which is also defined for $n_1 = 0$ and $n_1 = n_\mathrm{t}$.

4.2.3. Capacitance of a System with Three-Dimensional Top Electrode

Up to now we considered the top electrode to be composed of a two-dimensional electron system. But in most experiments the top gate has a finite thickness, which has to be characterized as three dimensional. When the capacitance of such a setup, i.e., a two-dimensional interface coupled to a three-dimensional top gate, is analyzed, the real situation is complex:

The application of an external voltage V_s shifts the chemical potentials with respect to each other, which induces a charge transfer between the electrodes. This in turn creates an electric field in the space between the two electron systems, the electrostatic potential of which causes both electrodes to be on the same electrochemical potential. Due to screening, in the three-dimensional electrode the voltage induced charge will be confined to a small volume adjacent to the surface that is exposed to the electric field, so that the density in the bulk n_V^3D is unaltered. The charge density in this volume is arranged inhomogeneously and the distribution has to be determined self-consistently.

Here we take a simpler approach: We focus our examination of the three-dimensional electrode to the volume element $\mathcal{V} = A \cdot \lambda$, where λ is the screening length. The electron density n_2^3D differs in $\mathcal{V}$ from the bulk density n_V^3D due to charge transfer. In Thomas-Fermi theory of screening the effect of the underlying lattice and ionic cores can be incorporated by an effective dielectric constant ϵ_c, so that $\lambda = \sqrt{\epsilon_c} \cdot \lambda_\mathrm{TF}$ (see, e.g., Ref. [1]), with

$$\lambda_\mathrm{TF} = \frac{1}{\sqrt{4\pi e^2 \mathcal{N}_2/\epsilon_0}} = \frac{1}{2}\sqrt{\frac{m_e}{m_2}} \left(\frac{\pi}{3n_\mathrm{V}^\mathrm{3D} a_\mathrm{B}^3}\right)^{1/6} a_\mathrm{B}, \tag{4.26}$$

where $\mathcal{N}_2$ is the DOS at the Fermi energy of the bulk and ϵ_0 the vacuum permittivity. The number of electrons in the three-dimensional top electrode is much larger than in the interface system if the top layer is sufficiently thick. Thus we assume that the volume density n_V^3D of

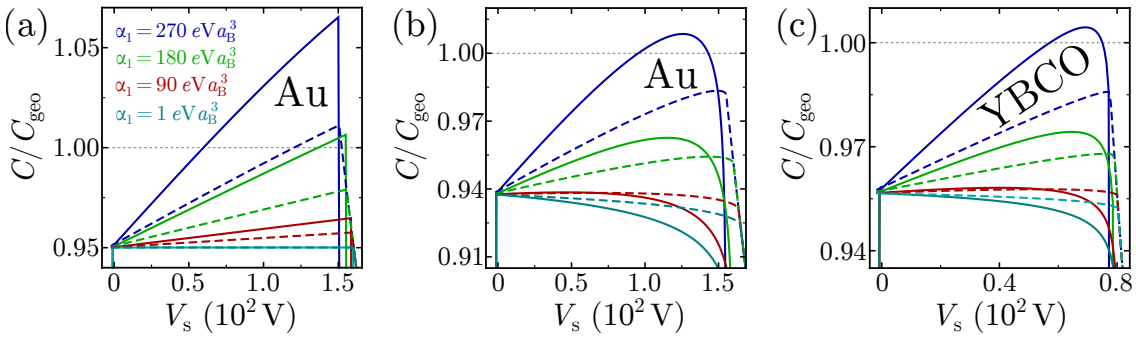

Figure 4.5.: Differential capacitances C_{diff} (solid) and capacitances $e\Delta n_1/\Delta_s$ (dashed) normalized to the geometric capacitance $C_{\text{geo}} = A\epsilon/4\pi d$ for three-dimensional electrodes on top of a LAO/STO heterostructure. In (a) and (b) the material of the top electrode is gold, while in (c) it is YBCO. The parameters of these materials are specified in the main text. The different colors refer to different strength of RSOC α_1, as labeled in (a). (b) and (c) describe the contribution from the top electrode as given in Eq. (4.28), while (a) uses an effective plate distance (Eq. (4.29)).

the bulk is effectively unaffected by the transfer of charge to the interface. This carries over to the screening length and thus the volume $\mathcal{V}$, as well. We further assume that the distribution of charge within this volume is spatially homogeneous on the ground that this does not alter the qualitative aspects of the problem. The three-dimensional density $n_2^{3\text{D}}$, which describes the electrons of the top electrode in the volume $\mathcal{V}$, can be projected on a two-dimensional density by $n_2 = \lambda \cdot n_2^{3\text{D}}$. For an unpolarized, free and non-interacting electron gas in the volume $\mathcal{V}$ the Helmholtz energy is, as introduced in Eq. (3.17),

$$F^{(3D)}\left(n_2^{3\text{D}}\right) = \frac{\hbar^2}{2m_2}\frac{3(3\pi^2)^{2/3}}{5}\mathcal{V}\left(n_2^{3\text{D}}\right)^{5/3} = \frac{\hbar^2}{2m_2}\frac{3(3\pi^2)^{2/3}}{5}A\lambda\left(\frac{n_2}{\lambda}\right)^{5/3} \tag{4.27}$$

The contribution to the inverse capacitance is obtained by taking the second derivative as defined in Eq. (2.31), either with respect to $n_2^{3\text{D}}$ or n_2, where care has to be applied regarding λ:

$$A/C_{\text{diff},2} = \left(\frac{\pi^4}{3}\right)^{1/3}\frac{a_{\text{B}}}{m_2/m_e}\frac{\left(n_2^{3\text{D}}\right)^{-1/3}}{\lambda} = \left(\frac{\pi^4}{3}\right)^{1/3}\frac{a_{\text{B}}}{m_2/m_e}\frac{(n_2)^{-1/3}}{\lambda^{2/3}} \tag{4.28}$$

Under the assumption that the density in $\mathcal{V}$ is approximately the bulk density $n_{\text{V}}^{3\text{D}}$, this result can be expressed in terms of the Thomas-Fermi screening length [12]:

$$A/C_{\text{diff},2}\left(n_{\text{V}}^{3\text{D}} \approx n_2^{3\text{D}}\right) = \frac{4\pi\lambda_{\text{TF}}}{\sqrt{\epsilon_c}} \tag{4.29}$$

This expression is independent of the charge, as λ_{TF} is a function of the constant bulk density $n_{\text{V}}^{3\text{D}}$. Consequently, this contribution can be treated as a correction to the term arising from the electrostatic energy, which is proportional to the effective plate distance and also density independent, i.e., this treatment of the three-dimensional electrode has the same effect as an increased effective plate distance of $d/\epsilon + \lambda/\epsilon_c$.

This has to be contrasted to Eq. (4.28), where the density dependence is taken into account. The differences between these two approaches are clearly visible by comparing Fig. 4.5a (contribution to differential capacitance $\propto \lambda$) with Fig. 4.5b. Both plots depict the differential capacitance normalized to the geometric capacitance $C_{\text{geo}} = A\epsilon/4\pi d$ for a three-dimensional gold electrode on top. Gold has a bulk density of $n_{\text{V}}^{3\text{D,Au}} = 59.0\times10^{21}\,\text{cm}^{-3} = 8.74\times10^{-3}\,a_{\text{B}}^{-3}$ [24, 111] and its conduction electrons have an effective mass of $1.1m_e$ [24]. With $\epsilon_c^{\text{Au}} = 6.9$ [112], this leads

to screening lengths of $\lambda_{\mathrm{TF}}^{\mathrm{Au}} = 1.06\,a_{\mathrm{B}}$ and $\lambda^{\mathrm{Au}} = 2.8\,a_{\mathrm{B}}$, respectively. This is approximately one order of magnitude smaller than the used effective plate distance of $d/\epsilon = 10\,a_{\mathrm{B}}$.

For a constant contribution from the top electrode to the capacitance (c.f. Fig. 4.5a), with $A/C_{\mathrm{diff},2} = 4\pi\lambda^{\mathrm{Au}}/\epsilon_c^{\mathrm{Au}}$, the only density dependence arises from the interface system with RSOC. As described in the previous subsection, the contribution of $s1$ is positive for small n_1 and negative for n_1 large enough, which induces the increase of the capacitance with external voltage V_{s}. We chose an offset in chemical potentials that ensures $n_1 = 2 \times 10^{13}\,\mathrm{cm}^{-2} = 5.6 \times 10^{-4}\,a_{\mathrm{B}}^{-2}$ at $V_{\mathrm{s}} = 0$. n_1 increases with V_{s} up to the total density $n_{\mathrm{t}} + \lambda n_{\mathrm{V}}^{\mathrm{3D,Au}}$, where $n_{\mathrm{t}} = 0.0184\,a_{\mathrm{B}}^{-2}$ denotes the charge carrier density originating from the topmost AlO_2 layer of LAO, which is reached at $V_{\mathrm{s}} \approx 60\,V$. Above this voltage the electron density on the gold electrode is smaller than the bulk density. The differential capacitance is smaller than the geometric capacitance, as for small n_1 the former is dominated by the positive geometric length d/ϵ and the length $\lambda^{\mathrm{Au}}/\epsilon_c^{\mathrm{Au}}$ arising from the top electrode contribution. The latter effective length, which amounts to around $0.4\,a_{\mathrm{B}}$, is about one order of magnitude smaller than the chosen d/ϵ, but, as established in Subsection 4.2.1, in the LAO/STO heterostructure the effective plate distance can be as small as $\approx 1.15\,a_{\mathrm{B}}$.

On the other hand, if Eq. (4.28) is employed to calculate C_{diff}, it displays a qualitative different behavior (c.f. Fig. 4.5b): The differential capacitance decreases for large V_{s} down to zero. This is easy to understand on the basis of Eq. (4.28): as $A/C_{\mathrm{diff},2} \propto 1/n_2^{1/3}$, this positive contribution diverges for $n_2 \to 0$, which is equivalent to $n_1 \to n_{\mathrm{t}} + \lambda n_{\mathrm{V}}^{\mathrm{3D,Au}}$. This behavior is a consequence of the neglect of the inhomogeneity of the charge distribution in the model. In a real three-dimensional electrode a depletion of charge carriers from the volume neighboring the surface would shift the surface towards the bulk and thus increase the effective plate distance. This decreases the differential capacitance, but the divergence in $A/C_{\mathrm{diff},2}$ present in our model does not appear. The latter limits the increase in capacitance compared to the case of Fig. 4.5a: The interface contribution becomes more negative for large n_1 and this is the same regime in which the positive divergence of the surface electrode contribution gains influence.

Figure 4.5c displays the differential capacitance for YBCO: We used a screening length $\lambda^{\mathrm{YBCO}} = 10\,a_{\mathrm{B}}$, which is close to the experimental values of $\propto 4.7\,\text{Å}$ [113, 114], an effective mass of $m_2 = 2\,m_e$ [115] and a volume density $n_{\mathrm{V}}^{\mathrm{3D,YBCO}} = 3 \times 10^{21}\,\mathrm{cm}^{-2} = 4.4 \times 10^{-4}\,a_{\mathrm{B}}^{-2}$ [116]. Although the screening length is considerably larger than in the case of gold, the differential capacitance at $V_{\mathrm{s}} = 0$ of YBCO is slightly larger, due to the large dielectric constant $\epsilon_c^{\mathrm{YBCO}} \approx 25$ [117] of YBCO.

4.3. Six-Band Model of a Layer with Spin-Orbit Coupling

4.3.1. Introduction to the Model

In the previous section the comparably simple Rashba Hamiltonian Eq. (4.3), which describes a free electron gas with k-linear RSOC, was used to characterize the effects of SOC on the capacitance and compressibility in a first approach. The results were related to electrons in the LAO/STO interface layer by employing corresponding parameters. A more adapted approach to examine the electron system at the LAO/STO interface utilizes a six-band model, as the electrons reside in the Ti_{3d} orbitals of $SrTiO_3$. The latter has a perovskite structure, where the Ti atom is surrounded by six oxygen atoms in an octahedral configuration. The degeneracy of the d-orbitals is partially lifted by the metal-oxygen bonding, so that the two e_g orbitals possess higher energy than the three t_{2g} orbitals [118], which is known as crystal field splitting, and only the latter need to be considered. A Rashba-like SOC arises then due to the combination of atomic SOC and the effects of the symmetry breaking electric field (SBEF). Note that the perovskite

structure with the conduction electrons in t_{2g} orbitals differs significantly from conventional semiconductors, where Rashba and Dresselhaus SOC were first described [118].

The Hamiltonian of the interface electron system consists of three terms [93, 102, 118]:

$$\mathcal{H} = \mathcal{H}_\mathrm{k} + \mathcal{H}_\mathrm{SO} + \mathcal{H}_\mathrm{z}. \tag{4.30}$$

The first term corresponds to intraorbital hopping and has the form,

$$\mathcal{H}_\mathrm{k} = \begin{pmatrix} \frac{k_x^2}{2\pi N_h} + \frac{k_y^2}{2\pi N_l} & 0 & 0 \\ 0 & \frac{k_x^2}{2\pi N_l} + \frac{k_y^2}{2\pi N_h} & 0 \\ 0 & 0 & \frac{k_x^2 + k_y^2}{2\pi N_\mathrm{l}} - \Delta_\mathrm{E} \end{pmatrix} \otimes \sigma_0, \tag{4.31}$$

in the d_{yz}, d_{zx}, d_{xy} basis. The DOS $N_i = m_i/\pi\hbar^2$ depends on the mass of light (m_l) or heavy (m_h) electrons. As the bonding network of the t_{2g} orbitals is decoupled, the hopping takes places over the p orbitals of neighboring oxygen atoms. For example, an electron in a d_{xy} orbital is only allowed to hop along the y or x direction through an intermediate p_x or p_y oxygen orbital to a d_{xy} orbital on a neighboring site [118]. The energy of the d_{xy} orbitals is lowered by Δ_E with respect to the other two orbitals due to the confinement of the electron system in z direction. As $\mathcal{H}_\mathrm{k}$ is degenerate in spin, it is multiplied by the 2×2 identity matrix σ_0.

The Hamiltonian arising from the atomic-like SOC $\mathcal{H}_\mathrm{SO}$ is given by

$$\mathcal{H}_\mathrm{SO} = \Delta_\mathrm{SO} \cdot \sum_{i=x,y,z} L_i \otimes \sigma_i, \tag{4.32}$$

where σ_i are the 2×2 Pauli-matrices. The representation of the angular momentum operator $\mathbf{L}$ in the basis of the t_{2g} orbitals is derived in App. A.6,

$$\mathbf{L} = \left(\begin{pmatrix} 0 & 0 & 0 \\ 0 & 0 & i \\ 0 & -i & 0 \end{pmatrix}, \begin{pmatrix} 0 & 0 & -i \\ 0 & 0 & 0 \\ i & 0 & 0 \end{pmatrix}, \begin{pmatrix} 0 & i & 0 \\ -i & 0 & 0 \\ 0 & 0 & 0 \end{pmatrix} \right) \tag{4.33}$$

Δ_SO is the strength of the atomic SOC and proportional to the effective nuclear charge Z, which is $Z \approx 8.1$ for the d orbitals in neutral Ti atoms [103].

The last contribution to the Hamiltonian, $\mathcal{H}_\mathrm{z}$ arises due to the absence of inversion symmetry. The electric field that is responsible for the asymmetry has two effects: it polarizes the atomic orbitals and creates a polar lattice displacement between the Ti cations and oxygen anions [118]. Without SBEF the hopping from the Ti d_{xz} orbital to the oxygen p_x orbital along the y direction and from d_{yz} to p_y along the x direction does not occur due to parity of the involved orbitals. The orbital polarization and the change of the Ti-oxygen bonding angle due to lattice distortion render those previously absent hopping processes possible, so that [93, 118]

$$\mathcal{H}_\mathrm{z} = \Delta_z \begin{pmatrix} 0 & 0 & -ik_x \\ 0 & 0 & -ik_y \\ ik_x & ik_y & 0 \end{pmatrix} \otimes \sigma_0. \tag{4.34}$$

Hopping from d_{xy} to d_{xz} appears only in the y direction and from d_{xy} to d_{yz} only in the x direction. For the other directions the hopping matrix element is zero, as it is an integral of an odd function in x (or y) [103]. Khalsa, Lee and McDonald [118] compared the spin splitting induced by orbital polarization with the spin splitting induced by lattice polarization and found the latter more than one order of magnitude larger in a perovskite structure. They concluded

that the Rashba-like SOC is stronger in materials that are more easily polarized, like $SrTiO_3$, which possesses a large dielectric constant due to this reason. The parameter Δ_z is characterized by the magnitude of the broken symmetry and depends on the SBEF, which is a function of the charge density n_1 on the interface: A transfer of electrons from the surface to the interface generates uncompensated positive charges, which in turn induce an electric field at the interface. Hence Δ_z can be expanded in n_1 and is given in linear approximation by

$$\Delta_z = \Delta_{z,0} + \Delta_{z,1} n_1, \tag{4.35}$$

where $\Delta_{z,0}$ is generated by, e.g., dipolar distortions in the LAO layer next to the interface.

The Hamiltonian (4.30) in the d_{yz}, d_{zx}, d_{xy} basis is a 6×6 matrix:

$$\mathcal{H} = \begin{pmatrix} \frac{k_x^2}{2\pi N_h} + \frac{k_y^2}{2\pi N_l} & 0 & i\Delta_{\mathrm{SO}} & 0 & -i\Delta_z k_x & -\Delta_{\mathrm{SO}} \\ 0 & \frac{k_x^2}{2\pi N_h} + \frac{k_y^2}{2\pi N_l} & 0 & -i\Delta_{\mathrm{SO}} & \Delta_{\mathrm{SO}} & -i\Delta_z k_x \\ -i\Delta_{\mathrm{SO}} & 0 & \frac{k_x^2}{2\pi N_l} + \frac{k_y^2}{2\pi N_h} & 0 & -i\Delta_z k_y & i\Delta_{\mathrm{SO}} \\ 0 & i\Delta_{\mathrm{SO}} & 0 & \frac{k_x^2}{2\pi N_l} + \frac{k_y^2}{2\pi N_h} & i\Delta_{\mathrm{SO}} & -i\Delta_z k_y \\ i\Delta_z k_x & \Delta_{\mathrm{SO}} & i\Delta_z k_y & -i\Delta_{\mathrm{SO}} & \frac{k_x^2+k_y^2}{2\pi N_l} - \Delta_{\mathrm{E}} & 0 \\ -\Delta_{\mathrm{SO}} & i\Delta_z k_x & -i\Delta_{\mathrm{SO}} & i\Delta_z k_y & 0 & \frac{k_x^2+k_y^2}{2\pi N_l} - \Delta_{\mathrm{E}} \end{pmatrix}$$

The transformation to a new basis diagonalizes this Hamiltonian and yields three spin-split doublets. The eigenenergies are known only for two special cases analytically: At $\mathbf{k} = 0$ the contribution from $\mathcal{H}_z$ vanishes and the doubly degenerate energies are

$$\varepsilon_1(k_x = 0, k_y = 0) = \frac{1}{2}\left(\Delta_{\mathrm{SO}} - \Delta_{\mathrm{E}} - \sqrt{9\Delta_{\mathrm{SO}}^2 + 2\Delta_{\mathrm{E}}\Delta_{\mathrm{SO}} + \Delta_{\mathrm{E}}^2}\right), \tag{4.36a}$$

$$\varepsilon_2(k_x = 0, k_y = 0) = -\Delta_{\mathrm{SO}}, \tag{4.36b}$$

$$\varepsilon_3(k_x = 0, k_y = 0) = \frac{1}{2}\left(\Delta_{\mathrm{SO}} - \Delta_{\mathrm{E}} + \sqrt{9\Delta_{\mathrm{SO}}^2 + 2\Delta_{\mathrm{E}}\Delta_{\mathrm{SO}} + \Delta_{\mathrm{E}}^2}\right) \tag{4.36c}$$

and for a symmetric interface system, i.e., $\Delta_z = 0$, and isotropic dispersion, i.e., $N_h = N_l$, three doubly generated solutions are found:

$$\varepsilon_1(k_x, k_y) = \frac{k_x^2 + k_y^2}{2\pi N_h} + \left(\Delta_{\mathrm{SO}} - \Delta_{\mathrm{E}} - \sqrt{9\Delta_{\mathrm{SO}}^2 + 2\Delta_{\mathrm{E}}\Delta_{\mathrm{SO}} + \Delta_{\mathrm{E}}^2}\right), \tag{4.37a}$$

$$\varepsilon_2(k_x, k_y) = \frac{k_x^2 + k_y^2}{2\pi N_h} - \Delta_{\mathrm{SO}}, \tag{4.37b}$$

$$\varepsilon_3(k_x, k_y) = \frac{k_x^2 + k_y^2}{2\pi N_h} + \left(\Delta_{\mathrm{SO}} - \Delta_{\mathrm{E}} + \sqrt{9\Delta_{\mathrm{SO}}^2 + 2\Delta_{\mathrm{E}}\Delta_{\mathrm{SO}} + \Delta_{\mathrm{E}}^2}\right) \tag{4.37c}$$

If one starts with $\mathcal{H}_{\mathrm{kin}}$ and adds $\mathcal{H}_{\mathrm{SO}}$ and $\mathcal{H}_{\mathrm{z}}$ successively, the band structure evolves as follows: First, for only $\mathcal{H}_{\mathrm{kin}}$ there exists a crossing point of the lowest doubly generated band with one of the other two doublets in each direction (k_x, k_y), where the direction determines the band. Adding $\mathcal{H}_{\mathrm{SO}}$ avoids these crossings [93, 103], but the three bands are still doubly degenerate. Only the asymmetry induced term $\mathcal{H}_{\mathrm{z}}$ lifts the spin degeneracy and induces a splitting between the doublets.

This splitting and the whole band structure depend on Δ_z, which in turn is a function of the density n_1 at the interface, as determined by Eq. (4.35). The band structure for two different densities is depicted in Fig. 4.6a and 4.6b. Here the light and heavy electron masses $m_l = 0.7\,m_e$ and $m_h = 15\,m_e$ were used, extracted from ARPES measurements of $SrTiO_3$ surfaces

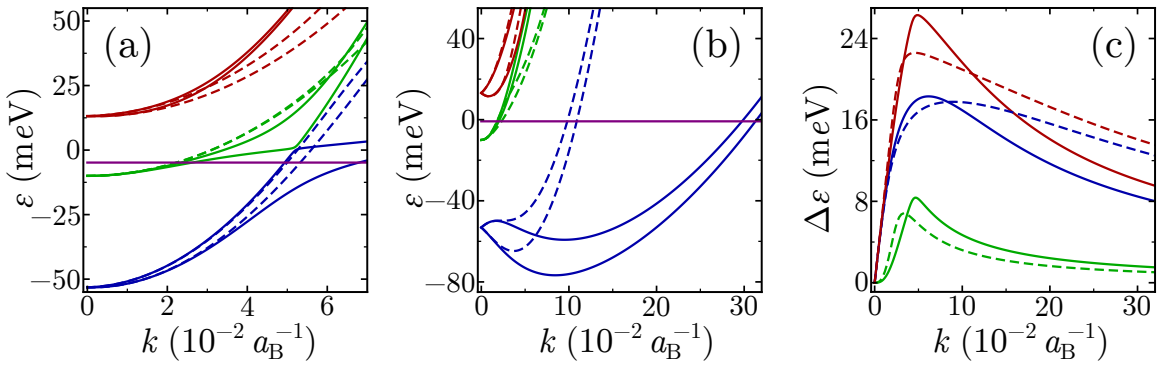

Figure 4.6.: Band structure ((a) and (b)) for $n_1 = 2\times10^{13}\,\mathrm{cm}^{-1} = 5.6\times10^{-4}\,a_\mathrm{B}^{-2}$ and $n_1 = 5.6\times10^{-3}\,a_\mathrm{B}^{-2}$, respectively. The parameters are $m_l = 0.7\,m_e$, $m_h = 15\,m_e$, $\Delta_\mathrm{SO} = 10\,\mathrm{meV}$, $\Delta_\mathrm{E} = 50\,\mathrm{meV}$, $\Delta_{z,0} = 1.66\times10^{-2}\,e\mathrm{V}a_\mathrm{B}$ and $\Delta_{z,1} = 225\,e\mathrm{V}a_\mathrm{B}^3$. The continuous curves correspond to a path from the Γ point to the X point and the dashed curves from the Γ point to the M point. The purple curve indicates the highest occupied energy level for the densities $n_1 = 5.6\times10^{-4}\,a_\mathrm{B}^{-2}$ (a) and $n_1 = 5.6\times10^{-3}\,a_\mathrm{B}^{-2}$ (b). Plot (c) displays the energy splitting of the bands pictured in (b), where the color corresponds to the according doublets. Adapted from Ref. [33].

in Ref. [108]. X-ray measurements [119] identified the crystal field splitting $\Delta_\mathrm{E} = 50\,\mathrm{meV}$, while the results of *ab initio* calculations [93] suggest $\Delta_\mathrm{E} = 250\,\mathrm{meV}$. We mostly focus on the first finding, but also consider the latter for the calculation of the capacitance in Fig. 4.7b. The value $\Delta_\mathrm{SO} = 10\,\mathrm{meV}$ was used here, as transport experiments [8, 101, 102] and *ab initio* calculations [120] indicate that the atomic SOC lies in the range $\Delta_\mathrm{SO} = 10 - 25\,\mathrm{meV}$.

The interorbital hopping coefficients $\Delta_{z,0}$ and $\Delta_{z,1}$ were determined by comparison to the experimental results of Caviglia *et al.* [8]. In Subsection 4.2.1 we identified the coefficients $\alpha_0 \approx 1.9\times10^2\,e\mathrm{V}a_\mathrm{B}$ and $\alpha_1 \approx 270\,e\mathrm{V}a_\mathrm{B}^3$ from the experiment of Ref. [8], with the RSOC parameter $\alpha_\mathrm{R} \approx \alpha_0 + \alpha_1 n_1$. The spin splitting $\Delta\varepsilon$ in the two-band model with RSOC, which was examined in the previous section, is linear in the wave vector, $\Delta\varepsilon = 2\alpha_\mathrm{R}k$. In the six-band model, the spin splitting of the lowest (and highest) doublet, induced by Δ_z, displays likewise a splitting linear in k for small wave vectors (c.f. Fig.4.6c). This identifies the proportionality factor $\alpha(\Delta_z)$ in $\Delta\varepsilon = 2\alpha(\Delta_z)k$ by extraction of the slope of $\Delta\varepsilon$ in k for a number of Δ_z. With

$$\alpha(n_1) = \alpha(\Delta_z(n_1)) = b(\Delta_{z,0} + \Delta_{z,1}n_1), \tag{4.38}$$

a comparison to the coefficients of α_R yields $b\Delta_{z,0} \equiv \alpha_0$ and $b\Delta_{z,1} \equiv \alpha_1$. Then, with $b \approx 3.3$ for $\Delta_\mathrm{E} = 50\,\mathrm{meV}$ and $\Delta_\mathrm{SO} = 10\mathrm{meV}$, it follows that $\Delta_{z,0} \approx 66\,\mathrm{meV}a_\mathrm{B}$ and $\Delta_{z,1} \approx 892\,e\mathrm{V}a_\mathrm{B}^3$. This fit for $\Delta_{z,0}$ and $\Delta_{z,1}$ is only a rough approximation to determine their orders of magnitude. In its derivation it was assumed that the spin splitting is isotropic, which is only true for very small wave vectors. Also, for larger k the spin splitting displays a non-linear behavior, which is not observed in the density range studied in Ref. [8].

For small k, the spin splitting as function of the wave vector (Fig. 4.6c) increases linearly for the lowest and highest doublets and cubic for the middle doublet. The spin splitting is maximal at the avoided crossings, due to the reduced gap between the doublets at this point [103], and decreases monotonically for larger k.

The density dependence of Δ_z has strong implications on the band structure: For small $n_1 = 2\times10^{13}\,\mathrm{cm}^{-1} = 5.6\times10^{-4}\,a_\mathrm{B}^{-2}$ and consequently small Δ_z (Fig. 4.6a) the avoided crossing point between the lowest band, which has always d_{xy}-like character for k small enough [102], and the middle band is clearly visible in the plot. If the density is increased to $n_1 = 5.6\times10^{-3}\,a_\mathrm{B}^{-2}$ (Fig. 4.6b), the avoided crossing is not recognizable anymore and the energy of the lowest doublet decreases, forming a minimum at finite k. The latter implicates only a small increase in chemical

potential and that almost all additional electrons of the density increase go into the lower band. On these grounds the influence of the lowest doublet on the capacitance and compressibility of the system dominates over the contributions from the other bands: For small densities n_1 the upper bands are empty. When the upper bands are occupied, the DOS of the lowest doublet is considerably larger than the DOS of the upper bands at the Fermi energy. A variation of n_1 by an external voltage V_s or change in n_t will then transfer most of the electrons into the lowest band—the available area in k-space at the Fermi energy is also clearly larger for the lowest doublet, due to the larger radius of k_F. The minimum in the lowest doublets, which emerges for large Δ_z, gives rise to the same phenomenom as in the case of strictly k-linear RSOC: As this minimum moves to lower energies and larger wave vectors with an increase of Δ_z, this may give rise to a decrease of chemical potential in the interface system with increased n_1. Furthermore, for Δ_z large enough, the states around $k = 0$ are unoccupied, i.e., there is a "hole" in the plane of occupied states in wave-vector space. In this regime the considerations made to extract a numerical value for $\Delta_{z,0}$ and $\Delta_{z,1}$ from experiment become invalid.

4.3.2. Capacitance and Compressibility for Different Electrostatic Layouts

We now consider the total Helmholtz free energy, consisting of the contributions of the interface system, the surface system, which here is taken to be a two-dimensional free electron gas, the electrostatic energy and a potential term. The latter terms are defined in Eq. (4.7), Eq. (4.6) and Eq. (4.5). First we investigate the symmetric polar heterostructure (SPH) (c.f. Fig. 2.5b), where the positive charge density $+en_\mathrm{t}$ is concentrated in the plane in the middle between the two electrodes, which have an effective distance of d/ϵ. This effective model is equivalent to a polar heterostructure with equal distance between its polar layers.

The density on the interface system can be tuned by a voltage source V_s (Fig. 4.7a, left scale), where we assume that an offset in chemical potentials $\mu_\mathrm{offset} \equiv \mu_\mathrm{off}$ fixes the interface density to $n_1 = 2 \times 10^{13}\,\mathrm{cm}^{-2} = 5.6 \times 10^{-4}\,a_\mathrm{B}^{-2}$ at $V_\mathrm{s} = 0$. The number of occupied bands in $s1$ increases with n_1 from two to five, but then decreases back down to two. An increase of the interface density also increases Δ_z, so that the lowest band becomes flatter and its minimum shifts to larger k, which increases the overall "capacity" of the lower doublet to accept electrons. Meanwhile, the compressibility of the total system is positive for all applied voltages (Fig. 4.7a, right scale) and displays two discontinuities at the transitions $n_1 = 0$, where the compressibility is independent of the interface system and $n_1 = n_\mathrm{t}$, where the compressibility is independent of the surface system. Another contribution to this discontinuity stems from the electrostatic energy. The differential capacitance per area C_diff/A is depicted in Fig. 4.7b for different sets of Δ_E and Δ_z. The band structure of $s1$ does not depend on the density for $\Delta_{z,1} = 0$ (cyan curve). In this case C_diff/A increases until the Fermi energy is at a value where the band structure is almost parabolic, i.e., has a constant second derivative with respect to the density. Due to the positive contributions from the kinetic energies of the surface and interface this capacitance is smaller than the geometric capacitance (black curve). For finite $\Delta_{z,1}$ the contribution from $s1$ to the inverse capacitance can become negative on account of the mechanism of shifting the minimum of the lower doublet, which was explained above. This renders an enhancement of the differential capacitance beyond the geometric capacitance possible; the larger $\Delta_{z,1}$, the larger C_diff/A is. For the blue curve the differential capacitance exceeds the geometric capacitance for a density at which the wave vectors around $k = 0$ of the lowest doublet are unoccupied (dashed part of blue curve).

While the density dependence of the band structure mediated by Δ_z may lead to an enhanced capacitance, this also carries the inherent potential of destabilizing the total system. The influence of the magnitude of the electrostatic term on the inverse compressibility by means of the effective plate distance d/ϵ is analyzed in Fig. 4.8 for a range of $\Delta_{z,1}$. Two offsets in chemical

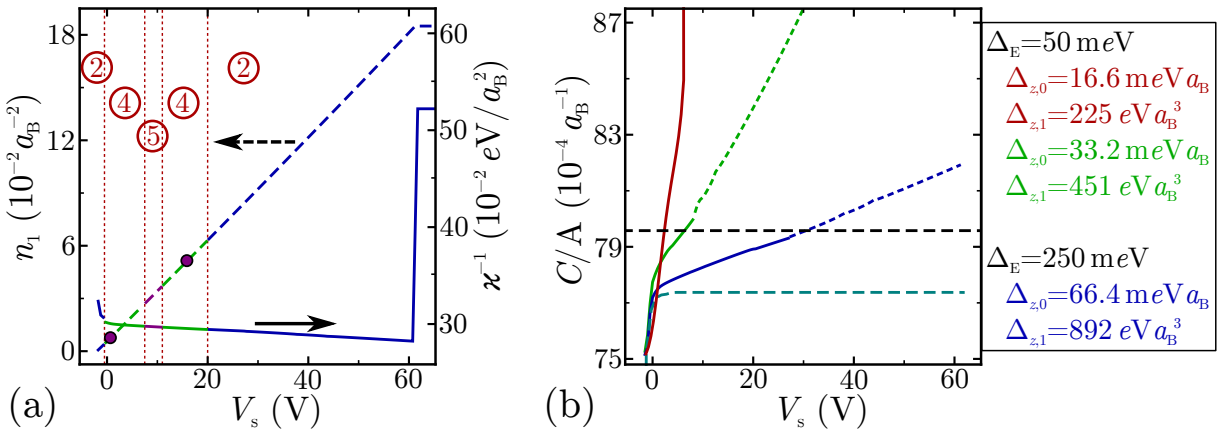

Figure 4.7.: A voltage source V_s tunes the density on the interface n_1, inverse compressibility κ^{-1} (a) and the capacitance per area C/A (b) of a system consisting of an interface described by Eq. (4.36a), coupled to a free electron gas at effective distance $d/\epsilon = 10\,a_B$. The parameters are $m_l = 0.7\,m_e$, $m_h = 15\,m_e$, $m_2 = m_e$, $\Delta_{SO} = 10\,meV$ and $n_t = 1e^-/uc = 0.0184\,a_B^{-2}$. (a) Density on the interface (left scale, dashed curve) and inverse compressibility (right scale, continuous curve) for $\Delta_E = 50\,meV$, $\Delta_{z,0} = 16.6\,meV a_B$ and $\Delta_{z,1} = 225\,eV a_B^3$. An offset in chemical potentials $\mu_{off} = -31.25\,V$ ensures that at $V_s = 0$ the density on the interface is $n_1 = 2 \times 10^{13}\,cm^{-2} = 5.6 \times 10^{-4}\,a_B^{-2}$. The colors of the curves, vertical red dashed lines and red numbers in circles denote the number of occupied bands for a given V_s: two (blue), four (green) and five (purple). The band structures of Fig. 4.6a and 4.6b, respectively, correspond to the densities indicated by the two purple circles. (b) Differential capacitance per area for three different sets of parameters as labeled on the right side, geometric capacitance per area (black) and differential capacitance per area for $\Delta_{z,0} = 8.3\,meV a_B$ and $\Delta_{z,1} = 0$ (cyan). Here $\mu_{off} = -31.25\,V$ for the blue and green curve, $\mu_{off} = -31.42\,V$ for the red curve and $\mu_{off} = -21.24\,V$ for the black and cyan curve. The energy splitting in the linear-in-k-regime of the blue and red curve corresponds to $\alpha_1 = 68\,eV a_B^3$ and for the green curve to $\alpha_1 = 136\,eV a_B^3$. For large density on the interface the $\mathbf{k} = 0$ wave vector is unoccupied, as indicated by the dashed part of the blue and green curves. Adapted from Ref. [33].

potentials μ_{off} were considered; on the one hand $\mu_{off} = 0$ (Fig. 4.8a) and on the other hand $\mu_{off} = -31\,V$ (Fig. 4.8b), which adjusted $n_1 = 5.6 \times 10^{-4}\,a_B^{-2}$ at $V_s = 0$, and $d/\epsilon = 10\,a_B$.

For $\mu_{off} = 0$ all electronic charge resides at the interface for small effective plate distances d/ϵ, which has two reasons: Firstly, the cost in electrostatic energy for this is low. Secondly, the band edge of the lowest doublet at the interface system is shifted with respect to the band edge of the surface electrode. This shift is $\Delta_E = 50\,meV$ in the absence of SOC, and with finite Δ_{SO} even larger. The presence of the total charge on the interface induces a negative compressibility of the total system for sufficiently large $\Delta_{z,1}$ and small d/ϵ, as the negative contribution from $s1$ dominates over the small positive terms derived from the surface and the electrostatic energy. As the electric field between the electrodes is fixed for $n_1 = n_t$, an increase of the plate distance increases the accompanying electrostatic potential difference between the two plates (or, equivalently, the electrostatic cost of storing all electrons in one electrode). Finally, for d/ϵ large enough, electrons are transferred to $s2$ (Fig. 4.8c); the critical distance where this happens increases with $\Delta_{z,1}$. The inverse compressibility exhibits a discontinuity at this point, which can be attributed to two contributions: For $n_1 < n_t$ the surface system contributes a constant positive term to the inverse compressibility and the contribution of the electrostatic energy drops to a lower value (c.f. the explanation at Eq. (4.22)–(4.25)), which is why κ^{-1} becomes smaller. For $n_1 = n_t$ the inverse compressibility increases linearly with d/ϵ, as the only dependence on the effective distance arises directly from the electrostatic energy. For large d/ϵ the energy is dominated by the electrostatic term, so that $n_1 \approx n_t/2$ minimizes the total

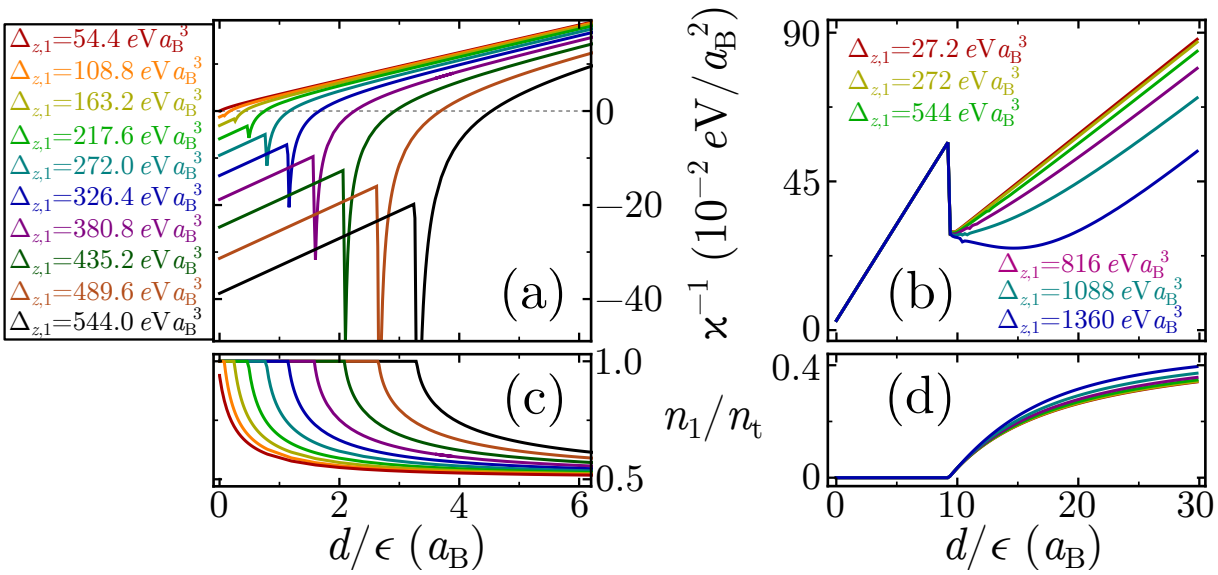

Figure 4.8.: The left-hand side shows the inverse compressibility (a) and the corresponding density on the interface (c) for an offset of $\mu_{\text{off}} = 0$ in chemical potentials as function of the effective electrode distance d/ϵ. The offset $\mu_{\text{off}} = -31\,\text{V}$ used in the plots on the right-hand side fixes the interface density (d) to $n_1 = 5.6 \times 10^{-4}\,a_{\text{B}}^{-2}$ at $d/\epsilon = 10\,a_{\text{B}}$. Plot (c) displays the resulting inverse compressibility. Here $m_l = 0.7\,m_e$, $m_h = 15\,m_e$, $m_2 = m_e$, $n_{\text{t}} = 1e^-/\text{uc} = 0.0184\,a_{\text{B}}^{-2}$, $\Delta_{\text{SO}} = 10\,\text{meV}$, $\Delta_{\text{E}} = 50\,\text{meV}$, $V_{\text{s}} = 0$ and $\Delta_{z,0} = 27.2\,\text{meV}a_{\text{B}}$. Adapted from Ref. [33].

free energy. The insertion of this value into F_{es} (Eq. (4.6)) and the application of the second derivative with respect to n_{t} yields half of the gradient of the $n_1 = n_{\text{t}}$ case.

There are no electrons at the interface for $\mu_{\text{off}} = -31\,\text{V}$ (Fig. 4.8d) at small d/ϵ. The inverse compressibility increases linearly in d/ϵ with the same slope as in the $n_1 = n_{\text{t}}$ case (see Eq. (4.22)) for $n_1 = 0$ and displays a discontinuity at the transition to finite n_1. For large plate distances the inverse compressibility increases linearly with half the slope of $n_1 = 0$. The comparison with the case of vanishing chemical offset reveals remarkable differences: The density on the interface starts at $n_1 = 0$ instead of $n_1 = n_{\text{t}}$ for small d/ϵ, which can be traced back to the offset $\mu_{\text{off}} = -31\,\text{V}$; in both cases the density on the interface for large d/ϵ is $n_1 \approx n_{\text{t}}/2$ due to the domination of F_{es} in this regime. The large density at $s1$ for $\mu_{\text{off}} = 0\,\text{V}$ induces a negative compressibility for small plate distances, which is not present at small n_1 as in the latter regime Δ_z is too weak to induce $\kappa^{-1} < 0$.

The results above suggest that for the experimentally identified density of about $n_1 = 5.6 \times 10^{-4}\,a_{\text{B}}^{-2}$ at the LAO/STO interface in the absence of external voltage, the total system is stable even in the presence of large $\Delta_{z,1}$. Actually, a larger charge density at the interface, induced by a finite V_{s}, does not render the compressibility negative in the range of reasonable parameters. In Fig. 4.9 the dependence of the inverse compressibility (a), electron density on the interface (b) and differential capacitance (c) are investigated for different total charge densities n_{t}. This may provide a first insight into the properties of other polar heterostructures with strong SOC. For each of the three plotted sets of different $\Delta_{z,1}$ the lowest used offset in chemical potentials $\mu_{\text{off}} \approx -31\,\text{V}$ ascertains for $V_{\text{s}} = 0$ that $n_1 = 5.6 \times 10^{-4}\,a_{\text{B}}^{-2}$, which corresponds to $n_1/n_{\text{t}} \simeq 0.03$ at $n_{\text{t}} = 0.0184\,a_{\text{B}}^{-2}$ of LAO/STO. If the surface and interface bands are not shifted against each other, i.e., for $\mu_{\text{off}} = 0$, and if $\Delta_{z,1}$ is not too large, approximately half of the total density will reside at the interface. The lowest d_{xy}-like band at the interface is, due to the crystal field splitting, shifted down by $\approx -\Delta_{\text{E}}$ against the surface bands. For very small n_{t} the lowest doublet at the interface is able to hold the total charge of the system, which explains the increase of

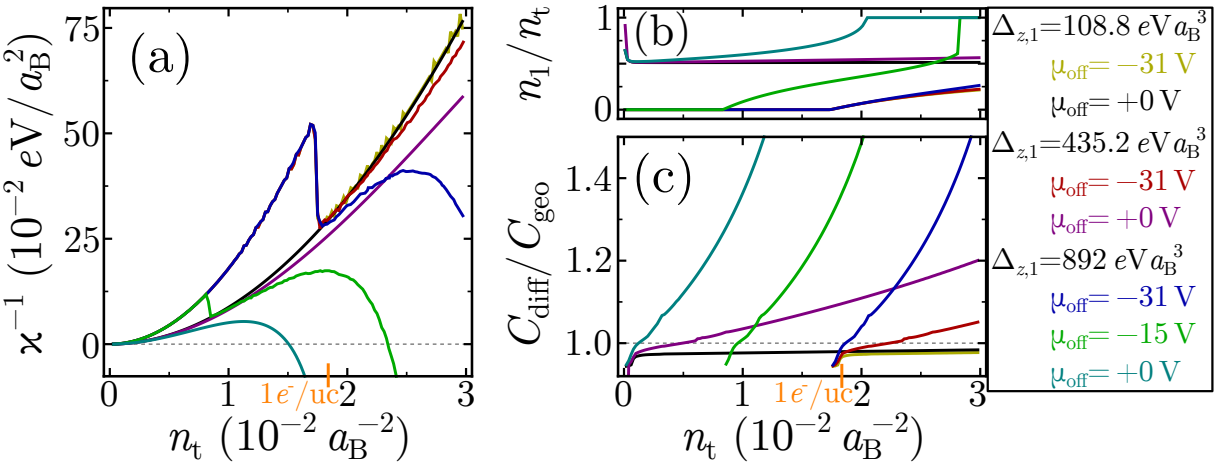

Figure 4.9.: The compressibility (a), interface electron density (b) and differential capacitance (c) depend on the total charge n_t of the system. The interface density is tuned by μ_{off}; for $\mu_{off} \approx -31\,V$, which is nearly identical of all three sets of $\Delta_{z,1}$, the density at the interface is $n_1 = 5.6 \times 10^{-4}\, a_B^{-2}$ at $n_t = 0.0184\, a_B^{-2}$, which corresponds to $1e^-/uc$ in LAO/STO and is marked in orange. Here $m_l = 0.7\, m_e$, $m_h = 15\, m_e$, $m_2 = m_e$, $d/\epsilon = 10\, a_B$, $\Delta_{SO} = 10\, meV$, $\Delta_E = 50\, meV$, $V_s = 0$ and $\Delta_{z,0} = 27.2\, meV a_B$. Adapted from Ref. [33].

C_{diff} in Fig. 4.9c for $\mu_{off} = 0$ at $n_t \to 0$. For $n_1 = 0$ the interface system does not contribute to the inverse compressibility, which increases then quadratically with n_t, as the second derivatives of F_2 and F_{es} with respect to n_t are constant. At the transition to finite $0 < n_1$, κ^{-1} displays a jump, which was in the text above traced back to a change in the contribution of F_{es}. Only for the largest value of $\Delta_{z,1} = 892\, eV a_B^3$, which is compatibly with experiments, the inverse compressibility may turn negative in the considered range. This is solely feasible if the density at the interface is large even in the absence of external voltage. The differential capacitance, which is only defined for $0 < n_1 < n_t$, (Fig. 4.9c) increases with n_t, as n_1 increases with n_t and this leads to a larger Δ_z. While the LAO/STO heterostructure is stable, it is possible that systems with a larger charge n_t in the polar layers may turn instable for sizable $\Delta_{z,1}$.

Up to now the compressibility was determined by taking the total second derivative of the Helmholtz free energy F_t with respect to the total charge density n_t, after identifying the interface density n_1 which minimizes the energy of the system. This n_1 depends on the total charge of the system: $n_1 = n_1(n_t)$. If $0 < n_1 < n_t$, i.e., the density on the interface was obtained by $\partial F_t/\partial n_1 = 0$ and $\partial^2 F_t/\partial n_1^2 > 0$ and is therefore no boundary value, then the compressibility can be expressed by the charge transfer function $\partial n_1/\partial n_t$ (see Section 2.3 and Eq. (2.42)):

$$\frac{1}{\kappa}\frac{\mathcal{V}}{n_t^2} = \frac{\partial^2 F_t}{\partial n_1^2}\frac{\partial n_1}{\partial n_t}\left(1 - \frac{\partial n_1}{\partial n_t}\right) + \left(\frac{\partial^2}{\partial n_t^2} + \frac{\partial^2}{\partial n_1 \partial n_t}\right) F_{es} \tag{4.39}$$

$$= \frac{e^2\mathcal{V}^2}{C_{diff}}\frac{\partial n_1}{\partial n_t}\left(1 - \frac{\partial n_1}{\partial n_t}\right) + \mathcal{D}F_{es} \tag{4.40}$$

As for the symmetric polar heterostructure the last term vanishes, $\mathcal{D}F_{es} = 0$, the condition of a stable system can directly be related to the charge transfer function:

$$\kappa > 0 \quad \Longleftrightarrow \quad 0 < \frac{\partial n_1}{\partial n_t} < 1 \tag{4.41}$$

In a stable system the increase of the total charge by δn_t will distribute a positive fraction of δn_t on each electrode, i.e., increase the electron density of both subsystems. If the total system is instable, then an increase of the total charge by δn_t will trigger a charge transfer between the

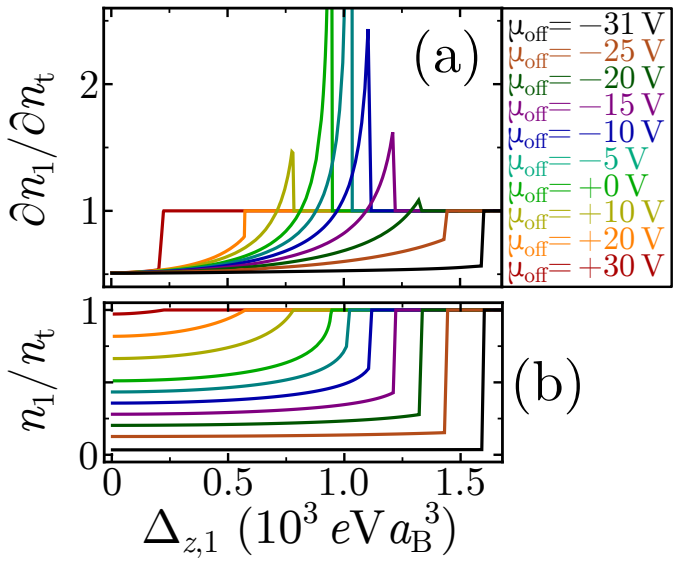

Figure 4.10.: The differential charge transfer $\partial n_1/\partial n_{\rm t}$ (a) as function of $\Delta_{z,1}$ for different values of $\mu_{\rm off}$, which controls together with Δ_z the density n_1 at the interface (b). The differential capacitance exceeds the geometric capacitance for $\partial n_1/\partial n_{\rm t} > 41/80$. At the transition $n_1 = n_{\rm t}$ the charge transfer function of (a) jumps to $\partial n_1/\partial n_{\rm t} = 1$. Here $m_l = 0.7\, m_e$, $m_h = 15\, m_e$, $m_2 = m_e$, $d/\epsilon = 10\, a_{\rm B}$, $n_{\rm t} = 1e^-/\mathrm{uc} = 0.0184\, a_{\rm B}^{-2}$, $\Delta_{\rm SO} = 10\,\mathrm{meV}$, $\Delta_{\rm E} = 50\,\mathrm{meV}$, $V_{\rm s} = 0$ and $\Delta_{z,0} = 27.2\,\mathrm{meV}a_{\rm B}$. Adapted from Ref. [33].

electrodes, i.e., the electron density of one subsystem is decreased. Note although, that without a change $\delta n_{\rm t}$ the system is stable against charge transfer between the electrodes, as this relation was derived under the premise that n_1 minimizes the energy; the phase separation of an instable system with $0 < n_1 < n_{\rm t}$ occurs in the plane of the subsystems.

The stability of the system depends strongly of the strength of the SOC interaction, which is a function of $\Delta_{z,1}$. Figure 4.10a and 4.10b display the charge transfer function and the density on the interface n_1, respectively, over $\Delta_{z,1}$. The density at $\Delta_{z,1} = 0$ depends on the offset in chemical potentials between the interface and surface. An increase of $\Delta_{z,1}$ lowers the energy of the lower bands of the interface and thus induces a transfer of electrons from the surface, which in turn increases Δ_z. The total system becomes instable for large Δ_z (see Fig. 4.10a), when a value of $\partial n_1/\partial n_{\rm t} = 1$ is reached. When $n_1 = n_{\rm t}$ the charge transfer function is no longer defined (n_1 is at a boundary value) and assumes the value 1 (see Fig. 4.10b).

If n_1 is not a boundary value, then Eq. (2.35) can be used to express the charge transfer function by second derivatives of $F_{\rm t}$:

$$\frac{\partial n_1}{\partial n_{\rm t}} = -\frac{\partial^2 F_{\rm t}}{\partial n_1 \partial n_{\rm t}} \Big/ \frac{\partial^2 F_{\rm t}}{\partial n_1^2} = \frac{\partial^2 F_{\rm t}}{\partial n_{\rm t}^2} \Big/ \frac{\partial^2 F_{\rm t}}{\partial n_1^2} \tag{4.42}$$

For the last relation the special dependency on $n_{\rm t}$ was used, i.e., that $\partial^2 F_{\rm t}/\partial n_1 \partial n_{\rm t} = -\partial^2 F_{\rm t}/\partial n_{\rm t}^2$, which is not valid for all electrostatic configurations. The denominator on the right-hand side is positive due to the condition that n_1 is a local minimum and the numerator is positive as the second derivates act effectively only on $F_2 = A(n_{\rm t} - n_1)^2/2N_2$ and $F_{\rm es} = D(n_1 + (n_{\rm t} - n_1)^2)$, so that the charge transfer function is positive. Condition Eq. (4.41) thus can be rewritten to

$$\begin{aligned} \kappa > 0 \quad &\Longleftrightarrow \quad \frac{\partial^2 F_{\rm t}}{\partial n_{\rm t}^2} < \frac{\partial^2 F_{\rm t}}{\partial n_1^2} \\ &\Longleftrightarrow \quad \frac{\partial^2 F_1}{\partial n_1^2} + \left(\frac{\partial^2}{\partial n_1^2} - \frac{\partial^2}{\partial n_{\rm t}^2} \right) F_{\rm es} > 0 \qquad (4.43) \\ &\Longleftrightarrow \quad \frac{\partial^2 F_1}{\partial n_1^2} + 2D > 0 \qquad (4.44) \end{aligned}$$

This important result states that the sign of the compressibility is independent of F_2 as long as $F_2 = F_2(n_{\rm t} - n_1)$ and is determined by the interface system and a contribution from the electrostatic energy. Eq. (4.43) is valid for $0 < n_1 < n_{\rm t}$ and electrostatic energies that fulfill

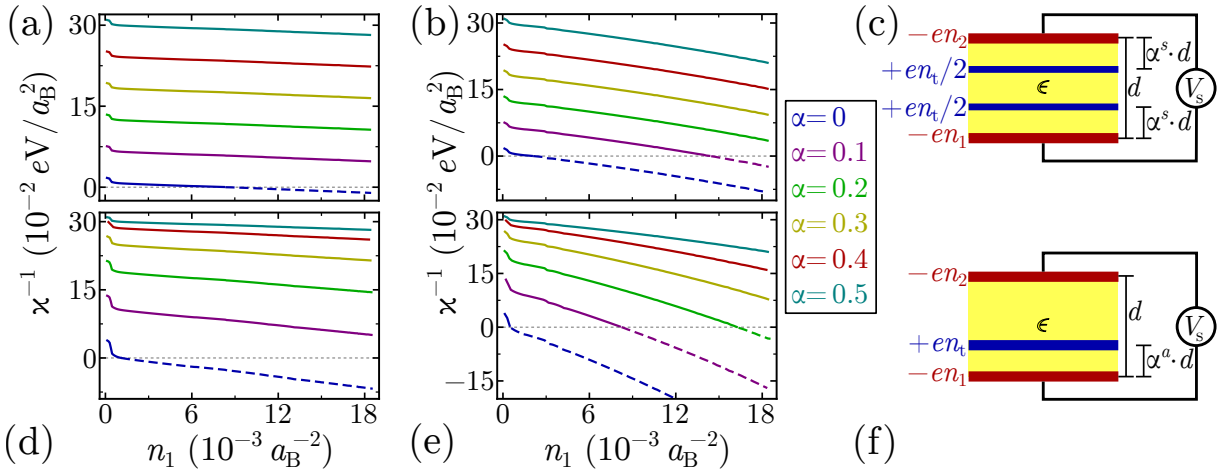

Figure 4.11.: Inverse compressibilities for different configurations of the positive background charge over n_1, which is controlled by the voltage V_s. (a) and (b) correspond to the symmetric distribution (c), where half of the total positive charge resides at distance of $\alpha \cdot d/\epsilon$ from each electrode. (d) and (e) correspond to the asymmetric case (f), where the total positive charge is concentrated in a layer at distance $\alpha \cdot d/\epsilon$ from the lower electrode. In (a) and (d) it is $\Delta_{z,0} = 16.6\,\mathrm{meV}a_B$ and $\Delta_{z,1} = 225\,e\mathrm{V}a_B^3$, while (b) and (e) use double of these values. This corresponds to the red and green curves of Fig. 4.7b. Here $m_l = 0.7\,m_e$, $m_h = 15\,m_e$, $m_2 = m_e$, $n_t = 1e^-/\mathrm{uc} = 0.0184\,a_B^{-2}$, $\Delta_{SO} = 10\,\mathrm{meV}$, $\Delta_E = 50\,\mathrm{meV}$, and individually for each curve, $\mu_{off} \approx -31\,\mathrm{V}$ so that $n_1 = 5.6 \times 10^{-4}\,a_B^{-2}$ at $V_s = 0$. Adapted from Ref. [32].

$\partial^2 F_{es}/\partial n_1 \partial n_t = -\partial^2 F_{es}/\partial n_t^2$. The surface system is, of course, relevant for the determination of the density n_1 on the interface and the exact value of the compressibility. The condition for the sign of the compressibility can alternatively be deduced directly from the combination of Eq. (2.54) with Eq. (2.55), which are valid under the same conditions as assumed above,

$$\frac{1}{\kappa}\frac{A}{n_t^2} = \frac{F_1'' F_2'' + 2D(F_1'' + F_2'' + 2D)}{F_1'' + F_2'' + 4D} = \frac{(F_1'' + 2D)(F_2'' + 2D)}{F_1'' + F_2'' + 4D}. \tag{4.45}$$

The compressibility depends strongly on the distribution of the positive background charge. In Chapter 2.3 a general electrostatic layout was established that allows to analyze its correlation with κ by means of two parameters, whereas the differential capacitance is unaffected by these parameters. Three special cases were introduced in Section 2.3, which depend only on one parameter. The effect of two of these models on the inverse compressibility is visualized in Fig. 4.11: In the symmetric distribution s half of the total positive background charge, $+en_t/2$, is located in two planes at distance $\alpha^s d$ from each electrode (c.f. Fig. 4.11c). On the other hand, the asymmetric distribution a describes the case where the total positive charge is concentrated in one plane at distance $\alpha^a d$ from the lower electrode (c.f. Fig. 4.11f).

The charge transfer function $\partial n_1/\partial n_t$ does not depend on the parameter α^s in the symmetric distribution, so that the shift of the inverse compressibility by the value $-n_t^2 D(1-2\alpha^s)/A$ does not depend on the interface density n_1 (see paragraph at Eq. (2.52)). The positive charge is closer to the layer of electrons for smaller α^s, so that the electrostatic energy decreases with smaller α^s,[4] which also determines the contribution to the inverse compressibility. That a system with

[4]The energy stored in the electric field is proportional to the product of the square of the field strength with the volume. The former is proportional to the difference in charge densities and the latter proportional to the distance between volume limiting charged planes. Here the volume between the electrodes is divided by the two planes of positive charge into three parts. The electric field in the volume next to $s1$ is proportional to n_1 and the field next to $s2$ to $n_t - n_1$, while the field between the two positive planes is the average of these

smaller α^s is less stable, is demonstrated in Fig. 4.11a and 4.11b. Here $\alpha^s = 1/2$ corresponds to the symmetric polar heterostructure (SPH), which was considered so far in this chapter for the distribution of the positive charge. The system parameters used in Fig. 4.11a are the same as in Fig. 4.7a, and Fig. 4.11b uses a Δ_z of twice the strength. It is evident that the shift of the positive charged planes in direction of the electrodes decreases the inverse compressibility; in fact, for $\alpha^s = 0$ the compressibility becomes even negative for interface densities n_1 large enough. At larger interorbital hopping, i.e., at $\Delta_{z,0} = 33.2\,\mathrm{meV}a_\mathrm{B}$ and $\Delta_{z,1} = 451\,e\mathrm{V}a_\mathrm{B}^3$ (Fig. 4.11b), the system becomes already for $\alpha^s = 0.1$ and large n_1 instable.

If the positive background charge is distributed according to the asymmetric case a (Fig. 4.11f) the position of the plane of positive charge for which the system is most stable is determined by $\alpha_m^a = (4D - F_1'' + F_2'')/8D$ and if this value is $\alpha_m^a \notin [0,1]$, then either $\alpha_m^a = 0$ or $\alpha_m^a = 1$ yield the largest inverse compressibility (c.f. Eq. (2.56)). Here $\alpha^a = 1/2$, which corresponds to the SPH, results in the most stable system in Fig. 4.11d and 4.11e in the range of analyzed values of α^a. As for the asymmetric distribution a, the relation $\mathcal{D}F_\mathrm{es}^a = 0$ holds and the stability of the system is determined by the charge transfer function $\partial n_1/\partial n_\mathrm{t}$, i.e., if the charge transfer function is < 0 or > 1, then $\kappa^{-1} < 0$. Moving the plane of positive charge closer to the lower electrode decreases the electrostatic cost of electron density transfer to $s1$, so that $\partial n_1/\partial n_\mathrm{t}$ becomes larger. This implies that inverse compressibility becomes negative for small α^a, as illustrated by Fig. 4.11d and 4.11e. A comparison with the symmetric layout s shows that the system is less stable for the asymmetric distribution a.

4.4. Summary of the Section

In this chapter the compressibility and capacitance of a system, which features one two-dimensional electrode with strong atomic SOC and a SBEF, that resulted in Rashba-like SOC, were analyzed. The sizable magnitude of the Rashba-like SOC (RSOC) at the conducting LAO/STO interface system is a consequence of the strong lattice polarization in the presence of electric fields [118]. The second electrode was characterized as "standard" metal and described as free electron gas. RSOC in this second electron system was neglected due to the absence of lattice polarization. The coupling of the RSOC parameter in the interface system to the electric field of uncompensated positive background charge outside of the interface introduces a mechanism that renders the band structure density dependent. This is true only under the premise that the total system, including the surface system and the positive background charge that generates the SBEF, is considered.

This mechanism establishes, besides the known exchange and correlation terms, the possibility for negative compressibility and a differential capacitance larger than the geometric capacitance. While exchange and correlation contributions to the compressibility and capacitance become dominant at low densities, the RSOC mechanism is more relevant at large electron densities, i.e., when the electric field at the interface is strong. The RSOC induced capacitance enhancement does therefore take place at larger densities, which is in contrast to the experimentally found increase at small densities by Lu Li *et. al.* [9].

The RSOC at the interface electron system was described by a six-band model arising from the three t_{2g} orbitals of Ti atoms in TiO_2. This model resulted in a linear spin splitting of the lowest doublet for small wave vectors k, which allowed the comparison to the effective two-band model introduced by Eq. (4.3), where the spin splitting is linear for all k. In the linear regime of spin splitting the parameters for the strength of interorbital hopping could be extracted from

two values. This implies that the square of the field between the planes of positive charge is smaller than the average of the squares of the fields next to the electrodes, so that the electrostatic energy is minimized by maximizing the volume between the positive planes, i.e., $\alpha^s = 0$.

experiment [8]. The LAO/STO interface system was shown to be stable in the range of these physically realistic parameters, contradicting the results of Grilli *et. al.* [99], who neglected to include the surface electron system and the electrostatic contributions into their analysis. It was also demonstrated that the spatial distribution of the the positive background charge has a large impact on the stability of the total system and that the symmetric polar heterostructure was the most stable configuration among the considered layouts.

5. Electron System with Rashba Spin-Orbit Coupling and Exchange Interaction

The two-dimensional free electron gas at zero temperature and low electron density displays a negative compressibility, which is induced by the exchange contribution (see Chapter 3). Depending on the polarization of the groundstate the electrons occupy either one circular disc (polarized) or two circular discs of equal radius (unpolarized) in k-space. On the other hand, the simple model with Rashba spin-orbit coupling (RSOC), which was analyzed in the previous chapter (see, e.g., Eq. (4.3)), neglected the electron-electron interactions beyond the Hartree term. We found three qualitatively different distributions of occupation in k-space in this model: If the strength of the RSOC was taken as density independent, an increase of electron density changed the shape of populated states in k-space from an annulus over a circle to two circles with different radii. But is the nature of the groundstate if both RSOC and exchange interaction act jointly and how is the compressibility affected by this combination? As this chapter developed chronologically at the end of this work, some of the results are of preliminary character, but nevertheless allow a first insight into the interaction between RSOC and exchange coupling.

5.1. Introduction of the Hamiltonian and its Diagonalization

To concentrate on these questions we analyze a single two-dimensional layer comprising an electron system that displays RSOC, which is, due to the absence of coupling to a second system, taken at fixed electron density. The Hamiltonian is split into three parts,

$$\hat{\mathcal{H}} = \hat{\mathcal{H}}_{\mathrm{kin}} + \hat{\mathcal{H}}_{\mathrm{s}} + \hat{\mathcal{H}}_{\mathrm{x}}. \tag{5.1}$$

$\hat{\mathcal{H}}_{\mathrm{kin}}$ denotes the kinetic energy of free electrons with effective mass m_0 and the DOS $N_0 = m_0/\pi\hbar^2$ in the absence of RSOC for both spin directions.

$$\hat{\mathcal{H}}_{\mathrm{kin}} = \sum_{\mathbf{k},\sigma} \frac{k^2}{2\pi N_0} \hat{c}^\dagger_{\mathbf{k}\sigma} \hat{c}_{\mathbf{k}\sigma} \tag{5.2}$$

Here $\hat{c}^\dagger_{\mathbf{k}\sigma}$ and $\hat{c}_{\mathbf{k}\sigma}$ are the creation and destruction operator, respectively, of one electron with spin $\sigma = |\uparrow\rangle, |\downarrow\rangle$ and wave vector $\mathbf{k}$ in a plane wave state. The spin part of the Hamiltonian includes in addition to the RSOC, which was given in Eq. (4.3), the Zeeman coupling of an in-plane magnetic field $\mathbf{B} = \mathbf{H}/\mu_{\mathrm{B}} = (H_x, H_y)/\mu_{\mathrm{B}}$ to the electron spin:

$$\begin{aligned}
\hat{\mathcal{H}}_{\mathrm{s}} &= \sum_{\mathbf{k}} \begin{pmatrix} \hat{c}^\dagger_{\mathbf{k}\uparrow} & \hat{c}^\dagger_{\mathbf{k}\downarrow} \end{pmatrix} \left(\alpha_{\mathrm{R}} (\boldsymbol{\sigma} \times \mathbf{k}) \cdot \mathbf{e}_z + \frac{g_s}{2} \mu_{\mathrm{B}} \boldsymbol{\sigma} \cdot \mathbf{B} \right) \begin{pmatrix} \hat{c}_{\mathbf{k}\uparrow} \\ \hat{c}_{\mathbf{k}\downarrow} \end{pmatrix} \\
&= \sum_{\mathbf{k}} \begin{pmatrix} \hat{c}^\dagger_{\mathbf{k}\uparrow} & \hat{c}^\dagger_{\mathbf{k}\downarrow} \end{pmatrix} \left(\alpha_{\mathrm{R}} (k_y \sigma_x - k_x \sigma_y) + \frac{g_s}{2} \mu_{\mathrm{B}} (B_x \sigma_x + B_y \sigma_y) \right) \begin{pmatrix} \hat{c}_{\mathbf{k}\uparrow} \\ \hat{c}_{\mathbf{k}\downarrow} \end{pmatrix} \\
&= \sum_{\mathbf{k}} \left\{ \left[\alpha_{\mathrm{R}} (k_y + i k_x) + (H_x - i H_y) \right] \hat{c}^\dagger_{\mathbf{k}\uparrow} \hat{c}_{\mathbf{k}\downarrow} + \left[\alpha_{\mathrm{R}} (k_y - i k_x) + (H_x + i H_y) \right] \hat{c}^\dagger_{\mathbf{k}\downarrow} \hat{c}_{\mathbf{k}\uparrow} \right\}
\end{aligned} \tag{5.3}$$

$\boldsymbol{\sigma} = (\sigma_x, \sigma_y, \sigma_z)$ is the vector of the Pauli spin matrices, μ_B the Bohr magneton and g_s the spin g-factor, which was set in the last step to 2. The general Hamiltonian of the full electron-electron interaction is of the form $1/2 \sum_{\alpha,\beta,\gamma,\delta} v_{\alpha\beta\gamma\delta} \hat{c}^\dagger_\alpha \hat{c}^\dagger_\beta \hat{c}_\gamma \hat{c}_\delta$. The matrix element $v_{\alpha\beta\gamma\delta}$ for plane wave states is specified in Eq. (3.9), so that

$$\hat{\mathcal{H}}_{e-e} = \frac{1}{2} \sum_{\sigma_1,\sigma_2} \sum_{\mathbf{q},\mathbf{k}_1,\mathbf{k}_2} v_\mathrm{x}(\mathbf{q}) \hat{c}^\dagger_{\mathbf{k}_1+\mathbf{q}\sigma_1} \hat{c}^\dagger_{\mathbf{k}_2-\mathbf{q}\sigma_2} \hat{c}_{\mathbf{k}_2\sigma_2} \hat{c}_{\mathbf{k}_1\sigma_1}, \qquad \text{with} \quad v_\mathrm{x}(\mathbf{q}) = \frac{2\pi e^2}{A \epsilon_\mathrm{eff} |\mathbf{q}|} \tag{5.4}$$

The application of the Hartree-Fock approximation, which was introduced in Section 3.1, on Eq. (5.4) yields two relevant terms: The Hartree term, which originates from the $\mathbf{q} = 0$ contributions, is—for a neutral system—compensated by the positive background charge (for a homogeneous state), so that it can be neglected. The Fock term has a negative sign due to the anticommutation relation and reads, after using $\langle \hat{c}^\dagger_{\mathbf{k}_1+\mathbf{q}\sigma_1} \hat{c}_{\mathbf{k}_2\sigma_2} \rangle = \delta_{\mathbf{k}_1+\mathbf{q},\mathbf{k}_2} \langle \hat{c}^\dagger_{\mathbf{k}_2\sigma_1} \hat{c}_{\mathbf{k}_2\sigma_2} \rangle$ and renaming the variables of summation

$$\begin{aligned} \hat{\mathcal{H}}_\mathrm{x} = -\frac{1}{2} \sum_{\sigma_1,\sigma_2} \sum_{\mathbf{k},\mathbf{q}} v_\mathrm{x}(\mathbf{k}-\mathbf{q}) \big(& \langle \hat{c}^\dagger_{\mathbf{k}\sigma_1} \hat{c}_{\mathbf{k}\sigma_2} \rangle \hat{c}^\dagger_{\mathbf{q}\sigma_2} \hat{c}_{\mathbf{q}\sigma_1} + \hat{c}^\dagger_{\mathbf{k}\sigma_1} \hat{c}_{\mathbf{k}\sigma_2} \langle \hat{c}^\dagger_{\mathbf{q}\sigma_2} \hat{c}_{\mathbf{q}\sigma_1} \rangle \\ & - \langle \hat{c}^\dagger_{\mathbf{k}\sigma_1} \hat{c}_{\mathbf{k}\sigma_2} \rangle \langle \hat{c}^\dagger_{\mathbf{q}\sigma_2} \hat{c}_{\mathbf{q}\sigma_1} \rangle \big). \end{aligned} \tag{5.5}$$

In the basis of plane wave states with spin up and down, the total Hamiltonian (5.1) is

$$\hat{\mathcal{H}} = \sum_\mathbf{k} \begin{pmatrix} \hat{c}^\dagger_{\mathbf{k}\uparrow} & \hat{c}^\dagger_{\mathbf{k}\downarrow} \end{pmatrix} \underline{\underline{M_\mathbf{k}}} \begin{pmatrix} \hat{c}_{\mathbf{k}\uparrow} \\ \hat{c}_{\mathbf{k}\downarrow} \end{pmatrix} + C_F \tag{5.6}$$

C_F originates from the operator independent part of the Fock term,

$$C_F = \frac{1}{2} \sum_{\mathbf{k},\mathbf{q}} v_\mathrm{x}(\mathbf{k}-\mathbf{q}) \left(\langle \hat{c}^\dagger_{\mathbf{k}\uparrow} \hat{c}_{\mathbf{k}\uparrow} \rangle \langle \hat{c}^\dagger_{\mathbf{q}\uparrow} \hat{c}_{\mathbf{q}\uparrow} \rangle + \langle \hat{c}^\dagger_{\mathbf{k}\downarrow} \hat{c}_{\mathbf{k}\downarrow} \rangle \langle \hat{c}^\dagger_{\mathbf{q}\downarrow} \hat{c}_{\mathbf{q}\downarrow} \rangle + 2 \langle \hat{c}^\dagger_{\mathbf{k}\uparrow} \hat{c}_{\mathbf{k}\downarrow} \rangle \langle \hat{c}^\dagger_{\mathbf{q}\downarrow} \hat{c}_{\mathbf{q}\uparrow} \rangle \right) \tag{5.7}$$

The matrix $M_\mathbf{k}$ has off-diagonal elements

$$\underline{\underline{M_\mathbf{k}}} = \begin{pmatrix} \dfrac{k^2}{2\pi N_0} - \displaystyle\sum_\mathbf{q} v_\mathrm{x}(\mathbf{k}-\mathbf{q}) \langle \hat{c}^\dagger_{\mathbf{q}\uparrow} \hat{c}_{\mathbf{q}\uparrow} \rangle & H e^{-i\vartheta} + i\alpha_\mathrm{R} k e^{-i\varphi_\mathbf{k}} - \displaystyle\sum_\mathbf{q} v_\mathrm{x}(\mathbf{k}-\mathbf{q}) \langle \hat{c}^\dagger_{\mathbf{q}\downarrow} \hat{c}_{\mathbf{q}\uparrow} \rangle \\ H e^{i\vartheta} - i\alpha_\mathrm{R} k e^{i\varphi_\mathbf{k}} - \displaystyle\sum_\mathbf{q} v_\mathrm{x}(\mathbf{k}-\mathbf{q}) \langle \hat{c}^\dagger_{\mathbf{q}\uparrow} \hat{c}_{\mathbf{q}\downarrow} \rangle & \dfrac{k^2}{2\pi N_0} - \displaystyle\sum_\mathbf{q} v_\mathrm{x}(\mathbf{k}-\mathbf{q}) \langle \hat{c}^\dagger_{\mathbf{q}\downarrow} \hat{c}_{\mathbf{q}\downarrow} \rangle \end{pmatrix}$$

The prefactor 1/2 of the Fock term in Eq. (5.5) is reduced by the double summation over spin and a renaming of the variables of summation. $\varphi_\mathbf{k}$ is the angle between vector $\mathbf{k}$ and the k_x-axis, while ϑ denotes the angle between the in-plane magnetic field $\mathbf{H}$ and the x-axis. The matrix $M_\mathbf{k}$ can be diagonalized by a transformation to the new basis $\hat{a}_{\mathbf{k}+}$ and $\hat{a}_{\mathbf{k}-}$.

$$\begin{aligned} \hat{c}_{\mathbf{k}\uparrow} &= u_\mathbf{k} e^{i\phi_\mathbf{k}} \hat{a}_{\mathbf{k}+} \quad - v_\mathbf{k} \hat{a}_{\mathbf{k}-} & \hat{a}_{\mathbf{k}+} &= u_\mathbf{k} e^{-i\phi_\mathbf{k}} \hat{c}_{\mathbf{k}\uparrow} \quad + v_\mathbf{k} \hat{c}_{\mathbf{k}\downarrow} \\ \hat{c}_{\mathbf{k}\downarrow} &= v_\mathbf{k} \hat{a}_{\mathbf{k}+} \quad + u_\mathbf{k} e^{-i\phi_\mathbf{k}} \hat{a}_{\mathbf{k}-} & \hat{a}_{\mathbf{k}-} &= -v_\mathbf{k} \hat{c}_{\mathbf{k}\uparrow} \quad + u_\mathbf{k} e^{i\phi_\mathbf{k}} \hat{c}_{\mathbf{k}\downarrow} \end{aligned} \tag{5.8}$$

Here $u_\mathbf{k}$ and $v_\mathbf{k}$ are real numbers with $u_\mathbf{k} = w_\mathbf{k}(s=+1)$ and $v_\mathbf{k} = w_\mathbf{k}(s=-1)$ with $u_\mathbf{k}^2 + v_\mathbf{k}^2 = 1$. $\phi_\mathbf{k}$ is the angle between the upper off-diagonal element and the x-axis:

$$\begin{aligned} w_\mathbf{k}(s) &= \left\{ \frac{1}{2} \left[1 + s \frac{\sum_\mathbf{q} v_\mathrm{x}(\mathbf{k}-\mathbf{q}) A_\mathbf{q}}{\sqrt{\left(\sum_\mathbf{q} v_\mathrm{x}(\mathbf{k}-\mathbf{q}) A_\mathbf{q} \right)^2 + 4 \left| H e^{-i\vartheta} + i\alpha_\mathrm{R} k e^{-i\varphi_\mathbf{k}} + \sum_\mathbf{q} v_\mathrm{x}(\mathbf{k}-\mathbf{q}) B_\mathbf{q} \right|^2}} \right] \right\}^{1/2} \\ e^{i\phi_\mathbf{k}} &= \frac{H e^{-i\vartheta} + i\alpha_\mathrm{R} k e^{-i\varphi_\mathbf{k}} + \sum_\mathbf{q} v_\mathrm{x}(\mathbf{k}-\mathbf{q}) B_\mathbf{q}}{\left| H e^{-i\vartheta} + i\alpha_\mathrm{R} k e^{-i\varphi_\mathbf{k}} + \sum_\mathbf{q} v_\mathrm{x}(\mathbf{k}-\mathbf{q}) B_\mathbf{q} \right|} \end{aligned} \tag{5.9}$$

$$A_{\mathbf{q}} = \langle \hat{c}^\dagger_{\mathbf{q}\uparrow} \hat{c}_{\mathbf{q}\uparrow} \rangle - \langle \hat{c}^\dagger_{\mathbf{q}\downarrow} \hat{c}_{\mathbf{q}\downarrow} \rangle = \left(u^2_{\mathbf{q}} - v^2_{\mathbf{q}}\right) \left(\langle \hat{a}^\dagger_{\mathbf{q}-} \hat{a}_{\mathbf{q}-} \rangle - \langle \hat{a}^\dagger_{\mathbf{q}+} \hat{a}_{\mathbf{q}+} \rangle \right) \tag{5.10}$$

$$B_{\mathbf{q}} = \langle \hat{c}^\dagger_{\mathbf{q}\downarrow} \hat{c}_{\mathbf{q}\uparrow} \rangle = u_{\mathbf{q}} v_{\mathbf{q}} e^{i\phi_{\mathbf{q}}} \left(\langle \hat{a}^\dagger_{\mathbf{q}-} \hat{a}_{\mathbf{q}-} \rangle - \langle \hat{a}^\dagger_{\mathbf{q}+} \hat{a}_{\mathbf{q}+} \rangle \right) \tag{5.11}$$

The eigenvalues $\varepsilon_\pm(\mathbf{k})$ of the matrix $\mathbf{M}$ correspond to the energy of the state connected to $\hat{a}^\dagger_{\mathbf{k}\pm}$, so that the Hamiltonian in diagonal form is

$$\hat{\mathcal{H}} = \sum_{\mathbf{k}} \left(\varepsilon_-(\mathbf{k}) \hat{a}^\dagger_{\mathbf{k}-} \hat{a}_{\mathbf{k}-} + \varepsilon_+(\mathbf{k}) \hat{a}^\dagger_{\mathbf{k}+} \hat{a}_{\mathbf{k}+} \right) + C_F \tag{5.12}$$

$$\varepsilon_\pm(\mathbf{k}) = \frac{k^2}{2\pi N_0} - \frac{1}{2} \sum_{\mathbf{q}} v_{\mathrm{x}}(\mathbf{k}-\mathbf{q}) C_{\mathbf{q}} \tag{5.13}$$

$$\pm \frac{1}{2} \left[\left(\sum_{\mathbf{q}} v_{\mathrm{x}}(\mathbf{k}-\mathbf{q}) A_{\mathbf{q}} \right)^2 + 4 \left| H e^{-i\vartheta} + i\alpha_{\mathrm{R}} k e^{-i\varphi_{\mathbf{k}}} + \sum_{\mathbf{q}} v_{\mathrm{x}}(\mathbf{k}-\mathbf{q}) B_{\mathbf{q}} \right|^2 \right]^{1/2},$$

$$C_{\mathbf{q}} = \langle \hat{c}^\dagger_{\mathbf{q}\uparrow} \hat{c}_{\mathbf{q}\uparrow} \rangle + \langle \hat{c}^\dagger_{\mathbf{q}\downarrow} \hat{c}_{\mathbf{q}\downarrow} \rangle = \langle \hat{a}^\dagger_{\mathbf{q}-} \hat{a}_{\mathbf{q}-} \rangle + \langle \hat{a}^\dagger_{\mathbf{q}+} \hat{a}_{\mathbf{q}+} \rangle \tag{5.14}$$

The transformation coefficients $u_{\mathbf{k}}$, $v_{\mathbf{k}}$ and $\phi_{\mathbf{k}}$ for the wave vector $\mathbf{k}$ are coupled to each other and depend on the transformation coefficients of other wave vectors $\mathbf{q}$, as mediated by Eq. (5.9)–(5.11). Note that $A_{\mathbf{q}}$ and $B_{\mathbf{q}}$ depend on the difference in occupation numbers between the new bands. This implies that the transformation coefficients have only to be determined for the set of wave vectors for which the lower band is occupied and the upper band is empty.

With the abbreviation $\langle \hat{a}^\dagger_{\mathbf{k}\pm} \hat{a}_{\mathbf{k}\pm} \rangle \equiv n_{\mathbf{k}\pm}$ the constant C_F from the Fock term is then in the new basis given by

$$C_F = \frac{1}{2} \sum_{\mathbf{k},\mathbf{q}} v_{\mathrm{x}}(\mathbf{k}-\mathbf{q}) \Big[n_{\mathbf{k}-} n_{\mathbf{q}-} + n_{\mathbf{k}+} n_{\mathbf{q}+} \tag{5.15}$$

$$- \left(u^2_{\mathbf{k}} v^2_{\mathbf{q}} - 2\cos(\phi_{\mathbf{k}} - \phi_{\mathbf{q}}) u_{\mathbf{k}} v_{\mathbf{k}} u_{\mathbf{q}} v_{\mathbf{q}} + v^2_{\mathbf{k}} u^2_{\mathbf{q}} \right) \left(n_{\mathbf{k}-} - n_{\mathbf{k}+} \right) \left(n_{\mathbf{q}-} - n_{\mathbf{q}+} \right) \Big]$$

The spin orientation of the electron states can be evaluated by taking the expectation value of the Pauli vector $\boldsymbol{\sigma} = (\sigma_x, \sigma_y, \sigma_z)$ in the eigenvectors of the matrix $M_{\mathbf{k}}$, which were used for its diagonalization (see, for example Ref. [84]):

$$|\psi_{\mathbf{k}+}\rangle = \begin{pmatrix} u_{\mathbf{k}} e^{i\phi_{\mathbf{k}}} \\ v_{\mathbf{k}} \end{pmatrix}, \qquad |\psi_{\mathbf{k}-}\rangle = \begin{pmatrix} -v_{\mathbf{k}} \\ u_{\mathbf{k}} e^{-i\phi_{\mathbf{k}}} \end{pmatrix}$$

$$\Rightarrow \langle \psi_{\mathbf{k}+} | \boldsymbol{\sigma} | \psi_{\mathbf{k}+} \rangle = \begin{pmatrix} 2u_{\mathbf{k}} v_{\mathbf{k}} \cos\phi_{\mathbf{k}} \\ -2u_{\mathbf{k}} v_{\mathbf{k}} \sin\phi_{\mathbf{k}} \\ u^2_{\mathbf{k}} - v^2_{\mathbf{k}} \end{pmatrix} = -\langle \psi_{\mathbf{k}-} | \boldsymbol{\sigma} | \psi_{\mathbf{k}-} \rangle \tag{5.16}$$

Here only the spin part of the wave function was considered. The spin of the lower band is always antiparallel to the spin of the upper band.

5.2. Analytical Solutions to the Diagonalization

The subject of this chapter is the analysis of the interplay between RSOC and exchange coupling. Nevertheless, we start by recovering the cases, where only one of those couplings is present, so that later results can be compared to these instances.

A system without RSOC is on hand for $\alpha_{\mathrm{R}} = 0$ and $\mathbf{H} = 0$. Then a set of solutions to the transformation coefficients is obtained by setting them independent of the wave vector, i.e.,

$u_{\mathbf{k}} = u$, $v_{\mathbf{k}} = v$ and $\phi_{\mathbf{k}} = \phi$. After this choice, every set of constant transformation coefficients that fulfills $u^2 + v^2 = 1$ solves Eqs. (5.9): The summations over $\mathbf{q}$ in the denominator of $w_{\mathbf{k}}(s)$ can be merged, so that the dependence on u and v vanishes, as $(u^2 - v^2)^2 + 4u^2v^2 = 1$. The denominator of $w_{\mathbf{k}}(s)$ appears also in the dispersion Eq. (5.13), so that using a set of wave-vector independent transformation coefficients yields

$$\varepsilon_{\pm}(\mathbf{k}) = \frac{k^2}{2\pi N_0} - \frac{1}{2}\sum_{\mathbf{q}} v_{\mathrm{x}}(\mathbf{k}-\mathbf{q}) C_{\mathbf{q}} \pm \frac{1}{2}\sum_{\mathbf{q}} v_{\mathrm{x}}(\mathbf{k}-\mathbf{q}) \left(\langle \hat{a}^{\dagger}_{\mathbf{q}-} \hat{a}_{\mathbf{q}-} \rangle - \langle \hat{a}^{\dagger}_{\mathbf{q}+} \hat{a}_{\mathbf{q}+} \rangle \right) \tag{5.17}$$

$$\Rightarrow \begin{cases} \varepsilon_{-}(\mathbf{k}) = \frac{k^2}{2\pi N_0} - \sum_{\mathbf{q}} v_{\mathrm{x}}(\mathbf{k}-\mathbf{q}) \langle \hat{a}^{\dagger}_{\mathbf{q}-} \hat{a}_{\mathbf{q}-} \rangle \\ \varepsilon_{+}(\mathbf{k}) = \frac{k^2}{2\pi N_0} - \sum_{\mathbf{q}} v_{\mathrm{x}}(\mathbf{k}-\mathbf{q}) \langle \hat{a}^{\dagger}_{\mathbf{q}+} \hat{a}_{\mathbf{q}+} \rangle \end{cases} \tag{5.18}$$

for the energy dispersion of both bands, which is the same result as derived in Section 3.1. There the Helmholtz free energy was evaluated in Eq. (3.16) as function of the electron density n. While the kinetic term is proportional to n^2, the exchange contribution has a negative sign and is proportional to $n^{3/2}$. The direction of the spin according to Eq. (5.16) depends on the choice of u, v and ϕ. For $u = 1$, $v = 0$ and arbitrary ϕ, the spin is oriented along the z direction.

The exchange interaction can be eliminated by setting $v_{\mathrm{x}}(\mathbf{k}) = 0$, so that only the kinetic and RSOC term remain. Then it follows straight away from Eqs. (5.9) that $u_{\mathbf{k}} = v_{\mathbf{k}} = 1/\sqrt{2}$ and $\phi_{\mathbf{k}} = \pi/2 - \varphi_{\mathbf{k}}$ for $\mathbf{H} = 0$ are the only solutions. Inserting these transformation coefficients into the dispersion and for the spin direction yields

$$\varepsilon_{\pm}(\mathbf{k}) = \frac{k^2}{2\pi N_0} \pm \alpha_{\mathrm{R}} k, \qquad \langle \psi_{\mathbf{k}+} | \boldsymbol{\sigma} | \psi_{\mathbf{k}+} \rangle = \begin{pmatrix} \cos\left(\frac{\pi}{2} - \varphi_{\mathbf{k}}\right) \\ -\sin\left(\frac{\pi}{2} - \varphi_{\mathbf{k}}\right) \\ 0 \end{pmatrix}. \tag{5.19}$$

The Helmholtz free energy arising from this dispersion was calculated in Eq. (4.8), while the distribution of the spin direction is displayed in Fig. 4.1. The spin points in the x-y plane and is perpendicular to the coordinate axes. As one moves in the lower band on a circle in k space clockwise around 0, the spin rotates counterclockwise.

We now return to the full problem with both RSOC and exchange coupling. For the examination of this system one has to identify the transformation coefficients and the distribution of occupied states $\langle \hat{a}^{\dagger}_{\mathbf{k}\pm} \hat{a}_{\mathbf{k}\pm} \rangle \equiv n_{\mathbf{k}\pm}$, which are connected to each other by Eqs. (5.9). The occupation of states adjusts in such a way that the Helmholtz free energy,

$$F(n) = \sum_{\mathbf{k}, s=\pm 1} \varepsilon_s(\mathbf{k}) \langle \hat{a}^{\dagger}_{\mathbf{k}s} \hat{a}_{\mathbf{k}s} \rangle + C_F, \tag{5.20}$$

is minimized for a given electron density n. This gives rise to a self-consistent evaluation of the transformation coefficients and occupation numbers $n_{\mathbf{k}\pm}$, which has to be performed numerically for the general case. Only two partial solutions, which are independent of each other, are known analytically: Firstly, one self-consistent solution for $u_{\mathbf{k}}$ and $v_{\mathbf{k}}$ is given by $u_{\mathbf{k}} = v_{\mathbf{k}} = 1/\sqrt{2}$, which is wave-vector independent. And secondly, if the difference in occupation numbers between the two bands, $\Delta n_{\mathbf{k}+-} \equiv n_{\mathbf{k}-} - n_{\mathbf{k}+}$ exhibits rotation symmetry around $\mathbf{k} = 0$, then $\phi_{\mathbf{k}} = \pi/2 - \varphi_{\mathbf{k}}$

for $\mathbf{H} = 0$. [1] The energy dispersions, which result from the combination of these two analytical solutions, read

$$\varepsilon_-(\mathbf{k}) = \frac{k^2}{2\pi N_0} - \alpha_\mathrm{R} k - \frac{1}{2}\sum_{\mathbf{q}} v_\mathrm{x}(\mathbf{k}-\mathbf{q}) \left[\left(1+\cos\left(\varphi_\mathbf{k}-\varphi_\mathbf{q}\right)\right) n_{\mathbf{q}-} + \left(1-\cos\left(\varphi_\mathbf{k}-\varphi_\mathbf{q}\right)\right) n_{\mathbf{q}+}\right] \tag{5.21a}$$

$$\varepsilon_+(\mathbf{k}) = \frac{k^2}{2\pi N_0} + \alpha_\mathrm{R} k - \frac{1}{2}\sum_{\mathbf{q}} v_\mathrm{x}(\mathbf{k}-\mathbf{q}) \left[\left(1-\cos\left(\varphi_\mathbf{k}-\varphi_\mathbf{q}\right)\right) n_{\mathbf{q}-} + \left(1+\cos\left(\varphi_\mathbf{k}-\varphi_\mathbf{q}\right)\right) n_{\mathbf{q}+}\right] \tag{5.21b}$$

and the constant C_F, which originates from the Hartree-Fock approximation, is given by

$$C_F = \frac{1}{2}\sum_{\mathbf{k},\mathbf{q}} v_\mathrm{x}(\mathbf{k}-\mathbf{q}) \Big[n_{\mathbf{k}-} n_{\mathbf{q}-} + n_{\mathbf{k}+} n_{\mathbf{q}+} + \frac{1}{2}\left(\cos\left(\varphi_\mathbf{k}-\varphi_\mathbf{q}\right)-1\right)\left(n_{\mathbf{k}-}-n_{\mathbf{k}+}\right)\left(n_{\mathbf{q}-}-n_{\mathbf{q}+}\right)\Big]. \tag{5.22}$$

According to Eq. (5.16), the spin is constrained to the x-y plane and has RSOC-like character, i.e., the spin shows the same orientation as in the pure Rashba model without exchange interaction, which was examined in Section 4.2. The cosine terms in the second line of Eq. (5.22) originate from the inclusion of off-diagonal exchange terms, which are not considered in a pure exchange model without RSOC. The dispersions in Eq. (5.21a) and (5.21b) have the form of a direct sum of the dispersion of the pure Rashba model and a term from electronic exchange interaction. In App. A.8 the cosine terms in the dispersion are set to 1: This preliminary approach decouples the dependence of the bands on the occupation number of the respective other band.

The Helmholtz free energy is obtained by integrating the dispersion over all occupied states in k space and by adding C_F. Therefore the wave-vector dependent occupation numbers $n_{\mathbf{k}\pm}$ have to be known. The dispersion of the lower band, $\varepsilon_-(k)$, displays a linear decrease in k for small wave vectors due to the RSOC. In the pure Rashba model this results in a minimum in the dispersion at finite wave vectors and hence a circular disc of unoccupied states around $k = 0$ at low densities (see Fig. 4.1). The upper band is then unoccupied. Combining this with the rotational symmetry of the problem, we assume that the shape of occupied states in wave-vector space in the lower band is that of an annulus, which is parameterized by two radii, r_{1-} and r_{2-}. Electronic states with $|\mathbf{k}| < r_{1-}$ are empty and states with $r_{1-} \leq |\mathbf{k}| \leq r_{2-}$ are occupied. The contribution of the exchange interaction to the dispersion depends on the radius of unoccupied

[1] If $\Delta n_{\mathbf{k}+-}$ is rotationally symmetric, then there exist solutions $u_\mathbf{k}$ and $v_\mathbf{k}$ that own the same symmetry, as all constituting terms in Eqs. (5.9) are rotationally symmetric. Under the assumptions that $\phi_\mathbf{k} = \pi/2 - \varphi_\mathbf{k}$ it is

$$\begin{aligned}\phi_\mathbf{k} &= \arg\left[\alpha_\mathrm{R} k e^{-i\left(\varphi_\mathbf{k}-\frac{\pi}{2}\right)} + \sum_\mathbf{q} v_\mathrm{x}(\mathbf{k}-\mathbf{q}) u_\mathbf{q} v_\mathbf{q} e^{-i\left(\varphi_\mathbf{q}-\frac{\pi}{2}\right)} \Delta n_{\mathbf{q}+-}\right] \\ &= \arg\left[e^{-i\left(\varphi_\mathbf{k}-\frac{\pi}{2}\right)}\left(\alpha_\mathrm{R} k + \sum_\mathbf{q} v_\mathrm{x}(\mathbf{k}-\mathbf{q}) u_\mathbf{q} v_\mathbf{q} e^{i\left(\varphi_\mathbf{k}-\varphi_\mathbf{q}\right)} \Delta n_{\mathbf{q}+-}\right)\right] \\ &= \frac{\pi}{2} - \varphi_\mathbf{k},\end{aligned}$$

which verifies the self-consistency. The last line follows from the fact that the term in the parantheses is real: With $e^{i(\varphi_\mathbf{k}-\varphi_\mathbf{q})} = \cos\left(\varphi_\mathbf{k}-\varphi_\mathbf{q}\right) + i\sin\left(\varphi_\mathbf{k}-\varphi_\mathbf{q}\right)$, it follows that, after a rotation of $-\varphi_\mathbf{k}$, the summation over the sinus vanishes, as the sinus is antisymmetric, while the remaining terms are symmetric.

states, r_{1-}: For $r_{1-} = 0$ it is most negative for $k = 0$ and increases with k, as the potential $v_{\mathrm{x}}(\mathbf{k}-\mathbf{q}) \propto 1/|\mathbf{k}-\mathbf{q}|$ decreases with distance between $\mathbf{k}$ and $\mathbf{q}$. On the other hand, for finite r_{1-}, the exchange contribution decreases for small k and has a minimum between r_{1-} and r_{2-}. Consequently, the contribution of the exchange interaction to the dispersion is consistent with the occupation. This carries over to $\varepsilon_+(k)$, where the RSOC part increases linearly with k, which alone would render the states around $k = 0$ occupied if electrons reside in the upper band. If these states are occupied, then the exchange interaction increases with k. The radius of occupied electronic states in the upper band is labeled as r_+. For the preliminary results presented in App. A.8 we found that the exchange interaction opens a gap at $k = 0$: This induces a range of electron densities for which all electrons reside in the lower band, while the states around $k = 0$ are occupied. We refer to this phase as P1. However, in the full treatment with non-constant cosine, this phase does not appear, as the gap at $k = 0$ is absent:

$$\varepsilon_-(k=0) = \varepsilon_+(k=0) = -\frac{1}{2}\sum_{\mathbf{q}} v_{\mathrm{x}}(\mathbf{q})\left(n_{\mathbf{q}-} + n_{\mathbf{q}+}\right) \tag{5.23}$$

The integration of the cosine terms in the equation above vanishes due to the rotational symmetry around $k = 0$ of the occupied states. The three radii r_{2-}, r_{1-} and r_+ are determined by the electron density n and the evaluation of Eq. (5.21a) and/or Eq. (5.21b) at the Fermi wave vector. We distinguish between two different phases, which depend on the occupation of the bands:

- $0 < r_{1-} < r_{2-}$, $r_+ = 0$ (P0): The upper band is empty and the electron density is given by the difference $4\pi n = r_{2-}^2 - r_{1-}^2$. The band energy is equal at the inner and outer radius, so that $\varepsilon_-(r_{1-}) = \varepsilon_-(r_{2-})$. These relations identify r_{2-} and r_{1-}.

- $r_{1-} = 0 < r_+ < r_-$ (P2): Electrons reside in the upper band and the density is the sum $4\pi n = r_-^2 + r_+^2$. The equality of the dispersions of the two bands at the Fermi wave vectors, $\varepsilon_-(r_-) = \varepsilon_+(r_+)$, determines r_- and r_+.

The dispersions can be rewritten as function of the three parameters r_{2-}, r_{1-} and r_+. If two bands are occupied, then the Fermi wave vector of the respective other band enters into the dispersion of a given band:

$$\varepsilon_-(k) = \frac{k^2}{2\pi N_0} - \alpha_{\mathrm{R}} k - \frac{1}{4\pi}\frac{e^2}{\epsilon_{\mathrm{eff}}}\begin{cases} I_{r_{2-}}(k) - I_{r_{1-}}(k) + J_{r_{2-}}(k) - J_{r_{1-}}(k) & , r_+ = 0 \\ I_{r_-}(k) + J_{r_-}(k) + I_{r_+}(k) - J_{r_+}(k) & , r_+ > 0 \end{cases} \tag{5.24a}$$

$$\varepsilon_+(k) = \frac{k^2}{2\pi N_0} + \alpha_{\mathrm{R}} k - \frac{1}{4\pi}\frac{e^2}{\epsilon_{\mathrm{eff}}}\Big\{ I_{r_-}(k) - J_{r_-}(k) + I_{r_+}(k) + J_{r_+}(k) \Big\} \tag{5.24b}$$

The function $I_r(k)$ depends on the complete elliptic integral of the second kind $E[x]$ and the incomplete elliptic integral of the second kind $E[\phi, x]$ (see App. A.7),

$$I_r(k) = 4r\left(E\left[\left(\frac{k}{r}\right)^2\right]\Theta\left[r-k\right] + E\left[\arcsin\left(\frac{r}{k}\right)\middle|\left(\frac{k}{r}\right)^2\right]\Theta\left[k-r\right]\right), \tag{5.25}$$

and $J_r(k)$ is given by the expression

$$J_r(k) = \int_0^{2\pi} \mathrm{d}\varphi\, \cos\varphi \left(\sqrt{k^2 - 2kr\cos\varphi + r^2} + k\cos\varphi \log\left[\frac{r - k\cos\varphi + \sqrt{k^2 - 2kr\cos\varphi + r^2}}{k(1-\cos\varphi)}\right]\right).$$

We were unable to solve $J_r(k)$ analytically. The thereby necessary numerical integration did not allow for the determination of the Fermi vectors with sufficient accuracy. These challenges have to be addressed in a later work.

However, the density n_1, which defines the phase transition between P0 and P2, can be identified even without knowledge of all Fermi wave vectors. At n_1 the upper band is not just yet occupied and the radius of unoccupied states in the lower band vanishes, $r_{1-} = 0$. The Fermi wave vectors are then given by $r_{1-} = 0$ and $r_{2-} = r_-$. The functions $I_r(k)$ and $J_r(k)$ in the dispersions simplify to analytical expressions at $k = r$: $I_r(r) = 4r$ and $J_r(r) = \frac{3}{2}c_{11}r$, where $c_{11} \approx 1.10924158$ is the numerical value of the integral defined in Eq. (A.137). As the dispersion is equal for all Fermi wave vectors, and the density is given by $4\pi n_1 = r_-^2$, we can write

$$\begin{aligned} \varepsilon_-(0) &= \varepsilon_-(r_-) \\ 0 &= \frac{r_-^2}{2\pi N_0} - \alpha_\mathrm{R} r_- - \frac{1}{4\pi}\frac{e^2}{\epsilon_\mathrm{eff}}\left(4 + \frac{3}{2}c_{11}\right) r_- \qquad (5.26) \\ \Rightarrow n_1 &= \pi N_0^2 \left[\alpha_\mathrm{R} + \frac{1}{4\pi}\frac{e^2}{\epsilon_\mathrm{eff}}\left(4 + \frac{3}{2}c_{11}\right)\right]^2 \qquad (5.27) \end{aligned}$$

In the pure Rashba model the density above which the second band is occupied is given by $n_1^\mathrm{pure} = \pi N_0^2 \alpha_\mathrm{R}^2$ (see Eq. (4.8) at the beginning of Section 4.2). The exchange interaction increases the capacity of the lower band to hold electrons and shifts the phase boundary between P0 and P2 to larger densities.

The dispersion relations Eq. (5.21a) and (5.21b) in combination with C_F determine the Helmholtz free energy,

$$\begin{aligned} F(n) = &\sum_{\mathbf{k},s=\pm}\left(\frac{k^2}{2\pi N_0} + s\cdot\alpha_\mathrm{R}k\right) n_{\mathbf{k}s} \qquad (5.28) \\ &- \frac{1}{4}\frac{2\pi e^2}{A\epsilon_\mathrm{eff}}\sum_{\mathbf{k},\mathbf{q}}\frac{1}{|\mathbf{k}-\mathbf{q}|}\left[(n_{\mathbf{q}-} + n_{\mathbf{q}+})(n_{\mathbf{k}-} + n_{\mathbf{k}+}) + \cos\left(\varphi_\mathbf{k} - \varphi_\mathbf{q}\right)(n_{\mathbf{q}-} - n_{\mathbf{q}+})(n_{\mathbf{k}-} - n_{\mathbf{k}+})\right] \end{aligned}$$

If only the lower band is occupied, i.e., the system is in phase P0 and $n_{\mathbf{k}+} = 0$, the Helmholtz free energy simplifies to

$$\begin{aligned} F_1(r_{1-}, r_{2-}) &= \sum_\mathbf{k}\left(\frac{k^2}{2\pi N_0} - \alpha_\mathrm{R}k\right) n_{\mathbf{k}-} - \frac{1}{4}\frac{2\pi e^2}{A\epsilon_\mathrm{eff}}\sum_{\mathbf{k},\mathbf{q}}\frac{1+\cos\left(\varphi_\mathbf{k}-\varphi_\mathbf{q}\right)}{|\mathbf{k}-\mathbf{q}|} n_{\mathbf{q}-} n_{\mathbf{k}-} \qquad (5.29) \\ &= \frac{A}{2\pi}\left(\frac{r_{2-}^4 - r_{1-}^4}{8\pi N_0} - \alpha_\mathrm{R}\frac{r_{2-}^3 - r_{1-}^3}{3}\right) - \frac{e^2 A}{16\pi^2\epsilon_\mathrm{eff}}\left[\left(\frac{8}{3} + c_{11}\right)\left(r_{1-}^3 + r_{2-}^3\right)\right. \qquad (5.30) \\ &\qquad \left. - 2I^b_{r_{2-}r_{1-}} - \frac{8}{3}\left(\left(r_{2-}^2 + r_{1-}^2\right) E\left[\frac{r_{1-}^2}{r_{2-}^2}\right] - \left(r_{2-}^2 - r_{1-}^2\right) K\left[\frac{r_{1-}^2}{r_{2-}^2}\right]\right) r_{2-}\right] \end{aligned}$$

$I^b_{r_{2-}r_{1-}}$ is an integral over trigonometric functions (see Eq. (A.134) in App. A.7 for details) and has to be evaluated numerically. $K[x]$ is the complete elliptic integral of the first kind. If both bands are occupied, the Helmholtz free energy is given by

$$\begin{aligned} F_2(r_+, r_-) = &\frac{A}{2\pi}\left(\frac{r_-^4 + r_+^4}{8\pi N_0} - \alpha_\mathrm{R}\frac{r_-^3 - r_+^3}{3}\right) - \frac{e^2 A}{16\pi^2\epsilon_\mathrm{eff}}\left[\left(\frac{8}{3} + c_{11}\right)\left(r_+^3 + r_-^3\right)\right. \qquad (5.31) \\ &\left. - 2I^b_{r_-r_+} + \frac{8}{3}\left(\left(r_-^2 + r_+^2\right) E\left[\frac{r_+^2}{r_-^2}\right] - \left(r_-^2 - r_+^2\right) K\left[\frac{r_+^2}{r_-^2}\right]\right) r_{2-}\right] \end{aligned}$$

The Rashba induced part of the energy depends on the same power in occupation radius as the exchange term, which is already recognizable in the dispersions Eq. (5.21a) and (5.21b):

The exchange potential is proportional to $\propto 1/k$ and the sum over $\mathbf{k}$ adds the dimension of k^2, so that the exchange contribution has the same power in k as $\pm\alpha_\mathrm{R}k$. This carries over to the dependence on the electron density n. The negative sign of the exchange term arises from the fermionic anticommutation relation between operators, while the RSOC contribution is negative as the lower band is considered. In the large density limit, i.e., for $n \gg n_1$, the splitting between the two bands is negligible (see App. A.7), so that approximately the same number of electrons reside in both bands. In this limit $r_+ \approx r_-$ and $2\pi n \approx r_-^2$ are valid and the Helmholtz energy in Eq. (5.31) reduces to

$$F_2^{n\gg n_2}(n) = \frac{An^2}{2N_0} - \frac{8e^2A}{3\sqrt{2\pi}\epsilon_\mathrm{eff}}n^{3/2}, \tag{5.32}$$

The result is independent of the RSOC and the energy of a free, unpolarized electron gas with exchange coupling and exactly the same expression as given by Eq. (3.16). The RSOC contribution is insignificant compared to the kinetic and exchange energy for large densities, as the RSOC terms of the lower and upper band cancel each other out, due to their different signs.

Consequently, the second derivative of the Helmholtz free energy with respect to the electron density, which is of special interest due to its importance for the stability and appearance in the inverse capacitance, is independent of the RSOC for large n.

5.3. Numerical Solution of the Hamiltonian

The results of the previous section were derived by the use of two special, analytically known solutions for the transformation coefficients. The gained advantage of the feasibility of an analytical treatment of the problem has to be contrasted to the imposed restrictions on the possible distributions of occupation numbers $\langle\hat{a}^\dagger_{\mathbf{k}\pm}\hat{a}_{\mathbf{k}\pm}\rangle$, in particular regarding symmetry, due to the employment of the wave vector independent $u_\mathbf{k} = 1/\sqrt{2}$ and rotational symmetric $\phi_\mathbf{k} = \pi/2 - \varphi_\mathbf{k}$.

In this section we allow for all solutions of the transformation coefficients that are in accordance with the self-consistent relations of Eqs. (5.9), which also depend on the occupation numbers $\langle\hat{a}^\dagger_{\mathbf{k}\pm}\hat{a}_{\mathbf{k}\pm}\rangle$. The distribution of occupied states has to minimize the Helmholtz free energy, which is given by the expectation value of the Hamiltonian (5.12). This leads to the three sets $u_\mathbf{k}$, $\phi_\mathbf{k}$ and $\langle\hat{a}^\dagger_{\mathbf{k}\pm}\hat{a}_{\mathbf{k}\pm}\rangle$ of entangled quantities that have to be evaluated successively and each self-consistently by numerical computations. One set of variables was calculated self-consistently while the other two sets were held fixed. After its convergence the next set was fed to a self-consistent loop, while holding the other two sets constant. This procedure was iterated until the control variable, in this case the Helmholtz free energy, converged.

The numerical computations were performed for different sets of parameters. We took $m_0 = 2\,m_e$ and $\epsilon_\mathrm{eff} = 5\ldots50$ for the most part and varied α_R in the range from $0.01\,e\mathrm{V}a_\mathrm{B}$ to $0.5\,e\mathrm{V}a_\mathrm{B}$. For comparison, experimental values of α_R for the electron system at the LAO/STO interface are in the range $0.02\,e\mathrm{V}a_\mathrm{B}$ to $0.1\,e\mathrm{V}a_\mathrm{B}$, as described in Section 4.3.1. Since the kinetic term dominates for high electron densities, the most interesting interplay between RSOC and exchange coupling takes place at low n, which was in the range $n < 40\times10^{-4}a_\mathrm{B}^{-2}$ for the used parameters.

The numerical analysis revealed the existence of more groundstate configurations, which occur besides the phases P0, P1 and P2 (see Fig. 5.1a–c) that were characterized in the previous section:

- P_x1: In this configuration only the lower band is occupied and the transformation coefficients are $u_\mathbf{k} \approx 1$. The projections of the spins on the x-y plane are approximately parallel for all occupied states and their direction, which is described by $\phi_\mathbf{k} \approx \phi$, varies randomly between different calculations. Figure 5.1d displays a scheme of this phase in wave vector space; the directions of the spins in the x-y plane were chosen to point in the

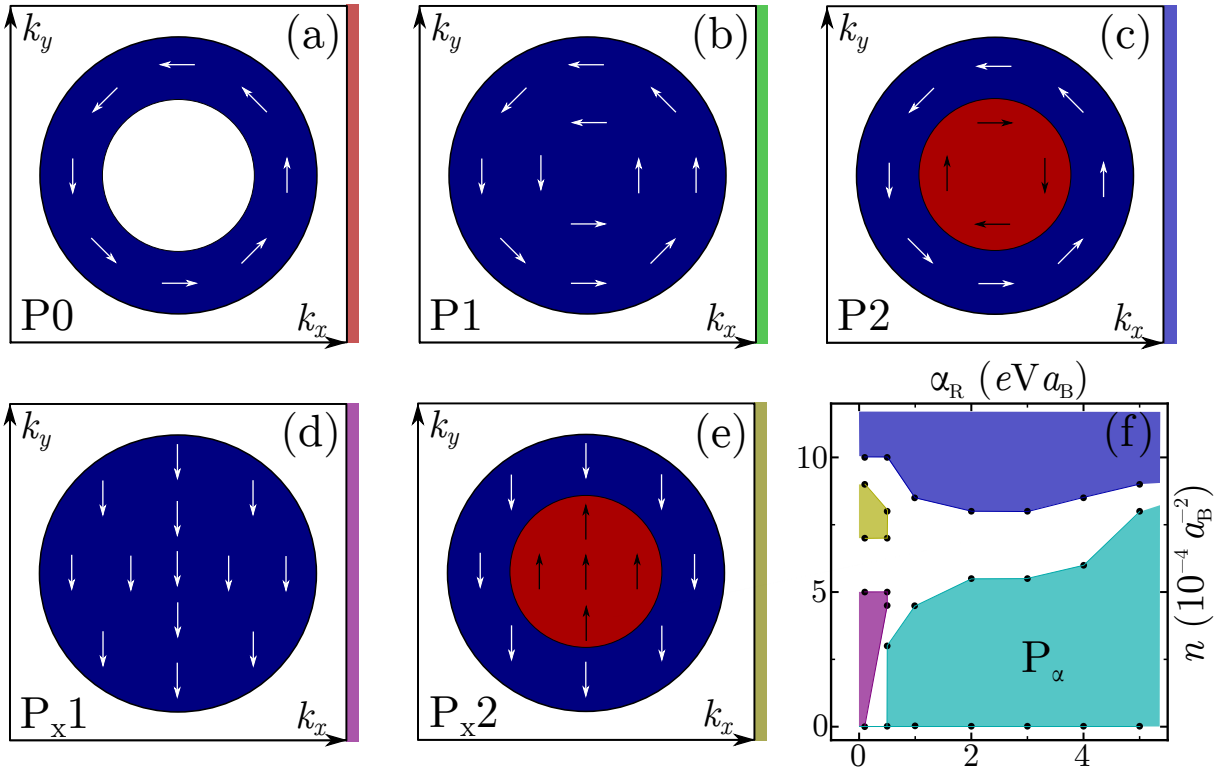

Figure 5.1.: (a)–(e) Schematic plot of the occupation of the lower (blue) and upper band (red) in wave vector space for 5 different symmetric phases found by numerical evaluation. The arrows indicate the projection of the direction of the spin onto the x-y plane; in (d) and (e), which correspond to phases P$_x$1 and P$_x$2, respectively, the spins are nearly completely aligned regarding each other, but the general direction is random. (f) Phase diagram for $m_0 = 2\,m_e$ and $\epsilon_{\text{eff}} = 20$ for different strengths of the RSOC α_{R} and electron densities n. Here blue refers to P2, purple to P$_x$1, yellow to P$_x$2 and cyan to P$_\alpha$, as indicated by the colored bar attached to the right side of (a)–(e). The white areas assign a range of transition between the phases, where, e.g., the spin rotates significantly more than zero but less than π when considered along the full diameter.

$-y$-direction. For $u_{\mathbf{k}} \approx 1$ the character of the new basis state $|\mathbf{k}, -\rangle$ is for the most part identical to the character of the old basis state $|\mathbf{k}, \downarrow\rangle$. This applies especially to the spin components, which are described by Eq. (5.16): An increase of $u_{\mathbf{k}}$ from $1/\sqrt{2}$, for which the spin lies completely in the x-y plane, tilts the spin out of this plane until for $u_{\mathbf{k}} = 1$ the spin points in z direction.

- P$_x$2: This phase possesses the same values $u_{\mathbf{k}} \approx 1$ and $\phi_{\mathbf{k}} \approx \phi$ for the transformation coefficients as P$_x$1, but both bands are occupied (Fig. 5.1e). The spin in the upper band is antiparallel to the spin in the lower band.

- Besides the two phases above, which exhibit similiar characteristics regarding the spin as a system without RSOC, we found also intermediate phases with $1/\sqrt{2} < u_{\mathbf{k}} < 1$. The transitions between the two phases above and P0, P1 and P2 are for the most part continuous, so that these interjacent groundstate configurations appear in between. They are indicated by the white region in the phase diagram in Fig. 5.1f.[2] The spin of these intermediate phases is neither completely parallel nor rotationally symmetric around 0 as for the analytic phases. If one goes along the diameter of the occupied k-space states in

[2]The white areas also indicate parameter regions for which the self-consistent loops did not converge on a reasonable timescale.

one band, the spin projection in the x-y plane will flip its sign for P0, P1 and P2 and retain its direction for P$_x$1 and P$_x$2. In the intermediate phases the direction of the spin will change by an angle larger than 0 but smaller than π. Electron systems in these transition phases, P$_x$1 or P$_x$2, exhibit a net spin polarization if both bands are unequal populated. This has to be contrasted to P0, P1 and P2, where the combined effect of the rotational symmetry of both the spin direction and the occupation distribution in k space prevents any spin polarization.

- P$_\alpha$: The rotation symmetry of the occupied states around 0 in k space, which all the previously described phases feature, is broken in this state (Fig. 5.2). This results in a finite center of wave vectors (COW) $\mathbf{c} = 1/A \sum_{\mathbf{k},s=\pm} \mathbf{k} \cdot n_{\mathbf{k},s}$. The transformation coefficients $u_\mathbf{k}$ are wave vector independent, $u_\mathbf{k} = 1/\sqrt{2}$. The spin part in the x-y plane is perpendicular to $\mathbf{c}$ for the wave vectors which lie on the straight line through 0 defined by the direction of $\mathbf{c}$.

The self-consistent relations for the transformation coefficients $u_\mathbf{k}$, as given in Eq. (5.9), sum only over the difference in occupation between the two bands. For high densities both bands are occupied and $n_{\mathbf{q}-} - n_{\mathbf{q}+}$ is non-zero only on an annulus in k space. The inner radius of this annulus, which corresponds to the radius of occupied states in the upper band, increases with n. This induces that the terms in Eq. (5.9) that depend on the exchange potential, which decreases with distance between two wave vectors as $v_\mathrm{x}(\mathbf{k}-\mathbf{q}) \propto 1/|\mathbf{k}-\mathbf{q}|$, become less important as compared to the term $\alpha_\mathrm{R} k$. Consequently, the denominator in the definition of $u_\mathbf{k}$ is much larger than the corresponding nominator for large densities, so that in this limit $u_\mathbf{k} = 1/\sqrt{2}$ is the only solution. The same arguments, i.e., the domination of the RSOC contribution over the exchange term in the self-consistent equations for $\phi_\mathbf{k}$, lead to $\phi_\mathbf{k} = \frac{\pi}{2} - \varphi_\mathbf{k}$, so that for large n the system is always in P2.

The solutions $u_\mathbf{k} \approx 1$ of P$_x$1 and P$_x$2 require, according to Eq. (5.9) and in absence of a magnetic field, that

$$\left(\sum_\mathbf{q} \frac{2\pi e^2}{A \epsilon_\mathrm{eff} |\mathbf{k}-\mathbf{q}|} A_\mathbf{q} \right)^2 \gg 4 \left| i\alpha_\mathrm{R} k e^{-i\varphi_\mathbf{k}} + \sum_\mathbf{q} \frac{2\pi e^2}{A \epsilon_\mathrm{eff} |\mathbf{k}-\mathbf{q}|} B_\mathbf{q} \right|^2 , \tag{5.33}$$

where $A_\mathbf{q}$ and $B_\mathbf{q}$ are given by Eq. (5.10) and (5.11),

$$A_\mathbf{q} = \left(u_\mathbf{q}^2 - v_\mathbf{q}^2\right)\left(n_{\mathbf{q}-} - n_{\mathbf{q}+}\right), \qquad B_\mathbf{q} = u_\mathbf{q} v_\mathbf{q} e^{i\phi_\mathbf{q}} \left(n_{\mathbf{q}-} - n_{\mathbf{q}+}\right)$$

The term including $B_\mathbf{q}$ is small compared to the term on the left-hand side of condition (5.33) for $u_\mathbf{k} \approx 1$, as then $v_\mathbf{q} \approx 0$. Hence the condition is satified if $4\alpha_\mathrm{R}^2 k^2$ is much smaller than the left-hand side, which can be fulfilled for small ϵ_eff compared to α_R and small densities. As only wave vectors of singly occupied states are relevant for the transformation coefficients, for smaller densities the summation over $1/|\mathbf{k}-\mathbf{q}|$ becomes larger compared to $|\mathbf{k}|$. This concurs with the phase diagram of Fig. 5.1f, where P$_x$1 and P$_x$2 were found only for $\alpha_\mathrm{R} \lesssim 0.05\, e\mathrm{V}a_\mathrm{B}$ at $\epsilon_\mathrm{eff} = 20$. The coefficients $\phi_\mathbf{k}$ are given by the direction of the complex number in the absolute value of condition (5.33). If the exchange term in the absolute value is larger than the RSOC term due to a sufficiently small $\alpha_\mathrm{R} \cdot \epsilon_\mathrm{eff}$, then $\phi_\mathbf{k} \approx const.$ is a solution, which yields in combination with $u_\mathbf{k} \approx 1$ the phases P$_x$1 and P$_x$2.

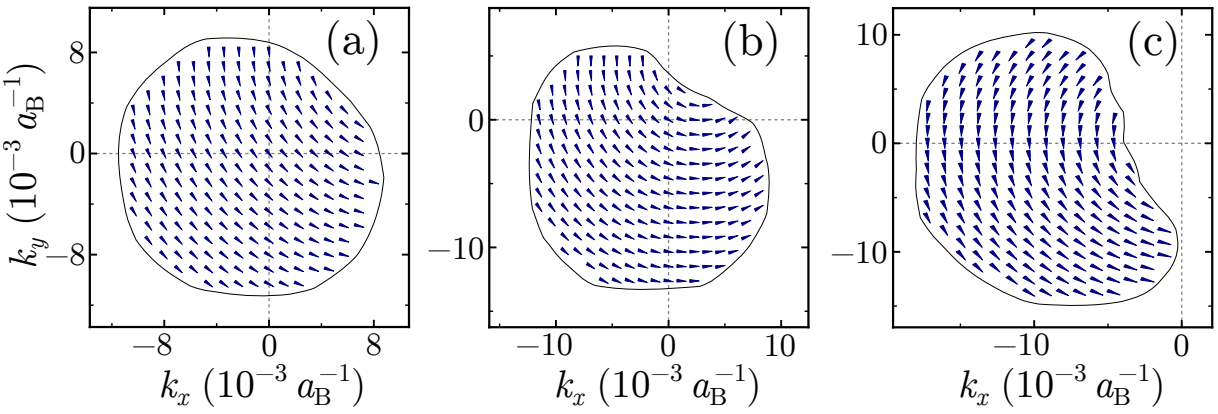

Figure 5.2.: Occupation of k-space vectors for the different values of $\alpha_\mathrm{R} = 0.2\,e\mathrm{V}a_\mathrm{B}$ (a), $\alpha_\mathrm{R} = 0.5\,e\mathrm{V}a_\mathrm{B}$ (b) and $\alpha_\mathrm{R} = 1.0\,e\mathrm{V}a_\mathrm{B}$ (c), where $n = 3 \times 10^{-4}\,a_B^{-2}$, $m_0 = 2\,m_e$ and $\epsilon_\mathrm{eff} = 20$ was used for all plots. The arrowheads mark the direction of the spin in the x-y plane. The average of k vectors of the system, which is in phase P_α for these parameters, is moved further away from the zero point in a random direction for larger values of α_R. The spin at the center of k vectors is perpendicular to this direction.

The phase P_α breaks the rotational symmetry of occupied wave vectors and is found for the value $u_\mathbf{k} = 1/\sqrt{2}$ of the transformation coefficients. The Helmholtz free energy for this $u_\mathbf{k}$ and an empty upper band, $n_{\mathbf{k}+} = 0$, is then

$$F^{\frac{1}{\sqrt{2}}} = \sum_\mathbf{k} \frac{k^2}{2\pi N_0} n_{\mathbf{k}-} - \sum_\mathbf{k} \left| i\alpha_\mathrm{R} k e^{-i\varphi_\mathbf{k}} + \frac{1}{2} \sum_\mathbf{q} \frac{2\pi e^2}{A\epsilon_\mathrm{eff}|\mathbf{k}-\mathbf{q}|} e^{i\phi_\mathbf{q}} n_{\mathbf{q}-} \right| n_{\mathbf{k}-} + \frac{1}{4} \sum_{\mathbf{k},\mathbf{q}} \frac{2\pi e^2}{A\epsilon_\mathrm{eff}|\mathbf{k}-\mathbf{q}|} \left(\cos\left(\phi_\mathbf{k} - \phi_\mathbf{q}\right) - 1\right) n_{\mathbf{k}-} n_{\mathbf{q}-} \tag{5.34}$$

The term in the second line is negative except for $\phi_\mathbf{k} = \phi_\mathbf{q}$, and its absolute value is smaller than the absolute value of the exchange term in the first line. Due to the negative sign in the first line in front of the absolute value, the Helmholtz free energy is minimized for a configuration that maximizes the exchange contribution. As the potential of this term falls of as $1/|\mathbf{k}-\mathbf{q}|$, it is maximized for a distribution of occupied states $n_{\mathbf{k}-}$ in form of a circular disc, where the center of the disc does not affect the energy. The latter is in contrast to the kinetic contribution, which is also minimized for a circular disc of occupied wave vector states, but only if it is centered around $k = 0$. On the other hand, the contribution from the RSOC term is minimal for occupied states as far away from $k = 0$ as possible. If only the kinetic and RSOC term are present, their combination leads to an annulus configuration of $n_{\mathbf{k}-} = 1$ at low density, while for a system with only kinetic and exchange term a circular disc centered at $k = 0$ minimizes the energy. So imagine we start in a system with low density without exchange interaction and then increase its magnitude. Without or with weak exchange interaction the groundstate configuration is an annulus, as the kinetic cost of placing the electrons in states away from $k = 0$ is overcome by the gain from the RSOC term. If the contributions of the exchange interaction and the RSOC to the energy are of similar order, then both energies are minimized by a configuration that both occupies states away from $k = 0$ (due to RSOC) and lumps them together (due to exchange coupling) in k space. In a picture, this corresponds to cutting the annulus open at a random position and pushing the two new ends towards the opposite of the cut, while the movement occurs on the ring of the old annulus. The shape of occupied wave vector states approaches a circular disc with its center offset from $k = 0$ for very large exchange interactions.

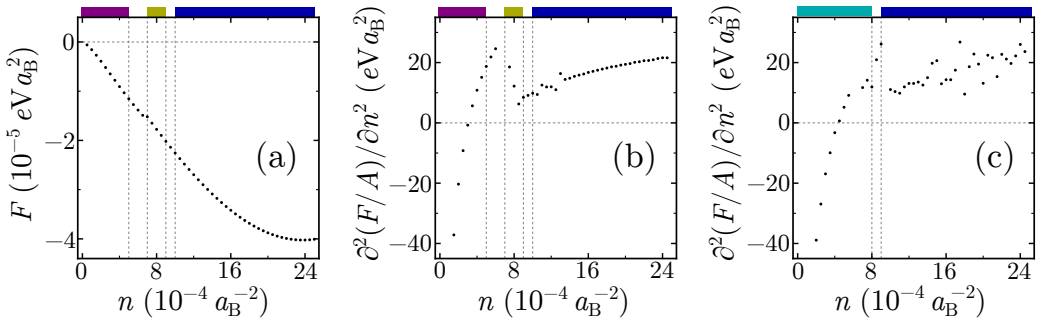

Figure 5.3.: (a) Free energy for $m_0 = 2\,m_e$, $\epsilon_{\text{eff}} = 20$ and $\alpha_{\text{R}} = 0.01\,e\text{V}a_{\text{B}}$ for the numerical evaluation. (b) Second derivative of the free energy for the numerical solution and the parameters of (a). The system is in P$_x$1 for $n < 5 \times 10^{-4}\,a_{\text{B}}^{-2}$, in P$_x$2 for $7 \times 10^{-4}\,a_{\text{B}}^{-2} < n < 9 \times 10^{-4}\,a_{\text{B}}^{-2}$ and in P2 for $n > 10 \times 10^{-4}\,a_{\text{B}}^{-2}$, as indicated by the colored bars on top. (c) Second derivative of the Helmholtz free energy for $m_0 = 2\,m_e$, $\epsilon_{\text{eff}} = 20$ and $\alpha_{\text{R}} = 0.5\,e\text{V}a_{\text{B}}$. The phase of the system is P$_\alpha$ for $n < 8 \times 10^{-4}\,a_{\text{B}}^{-2}$ and P2 for $n > 9 \times 10^{-4}\,a_{\text{B}}^{-2}$. The color of the bars on top of the plots refers to the color of the phases as introduced in Fig. 5.1.

For a given and constant electron density the radii of the annulus in a system without exchange interaction increase with α_{R}[3]. This carries over to phase P$_\alpha$, as depicted in Fig. 5.2, where α_{R} is increased from $\alpha_{\text{R}} = 0.2\,e\text{V}a_{\text{B}}$ (a) to $\alpha_{\text{R}} = 1.0\,e\text{V}a_{\text{B}}$ (c). It is clearly visible how the COW moves away from the zero point. The deformation of the occupied states increases with α_{R}. For small RSOC the comparatively strong exchange contribution dominates and the Fermi surface is more circle like, while at large RSOC the exchange contribution is roughly of the same order, so that the occupied states assume the form of a "kidney".

We found the phase P$_\alpha$ to be present for all strengths of RSOC examined if the exchange interaction exceeded a threshold. Yet, the density at which the groundstate is an annulus without exchange, i.e., for which the kinetic energy does not dominate over the RSOC energy, becomes very small for small α_{R}. For example, at $m_0 = 2\,m_e$ and $\alpha_{\text{R}} = 10^{-3}e\text{V}a_{\text{B}}$, the density below which an annulus exists is given, according to $\mu_1 = 0$ in Eq. (4.8), by $n \lesssim 1.7 \times 10^{-9} a_{\text{B}}^{-2}$.

The direction of the spin in the x-y plane in phase P$_\alpha$ can be identified by examining Eq. (5.34). If the RSOC and exchange contribution are roughly of the same order, then the energy is minimized by maximizing the sum in the absolute value. There both summands are complex numbers, so that the absolute value is largest if both complex numbers have the same polar angle, i.e., if the exchange term points in the same direction as $ie^{-i\varphi_{\mathbf{k}}}$. For a given wave vector $\mathbf{k}$, the exchange sum over $\mathbf{q}$ is maximal for the state $\mathbf{k}$ that is at the center of the distribution of occupied wave vectors, as the exchange potential decreases with $1/|\mathbf{k} - \mathbf{q}|$. This is the case for the COW $\mathbf{k}_c = \mathbf{c}$, so that for this $\mathbf{k}_c$ the complex numbers in the absolute value of Eq. (5.34) possess the same polar angle, i.e., $\phi_{\mathbf{k}_c} = \frac{\pi}{2} - \varphi_{\mathbf{k}_c}$. This justifies why the direction of the spin in Fig. 5.2 is always perpendicular to the COW $\mathbf{c}$. If now the exchange coupling is increased as compared to the RSOC, the term $ie^{-i\varphi_{\mathbf{k}}}$ looses influence in the self-consistency relations for $\phi_{\mathbf{k}}$, which are given by the direction of the absolute value in Eq. (5.34). Then the $\phi_{\mathbf{k}}$ align to one value, which is in this case given by the largest contribution, i.e., $\varphi_{\mathbf{k}_c}$. The comparison between Fig. 5.2c and Fig. 5.2a confirms the increased alignment of the spin direction with larger relative value of the exchange coupling.

Note that the direction of the COW $\mathbf{c}$ and hence the spin orientation are completely random due to the rotationally symmetry of the wave vector space. An infinitesimal small in-plane

[3] In Section 4.2 it was derived for the Rashba model that the minimum in energy is given at $k = \pi N_0 \alpha_{\text{R}}$ for a system with kinetic and RSOC term only.

magnetic field breaks this symmetry and couples to the spin direction. As the spin direction is connected to the COW, a finite magnetic field aligns the center of wave vectors $\mathbf{c}$.

Figures 5.3b and 5.3c compare the second derivatives of the Helmholtz free energy F (see Fig. 5.3a) for $\alpha_\mathrm{R} = 0.01\,e\mathrm{V}a_\mathrm{B}$ and $\alpha_\mathrm{R} = 0.5\,e\mathrm{V}a_\mathrm{B}$, respectively. Both systems are in P2 for $n \gtrsim 10 \times 10^{-4}\,a_\mathrm{B}^{-2}$. The system with stronger RSOC is in phase P_α below this density, while the other system is at P_x1 and P_x2. For sufficiently small densities n the compressibilities of both systems are negative, but for $\alpha_\mathrm{R} = 0.5\,e\mathrm{V}a_\mathrm{B}$ the density range of $\kappa^{-1} < 0$ is larger than for the weaker RSOC.

We investigated the interplay between exchange and Rashba spin-orbit coupling for a free two-dimensional electron gas. We found the two analytical solutions with predetermined symmetry P0 and P2 that are Rashba-like regarding the spin. P0 and P2 are reminiscent of the pure Rashba model. The full numerical treatment of the problem revealed, besides P_x1 and P_x2 and intermediate phases, a phase that breaks spontaneously the rotation symmetry of the problem. P_α occurs at densities for which the kinetic and RSOC energy are comparable in size and the exchange energy is not smaller than the RSOC energy. This phase features a finite center of wave vectors (COW) $\mathbf{c}$ with a random direction, which can be aligned by an infinitesimal in-plane magnetic field. As a finite COW corresponds to an electric current in the system, the phase P_α needs further examination. To do this, one could map the system on the surface of a tube by use of periodic boundary conditions and check for the presence of a current. There are also possibilities to avoid the finite current by modifying the Fermi surface: For example, one could construct a distribution of occupied states by two deformed circular discs opposing each other at a finite distance from $k = 0$, so that their combined COW is $\mathbf{c} = 0$. The groundstate is then determined by comparison of the Helmholtz free energy of different phases. It has to be emphasized that the Hartree term of a phase lacking the rotational symmetry does not necessarily compensate the energy of the positive background charge completely. A future analysis should incorporate this additional energy term for phase P_α. However, for very large exchange interactions the groundstate features rotational symmetry around the COW even in P_α, so that the deviation of the Hartree energy from the background energy decreases with the strength of the electron-electron interaction.

6. The Two-Dimensional Extended Hubbard Model

This chapter is based on Ref. [32] and Ref. [121].

6.1. The Extended Hubbard Model with Attractive Nearest-Neighbor Interaction

John Hubbard was the eponym for a model he introduced to describe electrons in $3d$ transition metals [122]. It was also proposed at the same time independently by Gutzwiller for the characterization of the metal-insulator transition [123] and by Kanamori for the characterization of itinerant ferromagnetism [124]. The model was able to explain the (Mott-Hubbard) metal-insulator transition [125, 126], antiferromagnetism [127, 128] and recently attracted attention as model for high-T_c superconductors [129, 130, 131].

The Hubbard model is based on a tight-binding description. The positions of the ions that provide the electronic states of the conduction electrons form a lattice. The small spatial extent of the electronic wave functions around the ions forces two electrons that reside at the same lattice site to be close together on average, which entails a large Coulomb energy. This particle-particle interaction is implemented in the Hubbard model by an on-site repulsion U. The single-particle part, characterized by the amplitudes t_{ij}, describes the hopping between two sites i and j. It is remarkable that this simple model is able to describe such a wide range of phenomena. An important role plays the occurrence of a "extended" (kinetic) part and a "local" (interaction) part and their interplay. This dichotomy appears also in many other important theoretical models, as, e.g., the φ^4 quantum field theory and the Kondo problem [132].

The Hubbard model represents the minimal model for the treatment of electronic correlations. It includes only the Coulomb interaction between electrons on the same lattice site. Already Hubbard noted [122] that in transition metals the unscreened Coulomb interactions between different sites are not small compared to the on-site contributions. The inclusion of the electrostatic interactions between electrons on different sites constitutes the so-called extended Hubbard model (eHm). It features an even richer phase diagram than the Hubbard model, including charge- and spin-density waves and phase separation [133, 134]. [135] In this work we focus on the homogeneous phase. The general Hamiltonian of the eHm is given by

$$\hat{\mathcal{H}}_{\mathrm{eHm}} = \sum_{i,j,\sigma} t_{ij} \hat{c}^{\dagger}_{i\sigma} \hat{c}_{j\sigma} + U \sum_{i} \hat{n}_{i\uparrow} \hat{n}_{i\downarrow} + \sum_{i,j} V_{ij} \hat{n}_i \hat{n}_j. \tag{6.1}$$

Here $\hat{c}^{\dagger}_{i\sigma}$ creates an electron with spin σ at site i, $\hat{n}_{i\sigma} = \hat{c}^{\dagger}_{i\sigma} \hat{c}_{i\sigma}$ is the occupation number operator and $\hat{n}_i = \hat{n}_{i\uparrow} + \hat{n}_{i\downarrow}$ is valid. V_{ij} is the matrix element of the Coulomb interaction between electrons at the (different) sites i and j and t_{ij} the matrix element for the hopping of electrons between site i and j. Both matrix elements decay fast with increasing distance between lattice sites. Hence we set all t_{ij} to zero, except for the hopping between nearest-neighbor (nn) sites, where $t^{nn}_{ij} \equiv t$, and the hopping between next-nearest neighbor (nnn) sites, where $t^{nnn}_{ij} \equiv t'$. Also, the matrix elements V_{ij} are restricted to be only non-vanishing for the interaction between

nn sites and for this case $V_{ij}^{nn} \equiv V$ can be written. All our evaluations are taken on a square lattice.

Typically, the Coulomb interaction between electrons on nearest-neighbor sites on a lattice is repulsive. However, under certain conditions the nn interaction can be attractive, as has been demonstrated for iron pnictides [136, 137]: The Fe atoms form a square lattice, which is sandwiched between two layers of As atoms. The hybridization of the electronic bands based on the iron $3d$ states, which host the conduction electrons, with the As states is small. As the arsenic ions possess a large radius, their polarizability is huge, so that the electrons on the Fe sites are surrounded by polarized As ions, which induces electronic polarons [136, 137]. The interaction of such polarons—in combination with a Fe-As-Fe bond angle smaller than 90°—results in an attractive nn Coulomb interaction [136]. This mechanism does not render the on-site interaction U negative, although the dressing of the electrons screens their interaction and thus reduces U: For the inter-site interaction term the electrons reside on different lattice sites and only the two As ions between them are "shared". On the other hand, for the on-site interaction term both electrons are surrounded by the same As ions. It is possible that other degrees of freedom, e.g., strong electron-lattice coupling, may induce polaronic effects that enhance an attractive nn interaction [138]. Soft-X-ray angle-resolved photoelectron spectroscopy identified polaronic effects in the LAO/STO heterostructure [139], so that $V < 0$ is conceivable in this material. The formation of polarons in LAO/STO was also investigated theoretically by a new "second principle" method based on density-functional theory [140].

In this chapter we analyze the case of negative V for the most part. An attractive electron-electron interaction may render the compressibility of the system negative: If the density in the system increases, the energy originating from the inter-site interaction decreases due to the negative sign of V, which may induce a decrease of the chemical potential.

6.2. The Slave-Boson Approach

As the Hamiltonian (6.1) contains four-operator terms due to the electron-electron interaction, approximate theories have to be applied for its solution. One of them is the so-called slave-boson (SB) approach, which is briefly sketched out in this section. More technical details can be found in Ref. [121] or [141]. Note that all the SB calculations were performed by an expert in this field, Raymond Frésard[1].

The slave-boson (SB) approach was introduced by Barnes [142, 143] to treat the single impurity Anderson model. Shortly afterwards this method was modified by Kotliar and Ruckenstein for the application to the Hubbard model [19] and then generalized to spin rotationally invariant (SRI) form by Wölfle *et al.* [144, 145]. The agreement between the SB Kotliar-Ruckenstein SRI approach and other numerical methods, is very good: For example, the deviations from the results produced by Monte Carlo simulations are quite small for groundstate energies [146] and for charge and spin structure factors [147]. It has also been demonstrated that the paramagnetic mean-field solution of the KR SB approach is identical to the Gutzwiller approximation [19].

Due to the on-site interaction U in the Hubbard model, the state of an electron at a given lattice site depends on the possible presence of a second electron at the same lattice site. Electrons on doubly occupied lattice sites possess a higher energy and for strong U their contribution to the low energy physics is quite small (of order t/U), which leads effectively to a projection of the Hilbert space onto a subspace devoid of doubly occupied states [148]. The slave-boson approach incorporates such a projection inherently by introduction of auxiliary bose fields: In the Hubbard model, a lattice site i is either empty, singly occupied or doubly occupied, so that the four possible states are $|0, i\rangle$, $|\downarrow, i\rangle$, $|\uparrow, i\rangle$ and $|\uparrow\downarrow, i\rangle$. Kotliar and Ruckenstein (KR) [19]

[1] Normandie Université, ENSICAEN, UNICAEN, CNRS, CRISMAT, Caen, France

related four bosonic fields e_i, $p_{i\downarrow}$, $p_{i\uparrow}$ and d_i to these states. The bosonic fields satisfy the Bose commutation relations. By applying these fields and the fermionic creation operators $f^\dagger_{i\sigma}$, which creates an electron with spin σ at site i, on the vacuum $|\,\rangle$

$$|0,i\,\rangle = e_i^+|\,\rangle, \qquad |\sigma,i\,\rangle = f^\dagger_{i\sigma}p^+_{i\sigma}|\,\rangle, \qquad |\uparrow\downarrow,i\,\rangle = d_i^+ f^\dagger_{i\downarrow}f^\dagger_{i\uparrow}|\,\rangle, \tag{6.2}$$

one recovers the local electronic states at site i. The introduction of additional fields increases the number of degrees of freedom, which is compensated by local constraints that the number operators of the bosonic fields have to fulfill.[2] Note that due to the fields $p_{i\downarrow}$ and $p_{i\uparrow}$, which assume a spin quantization axis, the spin-rotation invariance in boson space is broken, which may lead to qualitatively wrong results in approximate treatments of the problem [144]. In the KR approach the physical Hilbert space of fermion states is embedded in a much larger Hilbert space of auxiliary bosons, which do not possess spin-rotation invariance. Approximate treatments have therefore carefully to project on the SRI subspace [144]. To solve this problem, Wölfle *et al.* suggested in their SRI formulation [144] of the KR SB approach the replacement of $p_{i\sigma}$ by the 2×2 spin matrix operator $p_{i\sigma\sigma'}$, which induces the spin-rotation invariance from the outset. Then the state $|\sigma,i\,\rangle$ can be constructed by a scalar $p_{i,0}$ and a vector $\mathbf{p}_i = (p_{i,x}, p_{i,y}, p_{i,z})$:

$$|\sigma,i\,\rangle = \sum_{\sigma'} p^+_{i\sigma\sigma'} f^\dagger_{i\sigma'}|\,\rangle, \qquad p^+_{i\sigma\sigma'} = \frac{1}{2}\sum_{\mu=0,x,y,z} p^+_{i,\mu}\tau^\mu_{\sigma\sigma'}, \tag{6.3}$$

where τ^μ are the Pauli matrices for $\mu = x, y, z$ and the unity matrix for $\mu = 0$. In the new Hilbert space with the bosonic fields, the Hamiltonian of the problem becomes bi-linear in the fermionic fields: For example, the operators for the on-site interaction, $\hat{n}_{i\uparrow}\hat{n}_{i\downarrow}$, which are four-fermion terms, are replaced by products of two fields $d_i^+ d_i$.

In the KR SB formulation, the fermionic fields can easily be integrated out in the partition function Z, which incorporates the constraints by time-independent Lagrange multipliers, so that the result depends only on the bosonic fields. However, the resulting partition function permits an exact calculation only for special models, like, e.g., the Ising chain [149]. Further analyses are therefore conducted within the framework of the saddle-point approximation.

The extended Hubbard model we are interested in, i.e., which is characterized by Hamiltonian (6.1) with only nn and nnn hopping and nn Coulomb interaction V, was evaluated in the slave-boson Kotliar-Ruckenstein spin rotationally invariant approach [121, 141]. Then, in the translational invariant paramagnetic phase, all the local bosonic fields become independent of the site. It is also interesting to note that only the $k = 0$ component of the Fourier-transformed inter-site Coulomb interaction $V_{\mathbf{k}}$ is relevant for the saddle-point equations. Hence, the results of the SB evaluation in this work depend only on the zero-momentum Fourier component and not on the exact structure of the screened inter-site interaction $V_{\mathbf{k}}$ and are thus applicable to more general situations.

The one-loop approximation allows the calculation of the charge and density fluctuations around the saddle point. In the KR SB formulations the spin and charge degrees of freedom are decoupled. This carries over to the charge susceptibility $\chi_c(k)$, which depends only on the bosonic fields e_k and d_k. Here $k = (\mathbf{k}, \omega)$ denotes both the wave vector and the frequency. In the long wavelength and low frequency limit, one can recover the symmetric Landau parameter F_0^s from the charge susceptibility. The other two quantities utilized in this chapter, the effective mass m^* and the Helmholtz free energy F, are derived directly from the saddle-point evaluation.

[2] The bosonic fields are "enslaved" by these conditions.

6.3. Hartree-Fock Evaluation and Comparison to Slave-Boson Results

For the restriction to nn and nnn hopping and only nn Coulomb interaction, the Hamiltonian (6.1) of the extended Hubbard model reduces to

$$\hat{\mathcal{H}} = \sum_{\langle i,j\rangle,\sigma} t_{ij}\hat{c}^\dagger_{i\sigma}\hat{c}_{j\sigma} + U\sum_i \hat{n}_{i\uparrow}\hat{n}_{i\downarrow} + V\sum_{\langle i,j\rangle}\hat{n}_i\hat{n}_j. \tag{6.4}$$

Here $\langle i,j\rangle$ denotes the summation over nearest and next-nearest neighbors in the kinetic term and over nearest neighbors in the V term, whereby each pair of (i,j) is counted only once. The Hamiltonian can be decomposed into a sum of kinetic contribution $\hat{\mathcal{H}}_t$, on-site contribution $\hat{\mathcal{H}}_U$ and inter-site contribution $\hat{\mathcal{H}}_V$. The Fourier transformation of these summands yields

$$\hat{\mathcal{H}}_t = -\sum_{\sigma,\mathbf{k}} \left\{2t\left[\cos\left(ak_x\right)+\cos(ak_y)\right] + 4t'\cos(ak_x)\cos\left(ak_y\right)\right\}\hat{c}^\dagger_{\mathbf{k}\sigma}\hat{c}_{\mathbf{k}\sigma} \tag{6.5a}$$

$$\hat{\mathcal{H}}_U = \frac{U}{A}\sum_{\mathbf{k},\mathbf{p},\mathbf{q}} \hat{c}^\dagger_{\mathbf{k}+\mathbf{q}\uparrow}\hat{c}_{\mathbf{k}\uparrow}\hat{c}^\dagger_{\mathbf{p}-\mathbf{q}\downarrow}\hat{c}_{\mathbf{p}\downarrow} \tag{6.5b}$$

$$\hat{\mathcal{H}}_V = \frac{V}{A}\sum_{\sigma,\sigma'}\sum_{\mathbf{k},\mathbf{q}} \left\{-\left[\cos a(q_x-k_x)+\cos a(q_y-k_y)\right]\hat{c}^\dagger_{\mathbf{q}\sigma}\hat{c}_{\mathbf{q}\sigma'}\hat{c}^\dagger_{\mathbf{k}\sigma'}\hat{c}_{\mathbf{k}\sigma} + 2\hat{c}^\dagger_{\mathbf{k}\sigma}\hat{c}_{\mathbf{k}\sigma}\hat{c}^\dagger_{\mathbf{q}\sigma'}\hat{c}_{\mathbf{q}\sigma'}\right\}, \tag{6.5c}$$

where A is the area of the system and a the lattice spacing. The mean-field approximation produces an expression bi-linear in the operators:

$$\hat{\mathcal{H}}^{\mathrm{MFA}}_U = U\sum_{\mathbf{k},\sigma} n_{-\sigma}\hat{c}^\dagger_{\mathbf{k}\sigma}\hat{c}_{\mathbf{k}\sigma} - UAn_\downarrow n_\uparrow \tag{6.6}$$

$$\begin{aligned}\hat{\mathcal{H}}^{\mathrm{MFA}}_V = {} & V\sum_{\mathbf{k},\sigma}\left\{4(n_\uparrow+n_\downarrow) - \frac{2}{A}\sum_{\mathbf{q}\neq\mathbf{k}}\left[\cos a(q_x-k_x)+\cos a(q_y-k_y)\right]n_{\mathbf{q}\sigma}\right\}\hat{c}^\dagger_{\mathbf{k}\sigma}\hat{c}_{\mathbf{k}\sigma} \\ & + \frac{V}{A}\sum_\sigma\sum_{\substack{\mathbf{k},\mathbf{q}\\ \mathbf{k}\neq\mathbf{q}}}\left[\cos a(q_x-k_x)+\cos a(q_y-k_y)\right]n_{\mathbf{q}\sigma}n_{\mathbf{k}\sigma} - 2VA(n_\uparrow+n_\downarrow)^2.\end{aligned} \tag{6.7}$$

Here $n_\sigma = 1/A\sum_{\mathbf{q}} n_{\mathbf{q}\sigma} = 1/A\sum_{\mathbf{q}}\langle\hat{c}^\dagger_{\mathbf{q}\sigma}\hat{c}_{\mathbf{q}\sigma}\rangle$ is the density of electrons with spin σ. The Hartree term is composed of $\hat{\mathcal{H}}^{\mathrm{MFA}}_U$ and the first and the last summands of $\hat{\mathcal{H}}^{\mathrm{MFA}}_V$ in Eq. (6.7), while the remaining summands of Eq. (6.7) form the Fock term.

The dispersion $\varepsilon_\sigma(\mathbf{k})$ is given by the terms that are multiplied with $\hat{c}^\dagger_{\mathbf{k}\sigma}\hat{c}_{\mathbf{k}\sigma}$ in Eq. (6.5a), (6.6) and (6.7). The on-site interaction (6.6) increases the energy of band σ with the filling of band $-\sigma$. The dispersion $\varepsilon_\sigma(\mathbf{k})$ displays two[3] van Hove singularities (vHs) at $\mathbf{k}=(0,0)$ and $\mathbf{k}=(0,\pi)/\mathbf{k}=(\pi,0)$. The vHs at $\mathbf{k}=(0,0)$ appears at zero filling, independent of the parameters, while the position of the second vHs at $\mathbf{k}=(0,\pi)$ depends on the magnitude of the nnn hopping t'/t: For $t'=0$ the vHs occurs always at half filling. For negative values of t' the position of the vHs is moved to lower fillings and depends on the inter-site interaction if the Fock term is included.

The mean field Hamiltonian $\hat{\mathcal{H}}^{\mathrm{MFA}}$ was evaluated numerically for the Helmholtz free energy both with and without the inclusion of the Fock term. A comparison of the results with the SRI KR slave-boson data (see Fig. 6.1) for $U=t$, $t'=-0.45\,t$ and for both $V=-0.1\,t$ and

[3]There is also a third van Hove singularity that exists only for comparatively large nnn hopping $|2t'|>t$, which is out of the scope of this work.

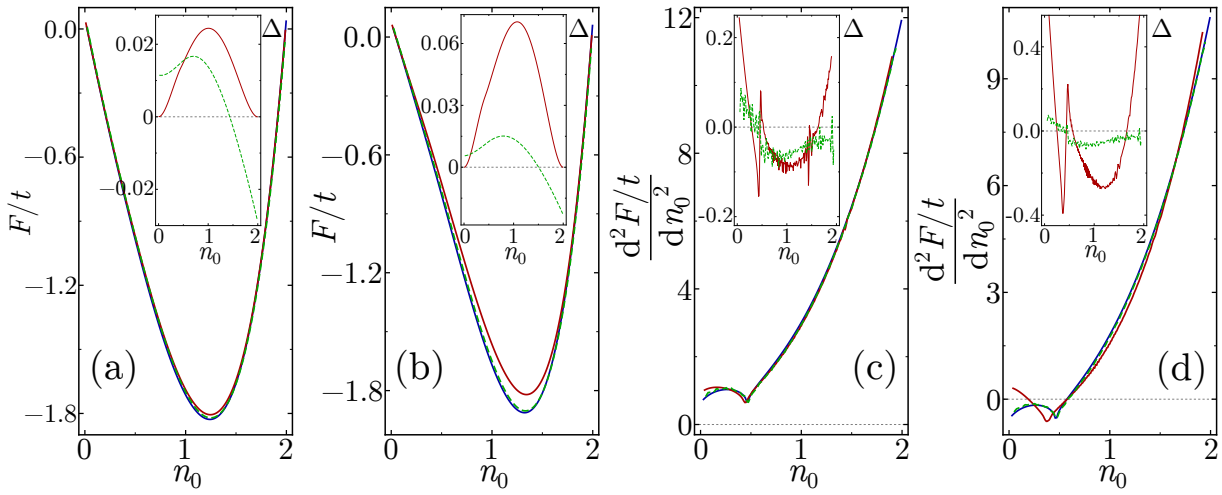

Figure 6.1.: Comparison of the results from the slave-boson evaluation (blue) with Hartree (green dashed) and Hartree-Fock (red) calculations for $U = t$ and $t' = -0.45\,t$. (a) and (b) display the Helmholtz free energy F as function of the electron density n_0 for $V = -0.1\,t$ and $V = -0.4\,t$, respectively. The second derivative of F with respect to n_0 is plotted in (c) for $V = -0.1\,t$ and in (d) for $V = -0.4\,t$. The insets show the difference Δ between the SB results and the Hartree (green) or Hartree-Fock (red) evaluations. Adapted from Ref. [32].

$V = -0.4\,t$ shows good agreement. Commonly, the slave-boson approach is best suited for strong coupling and high band fillings. However, the projection factors for the kinetic energy and inter-site interaction employed in the SRI KR formulation ensure that its weak-coupling limit is exact for $U = 0$ and even in first order of U. On the other hand, the KR SB approach does not take the exchange interaction for the inter-site Coulomb repulsion V into account. The contribution of the Fock term, which is proportional to V, to the energy is largest around half filling due to its dependence on the integration over $\cos a(q_i - k_i)$. Hence, the deviation between the results of the SB and Hartree-Fock evaluations is largest for $n_0 \approx 1$ and increases with $|V|$ (see insets of Fig. 6.1a and 6.1b, red curve). The agreement between the SB and the Hartree evaluations on the other hand is hardly affected by the strength of the inter-site interaction V used in our calculations: this can be seen by comparison between (a) and (b) and between (c) and (d) of the green curves in the insets of Fig. 6.1. Around the minimum of the free energy the relative difference between the SB and Hartree results is of the order of 1%.

The second derivatives of the free energy with respect to the electron density $n_0 = \sum_\sigma n_\sigma$ are proportional to the inverse compressibility of the system. They display a cusp at the position of the vHs (see Fig. 6.1c and 6.1d), which is shifted to $n_0 \approx 0.5$ due to the finite $t' < 0$. The agreement between the curves of the SB and Hartree data is as good as between their free energies and independent of V. On the other hand, the SB and Hartree-Fock evaluation differ notably not only around half filling, where their respective free energies have the largest deviation, but also for small and large fillings and around the vHs. For the free electron gas the contribution of the Fock term is most relevant at low electron densities, which clarifies the difference at low and high fillings in the Hubbard model. As the position of the vHs depends on the inter-site interaction V in case of the presence of the Fock term, the cusp is shifted to lower fillings with larger $|V|$, so that the SB and Hartree-Fock evaluations deviate around the vHs.

We would like to remark that the contribution of the Fock term to the inverse compressibility is positive for small densities (for attractive nn interaction V), as can be seen in Fig. 6.1d. Due to the anticommutation relation the Hartree and the Fock term have opposite signs. While the Fock term in Eq. (6.7) has a negative sign, this is compensated by $V < 0$. The differences

appearing in the terms $\cos a(q_i - k_i)$ are small for low fillings, so that the total contribution of the Fock term to the energy is positive. So—in contrast to the free electron gas—it is not the Fock term that drives the compressibility negative at low electron densities, but the Hartree term, due to the negative sign of V.

The SB approach, which displays its strengths at strong coupling, recovers the Hartree results sufficiently accurately in the weak-coupling regime. The deviation introduced by the neglection of the Fock contribution is limited, provided that the electron density is not too close to zero filling or $n_0 = 2$. In the following analysis for the capacitance and compressibility we use the results from the KR SB SRI evaluations for the most part, except for Fig. 6.6, which compares SB and Hartree-Fock calculations for κ^{-1} and C.

6.4. Compressibility and Capacitance of a System with Symmetric Electrodes

6.4.1. Polar Heterostructure

In this section we couple two two-dimensional electron systems that are characterized by the extended Hubbard model and possess the same parameters, i.e., are identical, and then analyze the capacitance and compressibility of the total system for weak coupling ($U = t$) and strong coupling ($U = 9\,t$). However, we start with the compressibility of an isolated system, which is the foundation for understanding the properties of the composite configuration.

For weak coupling ($U = t$) and $t' = 0$ the inverse compressibility displays a dip at half filling (see Fig. 6.2a). The vHs is located at this point. Increasing the strength of the inter-site interaction V from $V = 0$ (black curve) to $V = -0.4\,t$ shifts the inverse compressibility to lower values. According to the Hartree Hamiltonian given by Eq. (6.7), the energy contribution of the inter-site coupling to the Hartree term is $F_{\mathrm{Hartree}} = 2AVn_0^2$, so that the second derivative of this energy with respect to n_0 is proportional to $4V$. Hence, the Hartree evaluation results in a density independent shift of the second derivative due to V. This consideration is independent of the values of t, t' and U. As we limit $|V|$ with respect to the on-site repulsion U, the compressibility is positive for $t' = 0$. For $t' = -0.15\,t$ the vHs and the corresponding dip in the inverse compressibility is moved to lower densities and the system looses its particle-hole symmetry (Fig. 6.2b). At even more negative $t' = -0.45\,t$ the compressibility becomes negative for small electron densities (Fig. 6.2c). This is induced by the combined effect of the vHs and the inter-site coupling V: Normally, the negative contribution derived from the V term to the inverse compressibility is compensated by positive contributions from the kinetic and on-site interaction terms. Though, at the vHs the kinetic contribution is reduced and for large $|t'|$ the vHs occurs at small fillings, which renders the contribution from the on-site repulsion small.

Now the isolated system with eHm is connected to an identical system at distance d, where the insulator between the electrodes is characterized by the dielectric constant ϵ. The positive background charge is distributed according to the symmetric polar heterostructure (SPH) configuration, which we introduced in Section 2.3: In this effective layout the complete positive background charge is concentrated in a two-dimensional plane exactly in the middle between the electrodes. This distribution of positive charge yields the same electrostatic energy as a polar heterostructure with equal distance between the polar layers (see Fig. 2.5b for the SPH and Fig. 2.5e for the corresponding physical situation). The total density is $n_{\mathrm{t}} = n_1 + n_2$, where n_i is the density in subsystem $i = 1, 2$ which are referred to as $s1$ for the interface system and $s2$ for the surface system. The density on the interface (and simultaneously on the surface) can be adjusted by the application of an external voltage between $s1$ and $s2$. In the following analysis

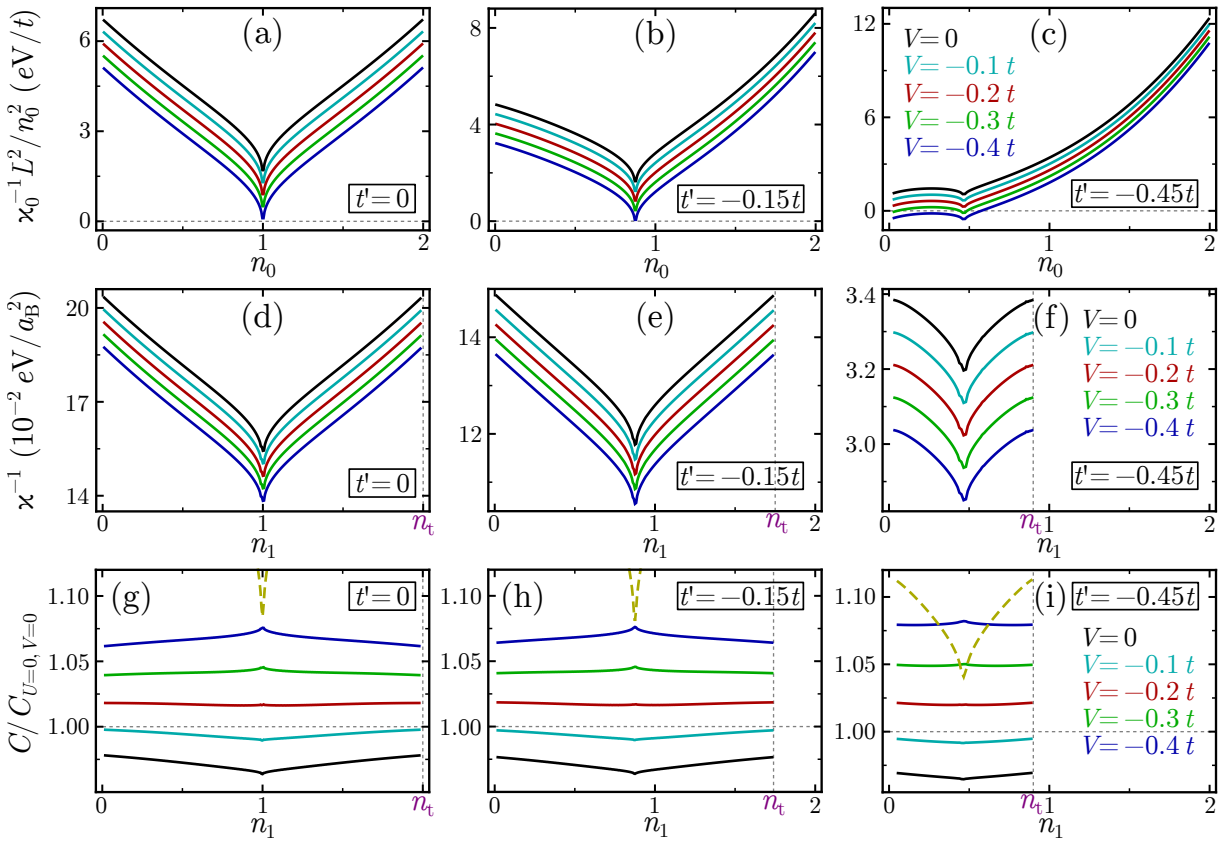

Figure 6.2.: Weak-coupling ($U = t$) results for the inverse compressibility κ_0^{-1} of an isolated system (first row, (a)–(c)) and inverse compressibility κ^{-1} (second row, (d)–(f)) and differential capacitance (third row, (g)–(i)) of a system consisting of two identical electronic subsystems, which are modeled by the eHm. The different colors refer to the values of inter-site coupling V as labeled in the legend of (f) and (i). The next-nearest neighbor hopping t' is varied between the columns, which shifts the electron densities at which the vHs appear. For the composite systems the total density n_t chosen guarantees that both electronic systems are at the vHs if half of n_t resides on each electrode. This is attained by $n_t = 2$ for $t' = 0$, by $n_t = 1.75$ for $t' = -0.15\,t$ and by $n_t = 0.93$ for $t' = -0.45\,t$. The differential capacitances in the last row are normalized to the capacitance of an interaction-free system with $U = 0$ and $V = 0$ and the dashed yellow curve corresponds to the normalized geometric capacitance $C_{geo}/C_{U=0,V=0}$, where this quantity depends on n_1 through $C^{-1}_{U=0,V=0}$. We used $d/\epsilon = 4\,a_B$ for the effective plate distance, $t = 0.5\,eV$ for the nearest-neighbor hopping and $a = 10\,a_B$ for the lattice constant. Adapted from Ref. [32].

the total density n_t is adjusted so—depending on different values of t'—that each system is at the vHs if half of the total electron density resides on each plate, i.e., for $n_1 = n_t/2 = n_2$.

We would like to note at this point that we use the terms electron "density" and electron "filling" in a broader sense in this chapter. Normally, electron density n_d is defined as electrons per area (in the two-dimensional case) while electron filling n_f is the average number of electrons per unit cell. Both quantities are connected by $n_d = n_f/a^2$, where a is the lattice constant. The Hamiltonian of an isolated Hubbard system scales with t and the resulting energy is an energy per unit cell. Thus the qualitative results for an isolated system are in principle independent of a, and therefore n_d and n_f are often used synonymously. However, the lattice constant becomes relevant if the energies are compared with other systems, as in this section. Nevertheless, we continue to use both terms, electron density and filling, as equivalent and are thereby referring to n_f. If needed, the "real" electron density can easily be recovered over the lattice constant

a. Derivatives with respect to n_f and n_d differ by a factor of a^2, which was always, even if not noted explicitly, considered.

The inverse compressibility of the total system for $t' = 0$ inherits the symmetry of the isolated system (Fig. 6.2d), so that both inverse compressibilities can be rescaled into each other, after the constant shift originating from the electrostatic energy is taken into account. We find that even in the case of negative compressibility of the isolated system, $\kappa_0 < 0$, which was observed for $t' = -0.45\,t$ and $V < -0.3\,t$ in Fig. 6.2c, the total system is stable (see Fig. 6.2f). This follows from the positive contribution of the electrostatic energy to κ^{-1} and the fact that if one of the subsystems is at a density with $\kappa_0^{-1} < 0$, then the other subsystem has to be at a density with $\kappa_0^{-1} > 0$. The particular adjustment of n_t entails this property.

The capacitance of the total system, as displayed in Fig. 6.2g–6.2i, increases with smaller, more negative values of the inter-site attraction V, which is directly correlated to the decrease of the inverse compressibility in the isolated system. The comparison of the differential capacitance C_diff with the differential capacitance of a system without electronic interactions ($U = 0$, $V = 0$) reveals that the finite $U = t$ renders $C_\mathrm{diff} < C_{U=0,V=0}$ and only for $V < -0.1\,t$ the capacitance is enhanced beyond this benchmark. For $t' = 0$ and $t' = -0.15\,t$ the differential capacitance is smaller than the geometric capacitance C_geo (yellow dashed curve), as the compressibilities of the isolated electron systems are positive. For $t' = -0.45\,t$ it is $\kappa_0 < 0$ for electron fillings at and below the vHs for $V < -0.3\,t$, so that for this values the capacitance is enhanced beyond the geometric value (see Fig. 6.2i).

The results for the strong-coupling regime $U = 9\,t$ (see Fig. 6.3) differ significantly from the findings above. The inverse compressibility of the isolated system κ_0^{-1} exhibits a broad peak instead of a dip for densities around half filling. The strong on-site repulsion U dominates in this regime over the kinetic term and generates the large positive contribution to the inverse compressibility, the so-called "correlation peak" centered at $n_0 = 1$. The vHs is concealed by the correlation peak at $t' = 0$ (Fig. 6.3a) and becomes observable again as it is moved away from half filling due to finite t' (Fig. 6.3b and 6.3c). As we used the same ratio between the inter-site interaction V and U as for the weak-coupling case, $|V|$ is much larger than in the $U = 1$ analysis. This induces the occurrence of negative compressibility in the considered regime. Nevertheless, the compressibility of the combined system κ stays positive for all used values of V. For $t' = 0$ the inverse compressibility is symmetric around $n_1 = 1$ and the correlation peak is clearly visible (Fig. 6.3d). The positive contribution of the peak translates to a dip in the differential capacitance (Fig. 6.3g), so that $C_\mathrm{diff} < C_\mathrm{geo}$ for $n_1 \approx 1$. But for electron densities away from half filling the on-site repulsion term is small compared to the contribution of the inter-site attraction, so that the capacitance may exceed the interaction free capacitance $C_{U=0,V=0}$ and even the geometric capacitance C_diff for sufficiently strong V.

For the finite nnn hopping $t' = -0.15\,t$ the inverse compressibility displays a "w-like" structure centered at $n_1 = n_\mathrm{t}/2$ (see Fig. 6.3e). The choice of n_t entails that both $s1$ and $s2$ are at the vHs if half of the total electron density resides on each electrode. If now charge is transferred from the interface to the surface electrode, $s1$ is at a lower filling with smaller inverse compressibility κ_0^{-1}, while $s2$ enters the regime of the correlation peak. As the positive contribution of the peak dominates, the total inverse compressibility increases. For even higher electron densities in the surface electrode, $s2$ is beyond the correlation peak, so that κ^{-1} declines again. This behavior is also apparent in the capacitance (Fig. 6.3h), which possesses correlation-induced minima for the densities at which one of the electron systems is close to half filling. If the electron densities of both electron systems are away from the correlation peak, the capacitance is enhanced by the attractive interaction V.

For $t' = -0.45\,t$ the total electron density of the system is $n_\mathrm{t} = 0.93$, which is smaller than half filling where the correlation peak occurs. Consequently, the on-site repulsion is of less relevance than in the previous cases, as none of the electron systems can be at $n_i = 1$. The inverse

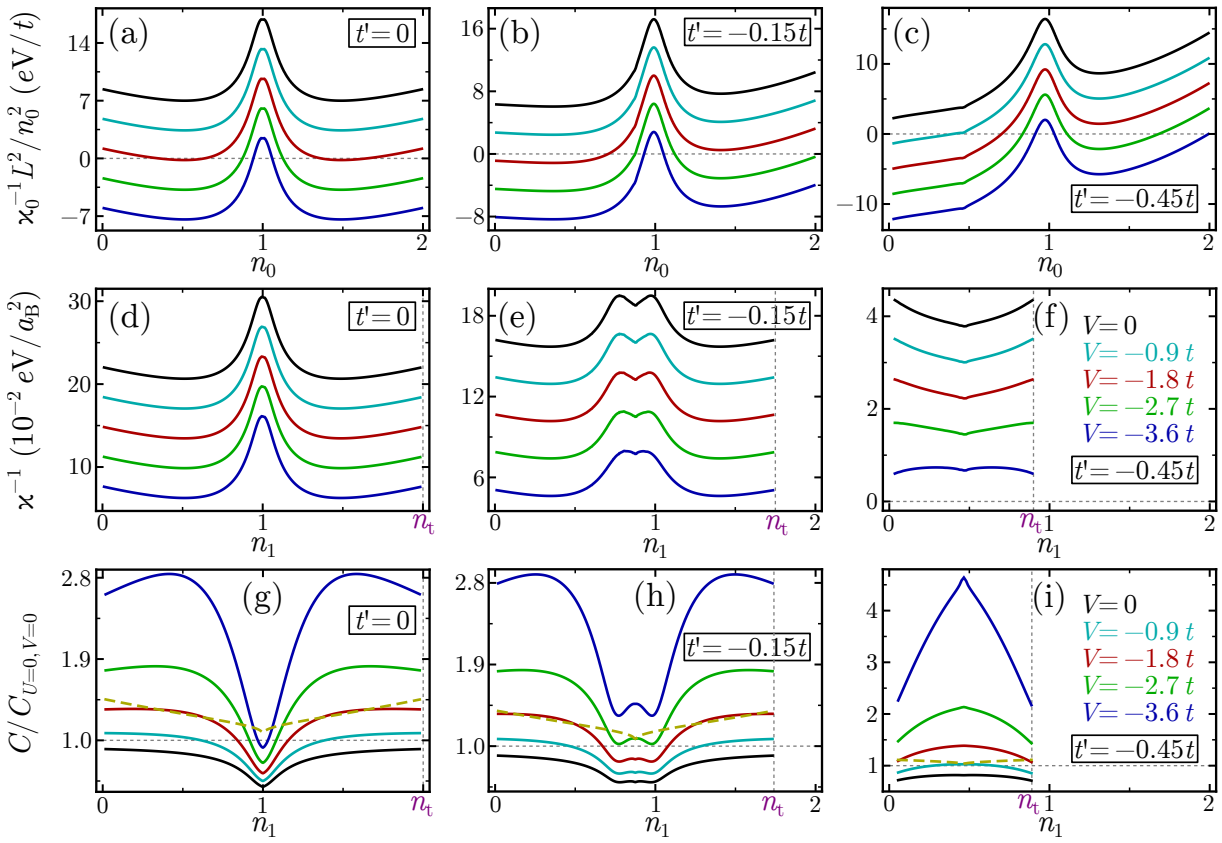

Figure 6.3.: Same setup as in Fig. 6.2 but for the strong-coupling regime $U = 9\,t$. The large on-site repulsion produces a smooth peak at half filling in the inverse compressibilities. As the same ratios between the on-site and inter-site coupling as in Fig. 6.2 were used, the absolute values of V are larger in the plot above. This reduces the inverse compressibility of the isolated systems (first row) and thus enhances the differential capacitances (last row). The dashed yellow curve corresponds to the normalized geometric capacitance $C_{\text{geo}}/C_{U=0,V=0}$, where this quantity depends on n_1 through $C^{-1}_{U=0,V=0}$. Adapted from Ref. [32].

compressibility κ^{-1} (Fig. 6.3f) and capacitance C_{diff} (Fig. 6.3i) are dominated by the inter-site interaction V, which translates into a considerable enhancement of the capacitance that is most pronounced at $n_1 = n_t/2$, i.e., when both systems are at the vHs. For small electron densities on one of the electrodes, the other electronic subsystem is near the correlation peak, which reduces the capacitance enhancement.

6.4.2. Symmetric and Asymmetric Standard Capacitor

In Section 2.3 we established a general electrostatic layout to investigate the effect of the spatial distribution of the positive background charge on the compressibility of the system. The relation for the inverse compressibility, Eq. (2.42),

$$\frac{1}{\kappa}\frac{A}{n_t^2} = \frac{e^2A^2}{C_{\text{diff}}}\frac{\partial n_1}{\partial n_t}\left(1-\frac{\partial n_1}{\partial n_t}\right) + \mathcal{D}F_{\text{es}} \tag{6.8}$$

is valid if the density n_1, which adjusts in such a way that the Helmholtz free energy of the system is minimized, is not a boundary value, i.e., $n_1 \neq 0$ and $n_1 \neq n_t$. The equation above depends on the electrostatic layout directly by $\mathcal{D}F_{\text{es}} = (\partial^2_{n_t} + \partial_{n_t}\partial_{n_1})F_{\text{es}}$ and indirectly over the charge-transfer function $\partial_{n_t} n_1$. We found in the framework of the general electrostatic layout

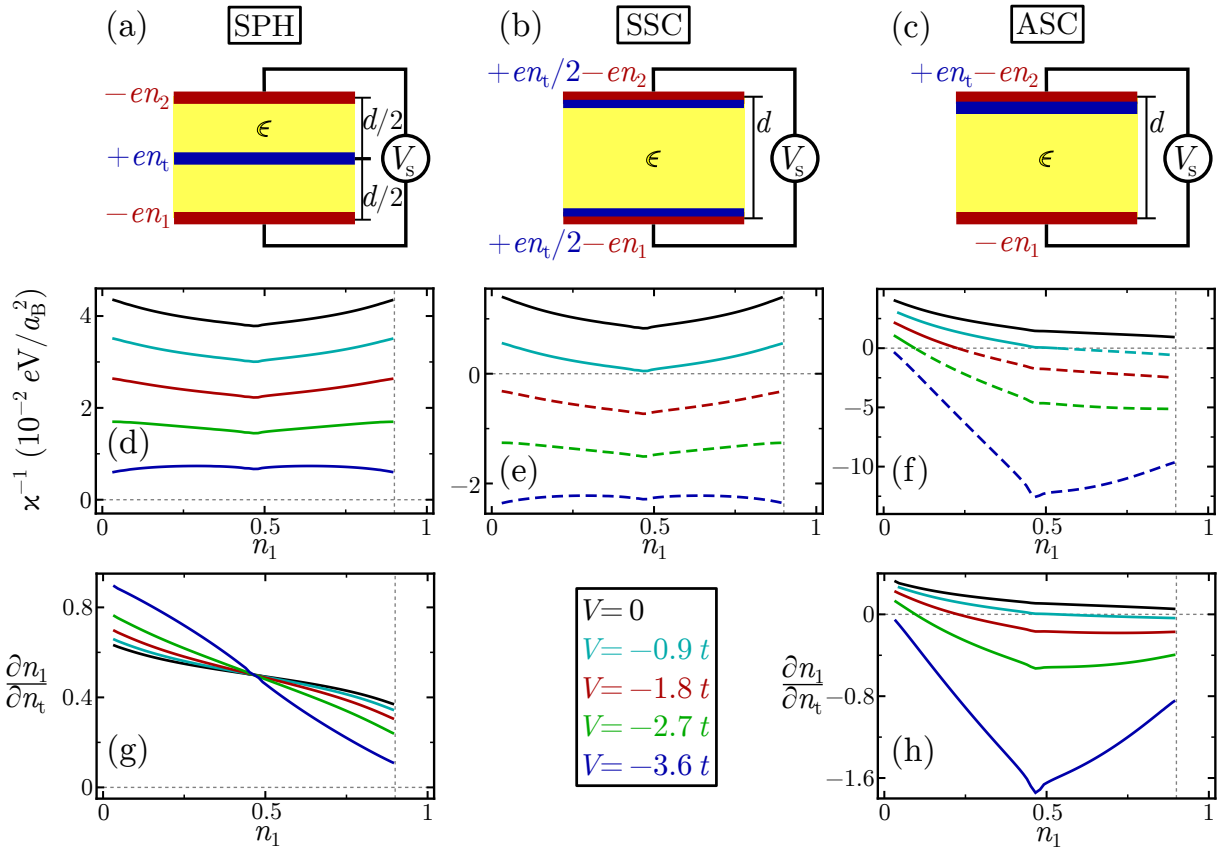

Figure 6.4.: Two identical electron systems with $t = 0.5\,e\mathrm{V}$, $t' = -0.45\,t$, $a = 10\,a_\mathrm{B}$ and $U = 9\,t$ residing in two-dimensional electrodes with an effective distance of $d/\epsilon = 4\,a_\mathrm{B}$ are coupled to each other so that $n_\mathrm{t} = 0.9$. The distribution of the positive background charge affects the inverse compressibility of the system ((a)–(c)): (a) refers to the SPH layout (d), while (b) corresponds to the SSC layout (e), and (c) refers to the ASC layout (f). The SPH and SSC layout produce the same symmetric charge-transfer function (g). The zeros in the charge-transfer functions of the ASC layout (h) correspond to the densities at which the compressibility has a change of sign. For the SPH layout the setup corresponds to Fig. 6.3f. The capacitance is equal for all three configurations and given by Fig. 6.3i. Adapted from Ref. [32].

that $\mathcal{D}F_\mathrm{es} = 0$ only if the total positive background charge is concentrated in one layer. If the derivative $\mathcal{D}F_\mathrm{es}$ vanishes, then a descriptive criterion for positive compressibility is provided by the charge-transfer function: $\kappa > 0 \Leftrightarrow 0 < \partial_{n_\mathrm{t}} n_1 < 1$. The system is instable if a positive change of the total charge density decreases the charge density on one of the electrodes.

Up to now the symmetric polar heterostructure (SPH) was used as configuration for the distribution of the positive background charge. Figure 6.4 compares the inverse compressibilities of the SPH with two other layouts: The symmetric standard capacitor (SSC) and the asymmetric standard capacitor (ASC). In the SSC half of the total positive background charge is located in the plane of each electrode (see Fig. 6.4b), while the ASC places the total positive charge in the layer of the top electrode (see Fig. 6.4c). As we assume the same effective plate distance d/ϵ for all three configurations, the differential capacitance C_diff is unaffected by the electrostatic layout. Only the SSC yields a non-vanishing derivative $\mathcal{D}F_\mathrm{es}^\mathrm{SSC} = -D$, where $D = \pi e^2 A d/\epsilon$.

As the first derivatives of the electrostatic energy of the SPH and SSC layout with respect to n_1 are identical, $\partial_{n_1} F_\mathrm{es}^\mathrm{SPH} = \partial_{n_1} F_\mathrm{es}^\mathrm{SSC} = 2D(2n_1 - n_\mathrm{t})$, and n_1 is determined from the condition $\partial_{n_1} F_\mathrm{t} = 0$, both layouts possess the same charge-transfer function (Fig. 6.4g). However, $0 < \partial_{n_\mathrm{t}} n_1 < 1$ is only for the SPH a condition for stability, as $\mathcal{D}F_\mathrm{es}^\mathrm{SSC}$ is finite. This is reflected in the inverse compressibilities of the SPH (Fig. 6.4d) and SSC (Fig. 6.4e) layouts: κ^{-1} of the SPH

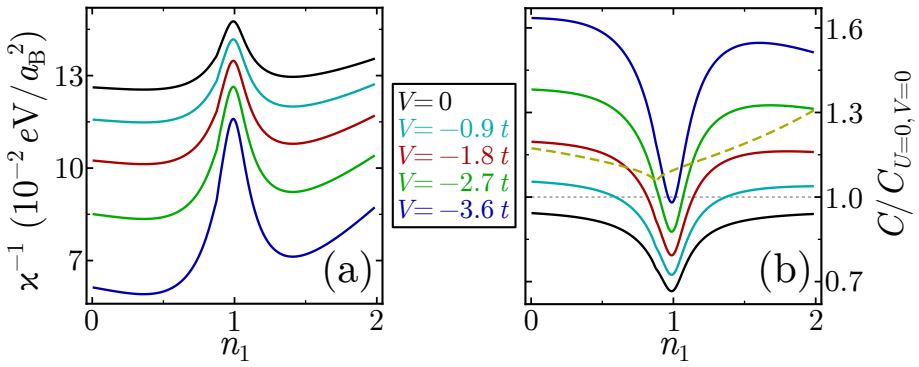

Figure 6.5.: Inverse compressibility (a) and differential capacitance (b) for two coupled electron systems at distance $d/\epsilon = 4\,a_B$ in the SPH layout and a total electron density of $n_t = 2.0$. The lower system is characterized by the eHm with parameters $t = 0.5\,e$V, $t' = -0.15\,t$, $a = 10\,a_B$ and $U = 9\,t$, and the different colors refer to values of the inter-site interaction V as labeled in the legend. The surface system is a 2DEG with $m_2 = 5\,m_e$. In (b) all capacitances are normalized to the capacitance $C_{U=0,V=0}$ of a non-interacting interface system with $U = 0$ and $V = 0$. The yellow curve corresponds to the geometric capacitance. Adapted from Ref. [32].

is always positive for the examined parameters, in accordance with the charge-transfer function, which is positive and smaller than 1. On the other hand, the SSC displays negative inverse compressibility for inter-site interactions $V < -0.9\,t$. As derived in Eq. (2.52), the inverse compressibilities between symmetric configurations differ by $n_t^2 \mathcal{D} F_{es}/A$, so that all values in Fig. 6.4e for the SSC are shifted down by $-n_t^2 D/A$ in comparison with the SPH in Fig. 6.4d. Out of the layouts with symmetric[4] distribution of the positive background charge, the SPH is the most stable.

In symmetric configurations of the positive background charge the system exhibits a symmetry of the Helmholtz free energy in respect of the density n_1 around $n_1 = n_t/2$, as the electronic systems are identical. This carries over to the charge-transfer function, which is $\partial_{n_t} n_1 = 1/2$ at n_1 (see Fig. 6.4g) and the inverse compressibilities. This symmetry is absent in the ASC layout, for which the inverse compressibility (Fig. 6.4f) is smaller than that of the SPH configuration and reaches negative values for $V \leq 0.9\,t$. The stability criterion arising from the charge-transfer function is confirmed in Fig. 6.4h: The inverse compressibility κ^{-1} and $\partial_{n_t} n_1$ are exactly zero at the same densities n_1. We also confirm that, as derived in Section 2.3, the inverse compressibility is larger if the positive background charge is in the same layer as the electronic subsystem that has the larger second derivative of its free energy with respect to its density: At $n_1 = 0$ the inverse compressibility is larger than at $n_1 = n_t$ in Fig. 6.4f. This is in accordance with the observation that for $n_1 = 0$ the inverse compressibility of the isolated electron system is smaller than for $n_1 = n_t = 0.93$ (see Fig 6.3c) and that the subsystem $s2$, where the positive background charge is located, is at $n_2 = n_t$ for $n_1 = 0$.

6.5. Compressibility and Capacitance of a System with Unequal Electrodes

In this section we expand our considerations to the case where one correlated electron system $s1$, characterized by the eHm, is coupled to a two-dimensional free electron gas (2DEG) $s2$. This corresponds, e.g., to the experimental setup found in the LAO/STO heterostructure, where the correlated interface electron system is coupled to a metallic surface system with negligible

[4] We define symmetry with respect to reflections at the plane located parallel at distance $d/2$ from each electrode.

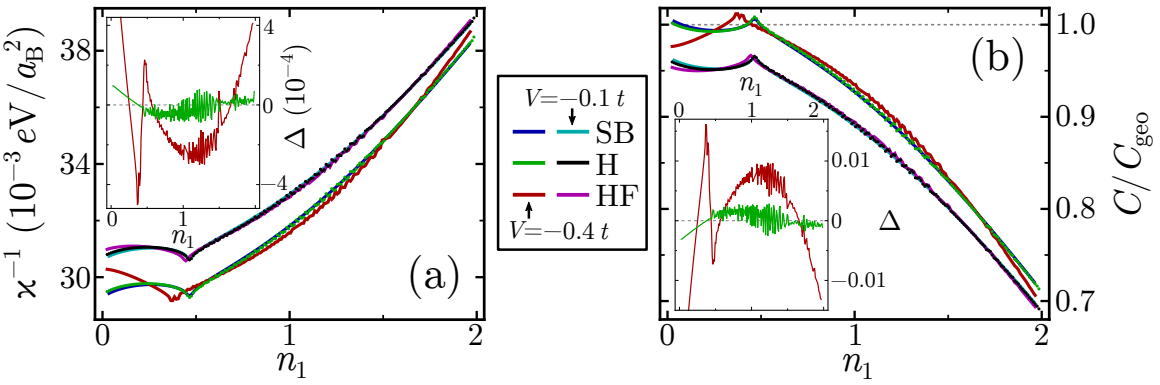

Figure 6.6.: Inverse compressibility (a) and differential capacitance (b) for the same layout as in Fig. 6.5 but for weak coupling $U = t$ and a next-nearest neighbor hopping of $t' = -0.45\,t$. Results from Slave-Boson (blue, cyan), Hartree (green and black dots) and Hartree-Fock (red, purple) evaluations for two different attractive Coulomb interactions $V = -0.4\,t$ and $V = -0.1\,t$ are compared. The insets of both plots depict the difference Δ between the SB and Hartree (green) and Hartree-Fock (red) results for $V = -0.4\,t$ in units of the embedding plot. The capacitances in (b) are normalized to the geometric capacitance $C_{\text{geo}} = A/(4\pi d/\epsilon)$. Adapted from Ref. [32].

correlations. The Helmholtz free energy of an unpolarized 2DEG was calculated in Section 2.1 and its kinetic energy is given by $F_2 = \pi\hbar^2 A n_2^2/2m_2$, where n_2 is the number of electrons per area in $s2$ and m_2 the effective mass. The second derivative of this energy, F_2'', with respect to n_2 is independent of the density. The differential capacitance and the inverse compressibility for the SPH, which is given by Eq. (2.54),

$$\frac{1}{\kappa}\frac{A}{n_t^2} = \frac{F_1'' F_2'' + 2D\,(F_1'' + F_2'' + 2D)}{F_1'' + F_2'' + 4D}, \tag{6.9}$$

depend only over the second derivative of the correlated electron system, F_1'', on the density. Consequently, the overall shape of κ^{-1} and C_{diff} as function of n_1 is determined by the Hubbard electron system at the interface.

In the strong-coupling regime, i.e., for $U = 9\,t$, the correlation peak in the inverse compressibility is clearly visible in Fig. 6.5a. The parameters of the system at the interface correspond to that of the isolated system analyzed in Fig. 6.3b and one would recover Fig. 6.3e if the uncorrelated metal at the surface were replaced by a copy of the interface system. The 2DEG reduces the symmetry of the system with respect to the density and hence removes the "w-like" structure present in Fig. 6.3e. The inverse compressibility of a system with a 2DEG at the top electrode is reduced compared to the case with two identical Hubbard systems, but still positive.

The correlation peak translates to a dip in the capacitance in Fig. 6.5b. As the contribution from the 2DEG to the inverse capacitance is constant and always positive, the enhancement of the capacitance is smaller than in the case of two identical Hubbard electron systems (compare Fig. 6.5b with Fig. 6.3h), where the second system may possess a negative isolated compressibility for sufficiently negative values of V.

The density dependence of $s1$ determines also for weak coupling $U = t$ the form of κ^{-1} in Fig. 6.6a, where we used $t' = -0.45\,t$, which corresponds to the single layer inverse compressibility of Fig. 6.2c. For small U, the attractive interaction V that powers the capacitance enhancement is also weaker, which affects the capacitance (Fig. 6.6b). An enhancement of a few percent beyond the geometric value is only found for $V = -0.4\,t$ and observable around a density at which $s1$ is at the vHs. For large fillings on the interface system, the positive contribution of the kinetic term in the Hubbard system to the inverse compressibility reduces the capacitance considerably below the geometric value.

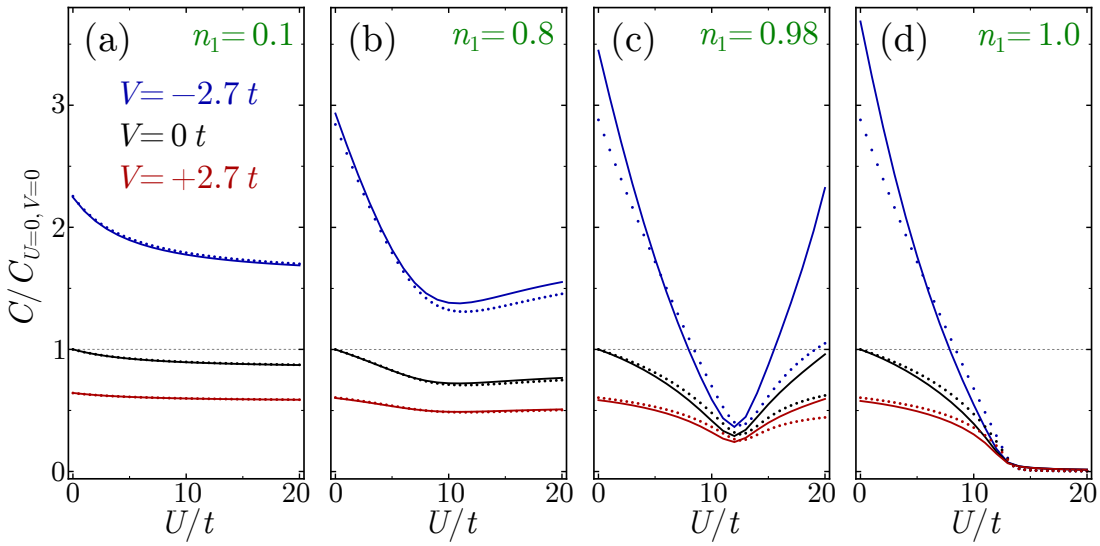

Figure 6.7.: Capacitance for two identical electron systems with $t = 0.5\,eV$ and $a = 10\,a_B$ at effective distance $d/\epsilon = 4\,a_B$ as function of the correlation strength U for three different inter-site interactions V. The total density in the system is $n_t = 2.0$ and the density on the lower electrode n_1 (see top right corner) is fixed by an external voltage for each of the four plots. The solid curves correspond to $t' = 0$ and the dots to $t' = -0.45\,t$. The latter nnn hopping shifts the vHs from half filling to $n = 0.47$. Adapted from Ref. [32].

The calculations of Fig. 6.6 were also performed with the Hartree and Hartree-Fock approach for the eHm electron system on the interface. Again, as in Section 6.3, we find excellent agreement between the SB and Hartree results. The Fock term induces deviations most prominently at low and high interface fillings and around the vHs, which exhibits a shift of its position.

6.6. Capacitance as Function of the On-Site Interaction U

The strength of the on-site Coulomb repulsion has great impact on the capacitance. The comparison between the weak and strong-coupling regime in the previous sections revealed the appearance of a dip at half filling in the capacitance for $U = 9\,t$, which is induced by the correlation peak. For small U, on the other hand, the vHs is not concealed by strong interactions and the kinetic term dictates the shape of C_{diff}. To obtain a clearer picture of the dependence of the capacitance on the magnitude of the on-site Coulomb interaction, we couple two identical electron systems, which are modeled by the eHm, and fix the total electron density in the system to $n_t = 2.0$. The density n_1 on the interface system—and consequently the density $n_2 = n_t - n_1$ on the surface electrode—is held constant by application of a voltage between the electrodes while U is varied.

In the Hartree evaluation the contribution of the on-site repulsion to the free energy is given by $UAn_\downarrow n_\uparrow$. As the second derivative of this term with respect to $n = n_\uparrow + n_\downarrow$ is proportional to U, one expects a decrease of the capacitance with increasing U. This is confirmed by Fig. 6.7a for the density $n_1 = 0.1$ and $V = 0$ (black curve). A positive inter-site repulsion V reduces the capacitance (red curve), while a negative V enhances it (blue curve). The capacitance decreases monotonically with U for all used values of V, whereby the slope is more pronounced for smaller V.

At $n_1 = 1$, i.e., when both electrodes are at half filling, the diminishment of the capacitance with U is even stronger (Fig. 6.7d) than for $n_1 = 0.1$. If U exceeds a critical value $U_c \approx 13\,t$, which is independent of V, the differential capacitance drops down to zero, as for $U > U_c$

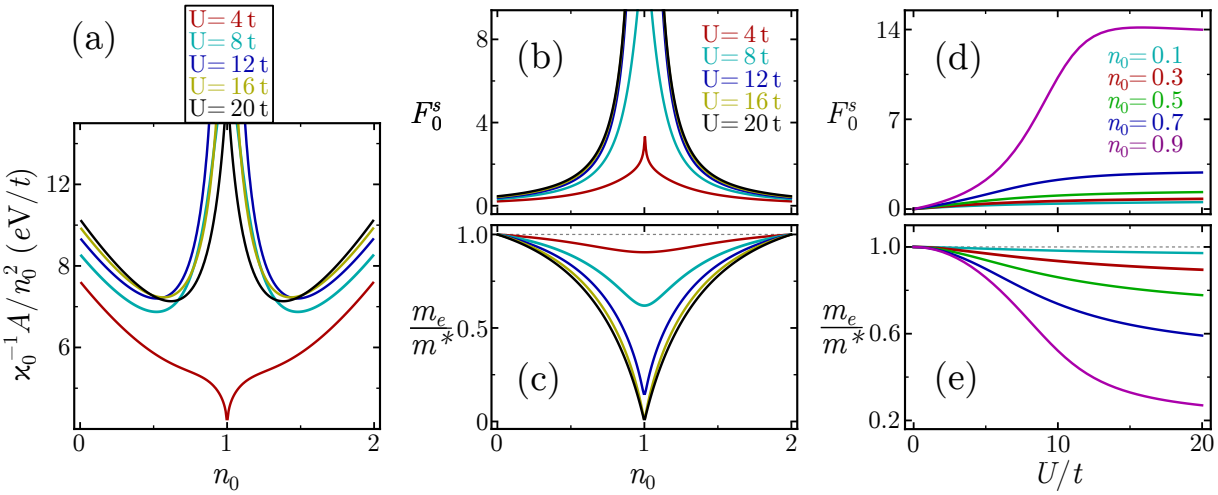

Figure 6.8.: (a) Inverse compressibility, calculated from the second derivative of the free energy with respect to n_0, of an isolated system with $t' = 0$ and $V = 0$ for different on-site repulsions U. The Landau parameter F_0^s (b) and inverse effective mass ratio m_e/m^* can be extracted directly from SB evaluation and are related to (a) by Eq. (6.10). (d) Landau parameter F_0^s and (e) inverse effective mass ratio m_e/m^* as function of U for $n_0 = 0.1$ (cyan), $n_0 = 0.3$ (red), $n_0 = 0.5$ (blue) and $n_0 = 0.9$ (purple). The Landau parameter F_0^s saturates for $n_0 = 0.5$ and $n_0 = 0.9$ beyond $U \simeq 12\,t$. Adapted from Ref. [32].

the system undergoes a phase transition to the incompressible Mott insulating state (see, e.g., Ref. [126]).

For interface electron densities in the range of $0.6 \lesssim n_1 < 1.0$ the capacitance displays an unanticipated behavior: After an initial decrease for small U the capacitance assumes a minimum and then increases again for larger values of U (see Fig. 6.7b and 6.7c). The position of the minimum is shifted from $U_0 \simeq 10\,t$ for $n_1 \simeq 0.6$ to larger values with increasing density at the interface and approaches U_c for $n_1 \simeq 1$. For $n_1 = 0.8$ and $n_1 = 0.98$ of Fig. 6.7b and 6.7c, respectively, the minimum is at $U_0 \simeq 12\,t$. The closer the electron density n_1 is to half filling, the more pronounced is the increase of the capacitance for $U_0 < U < U_c$. The minimum occurs for both negative and positive inter-site Coulomb interaction V, but is more noticeable for attractive interactions.

The inverse quantum capacitance, which induces this non-monotonic behavior of $C(U)$, is determined by the inverse compressibilities of the subsystems. We calculated κ_0^{-1} for an isolated system by taking the second derivative of its Helmholtz free energy with respect to the density n_0 for different values of U (see Fig. 6.8a). The results of Section 6.4 are retrieved: for weak coupling ($U = 4\,t$, red curve in Fig. 6.8a) the inverse compressibility exhibits a dip originating from the vHs at half filling, while for strong coupling $U > 8\,t$ the correlation peak emerges at $n_0 = 1$. For a small n_0 (and likewise for large n_0, as for $t' = 0$ the energy and its derivatives are symmetric around half filling), the inverse compressibility increases with U. However, for intermediate n_0 and U in the strong-coupling regime, the curves for different U cross each other; for example, the $U = 8\,t$ (cyan) curve intersects two times with the $U = 16\,t$ (yellow) curve. This implies that for a given density the inverse compressibility does not increase monotonically with U. The crossings can be traced back to a narrowing of the correlation peak with increasing on-site repulsion U.

In Landau-Fermi-liquid theory the inverse compressibility is related to the effective mass ratio m^*/m_e and the Landau parameter F_0^s by (see, for example, Ref. [56]):

$$\frac{\kappa_0(U=0)}{\kappa_0(U)} = (1 + F_0^s)\,\frac{m_e}{m^*}, \tag{6.10}$$

where $\kappa_0(U = 0)$ is the compressibility of the non-interacting system. These two quantities can be derived from the one-loop approximation in the slave-boson evaluation. The effective mass ratio corresponds to the quasiparticle residue $z_0^2 = m^*/m_e$. At half filling the analytical relations $F_0^s(U) = (1 - U/U_c)^{-2} - 1$ and $m_e/m^* = 1 - (U/U_c)^2$ are valid [150]. This implies that for $U \to U_c$ the Landau parameter diverges and the effective mass ratio vanishes, while the inverse susceptibility diverges [121, 141].

Figures 6.8b and 6.8c depict the symmetric Landau parameter F_0^s and the inverse effective mass ratio m_e/m^* as function of the density n_0. While F_0^s increases with U, the inverse effective mass decreases with U. For small (and due to the symmetry also for large) fillings the effect of the Landau parameter dominates in Eq. (6.10), so that the inverse compressibility increases with U. In the weak-coupling regime the deviation of the effective mass from the electron mass is quite small, so that F_0^s determines for all densities n_0 the shape of the inverse compressibility (see red curves). If U is in the strong-coupling regime, m_e/m^* becomes small at intermediate fillings, which counteracts and overcompensates the increase of F_0^s with U: The increase of F_0^s with U at densities close to half filling saturates beyond $U \simeq U_0 \simeq U_c$ (see purple curve, which corresponds to $n_0 = 0.9$ in Fig. 6.8d). The inverse effective mass, on the other hand, continues to decrease with U, although with reduced slope (see Fig. 6.8e).

A finite next-nearest neighbor hopping t' introduces a shift of the vHs away from half filling, but does not alter the considerations above qualitatively. The occurrence of minima in the $C(U)$ curve is also observable in Fig. 6.7, where the dots correspond to $t' = -0.45\,t$. Consequently, the increase of $C(U)$ beyond a given on-site repulsion U_0 for intermediate fillings can be attributed completely to strong-coupling effects.

We examined the effect of an attractive inter-site interaction V in the extended Hubbard model on the compressibility and capacitance. The eHm was evaluated with the Kotliar-Ruckenstein slave-boson approach in the spin rotationally invariant representation. The results are in good agreement with Hartree evaluations in the weak-coupling regime and at small densities. The deviations from Hartree-Fock calculations in the weak-coupling regime are only relevant for small and large fillings or at the van Hove singularity if V is sufficiently large.

We found that a negative V can generate an enhancement of the differential capacitance C_{diff} over the capacitance of a non-interacting system for weak coupling $U = t$ and even an enhancement over the geometric capacitance for strong coupling $U = 9\,t$. In the strong-coupling regime, a correlation peak in the inverse compressibility emerges at half filling $n_0 = 1$, which suppresses the capacitance. A finite next-nearest neighbor hopping t' moves the vHs, which decreases the inverse compressibility, away from $n_0 = 1$, so that large enhancements of the capacitance are possible (see Fig. 6.3i).

A setup that corresponds to a symmetric polar heterostructure was used and the impact of other distributions of the positive background charge on the stability of the system was investigated. We found that for the SPH the compressibility is positive in the considered parameter range and that this configuration was the most stable of the compared alternatives.

A striking result is that a non-monotonic behavior of the capacitance as function on the on-site repulsion U at fixed density for intermediate fillings could be identified. It is traced back to the distinct large-U behavior of the Landau parameter F_0^s and the inverse effective mass ratio m_e/m^*.

7. Summary

The functionality of many electronic devices is controlled by capacitive effects. As the miniaturization of electronic circuits proceeds, quantum mechanical phenomena grow in importance for the occurrent capacitances. For small effective distances between the plates of a capacitor, the properties of the electron systems on the electrodes determine the capacitance, jointly with the classical electrostatic contribution. This corresponds to a series connection of "quantum capacitances", which are in principal given by the compressibilities of the isolated electron subsystems, with the geometric capacitance. If the sum of the quantum capacitances is negative, then the resulting capacitance is enhanced beyond the classical geometric value.

While the inverse capacitance can be decomposed into a simple sum of contributions from the isolated subsystems and from the electrostatic energy, the compressibility of the total system is a more intricate quantity. The compressibility of the total system has to be positive in order to guarantee thermodynamic stability. For the capacitance to be enhanced beyond the geometric value, at least one of the constituting electronic subsystems has to be instable if it were considered as isolated. Then the (static) distribution of the positive background charge is a decisive factor that determines the stability of the overall system. For example, a layout where half of the positive background charge is homogeneously distributed on each electrode renders the total system always instable in the case of an enhanced capacitance, independent of the exact details of the electronic subsystems. We analyzed different configurations of the positive charge by means of a model that accounts for various physical setups and found the so-called symmetric polar heterostructure (SPH) to be most stable in a wide range of situations. The SPH describes a polar heterostructure with equal distances between its polar layers.

This work identified and examined three possible mechanisms for the enhancement of the capacitance: exchange and correlation effects in a free electron gas, spin-orbit coupling and an attractive nearest-neighbor interaction in the extended Hubbard model. The range of electron densities at which these mechanisms are capable to induce a capacitance enhancement varies considerably: While exchange and correlation contributions in a free electron gas drive an isolated system instable at low densities, the attractive interaction in the extended Hubbard model is effective at intermediate fillings. The spin-orbit coupling on the other hand provides an enhancement of the capacitance at large electron densities.

The second derivative of the free energy with respect to the density n is proportional to the inverse compressibility. In a two-dimensional free electron gas at zero temperature this quantity diverges to $-\infty$ for $n \to 0$ in Hartree-Fock approximation because of the Fock term. Finite temperature alters this behavior drastically: In first-order perturbation theory the divergence is lifted and the exchange contribution is finite (and negative) at $n = 0$. The emerging entropic contribution, which is absent for $T = 0$, to the inverse compressibility diverges to $+\infty$ for small densities. However, a range of densities for which the compressibility is negative due to the exchange term remains even at room temperature. These results are in better qualitative agreement with the experimental observation of enhanced capacitances in the $LaAlO_3/SrTiO_3$ heterostructure [9]: The capacitance displayed a peak at low electron densities but declined to zero for $n \to 0$. Further analysis for this low density case is needed: specifically, low temperature data would allow to identify the entropic contribution to the capacitance.

We investigated an electronic system with spin-orbit coupling (SOC) at an interface that is connected to a second electron system. If electrons are transferred to the interface from

the second system, uncompensated positive background charges create a symmetry breaking electrical field at the interface. This field enhances the strength of the SOC and thus increases the splitting between the bands. This mechanism may enhance the capacitance if the strength of the SOC is large enough, which is the case for large electron densities at the interface. The strength of the SOC in the $LaAlO_3/SrTiO_3$ interface electron system was extracted from experiment and used in the two-band Rashba model and a six-band model that accounts for the three t_{2g} orbitals of the Ti atoms at the interface in which the conduction electrons reside. The total system is stable in the range of parameters that are realistic for the $LaAlO_3/SrTiO_3$ heterostructure and for the SPH layout of the positive background charge. An enhancement of the capacitance over the geometric value in the six-band model occurs at high electron densities n_1 at the interface. For n_1 larger than a critical value, the spin-splitting between the two lowest bands is so strong, that electrons reside only in the lowest band, whereby the electronic states around the wave vector $k = 0$ are unoccupied. Although the capacitance is enhanced further beyond this point, the limit of validity for the extraction of the parameters from experiment is then exceeded.

An isolated two-dimensional free electron gas was used as a toy model to examine the interplay between exchange coupling and Rashba SOC. The two-band Hamiltonian was treated in mean-field theory and analytical results for the diagonalization were presented. A numerical diagonalization revealed an intriguing groundstate that breaks the rotational symmetry: It emerges at low electron densities when the exchange and SOC contribution are of the same order of magnitude. For low densities in a pure Rashba model, only the lower band is populated and the occupied states form an annulus with an unoccupied circular disc around $k = 0$. On the other hand, the contribution of the exchange interaction to the energy is minimal if the occupied states form a circular disc, whereby the position of its center in k space does not affect the energy. The combination of both couplings leads at low densities, when they dominate over the kinetic term, to a "kidney-like" Fermi surface with a finite center of wave vector. This phase needs further analysis, because in its derivation the electrostatic cost of the inhomogeneity was neglected.

In the extended Hubbard model with repulsive on-site interaction U the Coulomb interaction between electrons on neighboring lattice sites V can be rendered attractive. This attractive interaction may originate from the polarizability of background ions. This interaction V may induce an enhancement of the capacitance, whereby it competes with the kinetic contribution and the term from the on-site repulsion U. A van Hove singularity appears at half filling and can be shifted by a negative next-nearest neighbor hopping t' to lower densities. The Kotliar-Ruckenstein slave-boson spin rotationally invariant representation yields results that are nearly identical to the findings of the Hartree approximation for $U \lesssim t$. At weak coupling ($U = t$) the capacitance can be enhanced beyond the capacitance of an interaction free system for sufficiently negative V and even beyond the geometric capacitance for $t' = -0.45\,t$.

For strong coupling ($U = 9\,t$) the on-site repulsion induces a "correlation peak" in the inverse compressibility around half filling, which reduces the capacitance for these fillings. As the ratio between U and V was kept fixed, the attractive nearest-neighbor interaction V in the strong-coupling regime was also larger, so that away from half filling the capacitance was enhanced significantly beyond the geometric value. The enhancement was boosted by a shift of the van Hove singularity away from half filling by finite t'. The correlation peak in the inverse compressibility sharpens with increasing U. This creates a non-monotonic behavior of the capacitance as function of U for fillings $0.6 \lesssim n_1 \lesssim 1.4$ for symmetric electrodes with a total electron filling close to $n_\mathrm{t} = 2$. However, as U cannot be tuned readily in an experimental setup, it would be necessary to identify the non-monotonic behavior from a measurement series with electrodes from distinct materials comprising strongly correlated electron systems.

This theoretical work focused on perfectly two-dimensional electron systems. However, in most heterostructures the electrons are not necessarily restricted to one interface or surface layer only. For example, the electrons at the $LaAlO_3/SrTiO_3$ interface occupy not exclusively the Ti $3d$ states of the TiO_2 layer at the interface, but a fraction also resides in the adjacent TiO_2 layer. This can be modeled effectively by two two-dimensional electron systems with tunneling between them. The investigation of such metallic multilayer systems is a challenging perspective.

A. Appendix

A.1. Compressibility for Constant Volume

The derivation of the compressibility at constant volume in this section is based on [151]. For one particle species, the derivative of the Gibbs-Duhem equation,

$$\mathrm{d}\mu = \frac{\mathcal{V}}{N}\mathrm{d}p - \frac{S}{N}\mathrm{d}T, \tag{A.1}$$

with respect to the specific volume $v := \mathcal{V}/N$ at constant temperature is:

$$\left(\frac{\partial\mu}{\partial v}\right)_T = v\left(\frac{\partial p}{\partial v}\right)_T \tag{A.2}$$

The partial derivative can be taken at constant volume or at constant particle number:

$$\left(\frac{\partial}{\partial v}\right)_{T,\mathcal{V}} = \left(\frac{\partial N}{\partial v}\right)_{T,\mathcal{V}}\left(\frac{\partial}{\partial N}\right)_{T,\mathcal{V}} = -\frac{N^2}{\mathcal{V}}\left(\frac{\partial}{\partial N}\right)_{T,\mathcal{V}} \tag{A.3}$$

$$\left(\frac{\partial}{\partial v}\right)_{T,N} = \left(\frac{\partial \mathcal{V}}{\partial v}\right)_{T,N}\left(\frac{\partial}{\partial \mathcal{V}}\right)_{T,N} = N\left(\frac{\partial}{\partial \mathcal{V}}\right)_{T,N} \tag{A.4}$$

These relations are inserted into Eq. (A.2),

$$-\frac{N^2}{\mathcal{V}}\left(\frac{\partial\mu}{\partial N}\right)_{T,\mathcal{V}} = \mathcal{V}\left(\frac{\partial p}{\partial \mathcal{V}}\right)_{T,N}, \tag{A.5}$$

which is used for the isothermal compressibility of Eq. (2.4):

$$\frac{1}{\kappa} = -\mathcal{V}\left(\frac{\partial p}{\partial \mathcal{V}}\right)_{T,N} = \frac{N^2}{\mathcal{V}}\left(\frac{\partial\mu}{\partial N}\right)_{T,\mathcal{V}} \tag{A.6}$$

μ can be expressed by the free energy (c.f. Eq. (2.3)), so that

$$\frac{1}{\kappa} = \frac{N^2}{\mathcal{V}}\left(\frac{\partial^2 F}{\partial N^2}\right)_{T,\mathcal{V}} \tag{A.7}$$

With the density $n = N/\mathcal{V}$ and

$$\left(\frac{\partial}{\partial N}\right)_{T,\mathcal{V}} = \left(\frac{\partial n}{\partial N}\right)_{T,\mathcal{V}}\left(\frac{\partial}{\partial n}\right)_{T,\mathcal{V}} = \frac{1}{\mathcal{V}}\left(\frac{\partial}{\partial n}\right)_{T,\mathcal{V}} \tag{A.8}$$

this results in

$$\frac{1}{\kappa} = n^2\left(\frac{\partial^2 F/\mathcal{V}}{\partial n^2}\right)_{T,\mathcal{V}}, \tag{A.9}$$

which is equivalent to Eq. (2.6), with the only difference that the derivative is taken at constant volume.

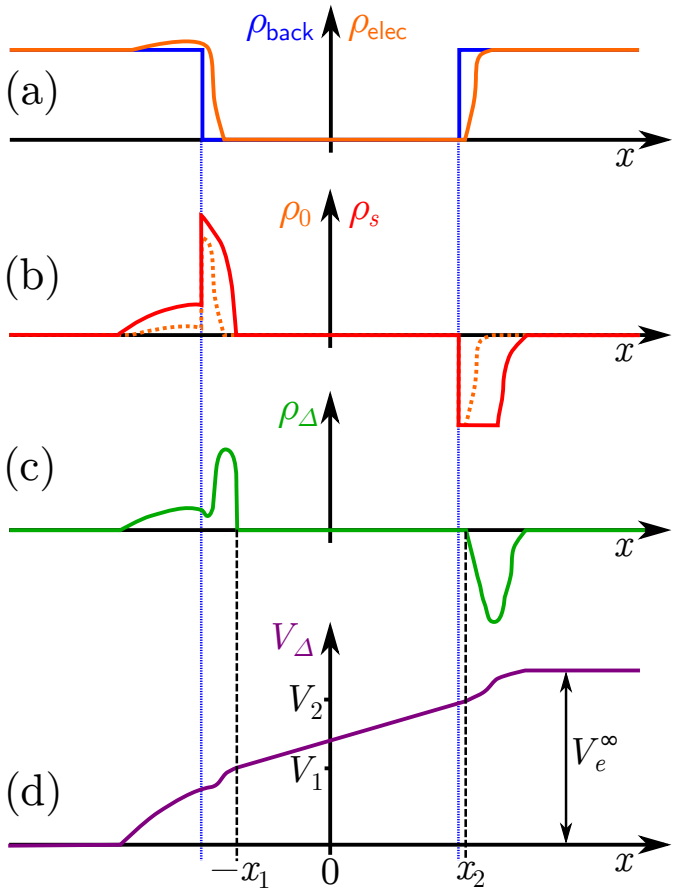

Figure A.1.: (a) Distribution of positive background charge ρ_b and electron density ρ_{elec} perpendicular to the surface of three-dimensional electrodes. (b) Charge distribution without (ρ_0) and with (ρ_s) applied voltage V_s. (c) $\rho_\Delta = \rho_s - \rho_0$ is induced by V_s and creates the potential V_Δ in (d). At $-x_1$ and x_2 ρ_Δ is zero and $x_1 + x_2$ defines the effective distance. In this illustrative example the electrons are spilled out of electrode 1 and pushed back from the surface of electrode 2. Under the assumption that the chemical potentials of both electrodes are equal, $V_e^\infty = V_s$ is valid.

A.2. Calculation of the Capacitance from a Charge Distribution

Assume two parallel three-dimensional electrodes with different work functions, the uniform positive background charge of which is at distance d. In this section we assume that the chemical potentials of both electrodes are equal, so that the work functions depend solely on the distribution of charge in the electrode, as, e.g., given by a surface dipole barrier. These electrostatic contributions to the work functions can be captured by the Poisson equation. There will be a finite charge distribution $\rho_0(x)$ on the electrodes. Here we assume that the distribution is uniform in the y-z plane, which is parallel to the surface of the electrodes, so that the problem can be mapped on one dimension. The charge on one electrode is given by

$$Q_0 = A \int_{-\infty}^{0} \mathrm{d}x \rho_0(x) = -A \int_{0}^{\infty} \mathrm{d}x \rho_0(x) \tag{A.10}$$

For finite V_s the charge distribution will change to $\rho_s(x)$. The charge Q, which was induced by the voltage, is

$$Q = A \int_{-\infty}^{0} \mathrm{d}x [\rho_s(x) - \rho_0(x)] = -A \int_{0}^{\infty} \mathrm{d}x [\rho_s(x) - \rho_0(x)]. \tag{A.11}$$

This charge generates an extra electric field E_Δ that is superpositioned on the field generated by Q_0. It is constant between the electrodes, in the space where $\rho_\Delta(x) \equiv \rho_s(x) - \rho_0(x) \equiv 0$. The point of origin of the x-coordinate is placed in the middle between the surfaces of the positive background charges. If the condition $\rho_\Delta(x) = 0$ is true for $x \in [-x_1, x_2]$ and there exist no $x_1' > x_1$ and $x_2' > x_2$, then $-x_1$ and x_2 define the position of the surfaces of the electrodes. Note

that $-x_1$ and x_2 depend on the voltage V_s. The potential difference between the surfaces of the electrodes due to Q is proportional to the electric field $E_\Delta = 4\pi Q/A\epsilon$:

$$V_\Delta(-x_1) - V_\Delta(x_2) \equiv V_1 - V_2 = \int_{-x_1}^{x_2} \mathrm{d}x E_\Delta = 4\pi \frac{x_1 + x_2}{\epsilon} \frac{Q}{A} \tag{A.12}$$

This reproduces the inverse capacitance Eq. (2.26) of Ku and Ullman [29] with $d = x_1 + x_2$. Here we assume that the background is described by the dielectric constant ϵ both for the region where the positive background charge resides and for the space in between.

On the other hand, the center of mass of the induced charge is x_i^{c}:

$$x_1^{\mathrm{c}} = \frac{\int_{-\infty}^{0} \mathrm{d}x x \rho_\Delta(x)}{\int_{-\infty}^{0} \mathrm{d}x \rho(x)}, \qquad x_2^{\mathrm{c}} = \frac{\int_{0}^{\infty} \mathrm{d}x x \rho_\Delta(x)}{\int_{0}^{\infty} \mathrm{d}x \rho(x)} \tag{A.13}$$

The one-dimensional Poisson equation for the voltage induced charge distribution $\nabla_x^2 V_\Delta(x) = -4\pi\rho_\Delta(x)/\epsilon$ can be used to transform the above equations:

$$\begin{aligned} x_1^{\mathrm{c}} Q/A &= -\frac{\epsilon}{4\pi} \int_{-\infty}^{-x_1} \mathrm{d}x x \frac{\partial^2}{\partial x^2} V_\Delta(x) = \frac{\epsilon}{4\pi} \left[\int_{-\infty}^{-x_1} \mathrm{d}x \frac{\partial}{\partial x} V_\Delta(x) - x \frac{\partial}{\partial x} V_\Delta(x) \Big|_{-\infty}^{-x_1} \right] \\ &= \frac{\epsilon}{4\pi} \left[V_\Delta(-x_1) - V_\Delta(-\infty) - x_1 E_\Delta \right] \end{aligned} \tag{A.14}$$

$$\begin{aligned} -x_2^{\mathrm{c}} Q/A &= -\frac{\epsilon}{4\pi} \int_{x_2}^{\infty} \mathrm{d}x x \frac{\partial^2}{\partial x^2} V_\Delta(x) = \frac{\epsilon}{4\pi} \left[\int_{x_2}^{\infty} \mathrm{d}x \frac{\partial}{\partial x} V_\Delta(x) - x \frac{\partial}{\partial x} V_\Delta(x) \Big|_{x_2}^{\infty} \right] \\ &= \frac{\epsilon}{4\pi} \left[V_\Delta(\infty) - V_\Delta(x_2) - x_2 E_\Delta \right] \end{aligned} \tag{A.15}$$

The potential $V_\Delta(x)$ is constant outside the capacitor (consequently also for $x \to \pm\infty$) and the electrical field $E_\Delta = -\nabla_x V_\Delta(x)$ is constant between $x = -x_1$ and $x = x_2$. The summation of x_1^{c} and $-x_2^{\mathrm{c}}$,

$$\begin{aligned} x_1^{\mathrm{c}} - x_2^{\mathrm{c}} &= \frac{A\epsilon}{4\pi Q/A} \left[V_\Delta(\infty) - V_\Delta(-\infty) + V_1 - V_2 - E_\Delta(x_1 + x_2) \right] \\ &= \frac{\epsilon}{4\pi Q} V_s \end{aligned} \tag{A.16}$$

is proportional to the applied voltage $V_s = V_\Delta(\infty) - V_\Delta(-\infty)$ if both electrodes are on the same chemical potential. In the last line Eq. (A.12) was used. The equation above yields the capacitance of Eq. (2.29) of Lang and Kohn [30].

Both capacitances Eq. (2.26) and Eq. (A.12) are equal, when the plate distance $d = x_1 + x_2$ is used for the result of Ullman under the restriction that both electrodes possess the same chemical potential.

A.3. Anisotropic Mass in the Two-Dimensional Free Electron Gas

In this section we calculate the Hartree-Fock energy of an uniform electron gas with anisotropic mass, i.e., the effective mass depends on the direction in k-space, so that we get for the unperturbed band energy:

$$\varepsilon(\mathbf{k}) = \frac{\hbar^2 k_x^2}{2m_x^*} + \frac{\hbar^2 k_y^2}{2m_y^*} \equiv a k_x^2 + b k_y^2 \tag{A.17}$$

The Helmholtz free energy of the system is given by the expectation value of the Hamiltonian Eq. (3.11):

$$F = \langle \hat{\mathcal{H}}^F \rangle = \frac{A}{(2\pi)^2} \sum_\sigma \int \mathrm{d}k^2 \varepsilon(\mathbf{k}) \langle \hat{a}^\dagger_{\mathbf{k}\sigma} \hat{a}_{\mathbf{k}\sigma} \rangle \tag{A.18}$$
$$- \frac{1}{2} \frac{e^2 A}{(2\pi)^4 \epsilon_{\text{eff}}} \sum_\sigma \int \mathrm{d}k^2 \int \mathrm{d}q^2 \frac{2\pi}{|\mathbf{q}|} \langle \hat{a}^\dagger_{\mathbf{k}+\mathbf{q}\sigma} \hat{a}_{\mathbf{k}+\mathbf{q}\sigma} \rangle \langle \hat{a}^\dagger_{\mathbf{k}\sigma} \hat{a}_{\mathbf{k}\sigma} \rangle$$

Going from isotrop to anisotropic mass the solutions to the Schrödinger equation, whose eigenvalue are Eq. (A.17), are still plane waves, so that the matrix elements $v_{\mathbf{k_1}\sigma_1,\mathbf{k_2}\sigma_2,\mathbf{k_3}\sigma_3,\mathbf{k_4}\sigma_4}$ stay the same. In the groundstate, all states with energy smaller than the chemical potential μ (or equivalently at $T = 0$ the Fermi energy ε_F) are occupied, so that we can replace the expectation of the number operator value by the Heaviside step function

$$\langle \hat{a}^\dagger_{\mathbf{k}\sigma} \hat{a}_{\mathbf{k}\sigma} \rangle = \Theta \left[\varepsilon_{\mathrm{F},\sigma} - \varepsilon(\mathbf{k}) \right]. \tag{A.19}$$

Thus we can rewrite

$$F = \frac{A}{(2\pi)^2} \sum_\sigma I_{1,\sigma} - \frac{1}{2} \frac{e^2 A}{(2\pi)^3 \epsilon_{\text{eff}}} \sum_\sigma I_{2,\sigma} \tag{A.20}$$
$$I_{1,\sigma} = \int \mathrm{d}k^2 \varepsilon(\mathbf{k}) \Theta \left[\varepsilon_{\mathrm{F},\sigma} - \varepsilon(\mathbf{k}) \right] \tag{A.21}$$
$$I_{2,\sigma} = \int \mathrm{d}k^2 \int \mathrm{d}q^2 \frac{1}{|\mathbf{q}|} \Theta \left[\varepsilon_{\mathrm{F},\sigma} - \varepsilon(\mathbf{k}+\mathbf{q}) \right] \Theta \left[\varepsilon_{\mathrm{F},\sigma} - \varepsilon(\mathbf{k}) \right] \tag{A.22}$$

In the following evaluation we will oppress the spin index of $I_{i,\sigma}$ and reintroduce it at the end. For this kind of problem, the use of elliptic coordinates is most appropriate:

$$k_x = \tau \cosh \varrho \cos \nu \tag{A.23}$$
$$k_y = \tau \sinh \varrho \sin \nu \tag{A.24}$$

Here τ and ν are the new variables. ϱ is a parameter, which is adjusted to bring $\varepsilon(\mathbf{k})$ in a simple form:

$$\begin{aligned} \varepsilon(\mathbf{k}) &= a k_x^2 + b k_y^2 = \tau^2 \left(a \cosh^2 \varrho \cos^2 \nu + b \sinh^2 \varrho \sin^2 \nu \right) \\ &= \tau^2 \left(\cos^2 \nu + \sin^2 \nu \right) = \tau^2 \end{aligned} \tag{A.25}$$

In the second line we chose

$$a \cosh^2 \varrho = 1 = b \sinh^2 \varrho \quad \Leftrightarrow \quad \cosh \varrho = \frac{1}{\sqrt{a}} \;\&\; \sinh \varrho = \frac{1}{\sqrt{b}} \tag{A.26}$$

The Jacobi determinant is needed to transform the differential elements under the integration to curvilinear coordinates:

$$\mathrm{d}k^2 = \mathrm{Det} \begin{pmatrix} \frac{\partial k_x}{\partial \tau} & \frac{\partial k_x}{\partial \nu} \\ \frac{\partial k_y}{\partial \tau} & \frac{\partial k_y}{\partial \nu} \end{pmatrix} \mathrm{d}\tau \mathrm{d}\nu = \mathrm{Det} \begin{pmatrix} \cosh \varrho \cos \nu & -\tau \cosh \varrho \sin \nu \\ \sinh \varrho \sin \nu & \tau \sinh \varrho \cos \nu \end{pmatrix} \mathrm{d}\tau \mathrm{d}\nu \tag{A.27}$$
$$= \tau \cosh \varrho \sinh \varrho (\cos^2 \nu + \sin^2 \nu) \mathrm{d}\tau \mathrm{d}\nu = \frac{\tau}{\sqrt{ab}} \mathrm{d}\tau \mathrm{d}\nu$$

Here we employed the special choice of ϱ in Eq. (A.26). The electron density for one spin direction can be easily calculated in this coordinates:

$$\begin{aligned} n_\sigma = \frac{N_\sigma}{A} = \frac{1}{A}\sum_{\mathbf{k}}\langle \hat{a}^\dagger_{\mathbf{k}\sigma}\hat{a}_{\mathbf{k}\sigma}\rangle &= \frac{1}{(2\pi)^2}\int_0^{2\pi}\mathrm{d}\nu\int_0^{\infty}\mathrm{d}\tau\frac{\tau}{\sqrt{ab}}\Theta[\mu-\varepsilon(\nu,\tau)] \\ &\overset{(A.25)}{=} \frac{1}{(2\pi)^2}\int_0^{2\pi}\mathrm{d}\nu\int_0^{\sqrt{\mu}}\mathrm{d}\tau\frac{\tau}{\sqrt{ab}} = \frac{1}{4\pi}\frac{\mu}{\sqrt{ab}} \end{aligned} \tag{A.28}$$

The integral of the kinetic energy is

$$\begin{aligned} I_1 &= \int_0^{2\pi}\mathrm{d}\nu\int_0^{\infty}\mathrm{d}\tau\frac{\tau}{\sqrt{ab}}\varepsilon(\nu,\tau)\Theta[\mu-\varepsilon(\nu,\tau)] = \int_0^{2\pi}\mathrm{d}\nu\int_0^{\sqrt{\mu}}\mathrm{d}\tau\frac{\tau^3}{\sqrt{ab}} \\ &= \frac{\pi}{2}\frac{\mu^2}{\sqrt{ab}} \overset{(A.28)}{=} 8\pi^3\sqrt{ab}n_\sigma^2 \end{aligned} \tag{A.29}$$

For the integral of the exchange interaction we need to evaluate the expressions

$$|\mathbf{k}| = \sqrt{k_x^2+k_y^2} = \left[\tau^2\cosh^2\varrho\cos^2\nu + \tau^2\sinh^2\varrho\sin^2\nu\right]^{1/2} = \tau\left[\frac{\cos^2\nu}{a}+\frac{\sin^2\nu}{b}\right]^{1/2} \tag{A.30}$$

and

$$\begin{aligned} \varepsilon(\mathbf{k}+\mathbf{q}) &= a(k_x+q_x)^2 + b(k_y+q_y)^2 = a\left(\frac{\tau_1\cos\nu_1}{\sqrt{a}}+\frac{\tau_2\cos\nu_2}{\sqrt{a}}\right)^2 + b\left(\frac{\tau_1\sin\nu_1}{\sqrt{b}}+\frac{\tau_2\sin\nu_2}{\sqrt{b}}\right)^2 \\ &= \tau_1^2(\cos^2\nu_1+\sin^2\nu_1) + 2\tau_1\tau_2(\cos\nu_1\cos\nu_2\sin\nu_1\sin\nu_2) + \tau_2^2(\cos^2\nu_2+\sin^2\nu_2) \\ &= \tau_1^2 + 2\tau_1\tau_2\cos(\nu_1-\nu_2) + \tau_2^2. \end{aligned} \tag{A.31}$$

The latter relation is used to assess one of the Heaviside step functions of I_2 as function of τ_2:

$$\Theta[\mu-\varepsilon(\mathbf{k}+\mathbf{q})] = \Theta[\mu-\tau_1^2-2\tau_1\tau_2\cos(\nu_1-\nu_2)-\tau_2^2] \tag{A.32}$$

Its argument is zero at

$$\tau_2^{\pm} = \tau_1\left[\pm\sqrt{\cos^2(\nu_1-\nu_2)+\left(\frac{\mu}{\tau_1^2}-1\right)}-\cos(\nu_1-\nu_2)\right]. \tag{A.33}$$

Note that the term in the parentheses under the square root is positive due to the second Heaviside step function of I_2. Thus the square root is larger than $|\cos(\nu_1-\nu_2)|$, so that $\tau_2^- \leq 0 \leq \tau_2^+$. Combining this result with Eq. (A.30), we can rewrite I_2 as

$$\begin{aligned} I_2 &= \int_0^{2\pi}\mathrm{d}\nu_1\int_0^{\infty}\mathrm{d}\tau_1\int_0^{2\pi}\mathrm{d}\nu_2\int_0^{\infty}\mathrm{d}\tau_2\frac{\tau_1\tau_2}{\sqrt{ab}^2}\frac{\Theta[\mu-\tau_1^2-2\tau_1\tau_2\cos(\nu_1-\nu_2)-\tau_2^2]\Theta[\mu-\tau_1^2]}{\tau_2\sqrt{\frac{\cos^2\nu_2}{a}+\frac{\sin^2\nu_2}{b}}} \\ &= \int_0^{2\pi}\mathrm{d}\nu_1\int_0^{\sqrt{\mu}}\mathrm{d}\tau_1\int_0^{2\pi}\mathrm{d}\nu_2\int_0^{\tau_2^+}\mathrm{d}\tau_2\frac{\tau_1}{\sqrt{ab}\sqrt{b\cos^2\nu_2+a\sin^2\nu_2}} \\ &= \int_0^{2\pi}\mathrm{d}\nu_1\int_0^{2\pi}\mathrm{d}\nu_2\int_0^{\sqrt{\mu}}\mathrm{d}\tau_1\frac{\tau_1\sqrt{\mu-\tau_1^2\sin^2(\nu_1-\nu_2)}-\tau_1^2\cos(\nu_1-\nu_2)}{\sqrt{ab}\sqrt{b\cos^2\nu_2+a\sin^2\nu_2}} \end{aligned} \tag{A.34}$$

The integration of the nominator over τ_1 yields:

$$\begin{aligned}
&\int_0^{\sqrt{\mu}} \mathrm{d}\tau_1 \left[\tau_1 \sqrt{\mu - \tau_1^2 \sin^2(\nu_1-\nu_2)} - \tau_1^2 \cos(\nu_1-\nu_2)\right] = \\
&\quad = \left[-\frac{1}{3\sin^2(\nu_1-\nu_2)}\left(\mu - \tau_1^2\sin^2(\nu_1-\nu_2)\right)^{3/2} - \frac{\tau_1^3}{3}\cos(\nu_1-\nu_2)\right]\Bigg|_{\tau_1=0}^{\tau_1=\sqrt{\mu}} \\
&\quad = -\frac{\mu^{3/2}}{3\sin^2(\nu_1-\nu_2)}\left[\left(\cos^2(\nu_1-\nu_2)\right)^{3/2} - 1\right] - \frac{\mu^{3/2}}{3}\cos(\nu_1-\nu_2)
\end{aligned} \tag{A.35}$$

The last term is proportional to $\cos(\nu_1-\nu_2)$ and gives zero when integrated over ν_1 in I_2. One can define the part of the integrand of the integral I_2 that depends on ν_1 as $f(\nu_1,\nu_2)$:

$$\begin{aligned}
I_2 &= \frac{\mu^{3/2}}{3\sqrt{ab}} \int_0^{2\pi} \mathrm{d}\nu_1 \int_0^{2\pi} \mathrm{d}\nu_2 \frac{1 - |\cos(\nu_1-\nu_2)|^3}{\sin^2(\nu_1-\nu_2)\sqrt{b\cos^2\nu_2 + a\sin^2\nu_2}} \\
&\equiv \frac{\mu^{3/2}}{3\sqrt{ab}} \int_0^{2\pi} \mathrm{d}\nu_1 \int_0^{2\pi} \mathrm{d}\nu_2 \frac{f(\nu_1,\nu_2)}{\sqrt{b\cos^2\nu_2 + a\sin^2\nu_2}}
\end{aligned} \tag{A.36}$$

This function is symmetric with respect to axes of reflection at $c_s = \nu_2 \pm s\pi/2$ in ν_1, where s is an integer number, as can be proven as follows: $\cos(x \pm \pi) = -\cos x$ and $\sin(x \pm \pi) = -\sin x$ ensure that $f(\nu_1 \pm \pi, \nu_2) = f(\nu_1,\nu_2)$ *(a)*, while $\cos -x = \cos x$ and $\sin -x = -\sin x$ induce $f(-\nu_1,-\nu_2) = f(\nu_1,\nu_2)$ *(b)*. A function is symmetric with respect to c_s, if $g(2c_s - x) = g(x)$ holds true. As $f(\nu_1,\nu_2) = f(\nu_1-\nu_2)$, we can write:

$$f(2c_s-\nu_1,\nu_2) = f(2c_s-\nu_1-\nu_2) = f(2\nu_2 \pm n\pi - \nu_1 - \nu_2) \overset{(a)}{=} f(\nu_2-\nu_1) \overset{(b)}{=} f(\nu_1,\nu_2), \tag{A.37}$$

so that the symmetry has been profen. Hence it is sufficient to integrate over ν_1 only between two points of symmetry and multiply the result by 4. We use the following antiderivatives from [152]:

$$\int \frac{\mathrm{d}x}{\sin^2 x} \overset{(287)}{=} -\frac{\cos x}{\sin x}, \qquad \int \frac{\mathrm{d}x \cos x^3}{\sin^2 x} \overset{(389)}{=} -\sin x - \frac{1}{\sin x} \tag{A.38}$$

We integrate over ν_1 from ν_2 to $\nu_2 + \pi/2$, where the cosine is positive and hence the absolute value can be dropped. Furthermore we perform the substitution $\nu_1' = \nu_1 - \nu_2$, so that

$$\begin{aligned}
I_2 &= \frac{\mu^{3/2}}{3\sqrt{ab}} \int_0^{2\pi} \mathrm{d}\nu_2 4 \int_0^{\pi/2} \mathrm{d}\nu_1' \frac{1-\cos {\nu_1'}^3}{\sin^2\nu_1' \sqrt{b\cos^2\nu_2 + a\sin^2\nu_2}} \\
&= \frac{4\mu^{3/2}}{3\sqrt{ab}} \int_0^{2\pi} \mathrm{d}\nu_2 \frac{1}{\sqrt{b\cos^2\nu_2 + a\sin^2\nu_2}} \left[\sin\nu_1 + \frac{1-\cos\nu_1}{\sin\nu_1}\right]\Bigg|_0^{\pi/2} \\
&= \frac{8\mu^{3/2}}{3\sqrt{ab}} \int_0^{2\pi} \mathrm{d}\nu_2 \frac{1}{\sqrt{b\cos^2\nu_2 + a\sin^2\nu_2}}
\end{aligned} \tag{A.39}$$

The second term of the antiderivative is zero according to the rule of l'Hospital [153]:

$$\lim_{x\to 0} \frac{1-\cos x}{\sin x} = \lim_{x\to 0} \frac{\sin x}{-\cos x} = 0 \tag{A.40}$$

One can show—with the same arguments as above—that the integrand of I_2 is symmetric with respect to the points $c_s' = \pm s\pi/2$, so that

$$I_2 = \frac{32\mu^{3/2}}{3\sqrt{ab}} \int_0^{\pi/2} \mathrm{d}\nu_2 \frac{1}{\sqrt{b\cos^2\nu_2 + a\sin^2\nu_2}} = \frac{32\mu^{3/2}}{3\sqrt{ab}} K\left[1 - \frac{b}{a}\right] \frac{1}{\sqrt{a}} \tag{A.41}$$

$K[k]$ is the complete elliptic integral of the first kind, which increases monotonically from $K[-\infty] = 0$ over $K[k = 0] = \pi/2$ to infinity at $k = 1$. Replacing μ by n with Eq. (A.28) yields

$$I_2 = \frac{256\pi^{3/2}}{3}\left(\frac{b}{a}\right)^{1/4} K\left[1 - \frac{b}{a}\right] n_\sigma^{3/2} \tag{A.42}$$

The insertion of the results for I_1 and I_2 into Eq. (A.20) yields

$$\begin{aligned} F &= \frac{A}{(2\pi)^2}\sum_\sigma 8\pi^3\sqrt{ab}n_\sigma^2 - \frac{1}{2}\frac{e^2 A}{(2\pi)^3\epsilon_{\text{eff}}}\sum_\sigma \frac{256\pi^{3/2}}{3}\left(\frac{b}{a}\right)^{1/4} K\left[1 - \frac{b}{a}\right] n_\sigma^{3/2} \qquad (A.43)\\ &= \frac{\pi\hbar^2}{2m_e^{-1}} A \frac{1+\xi^2}{\sqrt{m_x m_y}} n^2 - \frac{8}{3\pi}\frac{e^2 A}{\sqrt{2\pi}\epsilon_{\text{eff}}}\left(\frac{m_y}{m_x}\right)^{1/4} K\left[1 - \frac{m_y}{m_x}\right]\left[(1+\xi)^{3/2} + (1-\xi)^{3/2}\right] n^{3/2} \end{aligned}$$

Here we replaced n_σ by the polarization ξ and the total electron density n, which are related by

$$n_\uparrow = \frac{1+\xi}{2} n, \qquad n_\downarrow = \frac{1-\xi}{2} n \tag{A.44}$$

For $m_x = m_y$ Eq. (A.43) reduces to the energy of a two-dimensional electron gas with isotrop mass as given in Eq. (3.16).

A.4. Perturbation Theory at Finite Temperature

The grand potential Ω_0 of an exactly solvable one-particle Hamiltonian $\hat{\mathcal{H}}_0$ is given in Eq. (3.38):

$$\Omega_0 = -\frac{1}{\beta}\sum_{\mathbf{k},\sigma} \ln\left[1 + \exp\left(-\beta\varepsilon_\sigma^K(\mathbf{k})\right)\right], \tag{A.45}$$

where $\varepsilon_\sigma^K(\mathbf{k}) = \varepsilon_\sigma(\mathbf{k}) - \mu$ and $\varepsilon_\sigma(\mathbf{k})$ are the eigenvalues of $\hat{\mathcal{H}}_0$. Eq. (3.39) and Eq. (3.40) define the density n and the Fermi function $f_\sigma(\mathbf{k})$:

$$n = \frac{1}{\mathcal{V}}\sum_{\mathbf{k},\sigma} n_{\mathbf{k}\sigma} = \frac{1}{\mathcal{V}}\sum_{\mathbf{k},\sigma}\frac{1}{1 + \exp\left(\beta(\varepsilon_\sigma(\mathbf{k}) - \mu)\right)} = \frac{1}{\mathcal{V}}\sum_{\mathbf{k},\sigma} f_\sigma(\mathbf{k}) \tag{A.46}$$

It is useful for the following manipulations to write down two variations of the occupation number $n_{\mathbf{k}\sigma}$:

$$n_{\mathbf{k}\sigma} = \frac{1}{1 + \exp\left(\beta\varepsilon_\sigma^K(\mathbf{k})\right)} \qquad \Longleftrightarrow \qquad \exp\left(\beta\varepsilon_\sigma^K(\mathbf{k})\right) = \frac{1 - n_{\mathbf{k}\sigma}}{n_{\mathbf{k}\sigma}} \tag{A.47}$$

$$\Longleftrightarrow \qquad \beta\varepsilon_\sigma^K(\mathbf{k}) = \ln\left[1 - n_{\mathbf{k}\sigma}\right] - \ln\left[n_{\mathbf{k}\sigma}\right] \tag{A.48}$$

The first expression can be used to rewrite Ω_0:

$$\begin{aligned} 1 + \exp\left(-\beta\varepsilon_\sigma^K(\mathbf{k})\right) &= 1 + \frac{n_{\mathbf{k}\sigma}}{1 - n_{\mathbf{k}\sigma}} = \frac{1}{1 - n_{\mathbf{k}\sigma}}\\ \Rightarrow \quad \Omega_0 &= \frac{1}{\beta}\sum_{\mathbf{k},\sigma}\ln\left[1 - n_{\mathbf{k}\sigma}\right] \end{aligned} \tag{A.49}$$

For the calculation of the entropy S the derivative of $n_{\mathbf{k}\sigma}$ with respect to β is needed:

$$\begin{aligned} \frac{\partial n_{\mathbf{k}\sigma}}{\partial\beta} &= -\frac{\varepsilon_\sigma^K(\mathbf{k})\exp\left(\beta\varepsilon_\sigma^K(\mathbf{k})\right)}{\left(1 + \exp\left(\beta\varepsilon_\sigma^K(\mathbf{k})\right)\right)^2} = -\frac{1}{\beta}\beta\varepsilon_\sigma^K(\mathbf{k})\exp\left(\beta\varepsilon_\sigma^K(\mathbf{k})\right) n_{\mathbf{k}\sigma}^2\\ &\overset{(A.47,A.48)}{=} -\frac{1}{\beta}\left(\ln\left[1 - n_{\mathbf{k}\sigma}\right] - \ln\left[n_{\mathbf{k}\sigma}\right]\right)\left(1 - n_{\mathbf{k}\sigma}\right) n_{\mathbf{k}\sigma} \end{aligned} \tag{A.50}$$

The entropy S is the derivative of Ω_0 with respect to temperature T (c.f. Eq. (3.33)); it can also be expressed as derivative with respect to $\beta = 1/k_\mathrm{B}T$:

$$S = -\left(\frac{\partial\Omega_0}{\partial T}\right)_{\mathcal{V},\mu} = -\frac{\partial\Omega_0}{\partial\beta}\frac{\partial\beta}{\partial T} = k_\mathrm{B}\beta^2 \sum_{\mathbf{k},\sigma}\left(\frac{1}{\beta}\frac{-\frac{\partial n_{\mathbf{k}\sigma}}{\partial\beta}}{1-n_{\mathbf{k}\sigma}} - \frac{1}{\beta^2}\ln\left[1-n_{\mathbf{k}\sigma}\right]\right) \tag{A.51}$$

$$= -k_\mathrm{B}\sum_{\mathbf{k},\sigma}\left(-\left(\ln\left[1-n_{\mathbf{k}\sigma}\right] - \ln\left[n_{\mathbf{k}\sigma}\right]\right)n_{\mathbf{k}\sigma} + \ln\left[1-n_{\mathbf{k}\sigma}\right]\right) \tag{A.52}$$

$$= -k_\mathrm{B}\sum_{\mathbf{k},\sigma}\left(n_{\mathbf{k}\sigma}\ln\left[n_{\mathbf{k}\sigma}\right] + \left(1-n_{\mathbf{k}\sigma}\right)\ln\left[1-n_{\mathbf{k}\sigma}\right]\right) \tag{A.53}$$

We can solve the right-hand side of Eq. (A.51) after the term with $\ln\left[1-n_{\mathbf{k}\sigma}\right]$ and thus phrase Ω_0 as function of the entropy S:

$$\Omega_0 = \frac{1}{\beta}\sum_{\mathbf{k},\sigma}\ln\left[1-n_{\mathbf{k}\sigma}\right] = \sum_{\mathbf{k},\sigma}\frac{-\frac{\partial n_{\mathbf{k}\sigma}}{\partial\beta}}{1-n_{\mathbf{k}\sigma}} - TS = \sum_{\mathbf{k},\sigma}\frac{\varepsilon_\sigma^K(\mathbf{k})\exp\left(\beta\varepsilon_\sigma^K(\mathbf{k})\right)n_{\mathbf{k}\sigma}^2}{1-n_{\mathbf{k}\sigma}} - TS$$

$$\overset{(A.47)}{=} \sum_{\mathbf{k},\sigma}\varepsilon_\sigma^K(\mathbf{k})n_{\mathbf{k}\sigma} - TS = \sum_{\mathbf{k},\sigma}\left(\varepsilon_\sigma(\mathbf{k})-\mu\right)n_{\mathbf{k}\sigma} - TS \tag{A.54}$$

As $N = \sum_{\mathbf{k}\sigma} n_{\mathbf{k}\sigma}$, we can identify the first term as the internal energy E by comparison to Eq. (3.32). We are interested in the Helmholtz free energy F and obtain it by performing the Legendre transformation given in Eq. (3.32) on Ω_0:

$$F(T,\mathcal{V},N) = \Omega_0(T,\mathcal{V},\mu) + \mu N = \sum_{\mathbf{k},\sigma}\varepsilon_\sigma(\mathbf{k})n_{\mathbf{k}\sigma} - TS \tag{A.55}$$

The entropy S, which is given in Eq. (A.53), and the occupation number $n_{\mathbf{k}\sigma}$ depend on μ, which can be expressed as function of n via Eq. (A.46). The form of the free energy Eq. (A.55) is useful in the respect that it allows a comparison to the $T = 0$ case: Then the Fermi function reduces to the Heaviside step function, which equals 1 if $\varepsilon_\sigma(\mathbf{k}) < \mu$ and 0 otherwise, and the entropy vanishes.

In the following we calculate the temperature dependent free energy for a two-dimensional uniform electron gas without external potential, where the band energies are spin independent and $\varepsilon(\mathbf{k})$ is given by the kinetic energy dispersion

$$\varepsilon_\sigma(\mathbf{k}) = \varepsilon(\mathbf{k}) = \frac{\hbar^2k^2}{2m^*} \equiv ak^2 \tag{A.56}$$

This band energy entails analytic results for the free energy and its derivatives. We start by calculating the density n_σ

$$n_\sigma = \frac{1}{A}\sum_{\mathbf{k}} n_{\mathbf{k}\sigma} = \frac{1}{(2\pi)^2}\int_0^{2\pi}\mathrm{d}\varphi\int_0^\infty \mathrm{d}k\frac{k}{1+\exp\left(\beta\left(ak^2-\mu\right)\right)}$$

$$= \frac{1}{2\pi}\frac{-1}{2a\beta}\ln\left[1+\exp\left(-\beta\left(ak^2-\mu\right)\right)\right]\Big|_{k=0}^{k=\infty} = \frac{1}{4\pi a\beta}\ln\left[1+e^{\beta\mu}\right] \tag{A.57}$$

Under the assumption of a spin unpolarized electron gas, i.e., $n_\uparrow = n_\downarrow = n/2$, we get

$$2\pi na\beta = \ln\left[1+\exp\left(\beta\mu\right)\right]$$

$$\mu = \frac{1}{\beta}\ln\left[\exp\left(2\pi na\beta\right)-1\right] \equiv \frac{1}{\beta}\ln\left[e^\zeta - 1\right] \tag{A.58}$$

Here we introduced the abbreviation $\zeta \equiv 2\pi n a\beta$. The internal kinetic energy E_{kin} is

$$\begin{aligned}
E_{\text{kin}} &= \sum_{\mathbf{k},\sigma} ak^2 n_{\mathbf{k}\sigma} = 2\frac{A}{2\pi} a \int_0^\infty \mathrm{d}k \frac{k^3}{1+\exp\left(\beta(ak^2-\mu)\right)} = \frac{A}{\pi} a \frac{1}{2a\beta}\frac{1}{a\beta}\int_{-\mu\beta}^\infty \mathrm{d}p \frac{p+\mu\beta}{1+\exp(p)} \\
&= \frac{A}{2\pi a\beta^2}\left[\int_{-\mu\beta}^0 \mathrm{d}p \frac{p}{1+e^p} + \int_0^\infty \mathrm{d}p \frac{p}{1+e^p} + \mu\beta \int_{-\mu\beta}^\infty \mathrm{d}p \frac{1}{1+e^p}\right] \\
&= \frac{A}{2\pi a\beta^2}\left[\int_{-\mu\beta}^0 \mathrm{d}p \frac{p}{1+e^p} + \frac{\pi^2}{12} + \mu\beta \ln\left[\frac{1}{1+e^{-p}}\right]\Bigg|_{p=-\mu\beta}^{p=\infty}\right] \\
&= \frac{A}{2\pi a\beta^2}\left[\frac{\pi^2}{6} - \frac{1}{2}\mu^2\beta^2 + \mathrm{Li}_2\left[-e^{-\mu\beta}\right]\right]
\end{aligned} \tag{A.59}$$

In the first line the substitution $p = \beta(ak^2-\mu)$ was made and $\mathrm{Li}_n[x]$ is the polylogarithm function (or in case of the subscript 2 the dilogarithm). It increases monotonically from $x = -\infty$ to 0 at $x = 0$ and is defined up to $x = 1$, where $\mathrm{Li}_2[1] = \pi^2/6$. The entropy S of Eq. (A.53) can also be expressed in terms of the dilogarithm:

$$\begin{aligned}
S &= -2k_B\frac{A}{2\pi}\int_0^\infty \mathrm{d}k k\Bigg\{\frac{1}{1+\exp\left(\beta(ak^2-\mu)\right)}\ln\left[\frac{1}{1+\exp\left(\beta(ak^2-\mu)\right)}\right] \\
&\qquad + \frac{\exp\left(\beta(ak^2-\mu)\right)}{1+\exp\left(\beta(ak^2-\mu)\right)}\ln\left[\frac{\exp\left(\beta(ak^2-\mu)\right)}{1+\exp\left(\beta(ak^2-\mu)\right)}\right]\Bigg\} \\
&\overset{p=\beta(ak^2-\mu)}{=} -k_B\frac{A}{\pi}\frac{1}{2a\beta}\int_{-\mu\beta}^\infty \mathrm{d}p\left\{\frac{1}{1+e^p}\ln\left[\frac{1}{1+e^p}\right] + \frac{e^p}{1+e^p}\ln\left[\frac{e^p}{1+e^p}\right]\right\} \\
&= -\frac{k_B A}{2\pi a\beta}\left\{\int_{-\mu\beta}^{\mu\beta}\mathrm{d}p\frac{1}{1+e^p}\ln\left[\frac{1}{1+e^p}\right] + \int_{-\infty}^{\infty}\mathrm{d}p\frac{1}{1+e^p}\ln\left[\frac{1}{1+e^p}\right]\right\} \\
&= -\frac{k_B A}{2\pi a\beta}\left\{\frac{1}{2}\ln^2\left[1+e^{-\mu\beta}\right] - \frac{1}{2}\ln^2\left[1+e^{\mu\beta}\right] + \mathrm{Li}_2\left[-e^{-\mu\beta}\right] - \mathrm{Li}_2\left[-e^{\mu\beta}\right] - \frac{\pi^2}{6}\right\}
\end{aligned} \tag{A.60}$$

The free energy is obtained by the combination of Eq. (A.59) with Eq. (A.60):

$$\begin{aligned}
F_0 &= E_{\text{kin}} - TS \\
&= \frac{A}{2\pi a\beta^2}\left[\frac{1}{2}\ln^2\left[1+e^{-\mu\beta}\right] - \frac{1}{2}\ln^2\left[1+e^{\mu\beta}\right] - \frac{1}{2}\mu^2\beta^2 + 2\mathrm{Li}_2\left[-e^{-\mu\beta}\right] - \mathrm{Li}_2\left[-e^{\mu\beta}\right]\right] \\
&= \frac{A}{2\pi a\beta^2}\left[\frac{1}{2}\left(\ln^2\left[1-e^{-\zeta}\right] - \zeta^2 - \ln^2\left[e^\zeta - 1\right]\right) + 2\mathrm{Li}_2\left[\frac{1}{e^\zeta-1}\right] - \mathrm{Li}_2\left[1-e^\zeta\right]\right] \\
&\equiv E_{\text{kin}}^0 I_{\text{k-TS}}(\zeta)
\end{aligned} \tag{A.61}$$

Here the dependency on μ was replaced by ζ with Eq. (A.58). The definition in the last line separates the kinetic energy for $T = 0$, E_{kin}^0, from a temperature and density dependent factor:

$$\begin{aligned}
E_{\text{kin}}^0 &= \pi a A n^2 \\
I_{\text{k-TS}}(\zeta) &= \frac{1}{\zeta^2}\left[\ln^2\left[1-e^{-\zeta}\right] - \zeta^2 - \ln^2\left[e^\zeta - 1\right] + 4\mathrm{Li}_2\left[\frac{1}{e^\zeta-1}\right] - 2\mathrm{Li}_2\left[1-e^\zeta\right]\right]
\end{aligned}$$

The derivatives of E_{kin} and S with respect to the density n are simple analytic functions. The easiest way to compute them is to bring E_{kin} and S into a form where the only dependence on the density resides in the limits of integration. One can then use the fundamental theorem of calculus,

$$\frac{\partial}{\partial x}\int_{-g(x)}^{g(x)}\mathrm{d}y f(y) = \frac{\partial}{\partial x}\left\{F[g(x)] - F[-g(x)]\right\} = \left[\frac{\mathrm{d}}{\mathrm{d}x}g(x)\right]\left\{f[g(x)] + f[-g(x)]\right\}. \tag{A.62}$$

As we phrase E_{kin} and S as function of ζ, its derivatives are useful:

$$\zeta = 2\pi n a\beta, \qquad \frac{\partial\zeta}{\partial n} = 2\pi a\beta = \frac{\zeta}{n}, \qquad \frac{\partial^2\zeta}{\partial n^2} = 0 \tag{A.63}$$

By using the relation Eq. (A.58) between ζ and μ, we can rewrite the kinetic energy in the third line of Eq. (A.59) as

$$E_{\mathrm{kin}} = \frac{A}{2\pi a\beta^2}\left(\int_{-\ln\left[e^{\zeta}-1\right]}^{0} \mathrm{d}p \frac{p}{1+e^{p}} + \frac{\pi^2}{12} + \ln\left[e^{\zeta}-1\right]\zeta\right) \tag{A.64}$$

The derivatives are

$$\begin{aligned}\frac{\partial E_{\mathrm{kin}}}{\partial n} &= \frac{\partial E_{\mathrm{kin}}}{\partial\zeta}\frac{\partial\zeta}{\partial n} = \frac{A}{2\pi a\beta^2}\frac{\zeta}{n}\left(\frac{1}{1-e^{-\zeta}}\frac{-\ln\left[e^{\zeta}-1\right]}{1+e^{-\ln\left[e^{\zeta}-1\right]}} + \ln\left[e^{\zeta}-1\right] + \frac{\zeta}{1-e^{-\zeta}}\right) \\ &= \frac{A}{\beta}\frac{\zeta}{1-e^{-\zeta}} \equiv \frac{\mathrm{d}E^0_{\mathrm{kin}}}{\mathrm{d}n} J_{\mathrm{kin}}(\zeta)\end{aligned} \tag{A.65}$$

$$\frac{\partial^2 E_{\mathrm{kin}}}{\partial n^2} = \frac{A}{\beta}\frac{\zeta}{n}\frac{\partial}{\partial\zeta}\frac{\zeta}{1-e^{-\zeta}} = 2\pi a A\frac{e^{\zeta}\left(e^{\zeta}-1-\zeta\right)}{\left(e^{\zeta}-1\right)^2} \equiv \frac{\mathrm{d}^2E^0_{\mathrm{kin}}}{\mathrm{d}n^2}K_{\mathrm{kin}}(\zeta) \tag{A.66}$$

Here the first and second derivatives of the kinetic energy at zero temperature were split of from the factors $J(\zeta)$ and $K(\zeta)$, respectively. For the derivatives of the entropy we use the third line of Eq. (A.60),

$$-TS = \frac{A}{2\pi a\beta^2}\left(\int_{-\ln\left[e^{\zeta}-1\right]}^{\ln\left[e^{\zeta}-1\right]} \mathrm{d}p \frac{1}{1+e^{p}} \ln\left[\frac{1}{1+e^{p}}\right] - \frac{\pi^2}{6}\right), \tag{A.67}$$

so that the derivatives are

$$\begin{aligned}-T\frac{\partial S}{\partial n} &= \frac{A}{2\pi a\beta^2}\frac{\zeta}{n}\frac{1}{1-e^{-\zeta}}\left(\frac{-\zeta}{e^{\zeta}} + \frac{1}{1+\frac{1}{\left(e^{\zeta}-1\right)}}\ln\left[1-e^{-\zeta}\right]\right) \\ &= \frac{A}{\beta}\left(\frac{-\zeta}{e^{\zeta}-1} + \ln\left[1-e^{-\zeta}\right]\right)\end{aligned} \tag{A.68}$$

$$-T\frac{\partial^2 S}{\partial n^2} = \frac{A}{\beta}\frac{\zeta}{n}\frac{\partial}{\partial\zeta}\left(\frac{-\zeta}{e^{\zeta}-1} + \ln\left[1-e^{-\zeta}\right]\right) = 2\pi a A\frac{\zeta e^{\zeta}}{\left(1-e^{\zeta}\right)^2} \tag{A.69}$$

The combination of the derivatives of E_{kin} and $-TS$ yields the derivative of the Helmholtz free energy:

$$\frac{\mathrm{d}F_0}{\mathrm{d}n} = \frac{A}{\beta}\left(\frac{1-\zeta e^{-\zeta}}{1-e^{-\zeta}} + \ln\left[1-e^{-\zeta}\right]\right) \equiv \frac{\mathrm{d}E^0_{\mathrm{kin}}}{\mathrm{d}n}J_{\mathrm{k-TS}}(\zeta) \tag{A.70}$$

$$\frac{\mathrm{d}^2F_0}{\mathrm{d}n^2} = 2\pi a A\frac{e^{\zeta}}{e^{\zeta}-1} \equiv \frac{\mathrm{d}^2E^0_{\mathrm{kin}}}{\mathrm{d}n^2}K_{\mathrm{k-TS}}(\zeta) \tag{A.71}$$

We now investigate the effect of the electron exchange interaction on the free energy. We perform a low level Hartree-Fock approximation, where only the single "oyster" diagram is considered [76]. This is analogous to the work of Gupta and Rajagopal [81], but in two dimensions

instead of three. The exchange energy is the expectation value of the exchange part of the Fock Hamiltonian Eq. (3.11):

$$F_{\mathrm{x}} = -\frac{1}{2}\frac{e^2 A}{(2\pi)^3 \epsilon_{\mathrm{eff}}} \sum_{\sigma} \int \mathrm{d}k^2 \int \mathrm{d}q^2 \frac{1}{q} \langle \hat{a}^{\dagger}_{\mathbf{k}\sigma} \hat{a}_{\mathbf{k}\sigma} \rangle \langle \hat{a}^{\dagger}_{\mathbf{k}+\mathbf{q}\sigma} \hat{a}_{\mathbf{k}+\mathbf{q}\sigma} \rangle \tag{A.72}$$

In our approximation we use the band energy of free electrons, i.e., $\varepsilon_{\sigma}(\mathbf{k}) = ak^2$, as given in Eq. (A.56), so that the exchange does not enter the Fermi function. Inserting the latter into F_{x} in polar coordinates and then executing the substitutions $k' = \sqrt{a\beta}k$ and $q' = \sqrt{a\beta}q$, yields:

$$\begin{aligned} F_{\mathrm{x}} &= -\frac{1}{2}\frac{e^2 A}{(2\pi)^2 \epsilon_{\mathrm{eff}}} \sum_{\sigma} \int_0^{2\pi} \mathrm{d}\vartheta \int_0^{\infty} \mathrm{d}q \int_0^{\infty} \mathrm{d}k k \frac{1}{1+e^{\beta(ak^2-\mu)}} \frac{1}{1+e^{\beta(a(k^2+2kq\cos\vartheta+q^2)-\mu)}} \\ &= -\frac{1}{2}\frac{e^2 A}{(2\pi)^2 \epsilon_{\mathrm{eff}}} \frac{1}{(a\beta)^{3/2}} \sum_{\sigma} \int_0^{2\pi} \mathrm{d}\vartheta \int_0^{\infty} \mathrm{d}q \int_0^{\infty} \mathrm{d}k k \frac{1}{1+e^{k^2-\beta\mu}} \frac{1}{1+e^{k^2+2kq\cos\vartheta+q^2-\beta\mu}} \\ &\equiv F_{\mathrm{x}}^0 I_{\mathrm{x}}(\zeta) \end{aligned} \tag{A.73}$$

Here we split off the exchange energy at zero temperature F_{x}^0 from a temperature dependent factor $I_{\mathrm{x}}(\zeta)$:

$$F_{\mathrm{x}}^0 = -\frac{8}{3}\frac{e^2 A}{\sqrt{2\pi}\epsilon_{\mathrm{eff}}} n^{3/2} \tag{A.74}$$

$$I_{\mathrm{x}}(\zeta) = \frac{3}{8\zeta^{3/2}} \int_0^{2\pi} \mathrm{d}\vartheta \int_0^{\infty} \mathrm{d}q \int_0^{\infty} \mathrm{d}k k \frac{e^{\zeta}-1}{e^{\zeta}-1+e^{k^2}} \frac{e^{\zeta}-1}{e^{\zeta}-1+e^{k^2+2kq\cos\vartheta+q^2}} \equiv \frac{3}{8\zeta^{3/2}}\mathcal{I} \tag{A.75}$$

For the derivatives with respect to n, we use as above the relation $\mathrm{d}\zeta/\mathrm{d}n = \zeta/n$. As $F_{\mathrm{x}}^0 \sim n^{3/2}$, it is $\mathrm{d}F_{\mathrm{x}}^0/\mathrm{d}n = 3F_{\mathrm{x}}^0/2n$ and $\mathrm{d}^2F_{\mathrm{x}}^0/\mathrm{d}n^2 = \frac{1}{2n}\mathrm{d}F_{\mathrm{x}}^0/\mathrm{d}n$:

$$\frac{\mathrm{d}F_{\mathrm{x}}}{\mathrm{d}n} = \frac{\mathrm{d}F_{\mathrm{x}}^0}{\mathrm{d}n} I_{\mathrm{x}} + F_{\mathrm{x}}^0 \frac{\mathrm{d}I_{\mathrm{x}}}{\mathrm{d}\zeta}\frac{\zeta}{n} = \frac{\mathrm{d}F_{\mathrm{x}}^0}{\mathrm{d}n}\left(I_{\mathrm{x}} + \frac{2}{3}\zeta\frac{\mathrm{d}I_{\mathrm{x}}}{\mathrm{d}\zeta}\right) = \frac{\mathrm{d}F_{\mathrm{x}}^0}{\mathrm{d}n}\frac{1}{4\zeta^{1/2}}\frac{\mathrm{d}\mathcal{I}}{\mathrm{d}\zeta} \equiv \frac{\mathrm{d}F_{\mathrm{x}}^0}{\mathrm{d}n} J_{\mathrm{x}}(\zeta) \tag{A.76}$$

$$\frac{\mathrm{d}^2F_{\mathrm{x}}}{\mathrm{d}n^2} = \frac{\mathrm{d}^2F_{\mathrm{x}}^0}{\mathrm{d}n^2} J_{\mathrm{x}} + \frac{\mathrm{d}F_{\mathrm{x}}^0}{\mathrm{d}n}\frac{\mathrm{d}J_{\mathrm{x}}}{\mathrm{d}\zeta}\frac{\zeta}{n} = \frac{\mathrm{d}^2F_{\mathrm{x}}^0}{\mathrm{d}n^2}\left(J_{\mathrm{x}} + 2\zeta\frac{\mathrm{d}J_{\mathrm{x}}}{\mathrm{d}\zeta}\right) = \frac{\mathrm{d}^2F_{\mathrm{x}}^0}{\mathrm{d}n^2}\frac{\zeta^{1/2}}{2}\frac{\mathrm{d}^2\mathcal{I}}{\mathrm{d}\zeta^2} \equiv \frac{\mathrm{d}^2F_{\mathrm{x}}^0}{\mathrm{d}n^2} K_{\mathrm{x}}(\zeta) \tag{A.77}$$

For the analysis of the exchange term the integral $\mathcal{I}(\zeta)$ of Eq. (A.75) and its derivatives have to be calculated numerically. For small $\zeta \leq 25$ commercial programs as *Mathematica* or *Maple* provide reasonable results, but for larger ζ the derivatives of the exchange integral $\mathcal{I}$ are not smooth. The use of the *Gnu Scientific Library* in C++ provided smooth solutions after some transformations up to $\zeta \simeq 800$. For very low temperatures ζ is even larger than this value, so that we developed and used the following method to calculate the derivative of $\mathcal{I}$: First, we expressed the integrands of Eq. (A.75) as tangens hyperbolicus and wrote this expression as sum of Heaviside step functions:

$$g(x) \equiv \frac{1}{1+\exp(x)} = \frac{1}{2}\left(1 - \tanh\left(\frac{x}{2}\right)\right) = \lim_{N\to\infty}\frac{1}{N}\sum_{i=1}^{N}\Theta\left[x_i - \frac{x}{2}\right] \tag{A.78}$$

The values of the function $g(x)$ are $\in [0,1]$; we chose the subset of points $a_i = (i-1/2)/N$, which are evenly spaced, of this interval. The x_i are the values at which $g(x)$ matches the a_i, so that $x_i = g^{-1}(a_i)$. We use the inverse tangens hyperbolicus to identify x_i, so that the factor $1/2$ arises in the argument of the step function. In the second step we take the derivative of $\mathcal{I}$ with respect to $\mu\beta$ after both fractions were replaced by sum of Heaviside step functions as pointed

out. $\mu\beta$ appears only inside the Heaviside step function, so that the derivative yields the Dirac delta function $\delta[x]$ (multiplied by the second step function, according to the product rule). The integration over the delta and step function is executed carefully, so that

$$\frac{\partial\mathcal{I}}{\partial(\mu\beta)} = \lim_{N,M\to\infty}\sum_{j=1}^{M}\frac{2}{MN}\Theta[b_j]\Bigg\{\sum_{i=1}^{j-1}\left[2\sqrt{a_i}E\left[\vartheta_0|\frac{b_j}{b_i}\right]-\frac{b_i-b_j}{\sqrt{b_i}}F\left[\vartheta_0|\frac{b_j}{b_i}\right]\right] \tag{A.79}$$

$$2\sqrt{b_j}+\sum_{i=j+1}^{N}\left[2\sqrt{a_i}E\left[\frac{b_j}{b_i}\right]-\frac{b_i-b_j}{\sqrt{b_i}}K\left[\frac{b_j}{b_i}\right]\right]\Bigg\}\Theta[b_i] \tag{A.80}$$

$$b_j = 2\mathrm{arctanh}\left[1-2\frac{2j-1}{N}\right]+\mu\beta, \qquad \vartheta_0 = \arcsin\left[\sqrt{\frac{b_i}{b_j}}\right] \tag{A.81}$$

$F[\vartheta_0|x]$ is the elliptic integral of the first kind, $E[\vartheta_0|x]$ the elliptic integral of the second kind, $K[x]$ the complete elliptic integral of the first kind and $E[x]$ the complete elliptic integral. The expression for the derivative of $\mathcal{I}$ can be summed up quite easily by, e.g., *Mathematica*. As the resulting derivative of $\mathcal{I}$ with respect to ζ obtained by this method is only smooth for $\zeta > 10$, one has to fall back on the direct numerical approach for $\zeta < 10$.

We now determine the limits $\zeta \to 0$ and $\zeta \to \infty$, which correspond to the high temperature case $T \to \infty$ and $T \to 0$ respectively, if the density n is kept fixed. For the second derivative of E_{kin}

$$\lim_{\zeta\to 0}\frac{\partial^2 E_{\mathrm{kin}}}{\partial n^2} = 2\pi aA\lim_{\zeta\to 0}\frac{e^\zeta\left(e^\zeta-1-\zeta\right)}{(e^\zeta-1)^2} = 2\pi aA\lim_{\zeta\to 0}\left(\frac{1}{2}+\frac{\zeta}{6}-\frac{\zeta^3}{18-}+\mathcal{O}^4[\zeta]\right) = \pi aA \tag{A.82}$$

$$\lim_{\zeta\to\infty}\frac{\partial^2 E_{\mathrm{kin}}}{\partial n^2} = 2\pi aA\lim_{\zeta\to\infty}\frac{1-e^{-\zeta}-\zeta e^{-\zeta}}{(1-e^{-\zeta})^2} = 2\pi aA \tag{A.83}$$

is true. As the limits of the second derivative of $-TS$ are

$$\begin{aligned}\lim_{\zeta\to 0}\frac{\partial^2(-TS)}{\partial n^2} &= 2\pi aA\lim_{\zeta\to 0}\frac{\zeta e^\zeta}{(e^\zeta-1)^2} = 2\pi aA\lim_{\zeta\to 0}\frac{\zeta(1+\zeta+O[\zeta^2])}{(1+\zeta+O[\zeta^2]-1)^2}\\ &= 2\pi aA\lim_{\zeta\to 0}\frac{1}{\zeta} = A\lim_{n\beta\to 0}\frac{1}{n\beta} = \infty\end{aligned} \tag{A.84}$$

$$\lim_{\zeta\to\infty}\frac{\partial^2(-TS)}{\partial n^2} = 2\pi aA\lim_{\zeta\to\infty}\frac{\zeta e^{-\zeta}}{(1-e^{-\zeta})^2} = (2\pi a)^2 A\lim_{n\beta\to\infty} n\beta e^{-4\pi na\beta} = 0, \tag{A.85}$$

the contribution to the inverse compressibility arising from F_0 diverges for $n \to 0$ at finite T. This is in contrast to the exchange contribution, whose limit is more complicated to determine due to the unevaluated integral $\mathcal{I}$. The abbreviations $b \equiv \exp\left(k^2+2kq\cos\theta+q^2\right)$ and $c \equiv \exp\left(k^2\right)$ are introduced, so that

$$\begin{aligned}\lim_{\zeta\to 0}\frac{\mathrm{d}^2\mathcal{I}}{\mathrm{d}\zeta^2} &= \lim_{\zeta\to 0}\frac{\mathrm{d}^2}{\mathrm{d}\zeta^2}\int_0^{2\pi}\mathrm{d}\theta\int_0^\infty\mathrm{d}q\int_0^\infty\mathrm{d}k k\frac{e^\zeta-1}{e^\zeta-1+c}\frac{e^\zeta-1}{e^\zeta-1+b}\\ &= \lim_{\zeta\to 0}\int_0^{2\pi}\mathrm{d}\theta\int_0^\infty\mathrm{d}q\int_0^\infty\mathrm{d}k\frac{ke^\zeta}{\left(e^\zeta-1+c\right)^3\left(e^\zeta-1+b\right)^3}\Big[2c^2b^2+4c^2b^2(e^\zeta-1)\\ &\quad+3cb(c+b-2)(e^\zeta-1)^2+\left((c-b)^2-2(c+b)\right)(e^\zeta-1)^3-(c+b)\left(e^\zeta-1\right)^4\Big]\\ &= \int_0^{2\pi}\mathrm{d}\theta\int_0^\infty\mathrm{d}q\int_0^\infty\mathrm{d}k\frac{2b^2c^2k}{b^3c^3} = \int_0^{2\pi}\mathrm{d}\theta\int_0^\infty\mathrm{d}q\int_0^\infty\mathrm{d}k\frac{2k}{\exp\left(2k^2+2kq\cos\theta+q^2\right)}\\ &= \frac{1}{4}(2\pi)^{3/2}\end{aligned} \tag{A.86}$$

Hence we have

$$\lim_{\zeta\to 0}\frac{\mathrm{d}^2F_\mathrm{x}}{\mathrm{d}n^2}=\lim_{\zeta\to 0}\frac{\mathrm{d}^2F_\mathrm{x}^0}{\mathrm{d}n^2}\frac{\zeta^{1/2}}{2}\frac{1}{4}\left(2\pi\right)^{3/2}\sim\sqrt{\frac{1}{T}} \tag{A.87}$$

For $\zeta\to 0$, which is equal to $T\to\infty$ at finite density n or to $n\to 0$ at finite temperature T, the contribution of the kinetic and entropic part diverges,

$$\begin{aligned}\lim_{\zeta\to 0}\frac{\mathrm{d}^2F_0}{\mathrm{d}n^2}&\sim\lim_{n\beta\to 0}\frac{1}{n\beta}\\ \lim_{\zeta\to 0}\frac{\mathrm{d}^2F_\mathrm{x}}{\mathrm{d}n^2}&\sim-\lim_{n\beta\to 0}\sqrt{\beta},\end{aligned} \tag{A.88}$$

while the contribution from the exchange interaction stays finite. This means that at finite temperature the compressibility stays positive even for $n\to 0$, in contrast to the $T=0$ case: There the diverging negative exchange contribution dominates the constant kinetic contribution at small densities.

A.5. System with Rashba Spin-Orbit Coupling

Here we derive (c.f. Ref [33], App. A for the original version) the Helmholtz free energy $F_1(n_1)$ as given in Eq. (4.8) from integration of dispersion Eq. (4.4),

$$\varepsilon_\pm(\mathbf{k})=\frac{1}{2\pi N_0}\left(k\pm\pi N_0\alpha_\mathrm{R}\right)^2-\frac{\pi N_0}{2}\alpha_\mathrm{R}^2. \tag{A.89}$$

As outlined in Chapter 2.2, we treat the electron system with Rashba spin-orbit coupling (RSOC) as isolated, independent system. For that reason, the indices are dropped on the density and free energy and we label the DOS with index 0. The strength of the RSOC α_R of an isolated system depends on external fields only, so that α_R is not a function of the density n in that layer.

The number of electrons N in the system is received by integration over all states with energy lower than the chemical potential:

$$N=\sum_{\mathbf{k},\lambda=\pm}\Theta\left[\mu-\varepsilon_\lambda(\mathbf{k})\right]=\frac{A}{2\pi}\int_0^\infty\mathrm{d}k\cdot k\sum_{\lambda=\pm}\Theta\left[\mu-\left(\frac{\left(k-\lambda\pi N_0\alpha_\mathrm{R}\right)^2}{2\pi N_0}-\frac{\pi N_0}{2}\alpha_\mathrm{R}^2\right)\right] \tag{A.90}$$

It can be postulated that $\mu+\pi N_0\alpha_\mathrm{R}^2/2\geq 0$, as else the Heaviside functions and hence the integrals are zero. The argument of the Heaviside step function is zero at

$$k^\pm=\lambda\pi N_0\alpha_\mathrm{R}\pm\sqrt{2\pi N_0\mu+\pi^2N_0^2\alpha_\mathrm{R}^2}=\lambda\zeta\pm\sqrt{2\zeta\nu+\zeta^2}, \tag{A.91}$$

where $\zeta\equiv\pi N_0\alpha_\mathrm{R}$ and $\nu\equiv\frac{\mu}{\alpha_\mathrm{R}}$. For $k^-<k<k^+$ the step function simplifies to 1, i.e., one has to integrate k from k^- to k^+. A distinction of cases is necessary to determine the signs of $k^\pm$, as $k>0$ due to the introduction of polar coordinates. For $\mu<0$, the square root $\sqrt{2\zeta\nu+x^2}<x$, so that for $\lambda=-1$ both k^- and k^+ are negative, while for $\lambda=+1$ both k^- and k^+ are positive:
$\underline{\mu<0}$:

$$4\pi n=\int_{\zeta-\sqrt{2\zeta\nu+\zeta^2}}^{\zeta+\sqrt{2\zeta\nu+\zeta^2}}\mathrm{d}k\cdot 2k=4\zeta\sqrt{2\zeta\nu+\zeta^2} \tag{A.92}$$

$$\Rightarrow\nu=\frac{\pi^2n^2}{2\zeta^3}-\frac{\zeta}{2} \tag{A.93}$$

For positive $\mu > 0$, the square root $\sqrt{2\zeta\nu + x^2} > x$, which implies that for both $\lambda = \pm 1$ the lower boundary of integration $k^- < 0$ and the upper boundary $k^+ > 0$. Hence the integration starts at zero,
$\underline{\mu > 0:}$

$$4\pi n = \int_0^{-\zeta+\sqrt{2\zeta\nu+\zeta^2}} \mathrm{d}k \cdot 2k + \int_0^{\zeta+\sqrt{2\zeta\nu+\zeta^2}} \mathrm{d}k \cdot 2k = 4\zeta\nu + 4\zeta^2 \tag{A.94}$$

$$\Rightarrow \nu = \frac{\pi n}{\zeta} - \zeta \tag{A.95}$$

The distinction of cases transfers to the calculation of the free energy.
$\underline{\mu < 0:}$

$$\begin{aligned} F_0^< &= \sum_{\mathbf{k},\lambda=\pm} \varepsilon_\lambda(k)\Theta\left[\mu - \varepsilon_\lambda(\mathbf{k})\right] = \frac{A}{2\pi}\int_{\zeta-\sqrt{2\zeta\nu+\zeta^2}}^{\zeta+\sqrt{2\zeta\nu+\zeta^2}} \mathrm{d}k \cdot k\left(\frac{k^2}{2\zeta} - k\right)\alpha_\mathrm{R} \\ &= \frac{A}{3\pi}\zeta(\nu-\zeta)\sqrt{2\zeta\nu+\zeta^2}\alpha_\mathrm{R} = A\left(\frac{\pi^2 n^3}{6\zeta^3} - \frac{\zeta n}{2}\right)\alpha_\mathrm{R} \qquad \text{(A.96)} \\ &= A\left(\frac{n^3}{6\pi N_0^3\alpha_\mathrm{R}^2} - \frac{\pi}{2}N_0\alpha_\mathrm{R}^2 n\right) \qquad \text{(A.97)} \end{aligned}$$

$\underline{\mu > 0:}$

$$\begin{aligned} F_0^> &= \frac{A}{2\pi}\int_0^{-\zeta+\sqrt{2\zeta\nu+\zeta^2}} \mathrm{d}k \cdot k\left(\frac{k^2}{2\zeta} - k\right)\alpha_\mathrm{R} + \int_0^{\zeta+\sqrt{2\zeta\nu+\zeta^2}} \mathrm{d}k \cdot k\left(\frac{k^2}{2\zeta} + k\right)\alpha_\mathrm{R} \\ &= \frac{A}{2\pi}\left(\zeta\nu^2 - \frac{2\zeta^3}{3}\right)\alpha_\mathrm{R} = \frac{A}{2\pi}\left(\frac{\pi^2 n^2}{\zeta} - 2\pi\zeta n + \frac{\zeta^3}{3}\right)\alpha_\mathrm{R} \qquad \text{(A.98)} \\ &= A\left(\frac{n^2}{2N_0} - \pi N_0\alpha_\mathrm{R}^2 n + \frac{\pi^2}{6}N_0^3\alpha_\mathrm{R}^4\right) \qquad \text{(A.99)} \end{aligned}$$

The isolated layer with RSOC is then combined with a surface electrode, so that the Helmholtz free energy of the total system is given by $F_1(n_1)$, which was calculated above, $F_2(n_\mathrm{t} - n_1)$ (c.f. Eq. (4.7)) and $F_\mathrm{es}(n_1, n_\mathrm{t})$ (c.f. Eq. (4.6)). The phase boundary between phase $\mathrm{P1}^+$ and $\mathrm{P1}_0$ is obtained by setting $n_1 = n_\mathrm{t}$ in the total free energy, equalizing this to $F_\mathrm{tot}(n_1(n_\mathrm{t}))$ (where n_1 is the solution that minimizes the free energy) and then solving for D. This can be done analytically for $\alpha_0 = 0$ and the result is given in Eq. (4.21):

$$\frac{D}{A} = \frac{(3\pi N_1^2\alpha_1^2 n_\mathrm{t})^2 - 1}{12\pi N_1^3\alpha_1^2 n_\mathrm{t}}. \tag{A.100}$$

For smaller D than given by this equation, the system is in phase $\mathrm{P1}_0$ as the electrostatic cost of transferring all electrons to one layer is proportional to D. This can be inserted into the compressibility of $\mathrm{P1}_0$ (c.f. Eq. (4.20)) at $\alpha_0 = 0$:

$$\begin{aligned} \kappa_{\mathrm{P1}_0}^{-1} &\propto -3\pi N_1^2\alpha_1^2 n_\mathrm{t} + \frac{2DN_1}{A} \leq -3\pi N_1^2\alpha_1^2 n_\mathrm{t} + 2N_1\frac{(3\pi N_1^2\alpha_1^2 n_\mathrm{t})^2 - 1}{12\pi N_1^3\alpha_1^2 n_\mathrm{t}} \\ &= \frac{(3\pi N_1^2\alpha_1^2 n_\mathrm{t})(6\pi N_1^2\alpha_1^2 n_\mathrm{t} - 12\pi N_1^2\alpha_1^2 n_\mathrm{t}) - 2}{12\pi N_1^2\alpha_1^2 n_\mathrm{t}} < 0 \end{aligned} \tag{A.101}$$

At $\alpha = 0$ the compressibility of phase $\mathrm{P2}_0$ of Eq. (4.19) simplifies to

$$\kappa_{\mathrm{P2}_0}^{-1} \propto 1 - 6\pi N_1^2\alpha_1^2 n_\mathrm{t} + 2\pi^2 N_1^4\alpha_1^4 n_\mathrm{t}^2 + \frac{2DN_1}{A} \tag{A.102}$$

As two bands are occupied, the density has to be smaller than $n_t < 1/\pi N_1^2 \alpha_1^2$, for larger densities the transition to phase $P1_0$ takes place. The point at which the three phases $P1^+$, $P1_0$ and $P2_0$ is given by Eq. (A.100) and $n_t = 1/\pi N_1^2 \alpha_1^2$ and yields the condition $N_1 D/A = 2/3$. $P2_0$ at this boundary exhibits negative compressibility, as can directly calculated. The compressibility of $P2_0$ stays negative in the range

$$\kappa_{P2_0}^{-1} < 0 \qquad \Leftrightarrow \qquad n_- < n_t < n_+; \qquad n_\pm = \frac{\pi}{2} N_1^2 \alpha_1^2 \left[3 \pm \sqrt{9 - 2\left(1 + \frac{D N_1}{A}\right)} \right] \tag{A.103}$$

A.6. Atomic SOC in Basis of t_{2g} Orbitals

The atomic SOC, as given in Eq. (4.32), depends on the angular momentum operator $\mathbf{L}$. Its representation in the basis of the xy, xz and yz orbitals is derived in this section. For an orbital quantum number $l = 2$, the matrix elements of the angular momentum operator and its components are given by:

$$\begin{aligned}
\langle lm'|\mathbf{L}^2|lm\rangle &= \hbar^2 l(l+1)\delta_{m,m'} \\
\langle lm'|L_z|lm\rangle &= \hbar m \delta_{m,m'} \\
\langle lm'|L_+|lm\rangle &= \hbar\sqrt{(l-m)(l+m+1)}\delta_{m,m'+1} \quad \xrightarrow{l=2} \quad \hbar\sqrt{(2-m)(3+m)}\delta_{m,m'+1} \\
\langle lm'|L_-|lm\rangle &= \hbar\sqrt{(l+m)(l-m+1)}\delta_{m,m'-1} \quad \xrightarrow{l=2} \quad \hbar\sqrt{(2+m)(3-m)}\delta_{m,m'-1}
\end{aligned} \tag{A.104}$$

Hence the matrices with respect to the magnetic quantum number m (with the left index (m') as row and the right index (m) as column) are for $l = 2$:

$$L_+ = \hbar \begin{pmatrix} 0 & \sqrt{4} & 0 & 0 & 0 \\ 0 & 0 & \sqrt{6} & 0 & 0 \\ 0 & 0 & 0 & \sqrt{6} & 0 \\ 0 & 0 & 0 & 0 & \sqrt{4} \\ 0 & 0 & 0 & 0 & 0 \end{pmatrix}; \quad L_- = \hbar \begin{pmatrix} 0 & 0 & 0 & 0 & 0 \\ \sqrt{4} & 0 & 0 & 0 & 0 \\ 0 & \sqrt{6} & 0 & 0 & 0 \\ 0 & 0 & \sqrt{6} & 0 & 0 \\ 0 & 0 & 0 & \sqrt{4} & 0 \end{pmatrix}; \quad L_z = \hbar \begin{pmatrix} 2 & 0 & 0 & 0 & 0 \\ 0 & 1 & 0 & 0 & 0 \\ 0 & 0 & 0 & 0 & 0 \\ 0 & 0 & 0 & -1 & 0 \\ 0 & 0 & 0 & 0 & -2 \end{pmatrix}$$

$$L_x = \frac{1}{2}(L_+ + L_-) = \frac{\hbar}{2} \begin{pmatrix} 0 & \sqrt{4} & 0 & 0 & 0 \\ \sqrt{4} & 0 & \sqrt{6} & 0 & 0 \\ 0 & \sqrt{6} & 0 & \sqrt{6} & 0 \\ 0 & 0 & \sqrt{6} & 0 & \sqrt{4} \\ 0 & 0 & 0 & \sqrt{4} & 0 \end{pmatrix} \tag{A.105}$$

$$L_y = \frac{1}{2i}(L_+ - L_-) = \frac{\hbar}{2i} \begin{pmatrix} 0 & \sqrt{4} & 0 & 0 & 0 \\ -\sqrt{4} & 0 & \sqrt{6} & 0 & 0 \\ 0 & -\sqrt{6} & 0 & \sqrt{6} & 0 \\ 0 & 0 & -\sqrt{6} & 0 & \sqrt{4} \\ 0 & 0 & 0 & -\sqrt{4} & 0 \end{pmatrix}$$

According to, e.g., Ref. [154], the spherical harmonics are:

$$\begin{aligned}
Y_2^{\pm 2}(\theta,\varphi) &= \sqrt{\frac{15}{32\pi}} \sin(\theta)^2 e^{\pm 2i\varphi} \\
Y_2^{\pm 1}(\theta,\varphi) &= \mp\sqrt{\frac{15}{8\pi}} \sin(\theta)\cos(\theta) e^{\pm i\varphi} \\
Y_2^{0}(\theta,\varphi) &= \sqrt{\frac{5}{16\pi}} \left(3\cos(\theta)^2 - 1\right)
\end{aligned} \tag{A.106}$$

and the t_{2g} and e_g orbitals are given by:

$$d_{3z^2-r^2} = \sqrt{\frac{1}{2}}\left(3\cos(\theta)^2 - 1\right), \quad d_{x^2-y^2} = \sqrt{\frac{3}{2}}\sin(\theta)^2\cos(2\varphi), \quad d_{xy} = \sqrt{\frac{3}{2}}\sin(\theta)^2\sin(2\varphi)$$
$$d_{zx} = \sqrt{6}\sin(\theta)\cos(\theta)\cos(\varphi), \quad d_{yz} = \sqrt{6}\sin(\theta)\cos(\theta)\sin(\varphi) \tag{A.107}$$

By combining this, the t_{2g} and e_g orbitals can be expressed in spherical harmonics:

$$\begin{aligned} Y_2^{+2} + Y_2^{-2} &= \sqrt{\frac{15}{32\pi}}\sin(\theta)^2\left(e^{2i\varphi} + e^{-2i\varphi}\right) && \propto d_{x^2-y^2} \\ Y_2^{+2} - Y_2^{-2} &= \sqrt{\frac{15}{32\pi}}\sin(\theta)^2\left(e^{2i\varphi} - e^{-2i\varphi}\right) && \propto i d_{xy} \\ Y_2^{+1} + Y_2^{-1} &= \sqrt{\frac{15}{8\pi}}\sin(\theta)\cos(\theta)\left(-e^{i\varphi} + e^{-i\varphi}\right) && \propto -i d_{yz} \\ Y_2^{+1} - Y_2^{-1} &= \sqrt{\frac{15}{8\pi}}\sin(\theta)\cos(\theta)\left(-e^{i\varphi} - e^{-i\varphi}\right) && \propto -i d_{zx} \end{aligned} \tag{A.108}$$

Hence the d_{yz}, d_{zx} and d_{xy} orbitals are:

$$d_{yz} = \frac{i}{\sqrt{2}}\left(Y_2^{+1} + Y_2^{-1}\right) = \frac{1}{\sqrt{2}}\begin{pmatrix}0\\ i\\ 0\\ i\\ 0\end{pmatrix}; \quad d_{zx} = \frac{1}{\sqrt{2}}\left(Y_2^{-1} - Y_2^{+1}\right) = \frac{1}{\sqrt{2}}\begin{pmatrix}0\\ -1\\ 0\\ 1\\ 0\end{pmatrix} \tag{A.109}$$

$$d_{xy} = \frac{i}{\sqrt{2}}\left(Y_2^{-2} - Y_2^{+2}\right) = \frac{1}{\sqrt{2}}\begin{pmatrix}-i\\ 0\\ 0\\ 0\\ i\end{pmatrix}; \quad d_{x^2-y^2} = \frac{1}{\sqrt{2}}\left(Y_2^{+2} + Y_2^{-2}\right) = \frac{1}{\sqrt{2}}\begin{pmatrix}1\\ 0\\ 0\\ 0\\ 1\end{pmatrix},$$

while the $d_{3z^2-r^2}$ orbital is given by Y_2^0. Consequently, the matrices for the basis transformation are

$$S = \frac{1}{\sqrt{2}}\begin{pmatrix}0 & 0 & -i & 1 & 0\\ i & -1 & 0 & 0 & 0\\ 0 & 0 & 0 & 0 & \sqrt{2}\\ i & 1 & 0 & 0 & 0\\ 0 & 0 & i & 1 & 0\end{pmatrix}; \quad Z = (S^*)^T = \frac{1}{\sqrt{2}}\begin{pmatrix}0 & -i & 0 & -i & 0\\ 0 & -1 & 0 & 1 & 0\\ i & 0 & 0 & 0 & -i\\ 1 & 0 & 0 & 0 & 1\\ 0 & 0 & \sqrt{2} & 0 & 0\end{pmatrix} \tag{A.110}$$

The matrix L_i, expressed in the basis of eigenvectors of the L_z operator, is transformed by

$$\hat{L_i} = Z \cdot L_i \cdot S \tag{A.111}$$

into the new basis $\{d_{yz}, d_{zx}, d_{xy}, d_{x^2-y^2}, d_{3z^2-r^2}\}$. So that

$$\hat{L_z} = \frac{\hbar}{2}\begin{pmatrix}0 & 2i & 0 & 0 & 0\\ -2i & 0 & 0 & 0 & 0\\ 0 & 0 & 0 & 4i & 0\\ 0 & 0 & -4i & 0 & 0\\ 0 & 0 & 0 & 0 & 0\end{pmatrix}; \quad \hat{L_x} = \frac{\hbar}{4}\begin{pmatrix}0 & 0 & 0 & -4i & -4\sqrt{3}i\\ 0 & 0 & 4i & 0 & 0\\ 0 & -4i & 0 & 0 & 0\\ 4i & 0 & 0 & 0 & 0\\ 4\sqrt{3}i & 0 & 0 & 0 & 0\end{pmatrix};$$
$$\hat{L_y} = \frac{\hbar}{4i}\begin{pmatrix}0 & 0 & 4 & 0 & 0\\ 0 & 0 & 0 & 4 & -4\sqrt{3}\\ -4 & 0 & 0 & 0 & 0\\ 0 & -4 & 0 & 0 & 0\\ 0 & 4\sqrt{3} & 0 & 0 & 0\end{pmatrix} \tag{A.112}$$

The projection of the angular momentum operator on the d_{yz}, d_{zx} and d_{xy} orbitals can be read out directly by taking the corresponding rows and columns:

$$\mathbf{L} = \left(\begin{pmatrix} 0 & 0 & 0 \\ 0 & 0 & i \\ 0 & -i & 0 \end{pmatrix}, \begin{pmatrix} 0 & 0 & -i \\ 0 & 0 & 0 \\ i & 0 & 0 \end{pmatrix}, \begin{pmatrix} 0 & i & 0 \\ -i & 0 & 0 \\ 0 & 0 & 0 \end{pmatrix} \right) \hbar \tag{A.113}$$

A.7. Semi-Analytical Solution of a System with RSOC and Exchange Coupling

A free electron gas with kinetic energy, RSOC and exchange coupling, which was introduced in Chapter 5, can be diagonalized by means of wave-vector dependent transformation coefficients $u_{\mathbf{k}}$, $v_{\mathbf{k}}$ and $\phi_{\mathbf{k}}$. One set of solutions for the coupled coefficients is given by the constant $u_{\mathbf{k}} = v_{\mathbf{k}} = 1/\sqrt{2}$ and $\phi_{\mathbf{k}} = \pi/2 - \varphi_{\mathbf{k}}$, where $\varphi_{\mathbf{k}}$ is the angle between $\mathbf{k}$ and the x direction in wave vector space. For the solution of the last set of transformation coefficients $\phi_{\mathbf{k}}$ to be valid, the states that are only singly occupied in k-space must possess rotation symmetry around 0. Then it follows from the rotation symmetry of the energy dispersion (see Eq. (A.151a) and (A.151b)) that the occupation $\langle \hat{a}^\dagger_{\mathbf{k}\pm} \hat{a}_{\mathbf{k}\pm} \rangle \equiv n_{\mathbf{k}\pm}$ of the two bands is also rotationally symmetric, which implies that

$$n_{\mathbf{k}\pm} = \begin{cases} 1, & r_{1\pm} \leq |\mathbf{k}| \leq r_{2\pm} \\ 0, & \text{else} \end{cases} \tag{A.114}$$

Finite $r_{1\pm}$ indicates that a circular disc with this radius around 0 of states in k space is unoccupied. For simplicity, we assume $r_{1\pm} = 0$ in the following calculations, as the circular hole in occupied states can be recovered later by the subtraction of a circular disc of occupied states. As a consequence, as only one radius appears in the definition for $n_{\mathbf{k}\sigma}$,we also drop the index, so that $r_{2\pm} \equiv r_\sigma$. In the Helmholtz free energy, integrals of the form

$$I^a_{12} = \frac{1}{2\pi} \int \mathrm{d}\mathbf{k} \int \mathrm{d}\mathbf{q}\, \frac{1}{|\mathbf{k}-\mathbf{q}|} n_{\mathbf{k}1} n_{\mathbf{q}2} \tag{A.115}$$

$$I^b_{12} = \frac{1}{2\pi} \int \mathrm{d}\mathbf{k} \int \mathrm{d}\mathbf{q}\, \frac{\cos(\varphi_{\mathbf{k}} - \varphi_{\mathbf{q}})}{|\mathbf{k}-\mathbf{q}|} n_{\mathbf{k}1} n_{\mathbf{q}2} \tag{A.116}$$

originate from the electron-electron interaction. The second integral is a part the constant C_F, which is defined in Eq. (5.22). A substitution of variables $\mathbf{q}' = \mathbf{k} - \mathbf{q}$ and the representation in polar coordinates yields for the first integral

$$I^a_{12} = \frac{1}{2\pi} \int_0^{2\pi} \mathrm{d}\varphi_k \int_0^{2\pi} \mathrm{d}\varphi_q \int_0^\infty \mathrm{d}k\, k \int_0^\infty \mathrm{d}q\, q \frac{1}{q} n_{\mathbf{k}1} n_{\mathbf{k}-\mathbf{q}2} \tag{A.117}$$

$$= \frac{1}{2\pi} \int_0^{2\pi} \mathrm{d}\varphi_k \int_0^{2\pi} \mathrm{d}\varphi_q \int_0^\infty \mathrm{d}k\, k \int_0^\infty \mathrm{d}q\, \Theta\left[r_1^2 - k^2\right] \Theta\left[r_2^2 - \left(k^2 - 2kq\cos(\varphi_k - \varphi_q) + q^2\right)\right]$$

$$= \int_0^{2\pi} \mathrm{d}\varphi \int_0^\infty \mathrm{d}k\, k \int_0^\infty \mathrm{d}q\, \Theta\left[r_1^2 - k^2\right] \Theta\left[r_2^2 - \left(k^2 - 2kq\cos\varphi + q^2\right)\right] \tag{A.118}$$

In the last line the substitution $\varphi = \varphi_k - \varphi_q$ was made and the integration over φ_k was executed. The argument of the second Heaviside step function is positive for $q_- < q < q_+$, with

$$q_\pm = k\cos\varphi \pm \sqrt{k^2(\cos^2\varphi - 1) + r_2^2} \tag{A.119}$$

The roots $q_\pm$ exist only if the discriminant $r_2^2 - k^2\sin^2\varphi$ is positive. q_- is negative for $\varphi \in (\frac{\pi}{2}, \frac{3\pi}{2})$ and outside of this interval for $k^2 < r_2^2$. On the other hand, q_+ is positive for $\varphi \notin (\frac{\pi}{2}, \frac{3\pi}{2})$ and

else also for $k^2 < r_2^2$. The splitting of the integration over $\mathrm{d}\varphi$ and a case-by-case analysis results in a sum of two integrals,

$$I_{12}^a = \int_0^\infty \mathrm{d}k\, k\Theta\left[r_1^2 - k^2\right] \left\{ \int_{\frac{\pi}{2}}^{\frac{3\pi}{2}} \mathrm{d}\varphi \int_0^{q_+} \mathrm{d}q\, \Theta\left[r_2^2 - k^2\right] \right. \tag{A.120}$$
$$\left. + \left(\int_0^{\frac{\pi}{2}} + \int_{\frac{3\pi}{2}}^{2\pi} \right) \mathrm{d}\varphi \left(\int_0^{q_+} \mathrm{d}q\, \Theta\left[r_2^2 - k^2\right] + \int_{q_-}^{q_+} \mathrm{d}q\, \Theta\left[k^2 - r_2^2\right] \right) \right\} \Theta\left[r_2^2 - k^2 \sin^2\varphi\right]$$
$$= \int_0^\infty \mathrm{d}k\, k\Theta\left[r_1^2 - k^2\right] \left\{ \int_0^{2\pi} \mathrm{d}\varphi\, q_+ \Theta\left[r_2^2 - k^2\right] \right. \tag{A.121}$$
$$\left. + \left(\int_0^{\frac{\pi}{2}} + \int_{\frac{3\pi}{2}}^{2\pi} \right) \mathrm{d}\varphi\, (q_+ - q_-)\, \Theta\left[k^2 - r_2^2\right] \Theta\left[r_2^2 - k^2 \sin^2\varphi\right] \right\}$$

The insertion of $q_\pm$, where $m \equiv \mathrm{Min}[r_1, r_2]$, yields

$$I_{12}^a = \int_0^{2\pi} \mathrm{d}\varphi \int_0^m \mathrm{d}k \left(k^2 \cos\varphi + k\sqrt{r_2^2 - k^2 \sin^2\varphi} \right) \tag{A.122}$$
$$+ 2 \left(\int_0^{\frac{\pi}{2}} + \int_{\frac{3\pi}{2}}^{2\pi} \right) \mathrm{d}\varphi \int_{r_2}^{r_1} \mathrm{d}k\, \Theta\left[r_1 - r_2\right] \Theta\left[r_2^2 - k^2 \sin^2\varphi\right] k\sqrt{r_2^2 - k^2 \sin^2\varphi}$$
$$= \int_0^{2\pi} \mathrm{d}\varphi \left(\int_0^{r_1} \mathrm{d}k\, \Theta\left[r_2 - r_1\right] + \int_0^{r_2} \mathrm{d}k\, \Theta\left[r_1 - r_2\right] \right) k\sqrt{r_2^2 - k^2 \sin^2\varphi} \tag{A.123}$$
$$+ 2 \int_0^{\pi} \mathrm{d}\varphi \int_{r_2}^{r_1} \mathrm{d}k\, \Theta\left[r_1 - r_2\right] \Theta\left[r_2^2 - k^2 \sin^2\varphi\right] k\sqrt{r_2^2 - k^2 \sin^2\varphi}$$
$$= 2 \int_0^{\pi} \mathrm{d}\varphi \left(\int_0^{r_1} \mathrm{d}k\, \Theta\left[r_2 - r_1\right] + \int_0^{r_1} \mathrm{d}k\, \Theta\left[r_1 - r_2\right] \Theta\left[r_2^2 - k^2 \sin^2\varphi\right] \right) k\sqrt{r_2^2 - k^2 \sin^2\varphi}$$
$$\equiv I_{12;1}^a + I_{12;2}^a \tag{A.124}$$

In the third line it was used that the integration over one period of the $\cos\varphi$ is zero and the fourth line utilized a substitution $\varphi' = \varphi - \pi$. The upper limit of the integration over k of the second part of the integral, i.e., of $I_{12;2}^a$, is defined by the conditions $k^2 \sin^2\varphi < r_2^2$ and $k < r_1$:

$$I_{12;2}^a = 2 \int_0^{\pi} \mathrm{d}\varphi\, \Theta\left[r_1 - r_2\right] \left\{ \Theta\left[r_1 - \frac{r_2}{\sin\varphi}\right] \left(\frac{\sqrt{r_2^2 - k^2 \sin^2\varphi}^3}{-3\sin^2\varphi} \right) \Bigg|_{k=0}^{k=r_2/\sin\varphi} \right. \tag{A.125}$$
$$\left. + \Theta\left[\frac{r_2}{\sin\varphi} - r_1\right] \left(\frac{\sqrt{r_2^2 - k^2 \sin^2\varphi}^3}{-3\sin^2\varphi} \right) \Bigg|_{k=0}^{k=r_1} \right\}$$
$$= 2 \int_0^{\pi} \mathrm{d}\varphi\, \Theta\left[r_1 - r_2\right] \left\{ \Theta\left[\sin\varphi - \frac{r_2}{r_1}\right] \frac{r_2^3}{3\sin^2\varphi} + \Theta\left[\frac{r_2}{r_1} - \sin\varphi\right] \frac{r_2^3 - \sqrt{r_2^2 - r_1^2 \sin^2\varphi}^3}{3\sin^2\varphi} \right\}$$
$$= \frac{4}{3} r_2^3 \Theta\left[r_1 - r_2\right] \left\{ \int_{\arcsin\frac{r_2}{r_1}}^{\frac{\pi}{2}} \mathrm{d}\varphi\, \frac{1}{\sin^2\varphi} + \int_0^{\arcsin\frac{r_2}{r_1}} \mathrm{d}\varphi\, \frac{1 - \sqrt{1 - (r_1/r_2)^2 \sin^2\varphi}^3}{\sin^2\varphi} \right\} \tag{A.126}$$

The first term in the braces yields a simple expression after the substitution $t = \sin\varphi$,

$$\int_{\arcsin\frac{r_2}{r_1}}^{\frac{\pi}{2}} \mathrm{d}\varphi\, \frac{1}{\sin^2\varphi} = \int_{\frac{r_2}{r_1}}^1 \mathrm{d}t\, \frac{1}{t^2\sqrt{1 - t^2}} = \sqrt{(r_1/r_2)^2 - 1} \tag{A.127}$$

The second term in the braces gives with the abbreviation $\zeta \equiv r_1/r_2$

$$\int_0^{\arcsin\zeta^{-1}} \mathrm{d}\varphi \, \frac{1-\sqrt{1-\zeta^2\sin^2\varphi}^3}{\sin^2\varphi} = \Bigg[\left(\sqrt{1-\zeta^2\sin\varphi}-1\right) \frac{\sqrt{1-\sin\varphi}}{\sin\varphi} \tag{A.128}$$

$$+ \left(\left(\zeta^2+1\right) E\left[\varphi|\zeta^2\right] + \left(\zeta^2-1\right) F\left[\varphi|\zeta^2\right]\right) \Bigg] \Bigg|_{\varphi=0}^{\varphi=\arcsin\zeta^{-1}}$$

$$= -\sqrt{\zeta^2-1} + \left(\left(\zeta^2+1\right) E\left[\arcsin\zeta^{-1}|\zeta^2\right] + \left(\zeta^2-1\right) F\left[\arcsin\zeta^{-1}|\zeta^2\right]\right) \tag{A.129}$$

$F[\varphi|x]$ is the elliptic integral of the first kind and $E[\varphi|x]$ the elliptic integral of the second kind. The first term is compensated by the first integral in the braces in Eq. (A.126), so that

$$I^a_{12;2} = \frac{4}{3} r_2^3 \Theta\left[r_1-r_2\right] \left[\left(\left(\zeta^2+1\right) E\left[\arcsin\zeta^{-1}|\zeta^2\right] + \left(\zeta^2-1\right) F\left[\arcsin\zeta^{-1}|\zeta^2\right]\right)\right]. \tag{A.130}$$

For the remaining term $I^a_{12;1}$ the integration is similiar to the last term above, but without the restriction for φ, as $r_2 > r_1$:

$$I^a_{12;1} = 2\int_0^{\pi} \mathrm{d}\varphi \, \Theta\left[r_2-r_1\right] \left(\frac{\sqrt{r_2^2-k^2\sin^2\varphi}^3}{-3\sin^2\varphi}\right)\Bigg|_{k=0}^{k=r_1} \tag{A.131}$$

$$= \frac{4}{3} r_2^3 \Theta\left[r_2-r_1\right] \int_0^{\frac{\pi}{2}} \mathrm{d}\varphi \, \frac{1-\sqrt{1-(r_1/r_2)^2\sin^2\varphi}^3}{\sin^2\varphi} \tag{A.132}$$

$$= \frac{4}{3} r_2^3 \Theta\left[r_2-r_1\right] \left[\left(\zeta^2+1\right) E\left[\zeta^2\right] + \left(\zeta^2-1\right) K\left[\zeta^2\right]\right] \tag{A.133}$$

Here $K[x]$ is the complete elliptic integral of the first kind and $E[x]$ the complete elliptic integral.

For the determination of the second kind of integral I^b_{12} one has to start at Eq. (A.116), where it is most appropriate not to remove the denominator by a substitution of the variable $\mathbf{q}' = \mathbf{q}-\mathbf{k}$, as the cosine in the nominator depends on the angle $\varphi_{\mathbf{q}}$, which would also be transformed. Hence it is best to keep $\mathbf{k}$ and $\mathbf{q}$ unaltered and introduce polar coordinates, as then the integration over angle $\varphi_{\mathbf{k}} - \varphi_{\mathbf{q}}$ is the same in the nominator and denominator

$$I^b_{12} = \int_0^{2\pi} \mathrm{d}\varphi \int_0^{\infty} \mathrm{d}k \int_0^{\infty} \mathrm{d}q \, \frac{kq\cos\varphi}{\sqrt{k^2-2kq\cos\varphi+q^2}} \Theta\left[r_1-k\right]\Theta\left[r_2-q\right] \tag{A.134}$$

$$= \frac{1}{3}\int_0^{2\pi} \mathrm{d}\varphi \, \cos^2\varphi \Bigg\{ r_1^3 \log\left[\frac{r_2 - r_1\cos\varphi + \sqrt{r_1^2-2r_1r_2\cos\varphi+r_2^2}}{r_1-r_1\cos\varphi}\right] \tag{A.135}$$

$$+ \frac{r_1^2+r_2^2}{\cos\varphi}\sqrt{r_1^2-2r_1r_2\cos\varphi+r_2^2} + r_2^3 \log\left[\frac{r_1 - r_2\cos\varphi + \sqrt{r_1^2-2r_1r_2\cos\varphi+r_2^2}}{r_2-r_2\cos\varphi}\right]\Bigg\}$$

No analytical solution to the integration was found, so that this expression has to be evaluated numerically. Only for two circular discs of the same radius $r_1 = r_2$ an exact expression could be determined:

$$I^b_{11} = \frac{2}{3} r_1^3 \int_0^{2\pi} \mathrm{d}\varphi \, \cos\varphi \left\{\sqrt{2-2\cos\varphi} + \cos\varphi \log\left[\frac{1-\cos\varphi+\sqrt{2-2\cos\varphi}}{1-\cos\varphi}\right]\right\} \tag{A.136}$$

$$= c_{11} r_1^3 \tag{A.137}$$

Here $c_{11} \approx 1.10924158$ is the numerical value of the integral. For the integral I^a_{11}, we use the form of I^a_{12} as given in Eq. (A.121) and set $r_1 = r_2$, so that

$$I^a_{11} = \int_0^\infty \mathrm{d}k\, k\Theta\left[r_1^2 - k^2\right] \int_0^{2\pi} \mathrm{d}\varphi\, q_+ = \int_0^{2\pi} \mathrm{d}\varphi \int_0^{r_1} \mathrm{d}k\, k\sqrt{r_1^2 - k^2\sin^2\varphi} \tag{A.138}$$

$$= \frac{4}{3} r_1^3 \int_0^{\frac{\pi}{2}} \mathrm{d}\varphi\, \frac{1 - \sqrt{1-\sin^2\varphi}^3}{\sin^2\varphi} = \frac{8}{3} r_1^3 \tag{A.139}$$

The Helmholtz free energy of the system depends on the integrals I^a_{12} and I^b_{12}, which are a function of the radii r_1 and r_2 of the circular discs of occupied states. These radii are determined by two relations: The area of occupied states in k-space is proportional to the electron density n and if two bands are occupied the dispersion at the Fermi-wave vector of both bands yields the same energy, i.e., $\varepsilon_-(r_-) = \varepsilon_+(r_+)$. For a system with only kinetic energy and RSOC, which was examined in Chapter 4.2, the energy of the lower band decreases linear in k for small wave vectors. If the electron density is sufficiently small and the strength of the RSOC sufficiently large, this induces empty states around $k = 0$. This linear decrease is also present in the dispersion Eq. (A.151a) for the problem with RSOC and exchange coupling, so that we include the possibility of a disc of unoccupied states in the lower band. Formally this is introduced by a second radius, so that

$$n_{\mathbf{k}-} = \Theta\left[r_{2-} - |\mathbf{k}|\right] - \Theta\left[r_{1-} - |\mathbf{k}|\right] = n_{\mathbf{k}r_{2-}} - n_{\mathbf{k}r_{1-}}, \tag{A.140}$$

with $r_{2-} > r_{1-}$. The occupied states of the upper band are assumed to form a full circular disc with radius r_+ without holes. Thus the density of the electron system is

$$n = \frac{1}{A}\sum_{\mathbf{k}} \left(\langle \hat{a}^\dagger_{\mathbf{k}-} \hat{a}_{\mathbf{k}-} \rangle + \langle \hat{a}^\dagger_{\mathbf{k}+} \hat{a}_{\mathbf{k}+} \rangle \right) \tag{A.141}$$

$$= \frac{1}{(2\pi)^2} \int_0^{2\pi} \mathrm{d}\varphi \int_0^\infty \mathrm{d}k\, k \left(\Theta\left[r_{2-} - k\right] - \Theta\left[r_{1-} - k\right] + \Theta\left[r_+ - k\right] \right) \tag{A.142}$$

$$= \frac{1}{4\pi}\left(r_{2-}^2 - r_{1-}^2 + r_+^2\right) \tag{A.143}$$

The energy dispersion is given by Eq. (A.151a) and (A.151b) as

$$\varepsilon_\pm(\mathbf{k}) = \frac{k^2}{2\pi N_0} - \sum_{\mathbf{q}} v_{\mathrm{x}}(\mathbf{q}) n_{\mathbf{k}-\mathbf{q}\pm} \pm \alpha_{\mathrm{R}} k \tag{A.144}$$

For the evaluation of the exchange-induced contribution integrals of the form

$$I_1(k) = \int_0^{2\pi} \mathrm{d}\varphi \int_0^\infty \mathrm{d}q \frac{q}{q} \Theta\left[r_1^2 - \left(k^2 - 2kq\cos\varphi + q^2\right)\right] \tag{A.145}$$

$$= \int_0^{2\pi} \mathrm{d}\varphi\, q_+ \Theta\left[r_1^2 - k^2\right] + \left(\int_0^{\frac{\pi}{2}} + \int_{\frac{3\pi}{2}}^{2\pi} \right) \mathrm{d}\varphi\, (q_+ - q_-)\, \Theta\left[k^2 - r_1^2\right] \Theta\left[r_1^2 - k^2\sin^2\varphi\right]$$

have to be calculated. The second line corresponds to Eq. (A.121) without the summation over $\mathbf{k}$ and the factor $n_{\mathbf{k}2}$. These integrals transform to elliptic integrals,

$$I_1(k) = 4\int_0^{\frac{\pi}{2}} \mathrm{d}\varphi \sqrt{r_1^2 - k^2\sin^2\varphi}\, \Theta\left[r_1 - k\right] + 4\int_{\arcsin\eta^{-1}}^{\frac{\pi}{2}} \mathrm{d}\varphi \sqrt{r_1^2 - k^2\sin^2\varphi}\, \Theta\left[k - r_1\right] \tag{A.146}$$

$$= 4r_1 \left(\Theta\left[r_1 - k\right] \left(E\left[\varphi|\eta^2\right] \right)\Big|_{\varphi=0}^{\varphi=\frac{\pi}{2}} + \Theta\left[k - r_1\right] \left(E\left[\varphi|\eta^2\right] \right)\Big|_{\varphi=0}^{\varphi=\arcsin\eta^{-1}} \right) \tag{A.147}$$

$$= 4r_1 \left(E\left[\eta^2\right] \Theta\left[r_1 - k\right] + E\left[\arcsin\eta^{-1}|\eta^2\right] \Theta\left[k - r_1\right] \right), \tag{A.148}$$

where $\eta \equiv k/r_1$. For the determination of r_i one has to evaluate $I_1(k)$ at $k = r_1$, where it is not a well defined quantity due to the Heaviside step functions. Therefore one must insert $k = r_1$ directly at the beginning of the calculation, at Eq. (A.145):

$$I_1(r_1) = \int_0^{2\pi} \mathrm{d}\varphi \int_0^{\infty} \mathrm{d}q \Theta \left[r_1^2 - \left(r_1^2 - 2r_1 q\cos\varphi + q^2\right)\right] \tag{A.149}$$

$$= \int_0^{2\pi} \mathrm{d}\varphi\, 2r_1 \cos\varphi\, \Theta\left[\cos\varphi\right] = 4r_1 \int_0^{\frac{\pi}{2}} \mathrm{d}\varphi\, \cos\varphi = 4r_1 \tag{A.150}$$

A.8. Preliminary Results for the Semi-Analytical Solution of a System with RSOC and Exchange Coupling

In this section we assume $\cos\left(\varphi_{\mathbf{k}} - \varphi_{\mathbf{q}}\right) = 1$ for the energy dispersions Eq. (5.21a) and (5.21b), so that the dependence on the occupation of the respective other band vanishes:

$$\varepsilon_-(\mathbf{k}) = \frac{k^2}{2\pi N_0} - \sum_{\mathbf{q}} v_{\mathrm{x}}(\mathbf{k}-\mathbf{q})\langle \hat{a}^\dagger_{\mathbf{q}-}\hat{a}_{\mathbf{q}-}\rangle - \alpha_{\mathrm{R}} k \tag{A.151a}$$

$$\varepsilon_+(\mathbf{k}) = \frac{k^2}{2\pi N_0} - \sum_{\mathbf{q}} v_{\mathrm{x}}(\mathbf{k}-\mathbf{q})\langle \hat{a}^\dagger_{\mathbf{q}+}\hat{a}_{\mathbf{q}+}\rangle + \alpha_{\mathrm{R}} k, \tag{A.151b}$$

The resulting dispersion relations have the form of a direct sum of the dispersions between a pure Rashba model and a system comprising electronic exchange interaction. At the Fermi wave vectors the band energies are then given by

$$\varepsilon_-(r_{1-}) = \frac{r_{1-}^2}{2\pi N_0} - \alpha_{\mathrm{R}} r_{1-} - \frac{2}{\pi}\frac{e^2}{\epsilon_{\mathrm{eff}}}\left(E\left[\left(\frac{r_{1-}}{r_{2-}}\right)^2\right] r_{2-} - r_{1-}\right) \tag{A.152a}$$

$$\varepsilon_-(r_{2-}) = \frac{r_{2-}^2}{2\pi N_0} - \alpha_{\mathrm{R}} r_{2-} - \frac{2}{\pi}\frac{e^2}{\epsilon_{\mathrm{eff}}}\left(r_{2-} - E\left[\arcsin\left(\frac{r_{1-}}{r_{2-}}\right)\middle|\left(\frac{r_{2-}}{r_{1-}}\right)^2\right] r_{1-}\right) \tag{A.152b}$$

$$\varepsilon_+(r_+) = \frac{r_+^2}{2\pi N_0} + \alpha_{\mathrm{R}} r_+ - \frac{2}{\pi}\frac{e^2}{\epsilon_{\mathrm{eff}}} r_+ \tag{A.152c}$$

$$\varepsilon_-(0) = -\frac{e^2}{\epsilon_{\mathrm{eff}}}\left(r_{2-} - r_{1-}\right), \qquad \varepsilon_+(0) = -\frac{e^2}{\epsilon_{\mathrm{eff}}} r_+ \tag{A.152d}$$

The elliptic integral $E[\eta]$ can be expanded for small wave vectors as

$$E\left[\left(\frac{k}{r}\right)^2\right] = \frac{\pi}{2} - \frac{\pi}{8}\left(\frac{k}{r}\right)^2 - O\left[\frac{k}{r}\right]^4, \tag{A.153}$$

where the lowest order in k is quadratic. This implies that for small wave vectors the band energy of the lower band is decreasing with k, due to the RSOC. For finite r_{1-}, i.e., when there are unoccupied states around $k = 0$, the exchange contribution to the band energy decreases quadratically in k, since $r_{1-} < r_{2-}$. On the other hand, in the upper band the RSOC results in an increase of the band energy linear with k, so that the states around $k = 0$ are occupied even for small densities in the upper band.

For low electron densities only the lower band is occupied. Then $r_+ = 0$ and the parameters r_{1-} and r_{2-} are determined by their relation to the density Eq. (A.143), which yields $4\pi n = r_{2-}^2 - r_{1-}^2$, and by using that at the Fermi wave vectors the energy is constant, i.e., $\varepsilon_-(r_{1-}) = \varepsilon_-(r_{2-})$ as given in Eq. (A.152a) and (A.152b), respectively. Unfortunately, the latter equation involves

elliptic integrals, so that it is not possible to solve it analytically for r_{1-} or r_{2-} and numerical methods have to be employed.

The exchange contribution induces a gap at $k = 0$ between the two bands (see Eq. (A.152d)). If the chemical potential lies in this gap, then the electron states around $k = 0$ in the lower band are populated, so that $r_{1-} = 0$. This is ensured by a sufficiently large electron density $n > n_1$, where n_1 is the density below which the $k = 0$ state is unoccupied. The absence of r_{1-} is emphasized by relabeling $r_- \equiv r_{2-}$. The radius r_- is connected by Eq. (A.143) with the electron density to be $r_- = \sqrt{4\pi n}$. At the electron density n_1 the energy of the $k = 0$ state equals the Fermi energy, so that $\varepsilon_-(0) = \varepsilon_-(r_-^0)$:

$$\begin{aligned} -\frac{e^2}{\epsilon_{\text{eff}}} r_-^0 &= \frac{(r_-^0)^2}{2\pi N_0} - \alpha_{\text{R}} r_-^0 - \frac{2}{\pi}\frac{e^2}{\epsilon_{\text{eff}}} r_-^0 \\ \Rightarrow r_-^0 &= 2\pi N_0 \left[\alpha_{\text{R}} + \left(\frac{2}{\pi} - 1\right)\frac{e^2}{\epsilon_{\text{eff}}}\right] = \sqrt{4\pi n_1} \end{aligned} \tag{A.154}$$

This solution exists only for $\epsilon_{\text{eff}}\alpha_{\text{R}}/e^2 > 1 - \frac{2}{\pi} \approx 0.36338$; for smaller $\epsilon_{\text{eff}}\alpha_{\text{R}}$ all densities render the states around $k = 0$ occupied. The energy of the lower band decreases linearly for small k and thus features a minimum, which induces the existence of a point $r_0 > 0$ in k space with $\varepsilon_-(0) = \varepsilon_-(r_0)$, but this point does not necessarily coincide with r_-, which is determined by the density. The exchange induced part contributes to the dispersion by a term proportional to $-\frac{\pi}{2} r_-$ at $k = 0$ and proportional to $-r_-$ at $k = r_-$, i.e., the exchange contribution to the dispersion, which grows as $-E[(k/r_-)^2]$, is a monotonically increasing function in k. For the equality of energies at $k = 0$ and $k = r_-$ the RSOC induced term must compensate the positive increase between $k = 0$ and $k = r_-$, which is only possible for α_{R} large enough.

In case of two occupied bands we obtain the relation $4\pi n = r_-^2 + r_+^2$ from Eq. (A.143). The energy in both bands is equal at the Fermi wave vector, so that $\varepsilon_+(r_+) = \varepsilon_-(r_-)$, which determines r_- and r_+ by an equation of fourth order in these variables:

$$\frac{r_+}{2\pi N_0}\left[r_+ - 2\pi N_0\left(-\alpha_{\text{R}} + \frac{2}{\pi}\frac{e^2}{\epsilon_{\text{eff}}}\right)\right] = \frac{r_-}{2\pi N_0}\left[r_- - 2\pi N_0\left(\alpha_{\text{R}} + \frac{2}{\pi}\frac{e^2}{\epsilon_{\text{eff}}}\right)\right] \tag{A.155}$$

While this equation can in principle be solved analytically for r_- and r_+, the result is a long and unwieldy expression with little informative value, which is the reason why it is not stated here. Nevertheless, even without knowledge of the full analytical solution, two important conductions can be made. One simple solution is instantly recognizable by looking at the equation: For $r_+ = 0$ the left-hand side of the equation is zero and the right-hand side becomes zero for

$$r_- = 2\pi N_0\left(\alpha_{\text{R}} + \frac{2}{\pi}\frac{e^2}{\epsilon_{\text{eff}}}\right) \qquad \Rightarrow n_2 = \frac{4\pi^2 N_0^2}{4\pi}\left[\alpha_{\text{R}} + \frac{2}{\pi}\frac{e^2}{\epsilon_{\text{eff}}}\right]^2 \tag{A.156}$$

This defines the density n_2 above which the states of the upper band are populated by electrons, as $r_+ > 0$ for $n > n_2$. The comparison with Eq. (A.154) confirms $n_1 < n_2$, i.e., a range of densities exists for which only the lower band is occupied and where the states around $k = 0$ are filled. Analyzing Eq. (A.155) also reveals a condition for a second solution at $n = n_2$: If $r_+ > 0$, then the right-hand side of this equation is negative, as then $r_- < \sqrt{4\pi n_2}$. The left-hand side becomes negative for

$$r_+ < 2\pi N_0\left(\frac{2}{\pi}\frac{e^2}{\epsilon_{\text{eff}}} - \alpha_{\text{R}}\right) \equiv 2\pi N_0 c_+, \tag{A.157}$$

so that only for $c_+ > 0$ the second solution is present. The sign of the constant c_+, which depends on the difference in strength of the RSOC and exchange coupling, determines which

r_+ solves the problem: If $c_+ < 0$ then $r_+ = 0$ and else $r_+ > 0$ at $n = n_2$. That $r_+ = 0$ is no solution at $n = n_2$ for $c_+ > 0$ can be justified by reductio ad absurdum: Assume that $r_+^0 = 0$ (and consequently $r_2^0 = \sqrt{4\pi n_2}$) is a solution for $n = n_2$. Then increase the electron density by an infinitesimal amount of δn, so that $n = n_2 + \delta n$. The solutions for the new density n, $r_-(n)$ and $r_+(n)$ are functions of the density n, so that they can be expanded in δn to first order:

$$r_+(n) = r_+(n_2) + \left.\frac{\partial r_+}{\partial n}\right|_{n=n_2} \delta n = r'_+ \delta n, \tag{A.158}$$

$$r_-(n) = r_-(n_2) + \left.\frac{\partial r_-}{\partial n}\right|_{n=n_2} \delta n = \sqrt{4\pi n_2} + r'_- \delta n, \tag{A.159}$$

where $r'_\pm$ defines the partial derivative at $n = n_2$. The condition for the density,

$$4\pi n = 4\pi n_2 + 4\pi\delta n = r_-^2(n) + r_+^2(n) = 4\pi n_2 + 2\sqrt{4\pi n_2} r'_- \delta n + \left[\left(r'_-\right)^2 + \left(r'_+\right)^2\right](\delta n)^2, \tag{A.160}$$

determines $r'_- = 2\pi/\sqrt{4\pi n_2}$ by equating coefficients. The expansions for r_- and r_+ can be inserted into Eq. (A.155), which yields in linear order

$$\frac{r'_+ \delta n}{2\pi N_0}\left[r'_+ \delta n - 2\pi N_0 c_+\right] = \frac{\sqrt{4\pi n_2} + \frac{2\pi}{\sqrt{4\pi n_2}}\delta n}{2\pi N_0}\left[\frac{2\pi}{\sqrt{4\pi n_2}}\delta n\right] \tag{A.161}$$

The right-hand side of this equation is positive and the sign of the square brackets on the left-hand side is given by $-\text{signum}(c_+)$, so that the left-hand side of the equation is positive for $\text{signum}(r'_+) = -\text{signum}(c_+)$. For $c_+ > 0$ this implies that $r_+^0 = 0$ is decreasing with n to unphysical (and even unmathematical) values $r_+ < 0$.

Assume now that $c_+ < 0$ and $r_+ = 0$ is a solution at $n = n_2$ and then take the limit $c_+ \uparrow 0$ on Eq. (A.161), after division by δn. The right-hand side of this equation is unaffected by this limit and proportional to a finite positive constant. If $-2\pi N_0 c_+$ is of the order of $r'_+ \delta n$, then the term in the square brackets on the left-hand side is infinitesimal small, so that the factor r'_+ in front of the brackets has to be large for the equation being fulfilled. Thus, the coefficient r'_+ increases as c_+ approaches zero.

If $c_+ > 0$, then a finite $r_+ > 0$ solves $\varepsilon_-(r_-) = \varepsilon_+(r_+)$ at n_2. This solution exists in a density range $n_3 < n < n_2$, where at n_3 the radius r_+ jumps from a finite value to zero. If $c_+ > 0$, this term defines a lower boundary for $\sqrt{4\pi n_3}$. We designate the names P0, P1 and P2 to the phases above:

- $0 < r_{1-} < r_{2-}$, $r_+ = 0$ (P0): The upper band is empty and a circular disc of wave vectors with radius r_{1-} is unoccupied.
- $r_{1-} = r_+ = 0$, $r_{2-} \equiv r_-$ (P1): The electron states around $k = 0$ are occupied.
- $r_{1-} = 0 < r_+ < r_-$ (P2): Electrons reside in the upper band.

Figure A.2 illustrates the dispersions for the three phases P0, P1 and P2 and displays the radii as function of the density n. For small n a minimum forms in the dispersion at finite wave vector (Fig. A.2a), so that the states around $k = 0$ are unoccupied. An increase of n reduces the inner radius r_{1-} (yellow curve in Fig. A.2d) down to zero. At this point the system undergoes a phase transition to P2. The minimum at finite wave vector is present for $\alpha_\mathrm{R} = 0.5\,e\mathrm{V}a_\mathrm{B}$, but vanishes for $\alpha_\mathrm{R} = 0.2\,e\mathrm{V}a_\mathrm{B}$ (Fig. A.2b), as for the latter value $n_1 = 0$, so that the phase P0 does not exist in this parameter range. For even larger density electrons occupy the upper band.

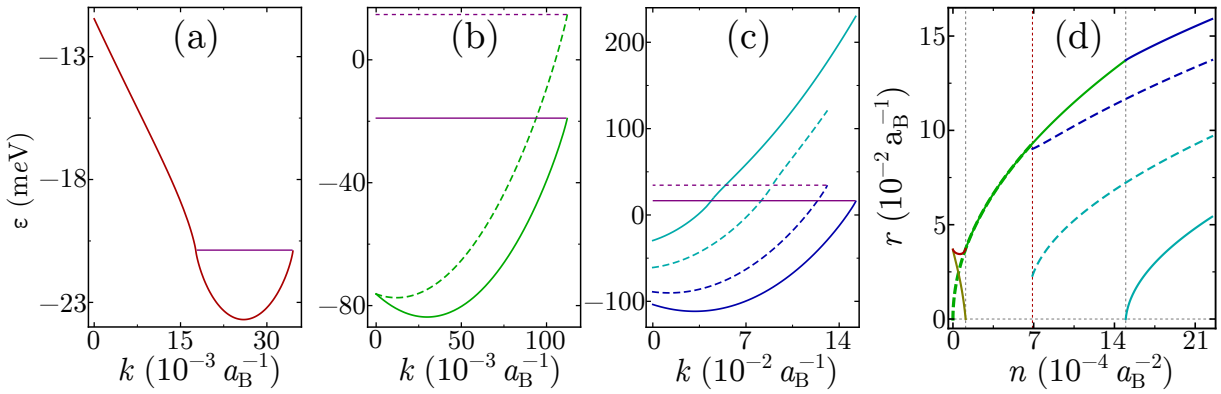

Figure A.2.: Band dispersions for phase (a) P0, (b) P1 and (c) P2 and (d) radii r_{2-}/r_{-} (upper curves) r_{1-}/r_{+} (lower curves) for $m_0 = 2\,m_e$, $\epsilon_{\text{eff}} = 20$, and $\alpha_{\text{R}} = 0.5\,e\text{V}a_{\text{B}}$ (solid curves) or $\alpha_{\text{R}} = 0.2\,e\text{V}a_{\text{B}}$ (dashed curves). The grey vertical dashed lines in (d) correspond to n_1 and n_2 for $\alpha_{\text{R}} = 0.5\,e\text{V}a_{\text{B}}$ and the red vertical dashed line to n_2 for $\alpha_{\text{R}} = 0.2\,e\text{V}a_{\text{B}}$. For the solid (dashed) curves the it is $c_+ < 0$ ($c_+ > 0$) valid. The electron density in (a) is $n = 0.7 \times 10^{-4}\,a_{\text{B}}^{-2}$, in (b) $n = 10 \times 10^{-4}\,a_{\text{B}}^{-2}$ and in (c) $n = 20 \times 10^{-4}\,a_{\text{B}}^{-2}$. The electronic states below the horizontal purple lines are occupied for these densities.

A comparison with the band structure of the pure Rashba model shows significant differences, which are induced by the exchange interaction. In the pure Rashba model, the splitting of the bands at $k = 0$ is zero, while the dispersions in the model with exchange coupling at $k = 0$ are

$$\varepsilon_-(0) = -\frac{e^2}{\epsilon_{\text{eff}}}\left(r_{2-} - r_{1-}\right), \qquad \varepsilon_+(0) = -\frac{e^2}{\epsilon_{\text{eff}}} r_+. \tag{A.162}$$

The exchange coupling opens a gap at $k = 0$, which increases with the difference in population of the two bands. The difference in occupation between the two bands is, inter alia, controlled by the strength of the RSOC due to the term $\pm\alpha_{\text{R}}k$, which appears in $\varepsilon_\pm(k)$. This is illustrated in Fig. A.2c and A.2d: For larger α_{R} (solid curve) more electrons are in the lower band and hence the gap is larger. The band gap is a prerequisite for the existence of phase P1, which cannot be found in the pure Rashba model. A large α_{R} shifts the phase boundary between P1 and P2 (right vertical dashed line in Fig. A.2d) to larger values of n, which is emphasized by Eq. (A.156). Only for α_{R} large enough, i.e., when $c_+ < 0$, we are able to specify the density of the phase boundary analytically; therefore in Fig. A.2d for $\alpha_{\text{R}} = 0.2\,e\text{V}a_{\text{B}}$, where $c+ > 0$, the vertical red dashed line indicates n_2, but not the phase boundary.

We now have all the tools available to calculate the Helmholtz free energy F by integrating Eq. (5.20) and inserting C_F from Eq. (5.22)

$$F(n) = \sum_{\mathbf{k}} \left(\varepsilon_-(\mathbf{k}) n_{\mathbf{k}-} + \varepsilon_+(\mathbf{k}) n_{\mathbf{k}+}\right) + \frac{1}{2}\sum_{\mathbf{k},\mathbf{q}} v_{\text{x}}(\mathbf{k}-\mathbf{q}) \Big[n_{\mathbf{k}-} n_{\mathbf{q}-} + n_{\mathbf{k}+} n_{\mathbf{q}+} + \frac{1}{2}\left(\cos\left(\varphi_{\mathbf{k}} - \varphi_{\mathbf{q}}\right) - 1\right)\left(n_{\mathbf{k}-} - n_{\mathbf{k}+}\right)\left(n_{\mathbf{q}-} - n_{\mathbf{q}+}\right) \Big] \tag{A.163}$$

If the upper band is empty, this expression simplifies to

$$F_1(n) = \sum_{\mathbf{k}} \left(\frac{k^2}{2\pi N_0} - \alpha_{\text{R}} k - \frac{2\pi e^2}{A\epsilon_{\text{eff}}|\mathbf{k}-\mathbf{q}|} n_{\mathbf{q}-} \right) n_{\mathbf{k}-} \tag{A.164}$$

$$+ \frac{1}{2}\sum_{\mathbf{k},\mathbf{q}} \frac{2\pi e^2}{A\epsilon_{\text{eff}}|\mathbf{k}-\mathbf{q}|} \frac{1}{2}\left(\cos\left(\varphi_{\mathbf{k}} - \varphi_{\mathbf{q}}\right) + 1\right) n_{\mathbf{k}-} n_{\mathbf{q}-} \tag{A.165}$$

One has to distinguish between $r_{1-} = 0$ and $r_{1-} > 0$. In the latter case the kinetic and RSOC energy are given by

$$\sum_{\mathbf{k}} \left(\frac{k^2}{2\pi N_0} - \alpha_{\mathrm{R}} k \right) n_{\mathbf{k}-} = \frac{A}{2\pi} \int_{r_{1-}}^{r_{2-}} \mathrm{d}k\, k \left(\frac{k^2}{2\pi N_0} - \alpha_{\mathrm{R}} k \right) = \frac{A}{2\pi} \left(\frac{r_{2-}^4 - r_{1-}^4}{8\pi N_0} - \alpha_{\mathrm{R}} \frac{r_{2-}^3 - r_{1-}^3}{3} \right), \tag{A.166}$$

while the exchange induced terms are

$$\begin{aligned}
\frac{1}{4} \frac{2\pi e^2}{A\epsilon_{\mathrm{eff}}} \sum_{\mathbf{k},\mathbf{q}} \frac{\cos(\varphi_{\mathbf{k}} - \varphi_{\mathbf{q}}) - 3}{|\mathbf{k} - \mathbf{q}|} n_{\mathbf{k}-} n_{\mathbf{q}-} &= \frac{e^2 A}{4\epsilon_{\mathrm{eff}}} \frac{1}{(2\pi)^3} \int \mathrm{d}\mathbf{k} \int \mathrm{d}\mathbf{q} \frac{\cos(\varphi_{\mathbf{k}} - \varphi_{\mathbf{q}}) - 3}{|\mathbf{k} - \mathbf{q}|} n_{\mathbf{k}-} n_{\mathbf{q}-} \\
&= \frac{e^2 A}{16\pi^2 \epsilon_{\mathrm{eff}}} \left[I^b_{r_{1-} r_{1-}} - 2 I^b_{r_{2-} r_{1-}} + I^b_{r_{2-} r_{2-}} - 3 \left(I^a_{r_{1-} r_{1-}} - 2 I^a_{r_{2-} r_{1-}} + I^a_{r_{2-} r_{2-}} \right) \right] && \text{(A.167)} \\
&= \frac{e^2 A}{16\pi^2 \epsilon_{\mathrm{eff}}} \Bigg[c_{11} \left(r_{1-}^3 + r_{2-}^3 \right) - 2 I^b_{r_{2-} r_{1-}} - 8 \left(r_{1-}^3 + r_{2-}^3 \right) && \text{(A.168)} \\
&\qquad + 8 \left(\left(r_{2-}^2 + r_{1-}^2 \right) E \left[\frac{r_{1-}^2}{r_{2-}^2} \right] - \left(r_{2-}^2 - r_{1-}^2 \right) K \left[\frac{r_{1-}^2}{r_{2-}^2} \right] \right) r_{2-} \Bigg]
\end{aligned}$$

For the last equality the results for I^a_{11} as in Eq. (A.139), for I^b_{11} as in Eq. (A.137), for as in I^a_{12} in Eq. (A.121) and for I^b_{12} as in Eq. (A.134) were used. If the electron density is large enough, then $r_{1-} = 0$, so that the kinetic and RSOC contribution to the energy are

$$\sum_{\mathbf{k}} \left(\frac{k^2}{2\pi N_0} - \alpha_{\mathrm{R}} k \right) n_{\mathbf{k}-} = \frac{A}{2\pi} \int_{0}^{r_{-}} \mathrm{d}k\, k \left(\frac{k^2}{2\pi N_0} - \alpha_{\mathrm{R}} k \right) = \frac{A}{2\pi} \left(\frac{r_{-}^4}{8\pi N_0} - \alpha_{\mathrm{R}} \frac{r_{-}^3}{3} \right), \tag{A.169}$$

while the exchange induced terms are

$$\begin{aligned}
\frac{1}{4} \frac{2\pi e^2}{A\epsilon_{\mathrm{eff}}} \sum_{\mathbf{k},\mathbf{q}} \frac{\cos(\varphi_{\mathbf{k}} - \varphi_{\mathbf{q}}) - 3}{|\mathbf{k} - \mathbf{q}|} n_{\mathbf{k}-} n_{\mathbf{q}-} &= \frac{e^2 A}{4\epsilon_{\mathrm{eff}}} \frac{1}{(2\pi)^3} \int \mathrm{d}\mathbf{k} \int \mathrm{d}\mathbf{q} \frac{\cos(\varphi_{\mathbf{k}} - \varphi_{\mathbf{q}}) - 3}{|\mathbf{k} - \mathbf{q}|} n_{\mathbf{k}-} n_{\mathbf{q}-} \\
&= \frac{e^2 A}{16\pi^2 \epsilon_{\mathrm{eff}}} \left(I^b_{--} - 3 I^a_{--} \right) = \frac{e^2 A}{16\pi^2 \epsilon_{\mathrm{eff}}} \left(c_{11} - 8 \right) r_{-}^3 && \text{(A.170)}
\end{aligned}$$

Thus, considering $r_{=} \sqrt{4\pi n}$, we obtain for the Helmholtz free energy

$$F_1(n) = A \frac{n^2}{N_0} - A \left[\frac{4\sqrt{\pi}}{3} \alpha_{\mathrm{R}} + \frac{e^2}{2\sqrt{\pi} \epsilon_{\mathrm{eff}}} \left(8 - c_{11} \right) \right] n^{3/2} \tag{A.171}$$

For two occupied bands it is $n_{\mathbf{k}+} \neq 0$ in Eq. (A.163), so that the kinetic and RSOC contributions to the Helmholtz free energy are given by

$$\sum_{\mathbf{k}} \left[\frac{k^2}{2\pi N_0} \left(n_{\mathbf{k}-} + n_{\mathbf{k}+} \right) - \alpha_{\mathrm{R}} k \left(n_{\mathbf{k}-} - n_{\mathbf{k}+} \right) \right] = \frac{A}{2\pi} \left(\frac{r_{-}^4 + r_{+}^4}{8\pi N_0} - \alpha_{\mathrm{R}} \frac{r_{-}^3 - r_{+}^3}{3} \right). \tag{A.172}$$

The exchange terms are

$$\begin{aligned}
&\frac{1}{4} \frac{2\pi e^2}{A\epsilon_{\mathrm{eff}}} \sum_{\mathbf{k},\mathbf{q}} \left[\frac{\cos(\varphi_{\mathbf{k}} - \varphi_{\mathbf{q}}) - 3}{|\mathbf{k} - \mathbf{q}|} \left(n_{\mathbf{k}-} n_{\mathbf{q}-} + n_{\mathbf{k}+} n_{\mathbf{q}+} \right) - \frac{\cos(\varphi_{\mathbf{k}} - \varphi_{\mathbf{q}}) - 1}{|\mathbf{k} - \mathbf{q}|} \left(n_{\mathbf{k}-} n_{\mathbf{q}+} + n_{\mathbf{k}+} n_{\mathbf{q}-} \right) \right] \\
&= \frac{e^2 A}{4\epsilon_{\mathrm{eff}}} \frac{1}{(2\pi)^3} \int \mathrm{d}\mathbf{k} \int \mathrm{d}\mathbf{q} \left[\frac{\cos(\varphi_{\mathbf{k}} - \varphi_{\mathbf{q}}) - 3}{|\mathbf{k} - \mathbf{q}|} \left(n_{\mathbf{k}-} n_{\mathbf{q}-} + n_{\mathbf{k}+} n_{\mathbf{q}+} \right) - 2 \frac{\cos(\varphi_{\mathbf{k}} - \varphi_{\mathbf{q}}) - 1}{|\mathbf{k} - \mathbf{q}|} n_{\mathbf{k}-} n_{\mathbf{q}+} \right] \\
&= \frac{e^2 A}{16\pi^2 \epsilon_{\mathrm{eff}}} \left(I^b_{--} + I^b_{++} - 3 I^a_{--} - 3 I^a_{++} - 2 I^b_{+-} - 2 I^a_{+-} \right) && \text{(A.173)} \\
&= \frac{e^2 A}{16\pi^2 \epsilon_{\mathrm{eff}}} \left[c_{11} \left(r_{-}^3 + r_{+}^3 \right) - 8 r_{-}^3 - 8 r_{+}^3 - 2 I^b_{+-} - \frac{8}{3} \left(\left(r_{-}^2 + r_{+}^2 \right) E \left[\frac{r_{+}^2}{r_{-}^2} \right] - \left(r_{-}^2 - r_{+}^2 \right) K \left[\frac{r_{+}^2}{r_{-}^2} \right] \right) r_{-} \right]
\end{aligned}$$

The radii r_- and r_+ are functions of the density and related by $4\pi n = r_-^2 + r_+^2$ in case of two occupied bands. Thus the kinetic contribution to the Helmholtz energy can be expressed by $r_+(n)$, so that its total second derivative is given by

$$F_{2,\mathrm{kin}}(n) = \frac{\left(4\pi n - r_+^2\right)^2 + r_+^2}{2\pi N_0} \tag{A.174}$$

$$\Rightarrow \frac{\mathrm{d}^2 F_{\mathrm{kin}}}{\mathrm{d}n^2} = \frac{1}{2\pi N_0}\left[2 - 8r_+ r_+' - 4(4\pi n - 6r_+^2)(r_+')^2 + 4r_+\left(2r_+^2 - 4\pi n\right) r_+''\right] \tag{A.175}$$

Under the condition that $c_+ < 0$, it is $r_+(n_2) = 0$, so that an evaluation of the second derivative at $n = n_2$ yields

$$\left.\frac{\mathrm{d}^2 F_{2,\mathrm{kin}}}{\mathrm{d}n^2}\right|_{n=n_2} = \frac{1}{2\pi N_0}\left[2 - 16\pi n_2 (r_+')^2\right] \tag{A.176}$$

The same procedure can be applied to the contribution from the RSOC to the Helmholtz free energy,

$$\left.\frac{\mathrm{d}^2 F_{2,\mathrm{RSOC}}}{\mathrm{d}n^2}\right|_{n=n_2} = -\alpha_{\mathrm{R}} \frac{3}{4\sqrt{4\pi n_2}}\left[1 - 16\pi n_2 (r_+')^2\right], \tag{A.177}$$

and also to the polynomial part of the exchange energy:

$$\left.\frac{\mathrm{d}^2}{\mathrm{d}n^2}\frac{e^2 A(c_{11} - 8)\left(r_-^3 + r_+^3\right)}{16\pi^2 \epsilon_{\mathrm{eff}}}\right|_{n=n_2} = -\frac{e^2 A(8 - c_{11})}{16\pi^2 \epsilon_{\mathrm{eff}}} \frac{3}{4\sqrt{4\pi n_2}}\left[1 - 16\pi n_2 (r_+')^2\right] \tag{A.178}$$

According to the last three equations the magnitude of the first derivative $r_+'(n_2)$ determines the signs of the contributions to the second derivative of the Helmholtz free energy with respect to n at n_2. For small r_+' the kinetic contribution is positive while the RSOC contribution and the polynomial part of the exchange contribution are negative. For large r_+' the signs are switched. Note that, according to the analysis following Eq. (A.161), the derivative $r_+'(n_2)$ diverges in the limit $c_+ \uparrow 0$, which induces the divergence of the kinetic contribution to negative values and of the two other contributions to positive values.

In the high density limit of two occupied bands the radii r_+ and r_- are large, so that the terms $r_+ - 2\pi N_0 c_+$ and $r_- - \sqrt{4\pi n_2}$ in Eq. (A.155) can be approximated by r_+ and r_-, respectively. The resulting solution $r_- = r_+ = \sqrt{2\pi n}$ can be inserted into the Helmholtz free energy:

$$F_2^{n \gg n_2}(n) = \frac{A n^2}{2N_0} - \frac{8e^2 A}{3\sqrt{2\pi}\epsilon_{\mathrm{eff}}} n^{3/2} \tag{A.179}$$

This recovers the result Eq. (3.16) of a free, unpolarized electron gas without RSOC but with exchange interaction, which was examined in Section 3.1.

The Rashba induced part of the energy depends on the same power in occupation radius as the exchange term, which is already recognizable in the dispersions Eq. (A.151a) and (A.151b): While the exchange potential there is $\propto 1/k$, the sum over $\mathbf{k}$ adds the dimension of k^2, so that the exchange contribution has the same power in k as $\pm\alpha_{\mathrm{R}} k$. This carries over to the dependence on the electron density n, which is visible in the energy of P1, as given in Eq. (A.171), where both the exchange and the RSOC term are $\propto -n^{3/2}$. The negative sign of the exchange term arises from the anticommutation relation between operators and the RSOC contribution is negative as the lower band is considered.

Consequently, also the second derivative of the Helmholtz free energy with respect to the electron density, which is of special interest due to its importance for the stability and appearance

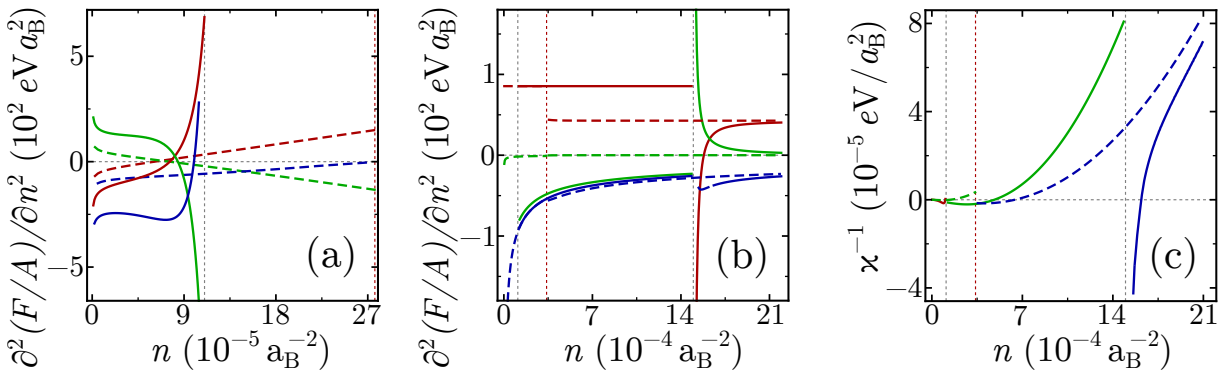

Figure A.3.: Second derivatives of the constituting parts of the Helmholtz free energy with respect to the density for (a) P0 and (b) P1 and P2, where red corresponds to the derivative of the kinetic term, green to the RSOC term and blue to the exchange term. It is $m_0 = 2\,m_e$ for all plots and $\epsilon_{\text{eff}} = 20$, and $\alpha_R = 0.5\,eVa_B$ for the solid curves in (a)-(c). The dashed curves in (a) correspond to $\epsilon_{\text{eff}} = 50$ and $\alpha_R = 0.5\,eVa_B$, while the dashed curves in (b) and (c) refer to $\epsilon_{\text{eff}} = 20$ and $\alpha_R = 0.01\,eVa_B$. (c) Inverse compressibility, where red corresponds to P0, green to P1 and blue to P2.

in the inverse capacitance, is independent of the RSOC for large n. Hence one has to concentrate on densities around and smaller than n_2, which marks the phase transition between P1 and P2 for $c_+ < 0$, for the study of the interplay between RSOC and exchange coupling. A weaker exchange coupling shifts the boundary of P0 to larger densities, but also reduces the absolute value of the second derivative of the kinetic, RSOC and exchange energy (Fig. A.3a). The RSOC parameter α_R determines both n_1 and n_2; only for sufficiently large α_R the phase P0 does exist and the density range of P1 increases with α_R. As the RSOC and exchange energy have the same negative sign and dependence on n in phase P1, their contribution to the second derivative is additive and $\propto -1/\sqrt{n}$, which renders the compressibility negative for small densities. Thus a larger α_R decreases the second derivative of the energy (Fig. A.3b). In P1 the second derivative of the kinetic energy is twice as large as in the large density limit of P2, which is analogous to the difference between a polarized and unpolarized free electron gas. For α_R large enough, c_+ becomes negative and $r_+ = 0$ at the phase boundary between P1 and P2. Then the sign of the RSOC and exchange contribution to the inverse compressibility is the same at $n = n_2$ in P2 (see App. A.7) and negative for sufficiently large $|c_+|$. The contribution from these two energies to κ^{-1} switches sign as $|c_+|$ approaches zero and increases its absolute value (App. A.7). The same statement is true for the kinetic contribution with the opposite sign and a slightly different value of $|c_+|$ for the sign switch (App. A.7). In Fig. A.3b the blue continuous curve refers to the exchange energy and assumes a large positive value approaching the right, vertical dashed line, which corresponds to the phase boundary between P1 and P2. Unfortunately, this region is not depicted in the plot for the exchange energy due to numerical difficulties. In P2 the inverse compressibility is smaller for larger α_R (Fig. A.3c). For $\alpha_R = 0.5\,eVa_B$ the system is in P1 left of the right, vertical dashed line, but it is in phase P2 for $\alpha_R = 0.01\,eVa_B$. So an increase of α_R can induce a phase transition at a given density from P1 to P2. This has two opposite effects on the inverse compressibility: While the second derivative of the exchange energy stays approximately unchanged, the kinetic contribution is larger in P1 than in P2 due to the difference of one versus two occupied bands. On the other hand, in P1 the RSOC adds a negative value proportional to α_R, while the second derivative of the RSOC term in P2 is small as the contributions from the lower and upper band neutralize each other.

Bibliography

[1] C. T. Black and J. J. Welser. *Electric-Field Penetration Into Metals: Consequences for High-Dielectric-Constant Capacitors.* IEEE Transactions on Electronic Devices **46**, 776 (1999).

[2] J. Mannhart and D. G. Schlom. *Oxide Interfaces—An Opportunity for Electronics.* Science **327**, 1607 (2010).

[3] J. Goniakowski, F. Finocchi and C. Noguera. *Polarity of oxide surfaces and nanostructures.* Reports on Progress in Physics **71**, 016501 (2008).

[4] N. Reyren, S. Thiel, A. D. Caviglia, L. Fitting Kourkoutis, G. Hammerl, C. Richter, C. W. Schneider, T. Kopp, A.-S. Rüetschi, D. Jaccard, M. Gabay, D. A. Muller, J.-M. Triscone and J. Mannhart. *Superconducting Interfaces Between Insulating Oxides.* Science **317**, 5842 (2007).

[5] A. Brinkman, M. Huijben, M. van Zalk, J. Huijben, U. Zeitler, J. C. Maan, W. G. van der Wiel, G. Rijnders, D. H. A. Blank and H. Hilgenkamp. *Magnetic effects at the interface between non-magnetic oxides.* Nature Materials **6**, 493 (2007).

[6] D. A. Dikin, M. Mehta, C. W. Bark, C. M. Folkman, C. B. Eom and V. Chandrasekhar. *Coexistence of Superconductivity and Ferromagnetism in Two Dimensions.* Physical Review Letters **107**, 056802 (2011).

[7] L. Li, C. Richter, J. Mannhart and R. C. Ashoori. *Coexistence of magnetic order and two-dimensional superconductivity at $LaAlO_3/SrTiO_3$ interfaces.* Nature Physics **7**, 762 (2011).

[8] A. D. Caviglia, M. Gabay, S. Gariglio, N. Reyren, C. Cancellieri and J.-M. Triscone. *Tunable Rashba Spin-Orbit Interaction at Oxide Interfaces.* Physical Review Letters **104**, 126803 (2010).

[9] L. Li, C. Richter, S. Paetel, T. Kopp, J. Mannhart and R. C. Ashoori. *Very large capacitance enhancement in a two-dimensional electron system.* Science **332**, 825 (2011).

[10] J. P. Eisenstein, L. N. Pfeiffer and K. W. West. *Negative compressibility of interacting two-dimensional electron and quasiparticle gases.* Physical Review Letters **68**, 674 (1992).

[11] J. P. Eisenstein, L. N. Pfeiffer and K. W. West. *Compressibility of the two-dimensional electron gas: Measurements of the zero-field exchange energy and fractional quantum Hall gap.* Physical Review B **50**, 1760 (1994).

[12] T. Kopp and J. Mannhart. *Calculation of the capacitances of conductors: Perspectives for the optimization of electronic devices.* Journal of Applied Physics **106**, 064504 (2009).

[13] D. Ceperley. *Ground state of the fermion one-component plasma: A Monte Carlo study in two and three dimensions.* Physical Review B **18**, 3126 (1978).

[14] B. Tanatar and D. M. Ceperley. *Ground state of the two-dimensional electron gas.* Physical Review B **39**, 5005 (1989).

[15] E. I. Rashba. *Symmetry of energy bands in crystals of wurtzite type: I. symmetry of bands disregarding spin-orbit interaction.* Sov. Phys. Solid State **1**, 368 (1959).

[16] E. I. Rashba and V. I. Sheka. *Symmetry of energy bands in crystals of wurtzite type: II. Symmetry of bands including spin-orbit interaction.* Fizika Tverd. Tela: Collected Papers **2**, 162 (1959).

[17] E. I. Rashba and V. I. Sheka. *Symmetry of Energy Bands in Crystals of Wurtzite Type II. Symmetry of Bands with Spin-Orbit Interaction Included.* New Journal of Physics **17**, 050202 (2015). Supplementary material of Ref. [88], translation of Ref [16].

[18] M. Breitschaft, V. Tinkl, N. Pavlenko, S. Paetel, C. Richter, J. R. Kirtley, Y. C. Liao, G. Hammerl, V. Eyert, T. Kopp and J. Mannhart. *Two-dimensional electron liquid state at $LaAlO_3$-$SrTiO_3$ interfaces.* Physical Review B **81**, 153414 (2010).

[19] G. Kotliar and A. E. Ruckenstein. *New Functional Integral Approach to Strongly Correlated Fermi Systems: The Gutzwiller Approximation as a Saddle Point.* Physical Review Letters **57**, 1362 (1986).

[20] R. Baierlein. *The elusive chemical potential.* American Journal of Physics **69**, 423 (2001).

[21] J. D. Van Der Waals. *Over de Continuiteit van den Gas- en Vloeistoftoestand.* Hoogeschool Te Leiden, Leiden (1873).

[22] C. B. Hanna, D. Haas and J. C. Díaz-Vélez. *Double-layer systems at zero magnetic field.* Physical Review B **61**, 13882 (2000).

[23] K. Steffen. *Quantum capacitance of macroscopic capacitors - diploma thesis.* University of Augsburg (2010).

[24] N. W. Ashcroft and N. D. Mermin. *Solid state physics.* Thomson Learning, 1. edition (1978).

[25] Y. Apertet, H. Ouerdane, C. Goupil and P. Lecoeur. *A note on the electrochemical nature of the thermoelectric power.* The European Physical Journal Plus **131**, 76 (2016).

[26] J. D. Jackson. *Classical electrodynamics.* Wiley-VCH, Weinheim, 3. edition (1998).

[27] M. Buettiker. *Capacitance, admittance, and rectification properties of small conductors.* Journal of Physics: Condensed Matter **5**, 9361 (1993).

[28] C. A. Mead. *Anomalous capacitance of thin dielectric structures.* Physical Review Letters **6**, 545 (1961).

[29] Y. H. Ku and F. G. Ullman. *Capacitance of thin dielectric structures.* Journal of Applied Physics **35**, 265 (1964).

[30] N. D. Lang and W. Kohn. *Theory of metal surfaces: induced surface charge and image potential.* Physical Review B **7**, 3541 (1973).

[31] J. G. Simmons. *An analytic form of Ku and Ullman's equations.* Applied Physics Letters **6**, 54 (1965).

[32] K. Steffen, R. Frésard and T. Kopp. *Capacitance and compressibility of heterostructures with strong electronic correlations.* Physical Review B **95**, 035143 (2017).

[33] K. Steffen, F. Loder and T. Kopp. *Spin-orbit controlled quantum capacitance of a polar heterostructure.* Physical Review B **91**, 075415 (2015).

[34] A. Ohtomo and Y. Hwang. *A high-mobility electron gas at the $LaAlO_3/SrTiO_3$ heterointerface.* Nature **427**, 423 (2004).

[35] S. Thiel, G. Hammerl, A. Schmehl, C. W. Schneider and J. Mannhart. *Tunable Quasi-Two-Dimensional Electron Gases in Oxide Heterostructures.* Science **313**, 1942 (2006).

[36] M. Sing, G. Berner, K. Goss, A. Müller, A. Ruff, A. Wetscherek, S. Thiel, J. Mannhart, S. A. Pauli, C. W. Schneider, P. R. Willmott, M. Gorgoi, F. Schäfers and R. Claessen. *Profiling the Interface Electron Gas of $LaAlO_3/SrTiO_3$ Heterostructures with Hard X-Ray Photoelectron Spectroscopy.* Physical Review Letters **102**, 176805 (2009).

[37] A. D. Caviglia, S. Gariglio, C. Cancellieri, B. Sacépé, A. Fête, N. Reyren, M. Gabay, A. F. Morpurgo and J.-M. Triscone. *Two-Dimensional Quantum Oscillations of the Conductance at $LaAlO_3/SrTiO_3$ Interfaces.* Physical Review Letters **105**, 236802 (2010).

[38] F. Bi, M. Huang, C.-W. Bark, S. Ryu, S. Lee, C.-B. Eom, P. Irvin and J. Levy. *Electro-mechanical response of top-gated $LaAlO_3/SrTiO_3$.* Journal of Applied Physics **119**, 025309 (2016).

[39] N. Bar-Chaim, M. Brunstein, J. Grünberg and A. Seidman. *Variations of the dielectric constant of pzt ferroelectric ceramics with electric field.* Ferroelectrics **6**, 299 (1974).

[40] S. Salahuddin and S. Datta. *Use of Negative Capacitance to Provide Voltage Amplification for Low Power Nanoscale Devices.* Nano Letters **8**, 405 (2008).

[41] C. M. Krowne, S. W. Kirchoefer, W. Chang, J. M. Pond and L. M. B. Alldredge. *Examination of the Possibility of Negative Capacitance Using Ferroelectric Materials in Solid State Electronic Devices.* Nano Letters **11**, 988 (2011).

[42] A. I. Khan, D. Bhowmik, P. Yu, S. J. Kim, X. Pan, R. Ramesh and S. Salahuddin. *Experimental evidence of ferroelectric negative capacitance in nanoscale heterostructures.* Applied Physics Letters **99**, 113501 (2011).

[43] A. I. Khan, K. Chatterjee, B. Wang, S. Drapcho, L. You, C. Serrao, S. R. Bakaul, R. Ramesh and S. Salahuddin. *Negative capacitance in a ferroelectric capacitor.* Nature Materials **14**, 182 (2014).

[44] W. Gao, A. Khan, X. Marti, C. Nelson, C. Serrao, J. Ravichandran, R. Ramesh and S. Salahuddin. *Room-Temperature Negative Capacitance in a Ferroelectric-Dielectric Superlattice Heterostructure.* Nano Letters **14**, 5819 (2014).

[45] S. V. Kravchenko, V. M. Pudalov and S. G. Semenchinsky. *Negative density of states of 2D electrons in a strong magnetic field.* Physics Letters A **141**, 71 (1989).

[46] S. Shapira, U. Sivan, P. M. Solomon, E. Buchstab, M. Tischler and G. B. Yoseph. *Thermodynamics of a Charged Fermion Layer at High r_s Values.* Physical Review Letters **77**, 3181 (1996).

[47] G. L. Yu, R. Jalil, B. Belle, A. S. Mayorov, P. Blake, F. Schedin, S. V. Morozov, L. A. Ponomarenko, F. Chiappini, S. Wiedmann, U. Zeitler, M. I. Katsnelson, A. K. Geim, K. S. Novoselov and D. C. Elias. *Interaction phenomena in graphene seen through quantum capacitance.* Proceedings of the National Academy of Sciences of the United States of America **110**, 3282 (2013).

[48] R. S. Lakes, T. Lee, A. Bersie and Y. C. Wang. *Extreme damping in composite materials with negative-stiffness inclusions.* Letters to Nature **410**, 565 (2001).

[49] T. Jaglinski, D. Kochmann, D. Stone and R. S. Lakes. *Composite Materials with Viscoelastic Stiffness Greater Than Diamond.* Science **315**, 620 (2007).

[50] S. T. F. Hale and J. K. Freericks. *Many-body effects on the capacitance of multilayers made from strongly correlated materials.* Physical Review B **85**, 205444 (2012).

[51] L. M. Falicov and J. C. Kimball. *Simple Model for Semiconductor-Metal Transitions: SmB_6 and Transition-Metal Oxides.* Physical Review Letters **22**, 997 (1969).

[52] J. K. Freericks. *Transport in Multilayered Nanostructures, The Dynamical Mean-Field Theory Approach.* Imperial College Press (2006).

[53] B. Skinner and B. I. Shklovskii. *Anomalously large capacitance of a plane capacitor with a two-dimensional electron gas.* Physical Review B **82**, 155111 (2010).

[54] R. Berktold and J. Mannhart. *Two-Port-Network-Based Method to Measure Electrical Characteristics of MIS Devices With Ultrathin Barriers.* IEEE Transactions on Electron Devices **64**, 2625 (2017).

[55] A. Liebsch. *Doping-driven Mott transition in $La_{1-x}Sr_xTiO_3$ via simultaneous electron and hole doping of t_{2g} subbands as predicted by LDA+DMFT calculations.* Physical Review B **77**, 115115 (2008).

[56] G. Giuliani and G. Vignale. *Quantum theory of the electron liquid.* Cambridge University Press, Cambridge, 1. edition (2008).

[57] G. C. Wick. *The evaluation of the collision matrix.* Physical Review **80**, 268 (1950).

[58] A. L. Fetter and J. D. Walecka. *Quantum Theory of Many-particle systems.* Dover Publications, 7. edition (2003).

[59] P. Gori-Giorgi, S. Moroni and G. B. Bachelet. *Pair-distribution functions of the two-dimensional electron gas.* Physical Review B **70**, 115102 (2004).

[60] G. D. Mahan. *Many-particle physics.* Springer US, New York, 3. edition (2000).

[61] F. Bloch. *Bemerkung zur Elektronentheorie des Ferromagnetismus und der elektrischen Leitfähigkeit.* F. Z. Physik **57**, 545 (1929).

[62] C. Attaccalite, S. Moroni, P. Gori-Giorgi and G. B. Bachelet. *Correlation energy and spin polarization in the 2D electron gas.* Physical Review Letters **88**, 256601 (2002).

[63] G. Ortiz, M. Harris and P. Ballone. *Zero temperature phases of the electron gas.* Physical Review Letters **82**, 5317 (1999).

[64] F. H. Zong, C. Lin and D. M. Ceperley. *Spin polarization of the low-density three-dimensional electron gas.* Physical Review E **66**, 036703 (2002).

[65] A. W. Overhauser. *Mechanism of antiferromagnetism in dilute alloys.* Journal of Physics and Chemistry of Solids **13**, 71 (1960).

[66] A. W. Overhauser. *Giant spin density waves.* Physical Review Letters **4**, 462 (1960).

[67] A. W. Overhauser. *Spin density waves in an electron gas.* Physical Review **128**, 1437 (1962).

[68] P. A. Fedders and P. C. Martin. *Itinerant antiferromagnetism.* Physical Review **143**, 245 (1966).

[69] E. Wigner. *On the interaction of electrons in metals.* Physical Review **46**, 1002 (1934).

[70] E. Wigner. *Effects of the electron interaction on the energy levels of electrons in metals.* Transactions of the Faraday Society **34**, 678 (1938).

[71] F. Rapisarda and G. Senatore. *Diffusion Monte Carlo study of electrons in two-dimensional layers.* Australian Journal of Physics **49**, 161 (1996).

[72] S. H. Vosko, L. Wilk and M. Nusair. *Accurate spin-dependent electron liquid correlation energies for local spin density calculations: a critical analysis.* Canadian Journal of Physics **58**, 1200 (1980).

[73] J. P. Perdew and Y. Wang. *Accurate and simple analytic representation of the electron-gas correlation energy.* Physical Review B **45**, 13244 (1992).

[74] J. P. Perdew and A. Zunger. *Self-interaction correction to density-functional approximations for many-electron systems.* Physical Review B **23**, 5048 (1981).

[75] D. M. Ceperley and B. J. Alder. *Ground state of the electron gas by a stochastic method.* Physical Review Letters **45**, 566 (1980).

[76] S. Hong and G. D. Mahan. *Temperature dependence of the Hartree-Fock approximation.* Physical Review B **50**, 7284 (1994).

[77] L. P. Kadanoff and G. Baym. *Quantum Statistical Mechanics.* W. A. Benjamin, New York (1962).

[78] K. A. Brueckner and J. L. Gammel. *Properties of nuclear matter.* Physical Review **109**, 1023 (1958).

[79] W. Kohn and J. M. Luttinger. *Ground-state energy of a many-fermion system.* Physical Review **118**, 41 (1960).

[80] J. M. Luttinger and J. C. Ward. *Ground-state energy of a many-fermion system. II.* Physical Review **118**, 1417 (1960).

[81] U. Gupta and A. K. Rajagopal. *Inhomogeneous electron gas at nonzero temperatures: Exchange effects.* Physical Review A **21**, 2064 (1980).

[82] R. Feynman. *Statistical Mechanics.* Addison-Wesley Publishing Company, California (1972).

[83] A. A. Abrikosov, L. P. Gorkov and I. E. Dzyaloshinski. *Methods of Quantum Field Theory in Statistical Physics.* Prentice-Hall, Englewood Cliffs (1963).

[84] R. Winkler. *Spin-orbit Coupling Effects in Two-Dimensional Electron and Hole Systems.* Springer-Verlag Berlin Heidelberg (2003).

[85] R. Gross and A. Marx. *Festkörperphysik.* De Gruyter, Oldenbourg, 2. edition (2014).

[86] H. A. Kramers. *Théorie générale de la rotation paramagnétique dans les cristaux.* Proceedings Koninklijke Akademie van Wetenschappen **33**, 959 (1930).

[87] G. Dresselhaus. *Spin-Orbit Coupling Effects in Zinc Blende Structures.* Physical Review **100**, 580 (1955).

[88] G. Bihlmayer, O. Rader and R. Winkler. *Focus on the Rashba effect.* New Journal of Physics **17**, 050202 (2015).

[89] A. Manchon, H. C. Koo, J. Nitta, S. M. Frolov and R. A. Duine. *New perspectives for Rashba spin-orbit coupling.* Nature Materials **14**, 871 (2015).

[90] F. Vas'ko. *Spin splitting in the spectrum of two-dimensional electrons due to the surface potential.* Pisma Zh. Eksp. Teor. Fiz. **30**, 574 (1979).

[91] Y. A. Bychkov and E. I. Rashba. *Oscillatory effects and the magnetic susceptibility of carriers in inversion layers.* Journal of Physics C: Solid State Physics **17**, 6039 (1984).

[92] Y. A. Bychkov and E. I. Rashba. *Properties of a 2D electron gas with lifted spectral degeneracy.* P. Zh. Eksp. Teor. Fiz. **39**, 66 (1984).

[93] Z. Zhong, A. Toth and K. Held. *Theory of spin-orbit coupling at $LaAlO_3/SrTiO_3$ interfaces and $SrTiO_3$ surfaces.* Physical Review B **87**, 161102(R) (2013).

[94] P. Ehrenfest. *Bemerkung über die angenäherte Gültigkeit der klassischen Mechanik innerhalb der Quantenmechanik.* Zeitschrift für Physik **45**, 455 (1927).

[95] A. Darr, J. P. Kotthaus and T. Ando. *Physics of Semiconductors: Proceedings of the 13th International Conference, Rome, August 1976.* p. 774. Marves, Amsterdam, 1. edition (1976).

[96] P. Pfeffer and W. Zawadzki. *Spin splitting of conduction subbands in III-V heterostructures due to inversion asymmetry.* Physical Review B **59**, R5312(R) (1999).

[97] R. Lassnig. *$\vec{k} \cdot \vec{p}$ theory, effective-mass approach, and spin splitting for two-dimensional electrons in GaAs-GaAlAs heterostructures.* Physical Review B **31**, 8076 (1985).

[98] L. Petersen and P. Hedegard. *A simple tight-binding model of spin-orbit splitting of sp-derived surface states.* Surface Science **459**, 49 (2000).

[99] S. Caprara, F. Peronaci and M. Grilli. *Intrinsic Instability of Electronic Interfaces with Strong Rashba Coupling.* Physical Review Letters **109**, 196401 (2012).

[100] D. Bucheli, M. Grilli, F. Peronaci, G. Seibold and S. Caprara. *Phase diagrams of voltage-gated oxide interfaces with strong Rashba coupling.* Physical Review B **89**, 195448 (2014).

[101] M. B. Shalom, M. Sachs, D. Rakhmilevitch, A. Palevski and Y. Dagan. *Tuning Spin-Orbit Coupling and Superconductivity at the $SrTiO_3/LaAlO_3$ Interface: A Magneto-transport Study.* Physical Review Letters **104**, 126802 (2010).

[102] A. Joshua, S. Pecker, J. Ruhman, E. Altman and S. Ilani. *A universal critical density underlying the physics of electrons at the $LaAlO_3/SrTiO_3$ interface.* Nature Communications **3**, 1129 (2012).

[103] Y. Kim, R. M. Lutchyn and C. Nayak. *Origin and transport signatures of spin-orbit interactions in one- and two-dimensional $SrTiO_3$-based heterostructures.* Physical Review B **87**, 245121 (2013).

[104] P. Boross, B. Dóra, A. Kiss and F. Simon. *A unified theory of spin-relaxation due to spin-orbit coupling in metals and semiconductors.* Nature Scientific Reports **3**, 3233 (2013).

[105] C. Richter, H. Boschker, W. Dietsche, E. Fillis-Tsirakis, R. Jany, F. Loder, L. F. Kourkoutis, D. A. Muller, J. R. Kirtley, C. W. Schneider and J. Mannhart. *Interface superconductor with gap behaviour like a high-temperature superconductor.* Nature **502**, 528 (2013).

[106] P. Brinks, W. Siemons, J. E. Kleibeuker, G. Koster, G. Rijnders and M. Huijben. *Anisotropic electrical transport properties of a two-dimensional electron gas at $SrTiO_3$-$LaAlO_3$ interfaces.* Applied Physics Letters **98**, 242904 (2011).

[107] K. Janicka, J. P. Velev and E. Y. Tsymbal. *Quantum Nature of Two-Dimensional Electron Gas Confinement at $LaAlO_3/SrTiO_3$ Interfaces.* Physical Review Letters **102**, 106803 (2009).

[108] A. F. Santander-Syro, O. Copie, T. Kondo, F. Fortuna, S. Pailhe, R. Weht, X. Qiu, F. Bertran, A. Nicolaou, A. Taleb-Ibrahimi, P. LeFe, G. Herranz, M. Bibes, N. Reyren, Y. Apertet, P. Lecoeur, A. Barthe and M. J. Rozenberg. *Two-dimensional electron gas with universal subbands at the surface of $SrTiO_3$.* Nature **469**, 189 (2011).

[109] G. A. Samara. *Low—temperature dielectric properties of candidate substrates for high—temperature superconductors: $LaAlO_3$ and ZrO_2 : 9.5 mol% Y_2O_3.* Journal of Applied Physics **68**, 4214 (1990).

[110] B.-E. Park and H. Ishiwara. *Formation of $LaAlO_3$ films on Si(100) substrates using molecular beam deposition.* Applied Physics Letters **82**, 1197 (2003).

[111] R. W. G. Wyckoff. *Crystal Structures.* Wiley (1963).

[112] I. N. Shklyarevskii and P. L. Pakhmov. *Separation of the contribution of free and bound electrons into real and imaginary parts of the dielectric constant of gold.* Optika i Spektroskopiya **34(1)**, 163 (1973).

[113] J. Mannhart. *Changes in the superconducting properties of high-T_c cuprates produced by applied electric fields.* Modern Physics Letters B **06**, 555 (1992).

[114] U. Schwingenschlögl and C. Schuster. *First-Principles Calculations of Electronic States and Self-Doping Effects at a 45° Grain Boundary in the High Temperature $YBa_2Cu_3O_7$ Superconductor.* Physical Review Letters **102**, 227002 (2009).

[115] W. J. Padilla, Y. S. Lee, M. Dumm, G. Blumberg, S. Ono, K. Segawa, S. Komiya, Y. Ando and D. N. Basov. *Constant effective mass across the phase diagram of high-T_c cuprates.* Physical Review B **72**, 060511(R) (2005).

[116] Y. J. Uemura and et al. *Universal Correlations between Tc and n_s/m (Carrier Density over Effective Mass) in High-Tc Cuprate Superconductors.* Physical Review Letters **62**, 2317 (1989).

[117] R. Aidam. *Untersuchung des epitaktischen Wachstums dünner $Pb(Zr_{0.52}Ti_{0.48})O_3$-Schichten und ihre Anwendung in ferroelektrischen supraleitenden Feldeffekttransistoren.* Dissertation Universität Karlsruhe (TH), Karlsruhe (1999).

[118] G. Khalsa, B. Lee and A. H. MacDonald. *Theory of t_{2g} electron-gas Rashba interactions.* Physical Review B **88**, 041302(R) (2013).

[119] M. Salluzzo, J. C. Cezar, N. B. Brookes, V. Bisogni, G. M. De Luca, C. Richter, S. Thiel, J. Mannhart, M. Huijben, A. Brinkman, G. Rijnders and G. Ghiringhelli. *Orbital Reconstruction and the Two-Dimensional Electron Gas at the $LaAlO_3/SrTiO_3$ Interface.* Physical Review Letters **102**, 166804 (2009).

[120] L. F. Mattheiss. *Energy Bands for $KNiF_3$, $SrTiO_3$, $KMoO_3$, and $KTaO_3$.* Physical Review B **6**, 4718 (1972).

[121] R. Frésard, K. Steffen and T. Kopp. *Charge instabilities of the two-dimensional Hubbard model with attractive nearest neighbour interaction.* Journal of Physics: Conference Series **702**, 012003 (2016).

[122] J. Hubbard. *Electron Correlations in Narrow Energy Bands.* Proceedings of the Royal Society of London A **276**, 238 (1963).

[123] M. C. Gutzwiller. *Effect of Correlation on the Ferromagnetism of Transition Metals.* Physical Review Letters **10**, 159 (1963).

[124] J. Kanamori. *Electron Correlation and Ferromagnetism of Transition Metals.* Progress of Theoretical Physics **30**, 275 (1963).

[125] N. F. Mott. *Metal-Insulator Transition.* Review of Modern Physics **40**, 677 (1968).

[126] W. F. Brinkman and T. M. Rice. *Application of Gutzwiller's Variational Method to the Metal-Insulator Transition.* Physical Review B **2**, 4302 (1970).

[127] P. W. Anderson. *Theory of Magnetic Exchange Interactions:Exchange in Insulators and Semiconductors.* Solid State Physics **14**, 99 (1963).

[128] M. Cyrot. *The Hubbard hamiltonian.* Physica B **91**, 141 (1977).

[129] P. W. Anderson. *The Resonating Valence Bond State in La_2CuO_4 and Superconductivity.* Science **235**, 1196 (1987).

[130] P. A. Lee and N. Nagaosa. *Gauge theory of the normal state of high-T_c superconductors.* Physical Review B **46**, 5621 (1992).

[131] C. J. Halboth and W. Metzner. *Renormalization-group analysis of the two-dimensional Hubbard model.* Physical Review B **61**, 7364 (2000).

[132] H. Tasaki. *From Nagaoka's Ferromagnetism to Flat-Band Ferromagnetism and Beyond: An Introduction to Ferromagnetism in the Hubbard Model.* Progress of Theoretical Physics **99**, 489 (1998).

[133] J. Sólyom. *The Fermi gas model of one-dimensional conductors.* Advances in Physics **28**, 201 (1979).

[134] A. Amaricci, A. Camjayi, K. Haule, G. Kotliar, D. Tanasković and V. Dobrosavljević. *Extended Hubbard model: Charge ordering and Wigner-Mott transition.* Physical Review B **82**, 155102 (2010).

[135] P. G. J. van Dongen. *Phase diagram of the extended Hubbard model at weak coupling.* Physical Review B **54**, 1584 (1996).

[136] G. A. Sawatzky, I. S. Elfimov, J. van den Brink and J. Zaanen. *Heavy-anion solvation of polarity fluctuations in pnictides.* Europhysics Letters **86**, 17006 (2009).

[137] M. Berciu, I. Elfimov and G. A. Sawatzky. *Electronic polarons and bipolarons in iron-based superconductors: The role of anions.* Physical Review B **79**, 214507 (2009).

[138] R. Micnas, J. Ranninger and S. Robaszkiewicz. *Superconductivity in narrow-band systems with local nonretarded attractive interactions.* Reviews of Modern Physics **62**, 113 (1990).

[139] C. Cancellieri, A. S. Mishchenko, U. Aschauer, A. Filippetti, C. Faber, O. S. Barisić, V. A. Rogalev, T. Schmitt, N. Nagaosa and V. N. Strocov. *Polaronic metal state at the $LaAlO_3/SrTiO_3$ interface.* Nature Communications **7**, 10386 (2016).

[140] P. García-Fernández, J. C. Wojde, J. Íniguez and J. Junquera. *Second-principles method for materials simulations including electron and lattice degrees of freedom.* Physical Review B **93**, 195137 (2016).

[141] G. Lhoutellier, R. Frésard and A. M. Oleś. *Fermi-liquid Landau parameters for a nondegenerate band: Spin and charge instabilities in the extended Hubbard model.* Physical Review B **91**, 224410 (2015).

[142] S. E. Barnes. *New method for the Anderson model.* Journal of Physics F: Metal Physics **6**, 1375 (1976).

[143] S. E. Barnes. *New method for the Anderson model. II. The U=0 limit.* Journal of Physics F: Metal Physics **7**, 2637 (1977).

[144] T. Li, P. Wölfle and P. J. Hirschfeld. *Spin-rotation-invariant slave-boson approach to the Hubbard model.* Physical Review B **40**, 6817 (1989).

[145] R. Frésard and P. Wölfle. *Unified Slave Boson Representation of Spin and Charge Degrees of Freedom for Strongly Correlated Fermi Systems.* International Journal of Modern Physics B **6**, 685 (1992).

[146] R. Frésard, M. Dzierzawa and P. Wölfle. *Slave-Boson Approach to Spiral Magnetic Order in the Hubbard Model.* Europhysics Letters **15**, 325 (1991).

[147] W. Zimmermann, R. Frésard and P. Wölfle. *Spin and charge structure factor of the two-dimensional Hubbard model.* Physical Review B **56**, 10097 (1997).

[148] P. Wölfle. *Slave boson theories of correlated electron systems.* Journal of Low Temperature Physics **99**, 625–635 (1995). ISSN 1573-7357.

[149] R. Frésard and T. Kopp. *Slave bosons in radial gauge: the correct functional integral representation and inclusion of non-local interactions.* Nuclear Physics B **594**, 769 (2001).

[150] D. Vollhardt. *Normal ^{3}He: an almost localized Fermi liquid.* Reviews of Modern Physics **56**, 99 (1984).

[151] M. Plischke and B. Bergersen. *Equilibrium statistical physics.* World Scientific, Singapore, 3. edition (2006).

[152] I. N. Bronstein, K. A. Semendjajew, G. Musiol and H. Mühlig. *Taschenbuch der Mathematik.* Verlag Harry Deutsch, Frankfurt am Main, 5. edition (2001).

[153] G. F. A. Marquis de L' Hospital. *Analyse des infiniment petits, pour l'intelligence des lignes courbes.* D'Limprimerie Royale (1716).

[154] C. Cohen-Tannoudji, B. Diu and F. Laloe. *Quantum Mechanics*, volume 1. Wiley (1977).

Acknowledgments

I would like to thank...

...Prof. Dr. Thilo Kopp for providing me the framework of this thesis and, which is even more important, for what goes beyond that: The motivation and fascination for physics that arose from nearly[1] every conversation, the insights that originated from his vast knowledge on so many fields, his understanding for technical problems and challenges and for the great time I was able to spend.

...Prof. Dr. Gert-Ludwig Ingold for kindly agreeing to be the second reviewer.

...Prof. Dr. Raymond Frésard for the exciting physics he introduced me to and the fruitful collaboration.

...Dr. Florian Loder for the helpful introduction to Mathematica, Latex and the iMac at the beginning of my work and for the sharing of his knowledge.

...the rest of our small but fine theory group: Dr. Daniel Braak, Patrick Seiler, Stefan Gorol and Elias Lettl for being such wonderful roommates and interlocutors.

...the whole chair for the pleasant atmosphere and especially our permanent members that were extra supportive at all times.

...my parents and friends for their support.

...Chenh Dung for her all-embracing support in so many respects.

[1] This excludes talks that were of prevailing administrative character.